Topics in the Mathematical Modelling of Nanotoxicity

Zofia Jones

Thesis submitted to The University of Nottingham
for the degree of Doctor of Philosophy

May 2011

A CASE Studentship with the Health and Safety Laboratories, Buxton.

Abstract

Over the last ten years questions related to the safety of nanoparticles and their possible toxic effects have become well-established. The government's Health and Safety Laboratories (HSL) at Buxton are currently attempting to determine their possible toxicity in the workplace. It is their responsibility to establish what levels are exposure can be considered safe in the workplace. This project is a CASE studentship with HSL and aims to start developing mathematical models relating to nanotoxicology. After reviewing the available literature, three key mechanisms which are involved in the possible toxicity of nanoparticles emerge. One mechanism is the oxidative stress they cause once they enter individual cells. The second mechanism is the damage done to the surface of the lung if they are not successfully phagocytosed on inhalation. Finally, the third mechanism is their propensity to aggregate both when dispersed in the air or when they are found inside the body. These three topics are dealt with in Parts I, II and III respectively.

There has been much concern over how carbon nanotubes (CNTs) may cause oxidative stress. Oxidative stress occurs when there is an overload negatively charged species in the cell. These are collectively known as Reactive Oxidative Species (ROS). ROS are always present in a cell as they are the natural product of the metabolic pathways. By their reactivity, they readily cause damage to other molecules in the cell, so every cell produces anti-oxidants in order to control the concentration of ROS. However, when the concentration of ROS becomes too high the concentration of anti-oxidants becomes depleted and the cell can become too damaged to function. In this case it dies by necrosis. When a cell dies by necrosis is can cause irritation and further damage to surrounding cells. Oxidative stress can also trigger the immune response so that the cell dies by self-programmed apoptotic cell death which limits this damage to surrounding cells. It is best to avoid unnecessary cell death, however, not undergoing apoptosis risks a more damaging necrotic death.

Part I introduces develops models of Tumor Necrosis Factor-α (TNF-α) activated pathways. This model consists of three signalling cascades. One pathway triggers apoptosis while a second inhibits apoptosis. These two models are based on pre-existing models. This work introduces a third pathway which activates Activator Protein-1 (AP-1). This pathway includes two well-known ROS sensitive elements. These are the ROS-sensitive activation of the Mitogen-Activated Protein Kinase (MAPK) cascade and the ROS-sensitive deactivation of the MAPK phosphatases.

These three pathways are regulated by three sets of inhibiting reactions and inhibitors to

these inhibitors. The effect of these inhibitors is to introduce a time-lag between the initial TNF-α extracellular signal and the death of the cell by apoptosis. This time-lag is regulated by the concentration of intracellular ROS and the concentration of anti-oxidants. Different combinations of inhibitors can be switched on or off before running the model. The effectiveness of the oxidative stress sensitive elements in regulating apoptosis can therefore be optimised while different sets of inhibitors are active. Two qualitatively different types of solutions are found. The cell can be either only transiently active, over a shorter period of time, or persistently active, over a longer period of time. This could provide some guidance to biologists investigation TNF-α activation of the immune system.

On inhalation, CNTs have been found to reach the alveoli, where air exchange occurs in the lung. The only mechanism available to remove debris in these delicate regions of the lung are lung macrophages. Macrophages work by enclosing unwanted matter in an organelle called a lysosome and then moving this debris away to where it can be cleared by cilia. Non-organic material does not trigger a macrophage response as strongly as organic material, which also triggers the immune system. The shape of fibrous material makes it more difficult for a macrophage to successfully form a lysosome and to move the material away once it has been engulfed. Frustrated phagocytosis releases harmful acids and enzymes which can damage the alveoli causing oxidative stress. If debris cannot be removed, then dead cells may form around the debris to protect the surrounding tissue, forming a granuloma. Both scarring from frustrated phagocytosis and granuloma formation will impair the function of the lung.

In Part II, insight is gained on how a cell membrane can engulf an object with a high aspect ratio. The mechanisms of phagocytosis are complex in terms of both cell signalling cascades and the polymerisation and de-polymerisation of the actin network. In order to find a model which takes into account the geometry of a cell as a whole, this picture has been simplified. An energy minimisation approach is used where the surface of a cell is taken to be a surface of rotation around an axis, which is taken to be the axis of a fibre.

In Chapter 4, the free energy is taken to be of a liquid drop, resting on a solid surface, in vapour where only the surface and volume energies are considered. The surface tension is taken to account for the tension in the lipid bilayer on the surface of the macrophage. In Chapter 5, the free energy is extended to also include a Helfrich or bending energy which specifically takes into account the energy taken to bend a lipid bilayer.

It is assumed that, in order to conserve the limited resources of a macrophage, the shape of a lipid membrane which has successfully engulfed a particle will be energetically stable with regards to these surface, volume and bending energies as a macrophage reaches the final stages of phagocytosis. This does not take into account the energy required to remodel the cytoskeleton for the cell to reach this shape. However, the bending energy associated with cell membranes of increasing length can be used to suggest the amount of energy required in this dynamical process.

It is found that in Chapter 4, when no Helfrich energy is included in the energy minimisation, the only limiting shape possible in the limit of increasing length to radius ratio of the fibre is a sphere. When the Helfrich energy is included, three different boundary conditions

are imposed. The first boundary condition sets the forces associated with the bending energy to zero at the edge of the membrane. At the point of contact between the membrane and the fibre, the forces reduce to that of a classical solid/liquid/vapour interface. The second boundary condition is imposes the length of the droplet. This length can be incrementally increased to find solutions of increasing length. Finally, a third boundary condition is imposed which sets the contact angle of the membrane at the surface of the fibre to zero. By imposing these three boundary conditions, a variety of membrane shapes were obtained. These results are expected to be a useful guide to experimentalists observing different shapes of macrophages under different conditions.

Part III in Section 7.1 pin-points frameworks of models which use concepts from polymer physics to possibly predict the volume of an aggregate of CNTs and also to understand how nanoparticles interact with chain-like protein. However, no new results are presented in Part III.

Acknowledgments

I would like to thank my friends and family who always manage to keep life interesting. Anyone and anything which has kept me distracted enough to focus is much appreciated. Thanks also to those who have spent time supervising me: John King, Andreas Münch and Richard Graham. I also acknowledge Susan Franks, my industrial supervisor at HSL.

Contents

Chapter 1

Introduction to Nanotoxicology

Over the last ten years, the question of whether, how and to what extent nanoparticles can be considered toxic has been examined. The topics related to this question have been developed in review papers such as [9, 63, 77, 112]. By summarising the discussion found in these and other review papers, this section puts the aims of the mathematical models in this thesis in context.

Nanoparticles, in the form of ultrafine particles [126], have always existed in the environment. Nanoscale oxides and colloids have existed in soil and water while ultrafine particles, both naturally occurring and a product of exhaust fumes, can be found in the air. Since the last quarter of the 20^{th} century, technology has progressed to the point that materials can be manipulated on an atomic scale. Nanoparticles are generally defined as particles whose length scale in at least one dimension is 1-10 nm and which have a small size distribution within a sample [9]. Any field of science is potentially controllable on a smaller scale than has previously been possible. Materials can be carefully designed to meet their desired purpose. For this reason, the group of materials classed as nanoparticles is a very diverse group of materials and compounds united only by their size classification. The different compound classes include carbonaceous nanomaterials such as carbon nanotubes, metal oxides, semiconductor materials including quantum dots, colloids and nanopolymers such as dendrimers. They have found extensive uses in electronics, cosmetics, sunscreen, paint among other uses listed in [55]. An inventory of products containing nanoparticles is listed on the website for the Project on Emerging Nanotechnologies [1].

The review in [55] lists several remarkable properties of different types of nanoparticles. As well as producing nanotechnologies of a uniquely small size, nanotechnology has also produced materials with unique properties not shared with larger scaled materials which share the same chemical make-up [9]. A prime example of this type of material is the carbon nanotube (CNT). A single-walled carbon nanotube (SWCNT) can be imagined as a two dimensional lattice of carbon molecules rolled up to form a cylinder with a nanoscale radius which is 10,000 times finer than a human hair. A multiwalled carbon carbon nanotubes (MWCNT) is a concentric assembly of several single-walled carbon nanotubes. CNTs are excellent thermal and electric conductors. SWCNT have a strength-to-weight ratio 460 times that of steel. Fullerenes are

another example of a carbon-based nanoparticle. They are spherical lattices of carbon atoms which are less stable and so less useful in commercial products than CNTS. Since the discovery of the fullerene in 1985 and the subsequent discovery of CNTs in 1991, CNTs are now mass manufactured in factories that can produce up to 1,500 tonnes/year. As noted in [55], annual production of SWCNT was expected to exceed 1,000 tonnes by 2011.

Metal oxides are another class of nanoparticle in mass production, especially zinc oxide (ZnO) and titanium oxide (TiO_2). Titanium oxide is a photocatalyst which has been used in solar cells, paints and coatings. Zinc and titanium oxide are widely used in products such as sunscreens and bottle coatings, which make direct contact with consumers. Production of metal oxides for skin care products is expected to be 1,000 tonnes a year in 2010.

The study of the potential toxicity of the different classes of nanotubes has lagged behind the explosion of their manufacture and use in consumer products. The story of asbestos stands as a cautionary tale of the damage that can be done if the usefulness of a new material delays a proper investigation of its toxic effects [28]. Asbestos is now known to cause asbestosis where the lung is significantly damaged and scarred and also, in rarer cases, mesothelioma, or cancer of the lung lining. The example of asbestos is particularly pertinent [28] as CNTs share its fibrous nature. CNTs can be likened to asbestos in terms of both high aspect ratio and biopersistance, which is the inability of the body to break down its structure.

The government's Health and Safety Executive (HSE) is responsible for setting the standards in all aspects of workplace safety from the management of toxic products to stress. Research on workplace safety is carried out in Health and Safety Laboratory (HSL) at Buxton. Evaluating the potential of nanotoxicity is one of their ongoing projects. This project is part of a worldwide effort to tackle the many different aspects of this problem. The challenges of evaluating the toxicity of nanoparticles are outlined in [63].

From 2006-2012 it has been envisioned that research effort is mainly concentrated on the challenge of developing laboratory based methods which can reliably evaluate the risk posed by nanoparticles in factories or to the consumer. For example, the work at HSL has been focused in two directions. Firstly, cell death counts or cell assays are made while tissue samples are exposed to nanoparticles. As a government laboratory, HSL needs to develop robust methods to give a clear indication of potential toxicity before examining the possible mechanisms of any potential toxicity in detail. Nanoparticles have a large surface to volume ratio, so that a large proportion of atoms are on the surface of the particle. It may well be that considering the total surface area, rather than the total mass per exposure may be a reliable enough way to quantify their toxicity.

Secondly, HSL is attempting to establish guidelines on how to handle nanoparticles during the manufacturing process in order to minimise the exposure of the workers to them. As nanoparticles are handled in a factory setting, they may be released into the air to form aerosols. The exposure pathway of primary concern is inhalation. Mathematical models of the pattern of deposition of particles in the trachea, bronchae and alveoli are available. In order to use these models, specific information on the dispersion of nanoparticles in air and their aerodynamic diameter must be obtained. The picture of nanoparticles in air is complicated

by the observation that, due to their high surface area to volume ratio, they commonly form aggregates, or loosely bonded groups of particles, in order to minimise their surface energy. HSL is experimenting with different sampling methods to determine these factors. Protocols must be developed and cost-effective equipment must be chosen in order to reliably test workplace environments for exposure.

Referring back to the broader picture of the progress of nanotoxicology in [63], other research groups around the world are also tackling questions on how to monitor the exposure of nanoparticles to the general public and to start building and testing specific mechanisms by which they could potentially be toxic. Models for predicting engineered nanomaterial behaviour in the body are expected to be ready for use by 2017. This puts into context the scope of this thesis. The most time consuming task in this thesis has been to develop and justify quantitative models related to potential mechanisms of nanoparticle toxicity. The results and properties of the models must be interesting and also mathematically and biologically relevant without information on specific parameters or even specific mechanisms from experimenal investigation. This work has been strongly guided by review papers from the major nanotoxicology research groups around the world.

In the UK, the investigation into nanotoxicology is being led by Ken Donaldson and Vicki Stone at Edinburgh Napier University. A commonly referenced review paper, [28], highlights their specific interest in the pulmonary toxicity of CNTs on inhalation. Vicki Stone is the editor-in-chief of "Nanotoxicology", a dedicated journal which has been in print since 2007. The first ever article of this journal [112] reviews the history of nanotoxicology up to 2007. Two categories of mechanisms which emerge from [112] are oxidative stress and, in the light of the asbestos experience, lung damage by high aspect ratio nanoparticles (HARN). There have also been specific findings, such as the discovery that quantum dots can penetrate the outer surface of the skin and the unique damage gold nanoparticles of a certain size can do to DNA. However, a systematic understanding of risk, exposure and toxicokinetic data was considered lacking.

Another research group of note is that of Andre Nel at the California Nanosystems Institute. His widely cited review in Science [77] and his subsequent review in Nature [76], clearly discuss the possible biochemical reactions of nanoparticles in the body which have been investigated and discussed in hundreds of related and unrelated experimental papers. The discussion in [77] provides a clear understanding of how nanoparticles could activate the immune response by releasing damaging free radicals into the cell causing oxidative stress.

The discussion in [76] focuses on how the small size of a nanoparticle allows it to interact with proteins, organelles and cell membranes. CNTs, for example, are very hydrophobic so, in order to understand their biological interactions, the object of interest is not the nanoparticle itself as much as the complex formed by the nanoparticle and proteins which have associated themselves to it. A series of papers from the Centre of BioNano Interactions, Dublin headed by Iseult Lynch have attempted to characterise this protein corona [59]. A pioneer in nanotoxicology is Günter Oberdörster at the University of Rochester, USA, who used his expertise in the toxicity of airborne particles to open up the discussion of nanotoxicology [80].

The consistently reoccurring topics in the review papers mentioned and accompanying research on nanoparticles have been

- Dermal Penetration - *can they penetrate the skin?*
- Uptake by cells via endocytosis - *can they enter an individual cell?*
- Oxidative Stress - *do they cause oxidative stress?*
- Fibrotic Response - *do they cause a fibrotic response?*
- Activation of Immune Response - *do they otherwise trigger the immune system?*
- Dispersion - *what is the expected size of agglomerates found in air?*
- Inhalation - *where are they deposited in the lungs?*
- Clearance via Phagocytosis - *can they be cleared by the body's frontline mechanism, phagocytosis?*
- Clearance by kidneys, liver lymphatic system - *once in the blood stream, can they be cleared?*
- Biological Persistence - *how long do they stay in the lungs or bloodstream?*
- Bio-reactivity - *can their biological interaction be characterised by their surface area, by their associated protein corona or by their geometry?*

A broad range of specialist knowledge will be required to answer these questions. In general, new science is not expected to be needed to answer these questions. However, new applications of known scientific approaches will be required. This can also be said about the development of theoretical models of nanotoxicology. Once nanoparticles have been characterised and evidence for specific temporal and spatial interactions has been found, then these findings can be used to guide the choice of parameters and boundary conditions in any number of existing models developed under the umbrella of mathematical biology.

Though there are not many models in the tradition of applied mathematics which incorporate nanoparticles, there has been much progress in simulating interactions and properties computationally *in silico*. Recently, the oxidative stress potentials of a selection of metal oxides have been found using quantum physics [11]. A molecular dynamics approach has also been used to successfully model various nanoparticle interactions, including the permeation of a nanoparticle through a lipid membrane, [17, 35].

Part I

Intracellular Oxidative Stress

Chapter 2

Intracellular Oxidative Stress Model

2.1 Oxidative Stress as a Possible Mechanism of CNT Toxicity

The task of developing a model of intracellular oxidative stress in relation to nanoparticle toxicity is motivated by two observations. Firstly, due to experimental investigations, such as those reviewed in [9] and [80], it is now established that nanoparticles can penetrate cells. Secondly, in many other review papers and reports such as [9, 28, 40, 108, 112], oxidative stress is considered to be one of the primary mechanisms of toxicity.

The review articles cite experimental papers, [26, 62, 106, 107]. From observing the activated proteins, these papers suggest that CNTs indeed induce oxidative stress. Particles which cause oxidative stress are commonly referred to as Reactive Oxidative Species (ROS). These are particles on which there is a concentrated negative charge which can damage proteins inside a cell and interfere with signalling pathways. It was noted in [84] and [85] that at least some of the toxicity of CNTs could be attributed to iron present in the impurities which have not been removed after manufacture. Through the iron-catalysed Haber-Weiss reaction, highly reactive hydroxyl radicals (OH^-) can be formed. Most CNTs do contain iron oxides and so it can be assumed that, even if the biochemistry specific to the nanoparticle structure is unknown, CNTs will induce oxidative stress. The oxidative stress potentials recently calculated in [11] can indicate how the concentration of ROS is related to the concentration of certain metal oxides inside a cell.

Additionally, the results from [26, 62, 106, 107] link the potential toxicity of CNTs with well-known immune response pathways. Cytokines are signalling proteins which are used in intercellular communication. Once a single cytokine binds with its receptor in the membrane of a cell, many signalling cascades may be triggered. The key cytokine associated with CNT-induced oxidative stress was found to be NF-κB. It was also found that proteins associated with TNF-α, such as NF-κB, the MAPK cascade and AP-1 are also activated.

These pathways are put into context by the discussion in Nel et al [77] where it was suggested that every cell has a three tiered response to oxidative stress. This three tiered response was summarised by the diagram reproduced here in Figure 2.1. In the lowest tier are the anti-oxidants such as glutathione (GSH). This first tier response is controlled by the transcription factor Nrf-2.These are produced continually by each cell to mop up the ROS which are routinely produced by the metabolic pathways. However, if CNTs are present inside a cell, there is an excess of ROS and anti-oxidants are depleted. At this stage, the next tier of response is triggered. This tier contains the cytokine TNF-α, the transcription factors NF-κB and AP-1 and their associated signalling proteins. These signalling cascades decide whether or not a cell undergoes self-activated cell death, apoptosis, or risk an unmanaged form of cell death, necrosis, which is more damaging to the surrounding tissue. If an apoptotic fate is chosen, then the third tier of response is triggered. This tier contains the apoptotic pathways triggered by the caspases.

The models in this chapter aim to capture the oxidative stress sensitive decision making pathways in the middle tier. They feature TNF-α, NF-κB and AP-1. Mechanisms by which anti-oxidants are upregulated are not included. It is assumed that the cell is in a state of

oxidative overload, much larger than that experienced during normal metabolism. The model focuses on the oxidative stress elements of the pathways which are triggered once the this pool of anti-oxidants is depleted.

The biological information contained within the construction of these models can be found in Section 2.2. Full mathematical details of these models are in Section 2.3. The model consists of three signalling pathways pathways which are referred to as the apoptotic, anti-apoptotic and oxidative stress sensitive pathways. The main oxidative stress sensitive elements are the activation of the MAPK kinases and the deactivation of the phosphatases, which act to deactivate the MAPK kinases. These three pathways upregulate three sets of inhibitors and inhibitors of these inhibitors. These inhibitors are upregulated by the anti-apoptotic pathway and act to block the signal along the apoptotic and oxidative stress sensitive pathways. The inhibitors of the inhibitors upregulated by the oxidative stress sensitive pathway act to "break the brake" of apoptosis as described in [58].

Information detailing specific interactions in TNF-α activated pathways is readily available. However, as these models was not developed in association with an experimental investigation, detailed kinetic data is not available. It can be assumed that no reaction will have an anonymously fast or slow associated rate as all the reactions featured in the model occur at the same temperature, inside one cell, outside of its nucleus. The model is complicated enough in structure, that it is the structure of the model itself, rather than small variations in the rate constants, which allows it to predict different types of response.

The analysis of these models in Section 2.4 focuses on the effectiveness of the oxidative stress sensitive pathway in regulating the apoptotic response when the different sets of inhibitors are set to be either active or inactive. This effectiveness is quantified by the change in the steady state value of DNA fragmentation when the inhibitors of the inhibitors are active rather than inactive.

The two types of response predicted by these models are a transient activation of the caspases, where the apoptotic response is limited by the concentration of caspase proteins inside a cell and a persistent activation, where the apoptotic response is less limited by the concentration of proteins inside a cell. These cases are examined separately in Sections 2.4.2 and 2.4.4 respectively. These two cases can act as a guide to experimentalists interested in establishing the pattern of oxidative stress sensitive caspase activation. The correlation between the extent of apoptosis and the initial concentration of proteins in the apoptotic and anti-apoptotic pathways was investigated in Sections 2.4.2.5 and 2.4.4.1. The method used in the sensitivity analysis follows commonly found examples, such as those in [94].

2.2 Overview of Oxidative Stress Model with Literature Review

TNF-α is a cytokine which is secreted into the tissue fluid in response to a variety of stressors. When it binds with a TNF-α receptor on the cell membrane it can trigger many pathways simultaneously. One of these pathways triggers apoptosis by activating the caspases. This pathway will be referred to as the apoptosis pathway. Another pathway activates the

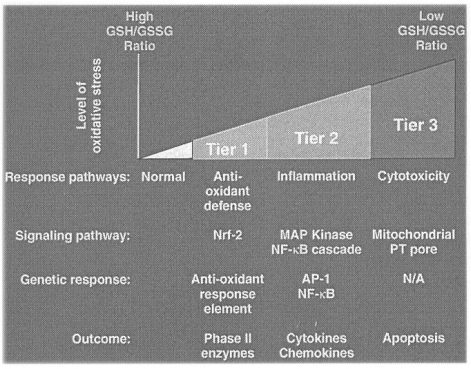

Figure 2.1: Three tier oxidative stress model from [77].

transcription factor NF-κB. This transcription factor can also upregulate a variety of anti-oxidants and also proteins which inhibit the apoptosis pathway. However, its anti-oxidant activity is not included in the current work. This second pathway will be referred to as the anti-apoptosis pathway. The apoptosis pathway is the centre pathway in Figure 2.5 while the anti-apoptosis pathway is on the right. The role of the apoptosis and anti-apoptosis pathways in jointly governing the fate of an individual cell has been discussed at length ([2, 5, 48, 109, 123]). The processes involved in the apoptosis and anti-apoptosis pathways can be found in Sections 2.2.2.

If nanoparticles cause oxidative stress, the cell's response to ROS inside the cell should also be considered. In [85] it is suggested that anti-oxidant treatment can afford near complete protection against cell death in the event of simulation by TNF-α in certain cell types. The work presented here introduces a third, oxidative stress sensitive, pathway. This is the pathway on the left hand side of Figure 2.5. Activating this pathway is generally thought to trigger apoptosis, so it will be referred to as the pro-apoptotic pathway.

Full discussion on the biological basis of the pro-apoptosis pathway can be found in Section 2.2.3. A recent paper [19] reviews various mechanisms by which oxidative stress is thought to regulate apoptosis. Review and discussion papers [3, 58, 74, 85] discuss ways in which TNF-α activates Jun -N-terminal kinase (JNK) which is an activator of the transcription factor Activator Protein-1 (AP-1). This activation is ROS sensitive due to the ROS sensitive activation of ASK1, a protein upstream to AP-1 and the ROS sensitive deactivation of the phosphatases, which inhibit protein upstream from AP-1. The mathematical description of the pro-apoptosis pathway can be found in Section 2.3.4.

The interaction between the specific proteins in these three pathways can be referred to as "cross-talk". The key outputs of the three pathway model are the concentration of DNA fragmentation, which indicates the extent of apoptosis, and the concentration of Reactive Oxidative Species (ROS), which indicates the extent of necrosis.

2.2.1 Summary of Existing Model

The apoptotic and anti-apoptotic pathways are the subject of mathematical models reviewed in [124]. The models investigate the role of TNF-α and NF-κB in apoptosis. Of the models reviewed Cho et al, [18], together with Rangamani and Sirovich, [89], are the most relevant to this problem. The apoptosis and anti-apoptosis pathways, as they appear in the current model, can be found in Sections 2.3.2 and 2.3.3. The apoptotic and anti-apoptotic pathways are the middle and right-hand side pathways respectively in Figures 2.5 and 2.6. This section introduces the mathematical framework used to build the final three pathway model. Justification for the choice of proteins which form these pathways is given in Section 2.2.

In both the apoptotic and anti-apoptotic pathways, a complex of proteins forms, which then breaks up, activating one protein, which can then continue to activate the apoptotic or pro-apoptotic pathways. These reactions follow simple mass law kinetics. A template model of a complex of two proteins can be given as

$$\dot{m}_1(t) = -k_1 m_1(t) m_2(t) + k_2 m_3(t), \tag{2.1}$$

$$\dot{m}_2(t) = -k_1 m_1(t) m_2(t) + k_2 m_3(t) + k_3 m_3(t), \tag{2.2}$$

$$\dot{m}_3(t) = k_1 m_1(t) m_2(t) - k_2 m_3(t) - k_3 m_3(t), \tag{2.3}$$

$$\dot{m}_4(t) = k_3 m_3(t), \tag{2.4}$$

where m_1 and m_2 combine to form the complex m_3 which then activates m_1 to form m_4. The three rate constants are k_1, the association constant, k_2, the diassociation constant and k_3, the activation constant. In the apoptosis pathway the formation of the death complex activates the initiators of cell death, the caspases. In the anti-apoptosis complex, the formation of a second complex leads to the activation of NF-κ which induces the inhibitor of apoptosis c-IAP. In [89] the structure of this model was revised slightly with reference to available literature.

The rate constants listed in [18] were used to guide the choice of rate constants in the current model which are listed in Table 2.2. These rate constants are the only available source of kinetic data available. The mathematical models reviewed in [124] also use the rate constants introduced in [18].

In [18], a set of rate constants was found which minimised the sensitivity of the model outputs to perturbations in these rate constants of up to 20% in the rate constants using experimental data as a reference. Full details can be found in [18].

The work in [18] revealed that if each of the rate constants k_1, k_2 and k_3 in the template model above were perturbed then the rate constant to which the output of their model was most sensitive to was k_1. It was then found that of all of the association constants in their model, the rate of association of TNF-α and TNF-Receptor 1 (TNFR1) was the once which most altered steady state values on perturbation. As the association, disassociation and activation constants not involved in the TNF-α/TNFR1 activation were much less sensitive to perturbation, all association, diassociation and activation constants were given the same value. The values of

the constants in the model were chosen to minimise the sensitivity of the steady state values to perturbations in k_1.

The signalling pathways in [18] branch off downstream from the TNF-α/TNFR1 complex at the TNF-α/TNFR1/TRADD complex. It is the extent of activation of TNF-α/TNFR1/TRADD which then determines the extent of apoptosis. The extent of activation of TNF-α/TNFR1/TRADD is determined by both the initial concentration of TNF-α and the value of k_1. In the current model, the protein which initiates the signalling cascade is taken to be TRADD. This simplifies the model so that the outputs are less sensitive to the value of k_1 and more dependent on the initial concentration of TRADD. This simplifies the analysis of the final model as the strength of the extracellular signal can be quantified as the initial concentration of TRADD rather than as a non-linear combination of the initial concentrations of TNF-α, TNFR1, TRADD and k_1.

2.2.2 Overview of Apoptosis and Anti-Apoptosis Pathways

TNF-α is a cytokine which is central to many aspects of the immune response. A good review of the signalling pathways of TNF-α can be found in [2] which includes a brief overview of the apoptosis, AP-1 and NF-κB pathways considered here. TRADD is a mediator of the TNF-α extracellular signal via TNFR1 to all three of these pathways. Figure 3 in [123] indicates the extent of proteins that can be associated with just two of the branches of the TNF/TNFR1 signalling pathway though not all these proteins are vital to the propagation of the extracellular signal.

Further details on the apototic pathway used in the current model can be found in Section 2.3.3 and those for the anti-apototic pathway can be found in Section 2.3.2. Coloured terms indicate interactions with the oxidative stress sensitive pathway which are discussed below in Section 2.2.3.

2.2.2.1 Apoptosis Pathway

TNF-α (Tumour Necrosis Factor-α) induced apoptosis is mediated by the caspase cascade. If TNF-α/TNFR1 binds with TRADD (TNF-α associated death domain), which then allows for the binding of FADD (fas associated death domain), the complex is able to bind to caspase-8 and activate it. Caspase-8 can then activate the DNA damage effector, which for the TNF-α pathway is caspase-3 or caspase-7. This effector can then enter the nucleus and induce DNA fragmentation. DNA fragmentation is itself a complicated biological process which is summarised in [18] by one step. Here DNA fragmentation is simply a component of the pathway with a given concentration.

2.2.2.2 Anti-Apoptosis Pathway

The activation of NF-κB is well studied [109]. In its unactivated state NF-κB is held in the cytoplasm by IκB. To free NF-κB, so that it can enter the nucleus to promote protein synthesis, IκB must be phosphorated to form IκB-P. Phosphorylation refers to the addition

of a phosphate group (PO_4) to a protein. The phosphorylation of IκB is done by activated IKK (IκB-kinase). NF-κB's most potent activator is TNF-α. Intracellular proteins bind with TNF-α/TNFR1 to form a complex which can activate IκB-kinase (IKK). To release NF-κB, IκB must also be ubiquinated. However, it can be assumed that phosphorylation rather than ubiquitination (the degradation of a protein), is the rate limiting step so unbiquitination is not included in this model.

NF-κB upregulates a variety of proteins including anti-oxidants, cell repair proteins and inhibitors of apoptosis such as c-IAP, FLIP and XIAP. The upregulation of a protein, such as NF-κB and AP-1, can be broken down into several stages and, like DNA fragmentation, is a complicated process. However, for the purpose of the current model, it will be modelled as a single step.

There are a variety of possible interactions between caspases and inhibitors of apoptosis which are discussed in detail in [96]. It is known that c-IAP binds to activated caspase-3 and it is this interaction which is the only example of cross-talk in the model found in [18].

2.2.3 Overview of Oxidative Stress Sensitive Pathway

The model for the third pathway attempts to combine several different elements. Firstly, TNF-α activates the MAPK cascade in a ROS sensitive way. This means that the third pathway does not activate immediately, like the other two pathways, but only activates when the concentration of ROS is suffiently high. The interaction between ROS, the anti-oxidants, which reduce the concentration of ROS, the MAPK cascade and AP-1 is summarised in Figure 2.2.

Prolonged AP-1 activation leads to the release of proteins (Bidj) which release caspases from inhibitor protein c-IAP. Another inhibitor protein (FLIP) regulated by NF-κB has been found to inhibit MAPK. This inhibitor can be itself inhibited by ITCH. Like Bidj, ITCH is also released after prolonged AP-1 activation. The two sets of inhibitors and the inhibitors of these inhibitors are summarised in Figure 2.3.

When caspase-3 is released from c-IAP by Bidj, it is free to be reactivated and to continue apoptosis. This means that the capases will be activated twice. The activation of the oxidative stress sensitive pathway is delayed until the concentration of ROS is high enough. The time delay between the initial and secondary activation will depend on the degree of oxidative stress within the cell while the extent of apoptosis due to the secondary activation will depend on the initial concentrations of the proteins involved especially TRADD.

2.2.3.1 Production of ROS

It is also important to consider how ROS are produced and contribute to cell death as well as being clear on possible interactions not included in the current model.

An event associated with the onset of apoptosis is an oxidative burst when the mitochondrial membrane is depolarised [84]. A certain increase in the concentration of ROS is associated with apoptosis and does not necessarily indicate necrosis. In this model, this is captured by

linking DNA fragmentation with an increase in the concentration of ROS.

There is enough evidence from literature to be confident that ROS mediate JNK activation by both activating third tier MAPKs and deactivating the MAPK phosphatases which leaves the MAPKs persistently activated. In this way they can be considered to be part of the cross-talk between the apoptotic and oxidative stress sensitive pathways. The question of whether ROS can also be produced downstream from JNK, independently of apoptosis, is more open [74, 85, 121]. In the current model the production of ROS by JNK has been allowed to allow the self-activation of JNK. In [74] it was suggested that there may not be a single molecular mechanism to account for this. If JNK produces ROS, then this may suggest that it plays a part in necrosis. This possibility has been discussed in [85]. However, in the current model, the ROS produced by JNK is taken to be minimal.

It was noted in [84] and [85] that at least some of the toxicity of CNTs could be attributed to iron present in the impurities which have not been removed after manufacture. Electron leakage from the electron transport chain causes formation of the superoxide radical (O_2^-). Through the iron-catalysed Haber-Weiss reaction, highly reactive hydroxyl radicals (OH^-) can be formed. Most CNTs do contain iron oxides and so it can be assumed that, even if the biochemistry specific to the nanoparticle structure is unknown, CNTs will induce oxidative stress. The oxidative stress potentials recently calculated in [11] can indicate how the concentration of ROS is related to the concentration of certain metal oxides inside a cell.

In this model, any toxins within the cell which may cause oxidative stress are represented by a single variable. If the concentration of this variable is set to zero then the concentration of ROS inside the cell is taken as the baseline amount associated with apoptotic death. If ROS is increased beyond a threshold level, this indicates a necrotic death.

Necrosis is a term used to describe cell death by means other than apoptosis. There may be forms of self-programmed cell death, other than apoptosis, which could be identified by some form of signalling cascade [23, 84]. However, in the current model, the extent of necrosis is quantified by concentration of ROS inside the cell in the way that apoptosis is quantified by DNA fragmentation.

There is emerging evidence that RIP (Receptor-Interacting Protein) may play some role in necrosis, which is discussed in detail in [23] and references therein, and ROS may have a further role as messengers of cell death. However, no attempt to capture these complexities has been made in the current model.

2.2.3.2 Production of Anti-Oxidants

Two key anti-oxidants upregulated by NF-κB are the ferritin heavy chain (FHC) and Manganese Superoxide Dismutase (Mn-SOD). FHC sequesters free iron which catalyses the Haber-Weiss reaction. Mn-SOD catalyses the superoxide radical (O_2^-) into hydrogen peroxide (H_2O_2). This antioxidant action suppresses the activation of JNK [74, 84]. All anti-oxidants are accounted for in a single variable. They are not continuously produced in the cell but are given an initial concentration which is depleted as ROS as produced.

2.2.3.3 AP-1 Activation by the ROS-sensitive MAPK Cascade

This section discusses the oxidative stress sensitive activation of AP-1 as summarised in Figure 2.2. JNK is a kinase from the MAPK pathway. JNK activates c-Jun which, together with c-Fos, forms the transcription factor AP-1. AP-1 is another major transcription factor, apart from NF-κB, which is activated by TNF-α signalling. Through JNK, AP-1 is thought to mediate TNF-α apoptosis while NF-κB, in its anti-apoptotic capacity, is thought to deactivate JNK.

The activation of JNK by TNF-α occurs through the second and third tier MAP kinases (MAPKs). The third tier (the MAP3Ks) involved in this pathway include MEKK1 and ASK1. TRAF2 acts as the mediator between TNF-α/TNFR1 and these kinases. In [16, 19, 42] it is suggested that TRAF2 binds with a complex of ASK1 and thioredoxin. ROS can then disassociate the thioredoxin from the TRAF2/ASK1 complex.

Activated MEKK1 and ASK1 are able to activate the second tier of kinases, MKK4 and MKK7, which are in turn able to activate JNK which leads to the formation of AP-1. In this model, the third and second tier kinases have been combined into a single variable, MAP2K in Figure 2.2, as any interactions which may differentiate between them have not been included.

The possibility that JNK may mediate apoptosis independently of the caspases by interacting with members of the Bcl-2 family [74] is ignored. The signalling pathways involved are not yet clear and are largely dismissed in the discussion in [58]. However, this mechanism is looked at in detail in the more recent review paper [19].

There is no activation complex in the oxidative stress sensitive pathway. The form of MAPK activation follows from the discussion given in [43]. The total number of activated ($MAPK_n^*$) and unactivated ($MAPK_n$) MAPKs for each tier is conserved as one tier activates the next so that the term for the unactivated MAPK can be substituted out. The resulting terms in the MAPK pathway are the subject of a separate model which can be found in Appendix A. Unlike the activating complexes in the other signalling pathways, MAPK proteins are not deactivated after they activate the next protein in the cascade. This means that MAPKs stay activated until they are deactivated by the action of the phosphatases.

There is evidence that there is a positive feedback loop between JNK activation and ROS in the cell. Two possible mechanisms are included in the present model. Firstly, the ROS sensitive activation of MAP2K and, secondly, the ROS sensitive deactivation of the phosphatases. Once the anti-oxidants are depleted, these ROS sensitive elements regulate when the interactions indicated by the blue arrrows in Figure 2.2 occur.

There is an implied cycle in which ROS releases ASK1 from its inhibitor thioredoxin, ASK1 is then free to trigger the activation of JNK and JNK-mediated apoptosis produces ROS, which then further activates ASK1. In this model, the role of ASK1 is taken by the variable MAP2K which activates JNK directly.

In [74] and [84] studies were quoted suggesting that the deactivators of MAPK kinases, the JNK phosphatases, are themselves deactivated by ROS. Deactivating phosphatases leaves the MAPKs in a persistently activated state.

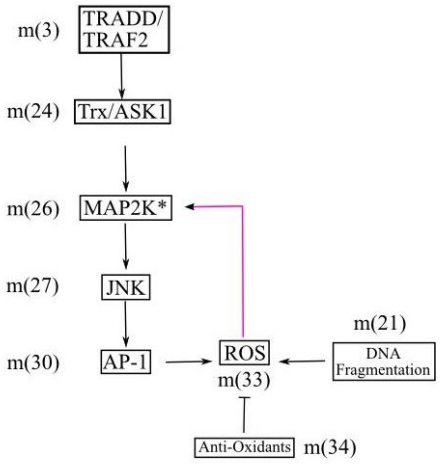

Figure 2.2: AP-1 activation by MAPK casade and ROS where labels correspond to those of the complete network in Figure 2.5. Interactions in blue occur after the pool of anti-oxidants is depleted.

An initial analysis of a mathematical model of the MAPK cascade can be found in Appendix A. It was found that a self-inhibition term is not sufficient to describe anti-oxidative action. A self-inhibition term assumes an infinitely large pool of anti-oxidants. If the pool of anti-oxidants in finite, then a higher concentration of ROS will deplete this pool faster. In this case the model is consistent with the hypothesis in [58] that the speed of MAPK activation dependent on the concentration of ROS. The sensitivity of the speed of MAPK cascade activation is also facilitated by ROS-sensitive MAP2K activation via Thioredoxin and ROS-sensitive phosphatase deactivation.

2.2.3.4 NF-κB inhibition of caspase-3 and AP-1

Some of the IAPs (inhibitor of apoptosis proteins) activated by NF-κB have been found to have dual roles, inhibiting both the caspases and the activation of JNK. FLIP is a protein which was first identified as an inhibitor of caspase-8. There is now evidence [73] that it is also an inhibitor of the second tier kinase, MKK7. Anti-oxidants such as Gadd45β, upregulated by NF-κB have also been shown to inhibit JNK activation [74, 85]. In [103] it was suggested that their main target may be the MKK4 kinase. However, in this model FLIP is taken to be representative of all possible interactions between proteins upregulated by NF-κB, which may inhibit the activation of JNK.

Prolonged activation of JNK may also lead to release and modification of proteins, such as Bidj, from the mitochondria that are able to inhibit the inhibition of the caspases by IAPs [58, 85]. This has been described in [58] as 'breaking the brake' of apoptosis.

The discussion in [73] also suggests that prolonged activation of AP-1 can lead to the upregulation of proteins, such as ITCH, that can inhibit proteins such as FLIP. This allows these MAPK proteins to be reactivated, allowing for further activation of AP-1 in a positive

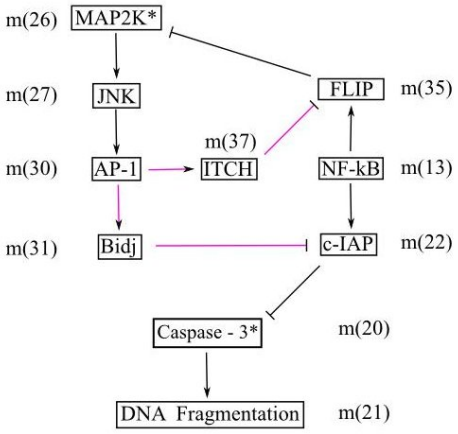

Figure 2.3: Network of inhibitors were labels correspond to those of the complete network in Figure 2.5. Interactions in blue occur after the pool of anti-oxidants is depleted and AP-1 is activated.

feedback loop.

2.2.4 Alternative FLIP/ITCH interaction

A clear limitation of the model is that the activation of the MAPK pathway is only effective in inducing apoptosis when there are enough upstream proteins to reactivate the caspase-3 once it is released, otherwise the oxidative stress sensitive pathway will not increase the steady state concentration of DNA fragmentation.

If the cell death complex rather than caspase-3 is inhibited, then reactivation on release is not necessary. Once the death domain is released then it is immediately free to activate caspase-8. FLIP is a well-established inhibitor of the cell death complex, which in the current model is taken to consist of TRADD and FADD. TRADD and FADD carry the molecular death domain which can activate caspase-8. FLIP is a catalytically inactive homologue of caspase-8, which can bind onto the death complex, preventing the activation of caspase-8.

There is growing evidence of the particular importance of the death domain/FLIP interaction. Review papers [116] suggest that the role of FLIP may have a clinically significant role in the progression of cancer and cardiovascular disease. The role of JNK in the fine-tuning of FLIP expression is discussed in detail in [4] and [53]. The JNK induced inhibitor of FLIP was taken to be ITCH which can ubiquitinate the caspase-like domain of FLIP.

Figure 2.4 summarises this alternative set of inhibitor interactions where there are two points where the anti-apoptotic pathway inhibits the apoptotic pathway. Figure 2.6 is the complete network diagram of the alternative version of the model.

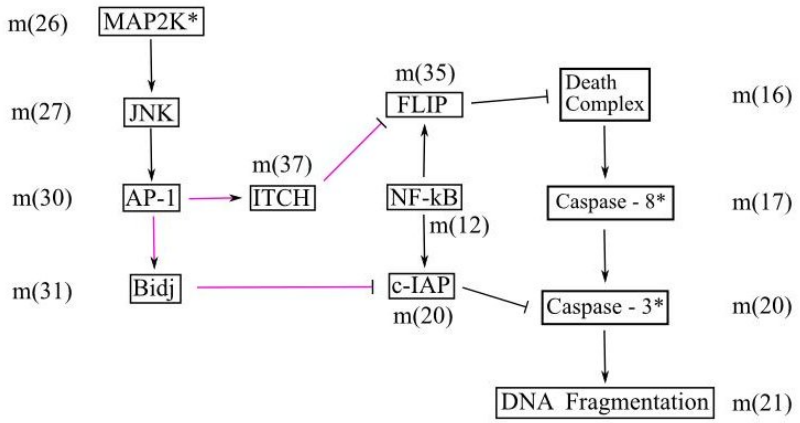

Figure 2.4: Alternative network of inhibitors with reference to variables in Figure 2.6. Interactions in blue occur during the second activation, after the pool of anti-oxidants and AP-1 is reactivated.

2.3 Intracellular Oxidative Stress Model

The variables and the ODEs associated with each of the three pathways are listed separately in Sections 2.3.2-2.3.4. Rate constants are discussed in Section 2.3.1. The discussion in each section summarises the information introduced in the literature review in Section 2.2. There are two main versions of this model. in In Model version A, as summarised in Figure 2.5, FLIP inhibits the MAPK cascade. However, model version B, as summarised in Figure 2.6, FLIP instead inhibits the death complex. The differences in model version A and B are summarised in Table 2.3.

The convention that the notation A/B refers to a complex formed by the association of protein A with protein B is used. All variables of the form m_* have units of $[\mu M]$. Note that the mass action laws used are of a very simple form. Discussion in some experimental papers may suggest more complicated terms. However, because of the large number of variables in the model and because the same level of information is not available for all parts of the network, simple mass-action laws and the MAPK model given in [43] are assumed to be sufficient to give some insight on the workings of the signalling network as a whole.

The initial conditions given in this section are provisional. In following sections the effectiveness of the oxidative stress sensitive pathway is optimised by allowing certain initial conditions to vary. The initial conditions for TRAF2 (m_2), FADD (m_{13}), caspase-8 (m_{15}) and caspase-3 (m_{18}) are reset in Sections 2.4.2 and 2.4.4 after further discussion.s

Figures 2.5 and 2.6 are network diagrams of the two versions of the model. All proteins are originally found unbound and unactivated (white boxes). The proteins then bind together to form complexes (circles), which eventually break apart to release the individual proteins and either activated IKK (IKK*) or activated caspase-8 (caspase-8*). The extent of apoptosis is given by the amount of DNA fragmentation (m_{21}) while the extent of necrosis is given by the concentration of ROS (m_{34}).

In the equations that follow, terms which correspond to the same arrow on the network diagram are underlined together. For each reaction step there is often a forward rate of association and a backward rate of disassociation.

2.3.1 Rate Constants

As noted in [18] and [89], there is more information on the role of proteins in the TNF-α signalling cascade than the relative rates at which they react or their relative initial concentrations inside the cell. The focus in the current model is therefore on how the structure of the model effects the key outputs of the model rather than seeing how the key outputs of the model are effected by choosing more extreme values for the rate constants. Where possible, the constants found in [18] are used. As discussed previously in Section 2.2.1, [18] provides generalised rates of association, disassociation, activation and also a rate of transcription of c-IAP. Otherwise, reasonable estimates of the rate constants were made to meet the aims of the model.

The constants k_1-k_5 in Table 2.2 are given the same relative values as the corresponding

Apoptotic Pathway
TRADD+FADD+caspase-8→ TRADD/FADD/caspase-8 → TRADD+FADD+caspase-8*
caspase-8*+caspase-3→ caspase-8*/caspase-3→ caspase-8 +caspase-3*
caspase-3* → DNA fragmentation
NF-κ B activation
TRADD+TRAF2+RIP-1+IKK→ TRADD/TRAF2/RIP-1/IKK→ TRADD+TRAF2+RIP-1+IKK*
NF-κB/IκB+IKK* → NF-κB/IκB/IKK* → NF-κB+IκB-P+IKK
NF-κB → c-IAP+FLIP
AP-1 activation
Thioredoxin/MAP2K+TRADD/TRAF2→ Thioredoxin/MAP2K/TRADD/TRAF2
→ Thioredoxin+TRADD+TRAF2+MAP2K*
MAP2K* → JNK*
JNK*+c-Fos→ AP-1
AP-1→ Bidj+ITCH
Caspase-3* Inhibition
c-IAP+caspase-3* → c-IAP/caspase-3*
Bidj+c-IAP/caspase-3* → Bidj/c-IAP/caspase-3* → Bidj+c-IAP+caspase-3*
MAP2K* Inhibition by FLIP (Model A)
FLIP+MAP2K* → FLIP/MAP2K*
ITCH+FLIP/MAP2K* → ITCH/FLIP/MAP2K* → ITCH+FLIP+MAP2K*
Death Complex Inhibition by FLIP (Model B)
FLIP+TRADD/FADD→ FLIP/TRADD/FADD
ITCH+FLIP/TRADD/FADD→ ITCH/FLIP/TRADD/FADD

Table 2.1: Complete list of interactions in intracellular oxidative stress model.

Constant	Role	Value	Units
k_1	default association constant	1	$\mu M^{-1}s^{-1}$
k_2	default disassociation constant	0.04	s^{-1}
k_3	default rate of reaction	2	$\mu M^{-1}s^{-1}$
k_4	rate of upregulation of proteins by NF-κB and AP-1	0.5	s^{-1}
k_5	rate DNA fragmentation	2	s^{-1}
k_6	default activation rate in ROS sensitive pathway	1	s^{-1}
k_7	rate of activation of MAP2K by ROS	1	s^{-1}
k_8	disassociation constant for the activation of first tier MAPK by ROS	10^4	μM^2
k_9	rate of MAPK deactivation by phosphatases	$k_{90}\exp(-k_d\ m_{32})$	s^{-1}
k_{90}	maximum value of k_9	5	s^{-1}
k_d	exponential decay constant for k_9	0.05	μM^{-1}
k_{10}	rate of binding of c-Fos to JNK	50	s^{-1}
k_{11}	disassociation constant for the binding of c-Fos to AP-1	1	$\mu M^{1/2}$
k_{12}	rate of production of ROS by fragmented DNA	0.5	s^{-1}
k_{13}	rate of removal of ROS by anti-oxidants	1.5	$\mu M^{-1}s^{-1}$
k_{14}	rate of production of ROS by nanoparticles in cell	0	$\mu M s^{-1}$

Table 2.2: Table of rate constants. The derivation of rate constants k_1-k_5 is described in [18].

constants in [18]. The values are relative as, for reasons of clarity, their values have been divided by the value of k_1 given in [18]. The constants determining the dynamics of the third MAPK pathway should not be too different from those of the other pathways, keeping within the aims of this model. Any interesting behaviour of the model should be due to the signalling network rather than extreme choices of initial or rate constants. For this reason, the rate of MAPK activation k_6 is taken to have the same value as the main association constant of the other pathways, k_1.

The activation of MAP2K* by ROS is modelled as a Hill function where k_7 is the activation rate and k_8 is the rate of disassociation. It is assumed that ROS act as enzymes which activate Thioredoxin using a limited number of activation sites. The binding of c-Fos to c-Jun is also modelled using a Hill function. This is consistent with the assumption used in the current model that the availability of c-Jun limits the activation of AP-1 rather than the availability of c-Fos. k_{10} is large due the large initial concentration of c-Fos required to sustain the activation of the oxidative stress sensitive pathway. The rate of removal of ROS by anti-oxidants, k_{13}, is set to be slightly higher than most other rates as it has to be large enough to suppress the activation of the MAPK cascade. Finally, the default rate of production of ROS by nanoparticles within the cell is 0. When $k_{14} = 0$, ROS is only produced as a result of apoptosis, setting the minimum concentration of ROS over which the cell may die by necrosis.

k_9 is a special rate of reaction, which is not in fact a constant, but a function of ROS (m_{32}). It is discussed in detail in Section 2.3.4. The value of constants k_{90} and k_d, 5 and 0.05 in k_9

Constant	Interaction	Model A	Model B
bind_A	inhibition of caspase-3* by c-IAP	1	1
bind_B	release of caspase-3 by Bidj	1	1
bind_C	inhibition of MAP2K* by FLIP	1	0
bind_D	release of MAP2K* by ITCH	1	0
bind_E	inhibition of TRADD/FADD by FLIP	0	1
bind_F	release of TRADD/FADD by ITCH	0	1
k_{FLIP}	FLIP production by NF-κB	b	1

Table 2.3: Constants which switch interactions on and off and can be given the value 0 or 1. The rate of production of FLIP (m_{34}) is allowed to be a continuous value.

Label	Description	Colour
A	ROS activation of AP-1	magenta
B	ROS sensitive phosphatases	blue
C	caspase-3*/c-IAP/Bidj interactions	green
D	MAP2K/FLIP/ITCH interactions	red
E	death complex/FLIP/ITCH interactions	cyan

Table 2.4: Interactions in the pro-apoptotic pathway.

can be adjusted to adjust the sensitivity of the oxidative stress sensitive pathway to ROS.

In the investigation of this model, specific rate constants are occasionally allowed to vary. These specific rates are k_{90}, k_d and k_8. k_d and k_8 will be varied by orders of magnitude, while k_{90} will only vary by a few units. The results of the model will mainly be investigated by switching the interactions in Table 2.3 on or off. Interactions will be switched on or off depending on whether model version A or B is being investigated. The relative rate of production of FLIP, k_{FLIP} will also be important when investigating the MAP2K*/FLIP/ITCH interaction in Section 2.4.2.4.

Colour-coding is used to distinguish terms which mediate certain stress sensitive responses as given in Table 2.3.1. Interactions labelled A and B refer to terms which mediate the oxidative stress sensitive activation of the MAPK cascade. The remaining interactions refer to the three sets of inhibiting interactions and the inhibition of thee inhibitors.

2.3.2 Anti-Apoptotic Pathway

The components of the anti-apoptotic pathway are listed in Table 2.5. In this pathway NF-κB (m_{12}) is activated and the caspase-3 (m_{18}) inhibitor, c-IAP (m_{22}), is upregulated. NF-κB is initially bound to $I\kappa B$. When IKK (m_6) is activated it phosphorylates $I\kappa B$ to form $I\kappa B - P$ (m_{11}). NF-κB is then free to upregulate c-IAP (m_{22}).

The crosstalk between the apoptotic and anti-apoptotic pathways where activated caspase-3 (m_{20}) is captured by c-IAP (m_{22}) to form caspase-3/c-IAP (m_{23}) is referred to at the 'anti-

Symbol	Component	Initial Value $[\mu M]$
$m_1(t)$	TRADD (Extracellular Signal)	20
$m_2(t)$	TRAF2	10 (provisional)
$m_3(t)$	TRADD/TRAF2	0
$m_4(t)$	RIP-1	10
$m_5(t)$	TRADD/TRAF2/RIP-1	0
$m_6(t)$	IKK	10
$m_7(t)$	TRADD/TRAF2/RIP-1/IKK	0
$m_8(t)$	IKK*	0
$m_9(t)$	NF-κB/IκB	10
$m_{10}(t)$	NF-κB/IκB/IKK*	0
$m_{11}(t)$	IκB-P	0
$m_{12}(t)$	NF-κB	0
$m_{22}(t)$	c-IAP	0
$m_{34}(t)$	FLIP	0

Table 2.5: Components of the Anti-Apoptotic Pathway

apoptotic flux'. This leads to the following system of ODEs:

$$\dot{m}_1 = -\underline{k_1 m_1 m_2 + k_2 m_3} - \underline{k_1 m_1 m_{13} + k_2 m_{14}} + \underline{k_3 m_7}, \tag{2.5}$$

$$\dot{m}_2 = -\underline{k_1 m_1 m_2 + k_2 m_3} + \underline{k_3 m_7}, \tag{2.6}$$

$$\dot{m}_3 = \underline{k_1 m_1 m_2 - k_2 m_3} - \underline{k_1 m_3 m_4 + k_2 m_5} - \underline{k_1 m_3 m_{24} + k_2 m_{25}}, \tag{2.7}$$

$$\dot{m}_4 = -\underline{k_1 m_3 m_4 + k_2 m_5} + \underline{k_3 m_7}, \tag{2.8}$$

$$\dot{m}_5 = \underline{k_1 m_3 m_4 - k_2 m_5} - \underline{k_1 m_5 m_6 + k_2 m_7}, \tag{2.9}$$

$$\dot{m}_6 = -\underline{k_1 m_5 m_6 + k_2 m_7} + \underline{k_3 m_7}, \tag{2.10}$$

$$\dot{m}_7 = \underline{k_1 m_5 m_6 - k_2 m_7} - \underline{k_3 m_7}, \tag{2.11}$$

$$\dot{m}_8 = \underline{k_3 m_7} - \underline{k_1 m_8 m_9 + k_2 m_{10}} + \underline{k_3 m_{10}}, \tag{2.12}$$

$$\dot{m}_9 = -\underline{k_1 m_8 m_9 + k_2 m_{10}}, \tag{2.13}$$

$$\dot{m}_{10} = \underline{k_1 m_8 m_9 - k_2 m_{10}} - \underline{k_3 m_{10}}, \tag{2.14}$$

$$\dot{m}_{11} = \underline{k_3 m_{10}}, \tag{2.15}$$

$$\dot{m}_{12} = \underline{k_3 m_{10}} - \underline{k_4 m_{12}} - \underline{k_4 m_{12}}, \tag{2.16}$$

$$\dot{m}_{22} = \underline{k_4 m_{12}} - \underline{\text{bind}_A\left(k_3 m_{20} m_{22}\right) + k_2 m_{23}}, \tag{2.17}$$

$$\dot{m}_{34} = \underline{k_4 m_{12}} - \underline{\text{bind}_C\left(k_1 m_{34} m_{26}\right) + k_2 m_{36}} - \underline{\text{bind}_E\left(k_1 m_{34} m_{14}\right) + k_2 m_{38}}. \tag{2.18}$$

2.3.3 Apoptotic Pathway

The components of the anti-apoptotic pathway are listed in Table 2.3.3. In this pathway caspase-3 is activated and initiates apoptosis. The death complex TRADD/FADD (m_{14}) bind

Symbol	Component	Initial Value $[\mu M]$
$m_{13}(t)$	FADD	10 (provisional)
$m_{14}(t)$	TRADD/FADD (death complex)	0
$m_{15}(t)$	caspase-8	10 (provisional)
$m_{16}(t)$	TRADD/FADD/caspase-8	0
$m_{17}(t)$	caspase-8*	0
$m_{18}(t)$	caspase-3	10 (provisional)
$m_{19}(t)$	caspase-8* /caspase-3	0
$m_{20}(t)$	caspase-3*	0
$m_{21}(t)$	Fragmented DNA	0
$m_{23}(t)$	caspase-3* /c-IAP	0

Table 2.6: Components of the Apoptotic Pathway

to caspase-8 (m_{15}) and activate it, which in turn activates caspase-3 (m_{18}). This leads to the following system of nonlinear ODEs:

$$\dot{m}_{13} = -\underline{k_1 m_1 m_{13} + k_2 m_{14}} + \underline{k_3 m_{16}}, \tag{2.19}$$

$$\dot{m}_{14} = \underline{k_1 m_1 m_{13} - k_2 m_{14} - k_1 m_{14} m_{15} + k_2 m_{16}} - \underline{\text{bind}_E\,(k_1 m_{34} m_{14}) + k_2 m_{38}} \tag{2.20}$$

$$+ \underline{k_3 m_{39}}, \tag{2.21}$$

$$\dot{m}_{15} = -\underline{k_1 m_{14} m_{15} + k_2 m_{16}} + \underline{k_3 m_{16}}, \tag{2.22}$$

$$\dot{m}_{16} = \underline{k_1 m_{14} m_{15} - k_2 m_{16}} - \underline{k_3 m_{16}}, \tag{2.23}$$

$$\dot{m}_{17} = \underline{k_3 m_{16}} - \underline{k_1 m_{18} m_{17} + k_2 m_{18}}, \tag{2.24}$$

$$\dot{m}_{18} = -\underline{k_1 m_{18} m_{17} + k_2 m_{18}} + \underline{k_3 m_{33}}, \tag{2.25}$$

$$\dot{m}_{19} = \underline{k_1 m_{18} m_{17} - k_2 m_{18}} - \underline{k_3 m_{19}}, \tag{2.26}$$

$$\dot{m}_{20} = \underline{k_3 m_{19}} - \underline{k_5 m_{20}} - \underline{\text{bind}_A\,(k_3 m_{20} m_{22}) + k_2 m_{23}}, \tag{2.27}$$

$$\dot{m}_{21} = \underline{k_5 m_{20}}, \tag{2.28}$$

$$\dot{m}_{23} = \underline{\text{bind}_A\,(k_3 m_{20} m_{22}) - k_2 m_{23}} - \underline{\text{bind}_B\,(k_1 m_{30} m_{23}) + k_2 m_{31}}. \tag{2.29}$$

2.3.4 Oxidative Stress Sensitive Pathway

The components of the oxidative stress sensitive or pro-apoptotic pathway are listed in Table 2.7. The conserved quantities for the MAPKs are given in Table 2.8. The ROS sensitive elements are colour-coded with reference to Table 2.3.1. In model version A interaction C is active while in model version B interaction D is active. It is assumed that none of the inhibitors c-IAP, FLIP or ITCH are re-usable so once the complex they are part of breaks up they do not re-enter the model.

ROS and Anti-Oxidants

The rate of production of ROS (m_{33}) by apoptosis is set to be proportional to DNA fragmentation (m_{21}). The proportionality constant k_{12} is set to be quite small so that the levels of ROS do not get large enough to slow down solving the ODEs on MATLAB. For the same reason, the rate of removal of ROS by anti-oxidants (m_{34}), k_{13}, is taken to be relatively high. The oxidative stress pathway will not be in a state of sustained activation until the anti-oxidants are depleted.

The rate of production of ROS by nanoparticles k_{14}, is initially set to zero to examine the behaviour of the model if ROS is produced by apoptosis and AP-1 only. This sets the minimum expected rate of increase of ROS, consistent with an apoptotic response. k_{14} can then be increased by orders of magnitude. If the concentration of ROS increases much faster than the concentration of DNA fragmentation, then this may be considered a necrotic response. The distinction between a necrotic and apoptotic response can be defined arbitrarily.

ROS activation of MAPKs

As TNF-α induces ROS by apoptosis after the initial activation of the caspases, this suggests that there is also a secondary activation of JNK. This second activation of JNK is held-off until the pool of anti-oxidants is depleted. The interactions which occur on the sustained activation of AP-1 are listed in Table 2.3.1 and are the interactions with blue arrow in Figures 2.2 and 2.3. Interactions A and B, relating to the activation of the oxidative stress sensitive pathway, are summarised in Figure 2.2 while interactions C and D, relating to inhibitor proteins which are produced by the oxidative stress pathway, are summarised in Figure 2.3.

The ROS sensitive activation of AP-1 (magenta) is mediated by the Thioredoxin/MAP2K complex (m_{24}) binding with TRADD/TRAF2 (m_3). These proteins are taken to associate and disassociate at the same rate as the complexes in the apoptotic and anti-apoptotic pathways. The rate of activation of the resulting TRADD/TRAF2/Thioredoxin/MAP2K (m_{25}) complex by ROS does not use the law of mass action. The rate at which it can activate the MAPK complex is taken to have a maximum due to the limited number of ROS-sensitive sites on the complex. The ROS-dependent contribution to the rate of MAP2K activation by ROS is written as a Hill function. As ROS is not a protein, it difficult to say whether it acts cooperatively or non-cooperatively so n, k_7 and k_8 can be chosen to set the time-scale and rate at which the secondary activation of the kinases occurs. Typically, $n = 2$ and $k_8 = 1$ so that the rate of activation will quickly plateau as the concentration of ROS increases.

The concentration of unactivated MAP2K is set by the initial concentration of Thioredoxin/MAP2K (m_{24}) while the concentration of unactivated JNK is set by the choice of C_{27} in Table 2.8. JNK* (m_{27}) binds with c-Fos to form AP-1. Again a Hill function is used for the rate of activation of AP-1 (m_{29}) to limit the maximum rate of activation. This activation must be steady and sustained over time in order for the activation of the MAPK pathway as a

whole to be sustained over time and not too dependent on the concentration of c-Fos. In the current model the power of concentration used is $n = 1/2$ and the disassociation constant k_{11} is large and the intitial concentration of c-Fos is large and will decrease to zero. The c-Fos/JNK* interaction should not switch off too suddenly in time as c-Fos decreases.

The role of c-Fos is to limit the extent to which the MAPK pathway can be reactivated. For example, when the MAPK pathway is reactivated by ITCH, ITCH continually released MAP2K* from FLIP. However, some of the released MAP2K* will be deactivated by the phosphatases. It will take time for the concentration of MAP2K* to increase. ITCH is produced by AP-1, and the amount of AP-1 available is limited by the initial concentration of c-Fos.

The deactivation of MAPKs by phosphatases (blue) is ROS sensitive. When $m_{32} = 0$, $k_9 = 5$ which is large enough to rapidly deactivate the MAPK pathway. It will decrease gradually with time if there is no independent source of oxidative stress in the cell, so the only source of ROS is apoptosis. This rate is small, so if there is any independent source of oxidative stress the phosphatases will rapidly deactivate.

c-IAP/Bidj

As the MAPK pathway is activated, Bidj (m_{31}) is released by AP-1 (m_{30}) which binds to the caspase-3*/c-IAP complex (m_{23}) and breaks it up. Caspase-3 is free to be reactivated by any available caspase-8* so it can continue apoptosis. The crosstalk between the pro-apoptotic and anti-apoptotic pathways where Bidj releases caspase-3 (m_{18}) from the resulting caspase-3/c-IAP/Bidj complex (m_{32}) is referred to as the 'pro-apoptotic flux.'

FLIP/ITCH

In model version A, FLIP (m_{35}), which has been transcribed by NF-κB, binds with MAP2K* (m_{26}), inhibiting the pro-apoptotic pathway. Once AP-1 (m_{30}) has been reactivated, it can transcribe ITCH (m_{37}), which can release MAP2K* (m_{26}), allowing for the further activation of AP-1. It is assumed that being bound to FLIP does not de-phosphorylate and so deactivate MAP2K.

In model version B FLIP (m_{35}) inhibits the death complex (m_{14}). ITCH (m_{37}) can ubiquitinate FLIP in the same way, releasing the death complex so that it can activate caspase-8 (m_{15}).

Symbol	Component	Initial Value $[\mu M]$
$m_{24}(t)$	Thioredoxin/MAP2K	1
$m_{25}(t)$	TRADD/TRAF2/Thioredoxin/MAP2K	0
$m_{26}(t)$	MAP2K*	0
$m_{27}(t)$	JNK*	0
$m_{28}(t)$	c-Fos	10
$m_{29}(t)$	AP-1	0
$m_{30}(t)$	Bidj	0
$m_{31}(t)$	caspase-3* /c-IAP/Bidj	0
$m_{32}(t)$	ROS	20
$m_{33}(t)$	Pool of Anti-Oxidants	0
$m_{35}(t)$	MAP2K*/FLIP	0
$m_{36}(t)$	ITCH	0
$m_{37}(t)$	MAP2K*/FLIP/ITCH	0
$m_{38}(t)$	TRADD/FADD/FLIP	0
$m_{39}(t)$	TRADD/FADD/FLIP/ITCH	0

Table 2.7: Components of the Oxidative Stress Sensitive Pathway

The resulting system of non-linear ODEs is therefore

$$\dot{m}_{24} = -k_1 m_3 m_{24} + k_2 m_{25}, \tag{2.30}$$

$$\dot{m}_{25} = k_1 m_3 m_{24} - k_2 m_{25} - k_7 m_{25} \frac{m_{32}^n}{m_{32}^n + k_8}, \tag{2.31}$$

$$\dot{m}_{26} = k_7 m_{25} \frac{m_{32}^n}{m_{32}^n + k_8} - \text{bind}_C\,(k_1 m_{34} m_{26}) + k_2 m_{35}, \tag{2.32}$$

$$+ \; k_3 m_{38} - k_9 m_{26}, \tag{2.33}$$

$$\dot{m}_{27} = k_6 m_{26}(1 - m_{27}/C_{27}) - k_{10} m_{27} \frac{m_{28}^{1/2}}{m_{28}^{1/2} + k_{11}} - k_9 m_{27}, \tag{2.34}$$

$$\dot{m}_{28} = -k_{10} m_{27} \frac{m_{28}^{1/2}}{m_{28}^{1/2} + k_{11}}, \tag{2.35}$$

$$\dot{m}_{29} = k_{10} m_{27} \frac{m_{28}^{1/2}}{m_{28}^{1/2} + k_{11}} - k_4 m_{29} - k_4 m_{29} \tag{2.36}$$

Constant	MAPK	Value	Units,
C_{27}	JNK	1	μM

Table 2.8: Concentration of unactivated MAPK proteins.

$$\dot{m}_{30} = k_4 m_{29} - \text{bind}_B\,(k_1 m_{30} m_{23}) + k_2 m_{31}, \tag{2.37}$$

$$\dot{m}_{31} = \text{bind}_B\,(k_1 m_{30} m_{23}) - k_2 m_{31} - k_3 m_{31}, \tag{2.38}$$

$$\dot{m}_{32} = k_{12} m_{21} - k_{13} m_{32} m_{33} + k_{14}, \tag{2.39}$$

$$\dot{m}_{33} = -k_{13} m_{32} m_{33}, \tag{2.40}$$

$$\dot{m}_{35} = \text{bind}_C\,(k_1 m_{34} m_{26}) - k_2 m_{35} - \text{bind}_D\,(k_1 m_{35} m_{36}) + k_2 m_{37}, \tag{2.41}$$

$$\dot{m}_{36} = k_4 m_{29} - \text{bind}_D\,(k_1 m_{35} m_{36}) + k_2 m_{37} - \text{bind}_F\,(k_1 m_{38} m_{36}) + k_2 m_{39}, \tag{2.42}$$

$$\dot{m}_{37} = \text{bind}_D\,(k_1 m_{35} m_{36}) - k_2 m_{37} - k_3 m_{37}, \tag{2.43}$$

$$\dot{m}_{38} = \text{bind}_E\,(k_1 m_{34} m_{14}) - k_2 m_{38} - \text{bind}_F\,(k_1 m_{38} m_{36}) + k_2 m_{39}, \tag{2.44}$$

$$\dot{m}_{39} = \text{bind}_F\,(k_1 m_{38} m_{36}) - k_2 m_{39} - k_3 m_{39}. \tag{2.45}$$

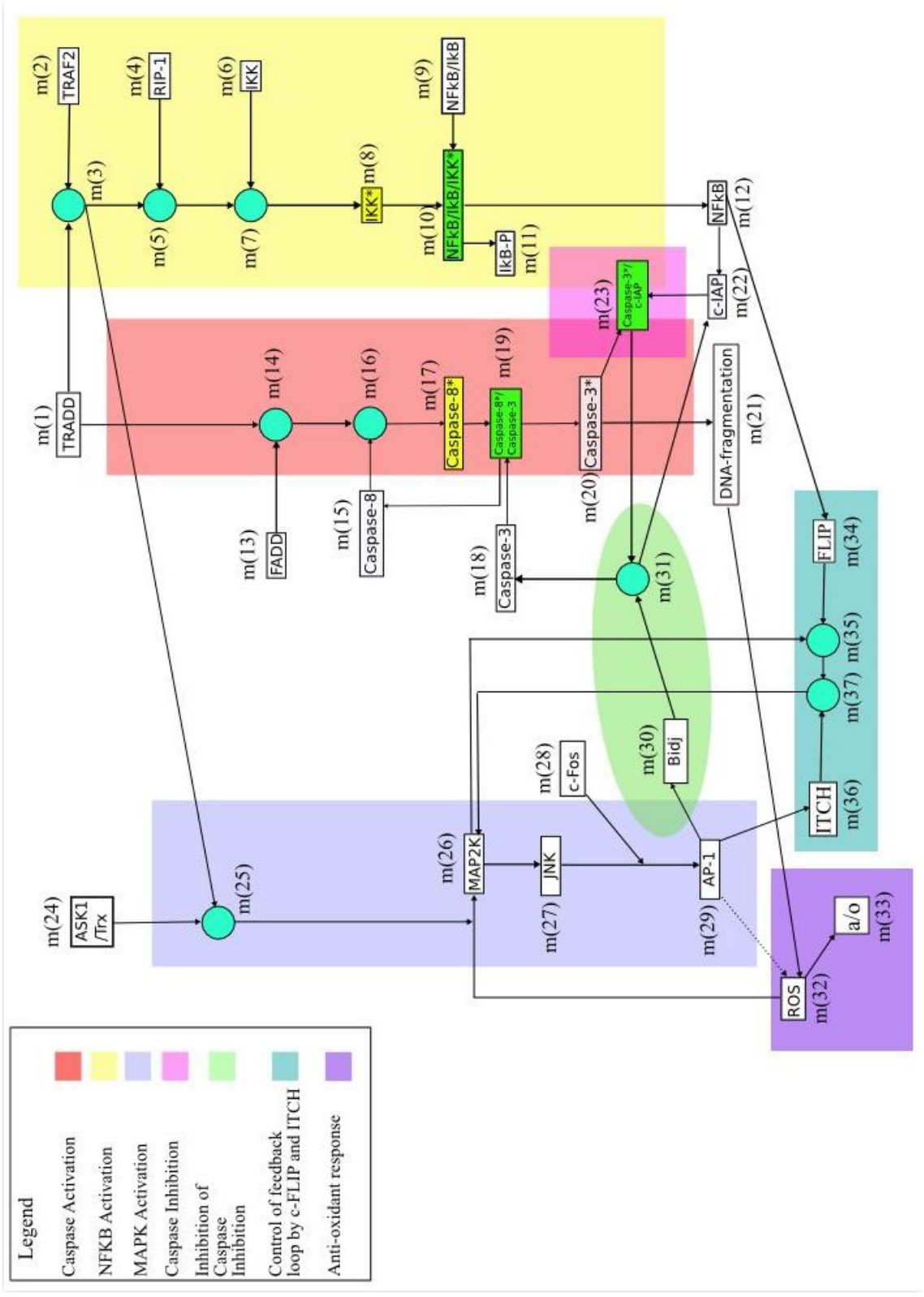

Figure 2.5: Network diagram of all variables in the oxidative stress model A.

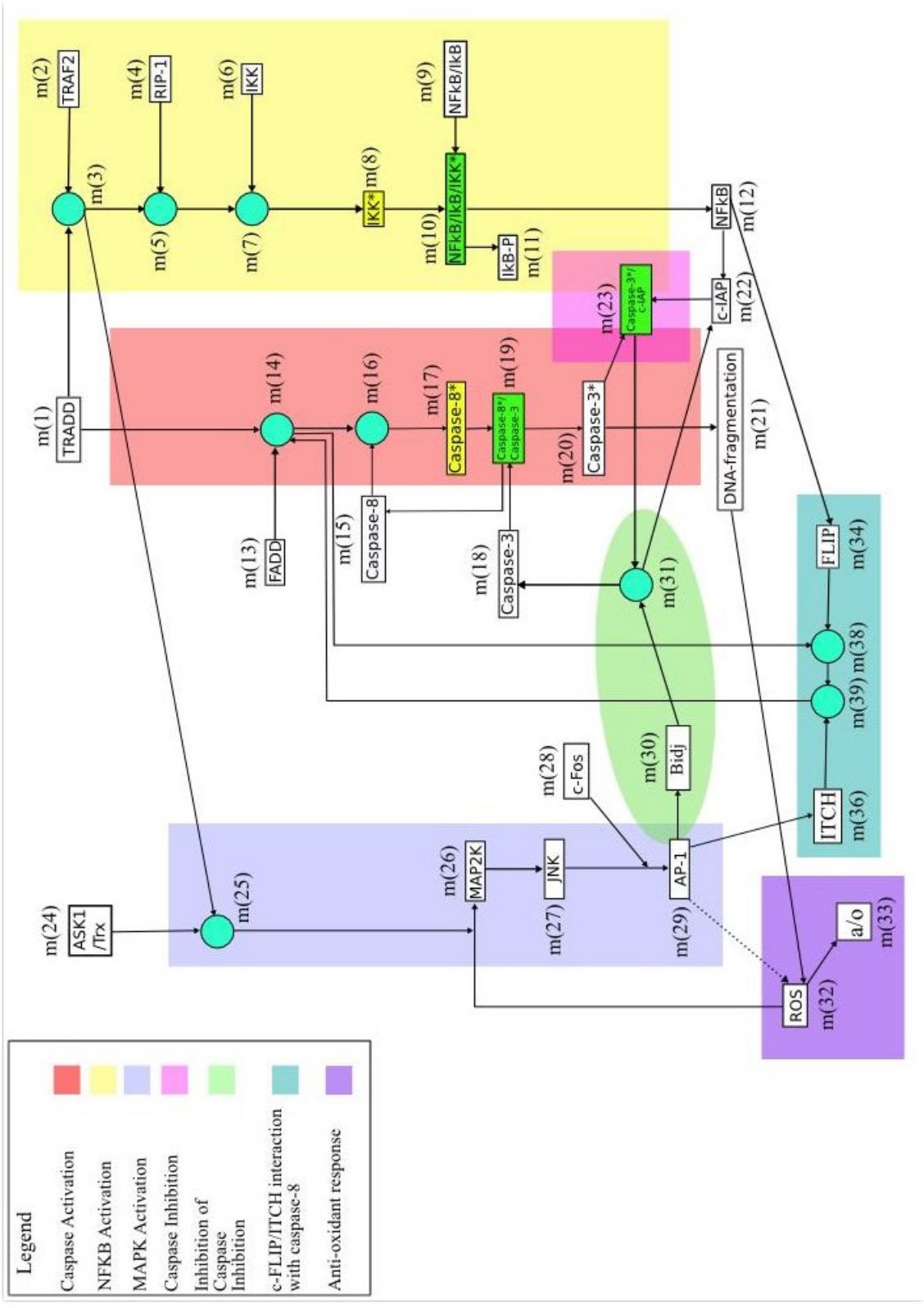

Figure 2.6: Network diagram of all variables in the oxidative stress model B.

2.4 Method of Investigation

The model as a whole is complex. The results of both oxidative stress model A and oxidative stress model B for a given set of initial conditions can be summarised by the key outputs given in Table 2.4. The effectiveness of the pro-apoptotic flux can be measured by the increase in steady state DNA fragmentation (Δm_{21}) when the inhibitors of the inhibitors, Bidj and ITCH are switched on to when they are switched off. Δm_{21} is found by running the model twice, once when the inhibitors of the inhibitors are switch off, to find m_{21}(off), and once when the inhibitors of the inhibitors are switched off, to m_{21}(on).

The sensitivity of the model to oxidative stress can be measured by the timing of the second activation of the caspases ΔT. ΔT has not been dealt with an a quantitative way but will be demonstrated by plotting numerical results. This sensitivity has been incorporated into the pro-apoptotic pathway by the five key elements summarised in Table 2.3.1. It is possible to assign a quantitative value to ΔT if two peaks in the activity of caspase-3* (m_{20}) can be resolved. ΔT is then the time lapsed between the occurrence of the two peaks.

The aim of this investigation is to understand maximise the effectiveness of the oxidative stress sensitive pathway. This is done by maxmising the relative amount of DNA fragmentation due to the activation of the oxidative stress sensitive pathway which is $\Delta m_{21}/m_{21}$(off). As discussed in Section 2.2.1, it has been assumed that the rate constants in this model are the same for association, disassociation and activation reactions. The aim of this investigation is to understand how $\Delta m_{21}/m_{21}$(off) is maximised when the initial concentrations of the proteins in the pathway are varied.

The value of Δm_{21} is determined by the initial concentrations of the proteins of the apoptotic and survival pathways, as will be demonstrated by the sensitivity analysis in Sections 2.4.2.5 and 2.4.4.1. The initial concentrations determine the concentration of caspases bound by inhibitors after the initial activation of the caspases. The value of Δm_{21} is largely determined by the peak concentrations of caspase-3/c-IAP (m_{23}) and death-complex/FLIP (m_{38}).

When ITCH and Bidj are induced the proteins are released. Whether the concentrations of c-IAP/caspase-3 and death-complex/FLIP decrease to zero over the second activation of the caspases depends on whether the pro-apoptotic pathway stays activated for long enough. The pro-apoptotic pathway can remain activated while the supply of MAPK, either bound to Thioredoxin (m_{24}) or FLIP (m_{36}), is not depleted. The initial concentration of c-Fos (m_{28}), which is required to form AP-1 (m_{29}), is also a limiting factor. It will take longer to produce the required amount of Bidj and ITCH to reactivate the pathway if the concentration of ROS is small. In this case, the rate of activation of MAP2K* (m_{26}) is low and phosphatases remain activated.

Model versions A and B have been previously introduced in Section 2.3. In model version A, FLIP acts on MAP2K while in model version B FLIP acts on the death complex. These versions have been investigated separately. For both model A and model B, solutions which maximise $\Delta m_{21}/m_{21}$(off) are found by varying selected initial conditions. Elements of the model which change $\Delta m_{21}/m_{21}$(off) and the sensitivity of the model to ROS are found to be separate and are

Output	Description
m_{21}(off)	Value of DNA fragmentation at steady state when $\text{bind}_B = 0$ and $\text{bind}_D = 0$
m_{21}(on)	Value of DNA fragmentation at steady state when $\text{bind}_B = 1$ and $\text{bind}_D = 1$
Δm_{21}	Increase in DNA fragmentation as a consequence of ROS dependent activation of caspases m_{21}(on)-m_{21}(off)
ΔT	Difference in time between the initial and second activation of the caspases
$m_{21}(\infty)$	Steady state concentration of DNA fragmentation

Table 2.9: Key outputs of the intracellular oxidative stress model. The definitions of bind_B and bind_D can be found in Table 2.3. Parameter bind_B acts to switch the caspase-3/Bidj interactions off or on while bind_D acts to switch the MAP2K*/ITCH interaction off or on.

investigated separately. The investigation aims to give a qualitative introduction to the range of results which are possible using the structure of the three pathway model using illustrative examples.

Model A is investigated in Section 2.4.2. Initially, before considering the full version of Model A, in which two pairs in inhibitors and inhibitors of inhibitors are active, we look at a simplified model where only one such pair is active. So rather than both the caspase-3*/c-IAP/Bidj interactions and the MAP2K*/FLIP/ITCH interactions being active, Section 2.4.2.1 considers the case when only the caspase-3*/c-IAP/Bidj interaction is active. This simplified model is used to investigate the maximisation of $\Delta m_{21}/m_{21}$(off) in Section 2.4.2.2 and the consequences of phosphatase deactivation in Section 2.4.2.3.

In Section 2.4.2.4 the ROS sensitive FLIP/MAP2K* interaction is examined. A simple sensitivity analysis for the apoptotic and survival pathways can be found in Section 2.4.2.5. Model B is investigated in Section 2.4.4 and a sensitivity analysis is included in Section 2.4.4.1. Results for model A are summarised in Section 2.4.3 and those for model B are summarised in Section 2.4.5.

In order for activation of the pro-apoptotic flux to be decisive regarding the survival of the cell the the greatest possible proportion of DNA damage must be due to the secondary activation of the caspases so that $\Delta m_{21}/m_{21}$(off) is maximised. For both versions of the model, the maximum value of $\Delta m_{21}/m_{21}$(off) will largely depend on the initial concentrations of caspase-8 (m_{15}) and caspase-3 (m_{18}).

The range in the value of $\Delta m_{21}/m_{21}$(off) and the response of this value to levels of ROS in the cell are qualitatively different depending on whether it is chosen that FLIP inhibits caspase-3 (Model A) or MAP2K* (Model B). If FLIP inhibits MAP2K*, then $\Delta m_{21}/m_{21}$(off) can be inhibited by FLIP is a ROS dependent way. However, if FLIP inhibits the death complex then both Δm_{21} and m_{21}(off) vary more strongly with $m_1(0)$. In this case, $\Delta m_{21}/m_{21}$(off) can be much larger and increase over a greater range of $m_1(0)$ than if FLIP does not inhibit the death complex.

2.4.1 Numerical Method

All results have been found by using the MATLAB ODE solver *ode45* using the default settings. A non-stiff solver was chosen as the rate constants in Table 2.2 were chosen to all be of a similar order of magnitude. In order to find Δm_{21}, a MATLAB program was written which runs the model twice in order to find both $m_{21}(\text{off})$ and $m_{21}(\text{on})$. When maximising $\Delta m_{21}/m_{21}(\text{off})$, the output function of this program was

$$y = -\Delta m_{21}/m_{21}(\text{off}), \tag{2.46}$$

while selected initial concentrations were taken to be the input variables. The MATLAB minimisation function *fminsearch* was used to minimise the output function. *fminsearch* uses the Nelder-Mead algorithm which is capable of finding the minimum of a single cost function which is dependent on many independent input variables.

2.4.2 Model A

2.4.2.1 Example

Referring to Table 2.3, this section presents typical results for the case

$$\begin{aligned} \text{bind}_A &= 1, \quad \text{bind}_B = 1, \\ \text{bind}_C &= 0, \quad \text{bind}_D = 0, \\ \text{bind}_E &= 0, \quad \text{bind}_F = 0, \end{aligned}$$

so that interaction D in Table 2.3.1, the MAP2K/FLIP/ITCH interaction, is switched off. Initial conditions are as given in Section 2.3 apart from

$$m_1(0) = 20, \quad m_{13} = 13.58, \quad m_{15} = 0.13 \text{ and } m_{18} = 1.38. \tag{2.47}$$

The rate of transcription of FLIP (m_{34}) is switched off as $k_{FLIP} = 0$. The initial conditions for m_{13}, m_{15} and m_{18} are those which maximise the value of $\Delta m_{21}/m_{21}(\text{off})$ for the given initial condition of m_1. The particular relevance of these initial conditions is discussed more fully in Section 2.4.2.2. In this section they are used as an example. For this example the constants related to phosphatase action are $k_{90} = 3$ and $k_d = 0.5$.

The results for the key outputs, DNA damage and ROS, can be found in Figure 2.7. When $\text{bind}_B = 1$, and Bidj acts as an inhibitor of the c-IAP inhibition of caspase-3*, then $\Delta m_{21} > 0$. When $\text{bind}_B = 0$, then in Figure 2.7(a), $m_{21}(\infty) = 0.487$, whereas when $\text{bind}_B = 1$, $m_{21}(\infty) = 1.186$ so that $\Delta m_{21}/m_{21}(\infty) = 1.44$. This happens to be the largest possible value of $m_{21}/m_{21}(\infty)$ found using model version A.

In this case, the concentration of ROS is that when it is assumed that DNA fragmentation acts as the only source of ROS, so that ROS increase at a rate proportional to m_{21}. The concentration of ROS in Figure 2.7(b) is the concentration of ROS when there are no anti-oxidants in the cell to decrease its concentration, and also no other sources of ROS which will increase its concentration. It is a baseline ROS concentration.

A threshold value of DNA fragmentation (m_{21}) can be defined above which it can be assumed that the cell has stopped functioning and has died by apoptosis. Similarly, a threshold value of ROS (m_{32}) can be defined above which it can be assumed that the cell has died by necrosis. If the threshold value of DNA fragmentation lies between the two steady state values of DNA fragmentation in Figure 2.7(a), then the decision of whether or not a cell dies by necrosis is sensitive to oxidative stress. In order for the oxidative stress sensitive pathway to be activated, ROS must be present inside the cell. However, this does not the cell's death is necrotic. As the solution for ROS in Figure 2.7(b) was found when there is no source of oxidative stress in the cell other than DNA fragmentation, and k_{14} in Table 2.2 is zero, then the threshold of ROS concentration for death by necrosis must lie above the concentrations shown. The timing of the activation of the oxidative stress pathway is important. For example, if the threshold for necrosis is reached before that for apoptosis then the cell dies by necrosis.

Results from the apoptotic pathway in Figures 2.8(a) and 2.8(b) show how DNA fragmentation in Figure 2.7(a) increases as upstream proteins such as caspase-8* and TRADD/FADD (m_{14}) are depleted. Similarly, Figure 2.8(c) shows that NF-κB (m_{12}) is activated as upstream proteins TRADD/TRAF2/RIP-1 (m_5) and NF-κB/Iκ B/IKK* (m_{10}) are activated. NF-κB transcribes c-IAP (m_{22}), which forms c-IAP/caspase-3 (m_{23}). This cascade is plotted in Figure 2.8(d). The concentration of caspase-3* (m_{20}) is not featured as its concentration is always $O(10^{-2})$. As it is activated, caspase-3* is rapidly either converted to DNA fragmentation or bound to c-IAP. The decrease in concentration of c-IAP/caspase-3 as Bidj is activated is plotted in Figure 2.9(a). Figure 2.9(b) indicates how the MAPK pathway is initially activated by the TNF-α signal and then deactivated by the phosphatases. As the phosphatases are deactivated by ROS then the MAPK kinases are reactivated, leading to the production of Bidj in Figure 2.9(a). The activation of the MAPK pathway is accompanied by the decrease in concentration of TRADD/TRAF2/Thioredoxin/MAP2K (m_{25}) in Figure 2.9(c) and c-Fos (m_{28}) in Figure 2.9(d).

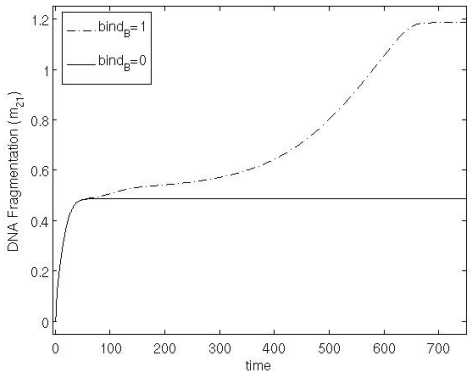

(a) DNA fragmentation (m_{21}) against time when $\text{bind}_B = 1$ and $\text{bind}_B = 0$.

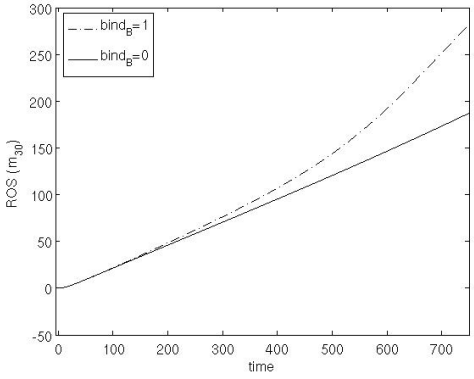

(b) ROS (m_{30}) against time when $\text{bind}_B = 1$ and $\text{bind}_B = 0$.

Figure 2.7: Results of model when $m_1(0) = 20$, $m_{13} = 13.58$, $m_{15} = 0.13$, $m_{18} = 1.38$ against time. Referring to Table 2.3, $\text{bind}_A = 1$, $\text{bind}_B = 1$ $\text{bind}_C = 0$, $\text{bind}_D = 0$, $\text{bind}_E = 0$ and $\text{bind}_F = 0$ so that FLIP is not active.

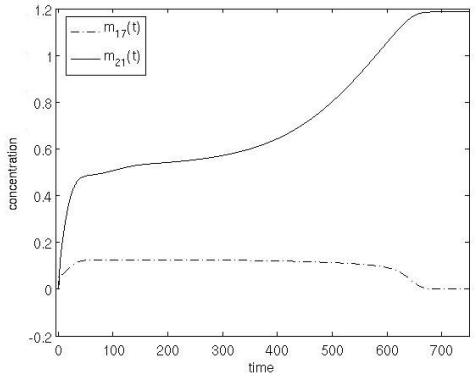

(a) Caspase-8* (m_{17}) and DNA fragmentation (m_{21}).

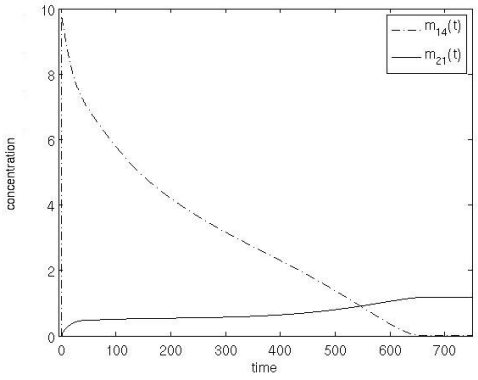

(b) TRADD/FADD (m_{14}) and DNA fragmentation (m_{21}).

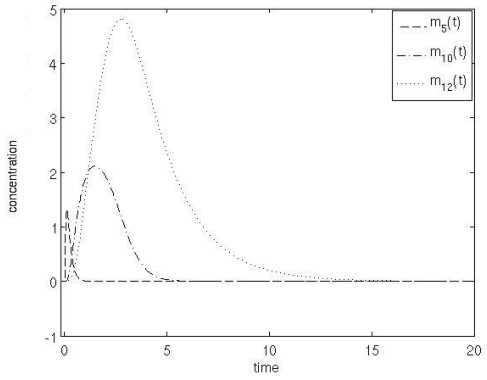

(c) TRADD/TRAF2/RIP-1 (m_5), NF-κB/IκB/IKK* (m_{10}) and NF-κB (m_{12}).

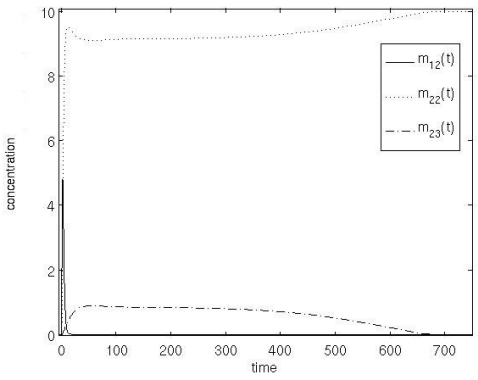

(d) NF-κB (m_{12}), c-IAP (m_{22}) and caspase-3*/c-IAP (m_{23}).

Figure 2.8: Results of model when $m_1(0) = 20$, $m_{13} = 13.58$, $m_{15} = 0.13$, $m_{18} = 1.38$ against time. Referring to Table 2.3, $\text{bind}_A = 1$, $\text{bind}_B = 1$ $\text{bind}_C = 0$, $\text{bind}_D = 0$, $\text{bind}_E = 0$ and $\text{bind}_F = 0$ so that FLIP is not active.

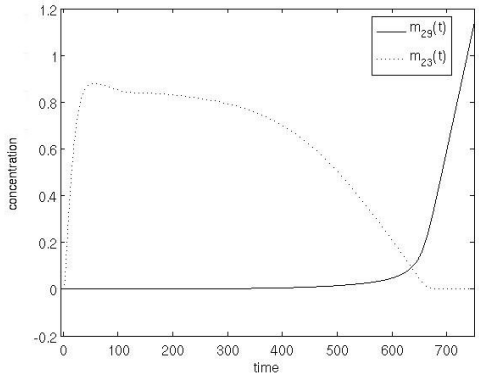

(a) Bidj (m_{29}) and caspase-3*/c-IAP (m_{23}).

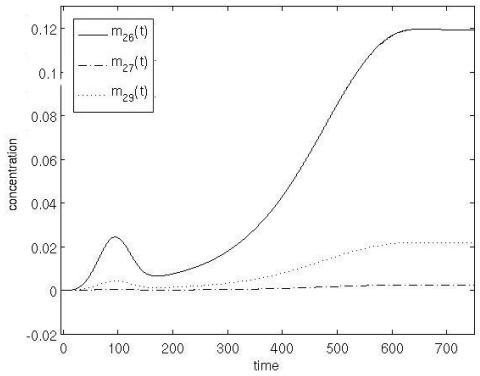

(b) MAP2K* (m_{26}), JNK* (m_{27}) and AP-1 (m_{29}).

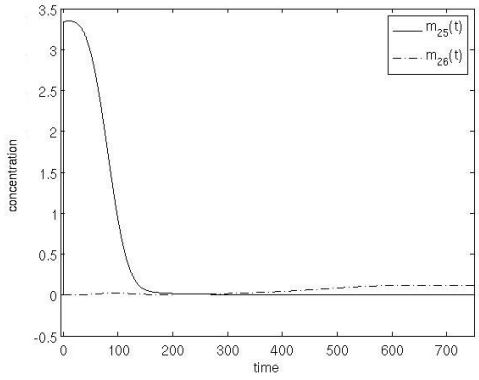

(c) TRADD/TRAF2/Thioredoxin/MAP2K (m_{25}) and MAP2K* (m_{26}).

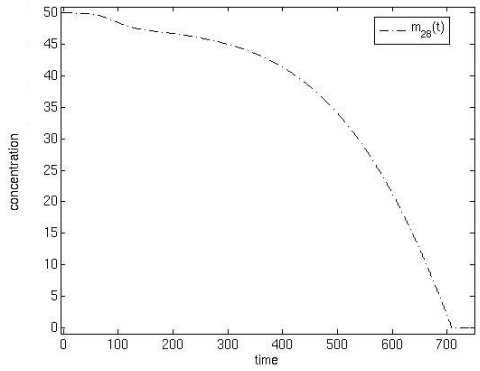

(d) c-Fos (m_{28}).

Figure 2.9: Results of model when $m_1(0) = 20$, $m_{13} = 13.58$, $m_{15} = 0.13$, $m_{18} = 1.38$ against time. Referring to Table 2.3, $\text{bind}_A = 1$, $\text{bind}_B = 1$ $\text{bind}_C = 0$, $\text{bind}_D = 0$, $\text{bind}_E = 0$ and $\text{bind}_F = 0$ so that FLIP is not active.

2.4.2.2 Maximisation of the Amount of ROS dependent Apoptosis

If c-IAP alone acts as the inhibitor of the apoptotic pathway, then there is a maximum value $\Delta m_{21}/m_{21}(\text{off})$ which can be found by varying the initial conditions of caspase-8 (m_{15}) and caspase-3 (m_{13}). The value of Δm_{21} increases as the maximum value of caspase-3*/c-IAP (m_{23}) increases. However, once released from c-IAP, the caspase-3 needs to be re-activated. Δm_{21} is limited by the amount of upstream activators, m_{14}, m_{16} and m_{17}, available to re-activate caspase-3.

The optimal choice of caspase-8 (m_{15}) and caspase-3 (m_{13}) is found using a MATLAB optimisation function such as *fminsearch*. Allowing other initial conditions and rate constants to be free variables in this optimisation problem may also vary the value of $\Delta m_{21}/m_{21}(\text{off})$. This method has been described in Section 2.4.1. However, *fminsearch* will not necessarily find a well-defined minimum. For example, if the the initial condition of FADD (m_{13}) or the rate of production of c-IAP are increased, then $\Delta m_{21}/m_{21}(\text{off})$ will always increase fractionally, even if FADD and c-IAP are already very large. For this reason, it is best to limit the number of initial conditions to be optimised to those which logically will have the most effect.

Figure 2.10 relates to a solution which optimises Δm_{21} when $m_1(0) = 65$ in the case that the rate of transcription of FLIP is set to zero. In this case, $\Delta m_{21} = 5.75$ and $m_{21}(\text{off}) = 22.33$. Figures 2.10(a) and 2.10(b) demonstrate how increasing or decreasing the initial conditions $m_{15}(0)$ and $m_{18}(0)$ move the solution away from this optimal value of Δm_{21}.

Figure 2.10(c) demonstrates how $m_{21}(\text{on})$ and $m_{21}(\text{off})$ are dependent on $m_1(0)$. As $m_1(0)$ is increased from 0, then the value of $m_{21}(\text{off})$ increases until it starts to reach a plateau. $\Delta m_{21} > 0$ only when $m_{21}(\text{off})$ is close to this plateau. Increasing m_1 further increases the concentration of excess upstream activators which could re-activate caspase-3 once it is released. Increasing m_1 past the point where $m_{21}(\text{off})$ plateaus increases the value of Δm_{21} until the maximum value of Δm_{21} is reached.

The dependence of the relative activation of the apoptotic, survival and oxidative stress sensitive pathways is summarised in Figure 2.10(d). The relative activation of the survival pathway is indicated by the maximum concentration of TRADD/TRAF2/RIP-1 (m_5). For the apoptotic pathway, this value was taken to be the maximum concentration of TRADD/FADD (m_{14}) while, for the oxidative stress sensitive pathway, the chosen variable was TRADD/TRAF2/Thioredoxin/MAP2K (m_{25}). The relative activation of the apoptotic pathway increased faster than that of the survival pathway. A smaller percentage of caspase-3* is inhibited by c-IAP as $m_1(0)$ is increased, so that $\Delta m_{21}/m_{21}(\text{off})$ decreases as $m_1(0)$ is increased. Figure 2.11 summarises results when Δm_{21} is maximised for the range of $m_1(0)$ given. Again, the rate of increase of $m_{21}(\text{off})$ is faster than that of Δm_{21}.

A solution for which $\Delta m_{21}/m_{21}(\text{off})$ is to be maximised was found by allowing FADD (m_{13}), caspase-8 (m_{15}) and caspase-3 (m_{18}) to be free parameters in the optimisation. As discussed above, the role of the initial concentration of caspase-8 and caspase-3 in determining the value of Δm_{21} is clear. Including the other protein in the apoptosis pathway, FADD, in the optimisation results in a much larger maximum value of $\Delta m_{21}/m_{21}(\text{off})$ than in possible

when only caspase-8 and caspase-3 are included in the optimisation. This solution was used as an example solution in 2.4.2.1.

As demonstrated in Figure 2.12, Δm_{21} and $m_{21}(\text{off})$ increase when $0 < m_{21}(0) \lesssim 12$ and only change in $O(10^{-2})$ when $m_1 > 12$. Referring to Table 2.3, when the transcription of FLIP (m_{34}) is switched on, $k_{FLIP} \neq 0$. When $k_{FLIP} \neq 0$, FLIP is produced at the expense of c-IAP (m_{22}) which inhibits apoptosis and increases the value of $m_{21}(\text{off})$.

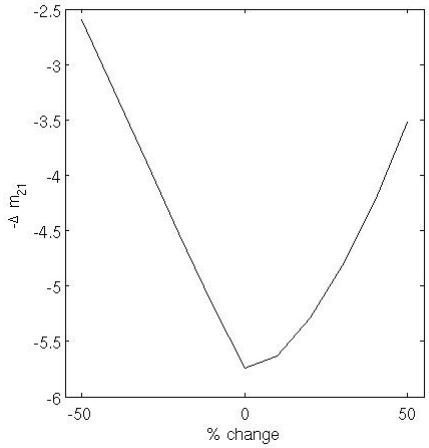

(a) Percentage change of $m_{18}(0)$ from optimal solution against Δm_{21}.

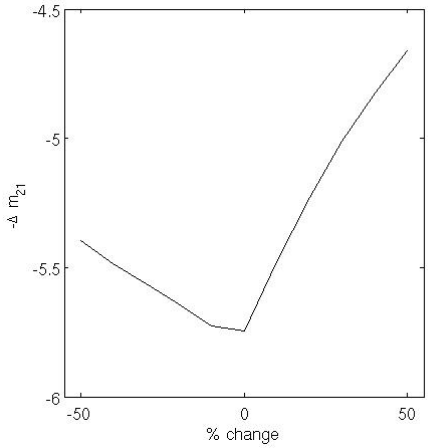

(b) Percentage change of $m_{15}(0)$ from optimal solution against Δm_{21}.

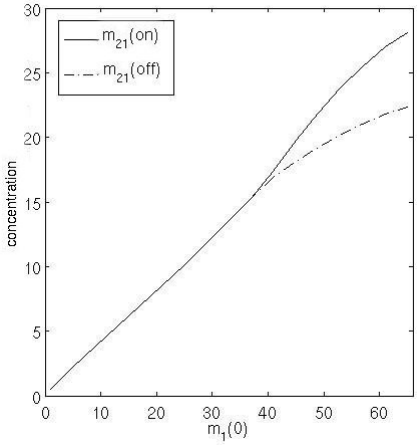

(c) m_{21}(on) and m_{21}(off) against $m_1(0)$.

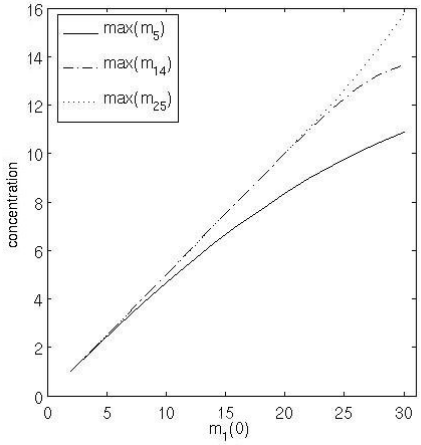

(d) Maximum concentration of m_5, m_{14} and m_{25} against $m_1(0)$ where values are normalised by their maximum concentration when $m_1(0) = 2$. This plot indicates the relative activation of the three pathways.

Figure 2.10: Effect of initial conditions $m_1(0)$, $m_{18}(0)$ and $m_{15}(0)$ on the ratio $\Delta m_{21}/m_{21}$(off).

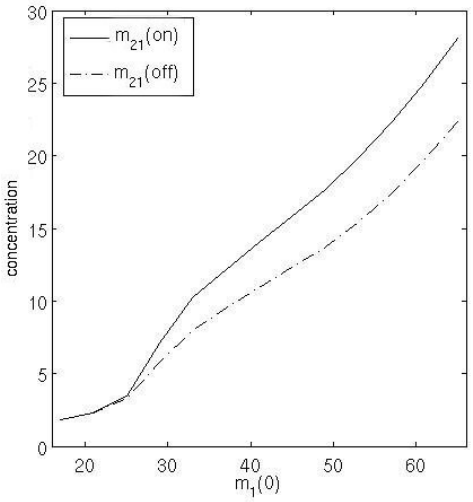

(a) m_{21}(on) and m_{21}(off) against $m_1(0)$.

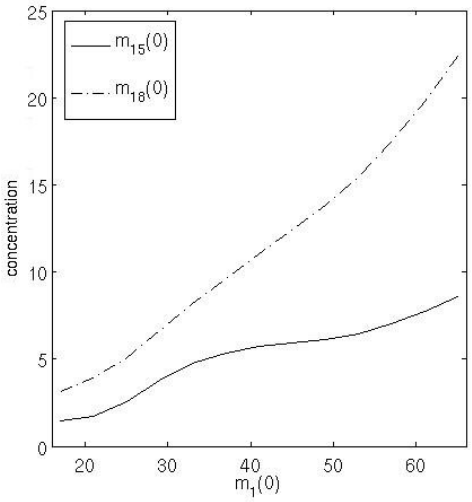

(b) $m_{15}(0)$ and $m_{18}(0)$ against $m_1(0)$.

Figure 2.11: Initial conditions which maximise Δm_{21} for a given $m_1(0)$.

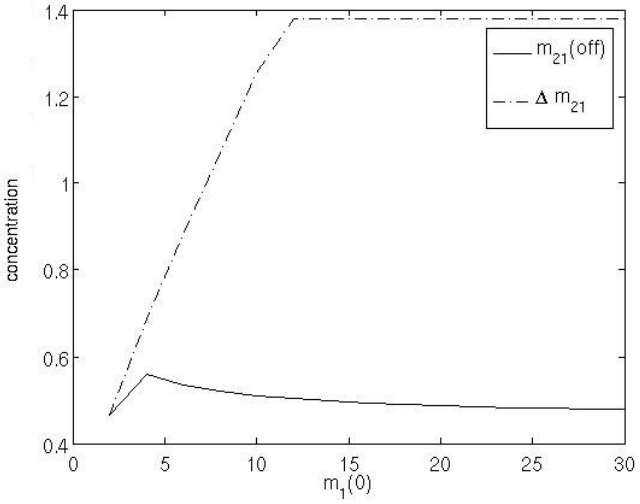

Figure 2.12: m_{21}(on) and m_{21}(off) against $m_1(0)$ for initial conditions given in Section 2.4.2.1 which maximise $\Delta m_{21}/m_{21}$(off).

2.4.2.3 Role of Phosphatases and Anti-Oxidants in Oxidative Stress Sensitive Pathway

When the production of FLIP is set to zero then, referring to Table 2.6 the sensitivity of the oxidative stress sensitive pathway is determined by the choice of phosphatase deactivation, the choice of the disassociation constant k_8 in the ROS-sensitive activation of MAP2K and the initial concentration of anti-oxidants (m_{33}). The rate associated with phosphatase deactivation is a function of ROS (m_{32}) defined as

$$k_9(m_{32}) = k_{90} \exp(k_d \; m_{32}). \tag{2.48}$$

As k_{90} is increased the reactivation of apoptosis in Figure 2.13(a) is slowed down. As the concentration of MAP2K* in Figure 2.13(b) is decreased then the rate of Bidj production, which is proportional to AP-1, is decreased. The rate at which caspase-3 is released from c-IAP is also slowed down so that, after its initial ROS-independent increase, DNA fragmentation only increases slowly. Figure 2.13(c) shows how increasing k_d can dramatically decrease the time a solution reaches its final steady state.

If the pool of anti-oxidants has a non-zero steady state, then, when the rate constant associated with the anti-oxidants k_{13} is sufficiently large, there will be no secondary activation of the caspases until it is depleted. In the current model $k_{13} = 1.5$. Notice that in Figure 2.13(d), when $m_{33} = 100$ then $m_{21}(\infty)$ is smaller than when $m_{33} < 100$. This is because anti-oxidants increase the time over which the oxidative stress sensitive pathway must be activated in order to release all the inhibited caspase-3. When $m_{33} < 100$, the supply of c-Fos (m_{39}) is depleted after constant reactivation of MAP2K* before enough Bidj is produced to release all the caspase-3 bound to c-IAP.

Increasing the disassociation constant k_8 can slightly increase the rate of re-activation when phosphatase deactivation is slow. This is demonstrated in Figure 2.14. Increasing k_8 broadens out the peak in MAP2K* by slowing down its initial release from TRADD/TRAF2/Thioredoxin/MAP2K. So a larger value of k_8 increases the sensitivity of MAP2K activation to ROS. For this reason it is generally taken that for model version A, $k_8 = 10^4$ as given in Table 2.2. However, it was found a smaller value of k_8 increases the sensitivity of the MAP2K*/FLIP/ITCH interaction to ROS which is explored in Section 2.4.2.4. For model version B, as discussed in Section 2.4.4, $k_8 = 10^7$ to ensure that MAP2K* can reach its maximum steady state concentration.

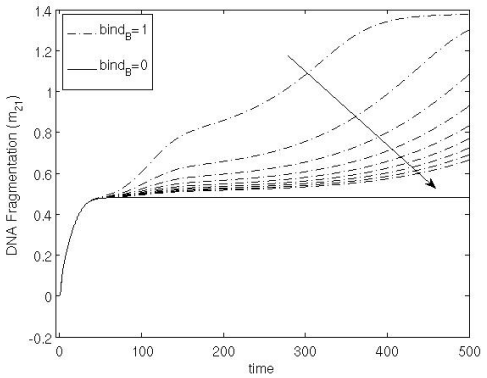

(a) Effect of increasing k_{90}, $1 \geq k_{90} \geq 9$, on DNA fragmentation (m_{21}).

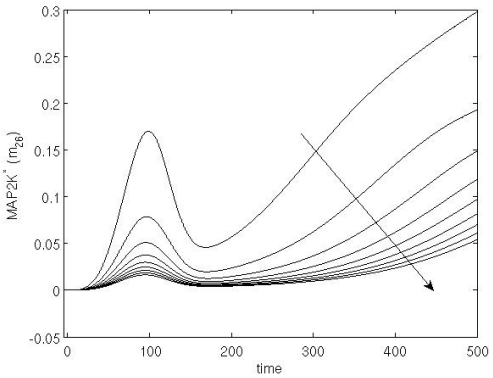

(b) Effect of increasing k_{90}, $1 \geq k_{90} \geq 9$, on MAP2K* (m_{26}) activation.

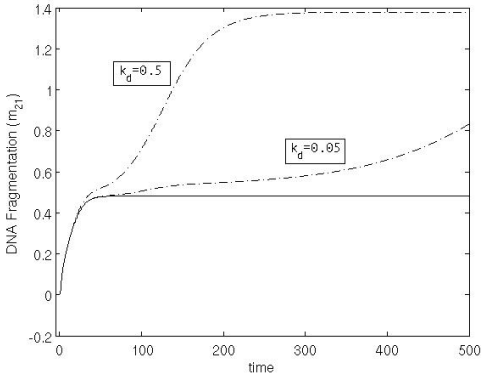

(c) Effect of changing the decay constant k_d from 0.05 to 0.5 on DNA fragmentation (m_{21}) when $k_{90} = 5$. k_d is the rate of exponential decay with which the rate of phosphatase deactivation decreases.

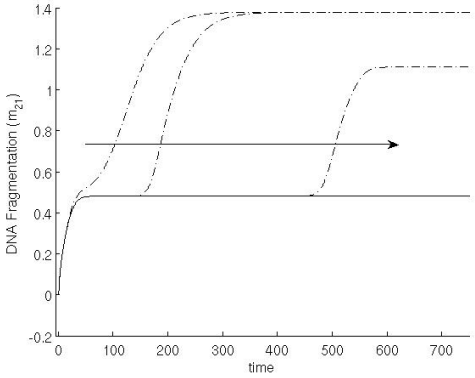

(d) Initial pool of anti-oxidants ($m_{33}(0)$) are given the values $m_{33} = 0$, 25 and 100 while $k_{90} = 5$ and $k_d = 0.5$.

Figure 2.13: ROS sensitive activation when the rate of FLIP transcription is set to zero and initial conditions are those in Section 2.4.2.1. Arrows indicate that values stated are increasing.

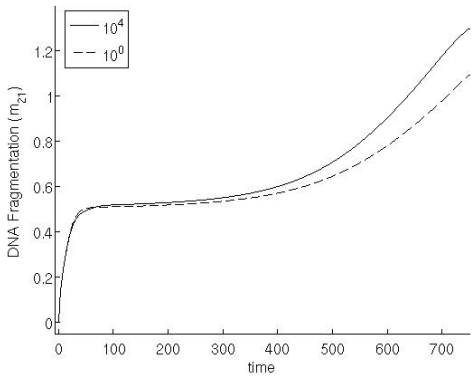

(a) DNA fragmentation (m_{21}).

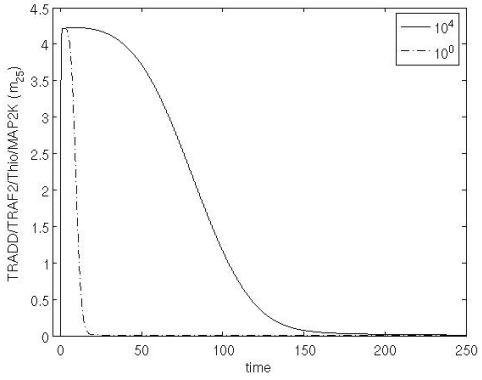

(b) TRADD/TRAF2/Thioredoxin/MAP2K (m_{25}).

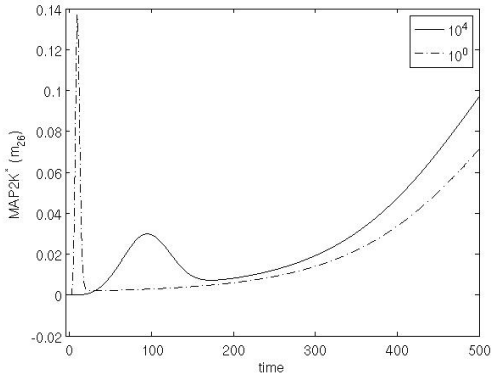

(c) MAP2K* (m_{26}).

Figure 2.14: Dependence of ROS sensitive activation on disassociation constant k_8 when the rate of FLIP transcription is set to zero and initial conditions are those in Section 2.4.2.1. Change in results when k_8 is increased from 1 to 10^4 while $k_{90} = 5$ and $k_d = 0.05$.

2.4.2.4 Role of FLIP in Oxidative Stress Sensitive Pathway

In Sections 2.4.2.1 and 2.4.2.3, the FLIP/MAP2K* inhibition, interaction D in Table 2.6, has been switched off and the rate of production of k_{FLIP} in Table 2.3 is set to zero. The production of FLIP diverts the signal in the anti-apoptotic pathway away from inhibiting c-IAP to inhibiting MAP2K so that $\Delta m_{21}/m_{21}(\text{mid})$ will decrease. However, the resultant FLIP/MAP2K* interaction is ROS dependent. Referring to Table 2.2, it is found to be dependent on the maximum rate of phosphatase deactivation of MAP2K and JNK, k_{90}, the rate of ROS production by nanoparticles, k_{14} and the relative rate of FLIP production, k_{FLIP}. Here, it is assumed that k_d from (2.48) is constant.

The initial concentration of Thioredoxin/MAP2K (m_{24}) in Section 2.3.4 is lower than those for other intermediatary proteins. This has been done so that the FLIP/MAP2K* interaction can be effective in switching Δm_{21} on or off for small values of k_{FLIP}. If $m_{24}(0)$ is small then a smaller concentration of FLIP is required to delay the activation of the oxidative stress sensitive pathway. This means that the ROS sensitive inhibition of the oxidative stress pathway is not at the expense of a much larger value of $m_{21}(\text{off})$ due to a smaller concentration of c-IAP.

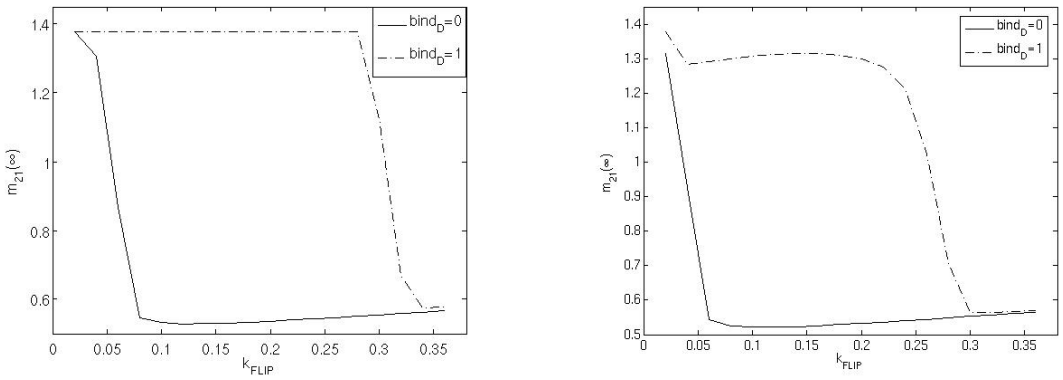

(a) $k_8 = 10^4$ (b) $k_8 = 1$

Figure 2.15: Steady state DNA fragmentation (m_{21}) against k_{FLIP} in the case that $\text{bind}_C = 1$, $\text{bind}_D = 1$ or $\text{bind}_D = 0$, $k_{90} = 0$ and $k_{14} = 0$.

Firstly, set $k_{90} = 0$, $k_{14} = 0$ and $k_{FLIP} = b$ and find $m_{21}(\infty)$ using the initial conditions introduced in (2.47) in the case that the constants in Table 2.3 have the value

$$\begin{aligned} &\text{bind}_A = 1, \quad \text{bind}_B = 1, \\ &\text{bind}_C = 1, \quad \text{bind}_D = 0, \\ &\text{bind}_E = 0, \quad \text{bind}_F = 0, \end{aligned}$$

so that the ITCH/FLIP interaction is switched off but the FLIP/MAP2K* interaction is switched on. The same results can be found in the case that $\text{bind}_D = 1$. The results are given in Figure 2.15 where in Figure 2.15(a) the disassociation constant $k_8 = 10^4$ and in

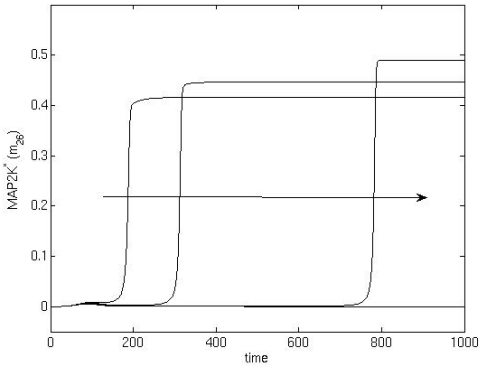

(a) $k_8 = 10^4$ and $0.18 \leq k_{FLIP} \leq 0.34$

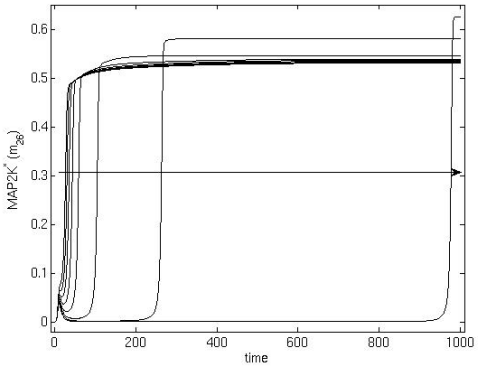

(b) $k_8 = 1$ and $0.24 \leq k_{FLIP} \leq 0.30$

Figure 2.16: MAP2K* (m_{26}) against time where arrow indicates solutions with increasing values of k_{FLIP} with $k_{90} = 0$ and $k_{14} = 0$.

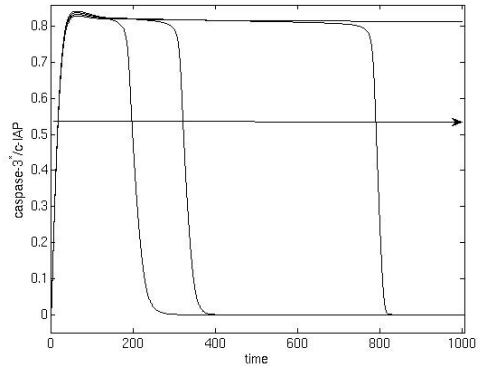

(a) $k_8 = 10^4$ and $0.18 \leq k_{FLIP} \leq 0.34$

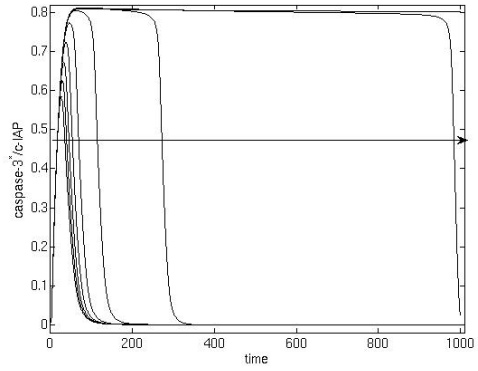

(b) $k_8 = 1$ and $0.24 \leq k_{FLIP} \leq 0.30$

Figure 2.17: caspase-3*/c-IAP (m_{23}) against time where arrow indicates solutions with increasing values of k_{FLIP} with $k_{90} = 0$ and $k_{14} = 0$.

Figure 2.15(b) $k_8 = 1$. These results show that there is a minimum value of k_{FLIP} at which the FLIP/MAP2K* interaction alone is sufficient to prevent the reactivation of the MAPK cascade. When $\text{bind}_D = 0$, the value of k_{FLIP} is small, while when $\text{bind}_D = 1$ the value is much larger. When $k_8 = 1$ the rate of decrease of $m_{21}(\infty)$ as k_{FLIP} is decreased is sharper than when $k_8 = 10^4$. When k_8 is larger the activation of the MAPK pathway is less FLIP/ITCH dependent and more ROS dependent.

When $\text{bind}_D = 1$ and $k_8 = 10^4$, the range of k_{FLIP} over which $m_{21}(\infty)$ decreases is $0.28 \leq k_{FLIP} \leq 0.34$, while when $k_8 = 1$ this range is $0.18 \leq k_{FLIP} \leq 0.30$. Solutions for different variables for which k_{FLIP} falls in this range are plotted in Figures 2.16-2.19. Figure 2.16 shows how the activation of the MAPK pathway is delayed as k_{FLIP} is increased. This delays the release of caspase-3 from caspase-3*/c-IAP (m_{23}), as shown in Figure 2.16. In Figure 2.18, the concentration of MAP2K*/FLIP (m_{35}) increases in time until the concentration of

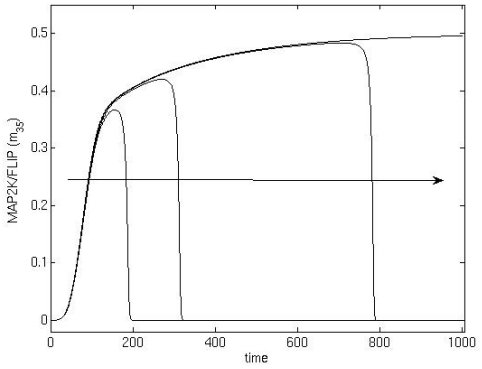

(a) $k_8 = 10^4$ and $0.18 \leq k_{FLIP} \leq 0.34$

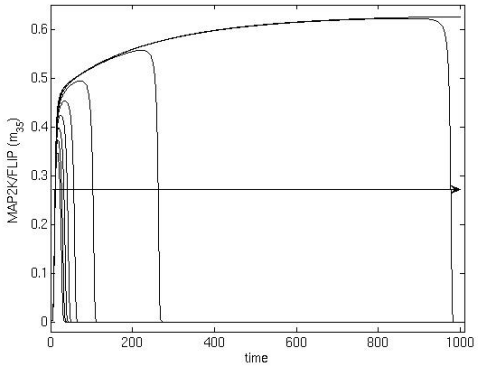

(b) $k_8 = 1$ and $0.24 \leq k_{FLIP} \leq 0.30$

Figure 2.18: MAP2K/FLIP (m_{35}) against time where arrow indicates solutions with increasing values of k_{FLIP} with $k_{90} = 0$ and $k_{14} = 0$.

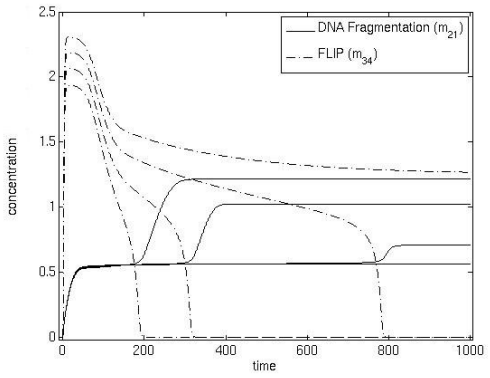

(a) $k_8 = 10^4$ and $0.18 \leq k_{FLIP} \leq 0.34$

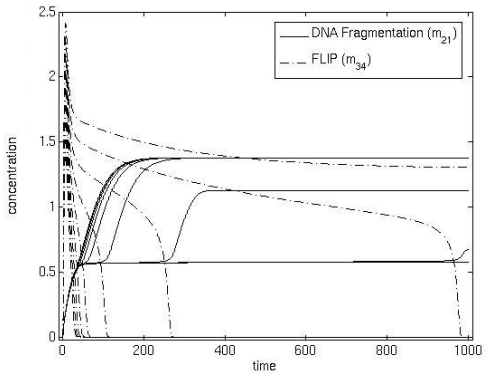

(b) $k_8 = 1$ and $0.24 \leq k_{FLIP} \leq 0.30$

Figure 2.19: DNA Fragmentation (m_{21}) and FLIP (m_{34}) against time where arrow indicates solutions with increasing values of k_{FLIP} with $k_{90} = 0$ and $k_{14} = 0$.

activated FLIP is exhausted. Figure 2.19 shows how when FLIP is exhausted, the concentration of DNA fragmentation again increases. The steady state concentration of DNA fragmentation in Figure 2.19 also decreases with k_{FLIP}. This is because the prolonged activation of the MAPK pathways has exhausted the initial supply of c-Fos (m_{28}).

The concentration of MAP2K*/FLIP increases as long as the MAPK pathways remain unactivated. The concentration of FLIP is large enough that all available MAP2K* are immediately inhibited by FLIP before they can activate JNK (m_{27}). As the concentration of FLIP is decreased, the concentration of MAP2K* is increased. This allows ITCH to be upregulated and the activation feedback loop between MAP2K* and AP-1 brings the MAP2K pathway to steady state. The maximum concentration of MAP2K* increases as k_{FLIP} increases, as the concentration of MAP2K/FLIP when this feedback loop is activated is larger as k_{FLIP} is decreased.

Figure 2.16 indicates how the initial activation of MAP2K* is sharper when $k_8 = 1$ than when $k_8 = 10^4$. The initial peak in FLIP in Figure 2.19 is also sharper when $k_8 = 1$ than when $k_8 = 10^4$ as the initial activation of $MAP2K^*$ is slower. In order to isolate the activity of the ITCH/FLIP/MAP2K* interaction from that of the ROS-dependent disassociation of MAP2K* from Thioredoxin, $k_8 = 1$ for the remaining results in this section.

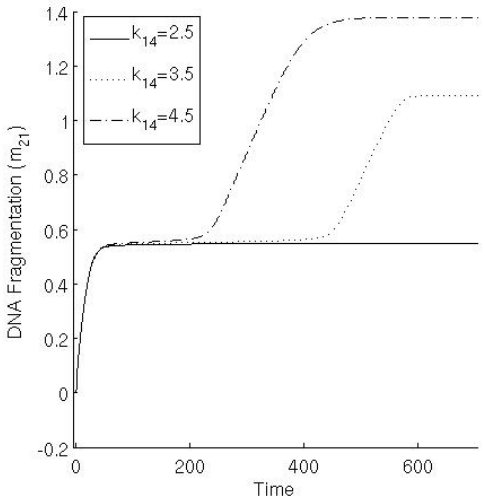

(a) DNA Fragmentation (m_{21}).

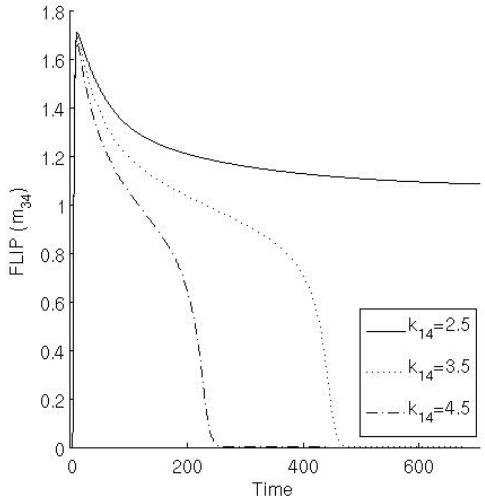

(b) FLIP (m_{34}).

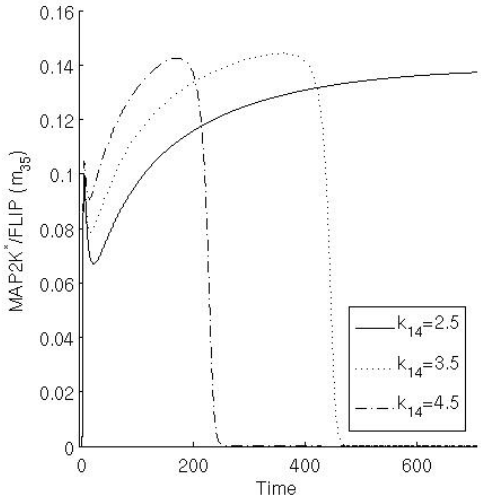

(c) MAP2K*/FLIP (m_{35}).

Figure 2.20: Selection of results when $\text{bind}_C = 1$, $\text{bind}_D = 1$, $k_{FLIP} = 0.24$, $k_{90} = 3$ and $k_{14} \neq 0$.

If $k_{90} \neq 0$ then instead of being inhibited by FLIP, MAP2K* can be deactivated by phosphatases. Figure 2.20 summarises the behaviour of the model as the rate of production of ROS by nanoparticles, k_{14}, is increased and $k_{90} = 3$. When k_{14} is below a certain value, for a given k_{FLIP} and k_{90}, $\Delta m_{21} = 0$.

As k_{14} increases, then the phosphatases will deactivate more rapidly. Figures 2.20(b) and

2.20(c) show how FLIP will decrease more rapidly to form more MAP2K*/FLIP as k_{14} is increased. So as k_{14} is increased more MAP2K* is stored by being bound to FLIP than is deactivated by the phosphatases. If more MAP2K is stored the oxidative stress pathway reactivates more quickly, as already discussed.

Figure 2.21(b) indicates how the minimum value of MAP2K* after the initial activation and deactivation of the MAPK cascade increases with k_{14}. If the minimum value of MAP2K* increases then this also means that the oxidative stress reactivates faster.

If the oxidative stress pathway is reactivated too slowly, the supply of c-Fos, required to form AP-1 (m_{29}), is depleted. Figures 2.21(c) and 2.20(a) show how the supply of c-Fos is depleted before $m_{21}(\infty)$ reaches its maximum possible value.

It was chosen that k_9 is an exponentially decaying function with ROS (m_{32}). So if k_{90} is increased, it will take a longer and longer time for the oxidative stress pathway to reactivate for a given k_{14}.

For each k_{90} and k_{FLIP} there is a minimum value of k_{14} for which $\Delta m_{21} > 0$. Figure 2.22(a) indicates that as k_{14} is increased, Δm_{21} will reach its maximum possible value. Figure 2.22(a) also indicates how, as k_{90} is increased, the minimum value of k_{14} for which $\Delta m_{21} > 0$ increases.

Figure 2.22(b) plots the values of k_{14} for which $m_{21}(500) = 1.38$ (to within an error of 10^{-2}) when $k_{FLIP} = 0.22$, 0.24, 0.26 and 0.28 and $k_{90} = 1$. $m_1 = 1.38$ is the maximum possible value of DNA fragmentation (m_{21}) at steady state when $k_{FLIP} \approx 0.25$. As k_{90} increases then the corresponding value of k_{14} also increases. A small increase in k_{FLIP} also increases the corresponding value of k_{14}. The spread in k_{14} for a given k_{90} also increases with k_{FLIP}.

Figure 2.22(a) shows that the range in k_{14} over which $0 \leq \Delta m_{21} \leq 1.38$ is small. Figure 2.22(a) also shows that the range in k_{14} over which $0 \leq \Delta m_{21} \leq 1.38$ do not overlap for values of k_{90} given. The sensitivity of the model to ROS depends strongly on k_{90}. However, 2.22(b) suggests that the sensitivity of the model to variation in k_{FLIP} will decrease if k_{90} is smaller. As k_9 is chosen to decay exponentially, any difference in the value of k_{14} required to see a reactivation of the oxidative stress sensitive pathway will increase as k_{90} is increased.

The results in Figure 2.21 are strongly dependent on the form of k_9 in Table 2.2. However, they do demonstrate the idea that the FLIP/ITCH and phosphatase interactions can act together ensure that there is not a second activation of the caspases if there is not a threshold amount of ROS inside the cell. They also act to control the speed of this second activation of the caspases.

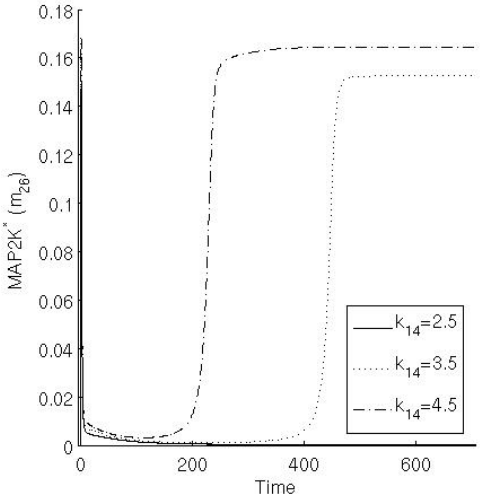

(a) MAP2K* (m_{26}).

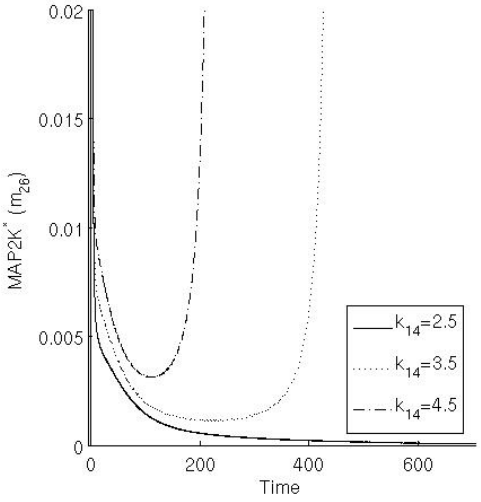

(b) Close-up of Figure 2.21(a), indicating the minimum concentration of MAP2K* (m_{26}) after initial activation. Note scale on y-axis.

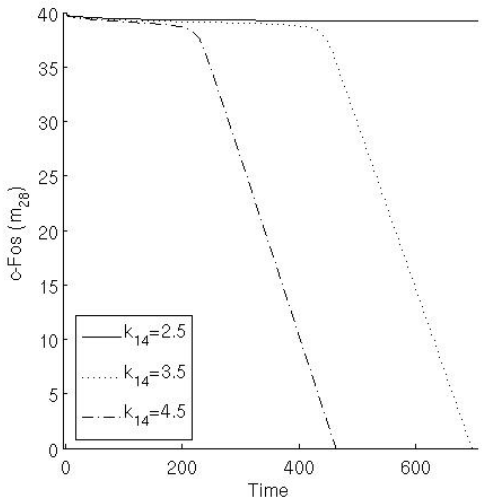

(c) c-Fos (m_{28}).

Figure 2.21: Selection of results when $\text{bind}_C = 1$, $\text{bind}_D = 1$, $k_{FLIP} = 0.24$, $k_{90} = 3$ and $k_{14} \neq 0$.

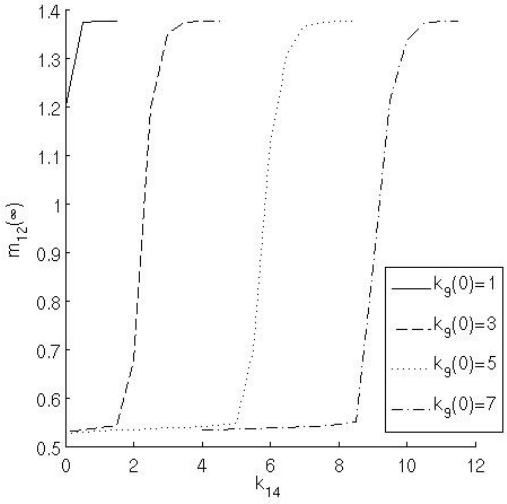

(a) $m_{21}(\infty)$ against k_{14} for given values of k_{90} when $k_{FLIP} = 0.22$.

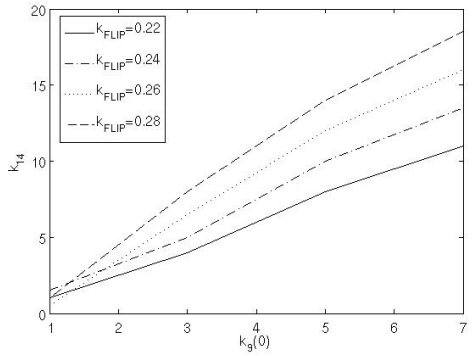

(b) Value of k_{14} at which $m_{21}(\infty)$ is at is maximum for given values of k_{90} and k_{FLIP}.

Figure 2.22: Selection of results when $\text{bind}_C = 1$, $\text{bind}_D = 1$, $k_{FLIP} = 0.24$, $k_{90} = 3$, $k_8 = 1$ and $k_{14} \neq 0$.

2.4.2.5 Sensitivity Analysis for Model Version A

The oxidative stress sensitive elements of the model as listed in Table 2.3.1 ensure that the rate at which the oxidative stress sensitive pathway activates is determined by the concentration of ROS. These mechanisms have been discussed in the preceeding sections. However, it is the initial concentrations of the proteins and their associated rate constants which determine the maximum possible value of Δm_{21}. This section sets out to establish whether the value of Δm_{21} is more sensitive to the strength of the extracellular signal and so $m_1(0)$, or the initial concentrations of other proteins in the model. If the extent of DNA fragmentation is more sensitive to the intracellular proteins rather than the extracellular signal then there is no quantitative dependence between the extent of DNA fragmentation and extracellular signal. Given a minimum concentration, the extracellular signal only has a switch-like effect.

The aim of the sensitivity analysis in this section and also in Section 2.4.4.1 is to establish how inputs to the model, in the form of initial concentrations of proteins, correlation to outputs, in the form of Δm_{21}. This has been done by finding the relevant product moment coefficients [94]. This is a common method, of which there are many variations.

Two simple methods were used to quantify the sensitivity of Δm_{21} to perturbations in the initial protein concentrations and reaction constants. Initial concentrations of proteins which are to be perturbed will be referred to by their index i in (2.49).

$$\mathbf{m} = [m_1,\, m_2,\, m_4,\, m_6,\, m_9,\, m_{13},\, m_{15},\, m_{18},\, m_{24}]. \tag{2.49}$$

Their unpertubed values are those given in Section 2.4.2.1. The vector of rate constants which were perturbed in the sensitivity analysis is defined in Appendix B. These are the rate constants which are not associated with the MAPK activation cascade. Rate constants which are varied will be referred to by their index j in $\mathbf{K}$. The unperturbed rate constants are those in Table 2.2.

In the first method, all of either the selected initial protein concentrations or selected rate constants are varied over n runs. Initial concentrations of proteins which are varied will be referred to by their index i in (2.49). The vector of rate constants which were varied in the sensitivity analysis is defined in Appendix B. Perturbed rate constants will be referred to by their index j in $\mathbf{K}$.

Over n runs for each initial condition, m_i, in the vector $\mathbf{m}$, and rate constant, K_j, in the vector $\mathbf{K}$, a random number r_{ni} and s_{ni} is chosen from a continuous uniform distribution $U[-0.25, 0.25]$ so that

$$\tilde{m}_{ni} = m_i(1 + r_{ni}), \tag{2.50}$$

$$\tilde{K}_{nj} = K_j(1 + s_{nj}). \tag{2.51}$$

The output from each run is $q_n = \Delta m_{21}/m_{21}(\text{off})$. A Pearson correlation coefficient coefficent ρ_i or ρ_j can be found for each initial condition in $\mathbf{m}$ and rate constant in $\mathbf{K}$ respectively so

that

$$\rho_i = Cor\left(\tilde{m}_{ni}, q_n\right), \tag{2.52}$$

$$\rho_j = Cor\left(\tilde{K}_{nj}, q_n\right). \tag{2.53}$$

The i at which $|\rho_j|$ is a maximum indicates the initial condition to which $\Delta m_{21}/m_{21}(\text{off})$ is most sensitive to. Similarly, the j at which $|\rho_j|$ is a maximum indicates the rate constant to which $\Delta m_{21}/m_{21}(\text{off})$ is most sensitive to. ρ is the product moment correlation coefficient as defined in many books such as [94] which measures the correlation between an input and an output in a model. The results of this sensitivity analysis can be found in Figure 2.23 when $n = 722$.

In the second method, each of these initial concentrations and rate constants are in turn increased then decreased by 25%. The results of this perturbation test can be found in Figure 2.24.

The results in Figure 2.23(b) for perturbing the initial concentrations suggest that $\Delta m_{21}/m_{21}(\text{off})$ is most sensitive to small changes in initial condition $i = 8$ or caspase-3 ($m_{18}(0)$). The maximum value of $m_{21}(\infty)$ is determined by the initial condition of caspase-3. If there is excess caspase-8*, then increasing $m_{18}(0)$ will increase Δm_{21}. The second most significant correlation was between $\Delta m_{21}/m_{21}(\text{off})$ and Nκ-B/Iκ B ($m_9(0)$). If this initial concentration is increased, then the maximum value of c-IAP (m_{22}) will increase. This will increase the percentage of caspase-3 bound to c-IAP, decreasing $m_{21}(\text{off})$ and increasing Δm_{21}. Figure 2.24(a) confirms that increasing the initial concentration of either caspase-3 or Nκ-B/Iκ B will increase $\Delta m_{21}/m_{21}(\text{off})$.

The results of the sensitivity analysis with respect to the initial concentrations of the proteins in the apoptotic and anti-apoptotic pathways show that the extent of apoptosis is controlled by the conditions inside the cell rather than the extracellular signal. The extracellular signal acts as a switch, where, above a certain concentration, it does not determine the extent of apoptosis. The organism does not have to tightly regulate the concentration of extracellular signal is order to ensure an apoptotic response.

The results for perturbing the rate constants in Figure 2.23(d) suggest that $\Delta m_{21}/m_{21}(\text{off})$ is most sensitive to small changes in rate constant K_{20}. Increasing K_{20} increases the rate at which caspase-3* converts into DNA damage. If K_{20} is decreased then $m_{21}(\text{off})$ will increase and Δm_{21} will decrease, as less caspase-3* will be captured by c-IAP (m_{22}). The results from the perturbation analysis in Figure 2.24(b) suggest that perturbations in K_{21} could also cause perturbations in $\Delta m_{21}/m_{21}(\text{off})$. This is the rate at which caspase-3* binds with c-IAP (m_{22}). If this is increased then $m_{21}(\text{off})$ will decrease and Δm_{21} will increase. However, in the sensitivity analysis the correlation between K_{21} and $\Delta m_{21}/m_{21}(\text{off})$ is lost when all rate constants and initial concentrations are made perturbed over a series of solutions.

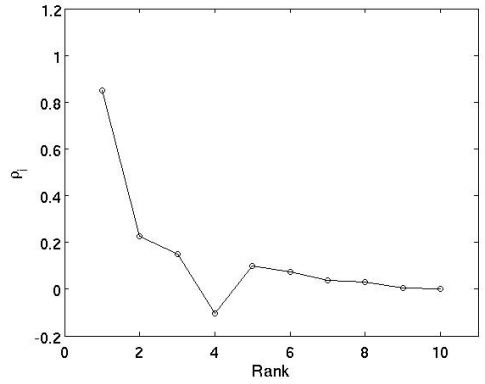

(a) ρ_i ranked by absolute magnitude.

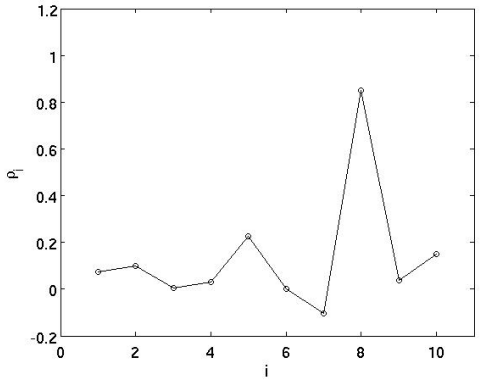

(b) ρ_i against i.

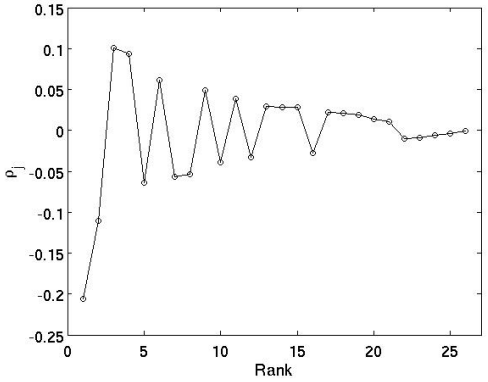

(c) ρ_j ranked by absolute magnitude.

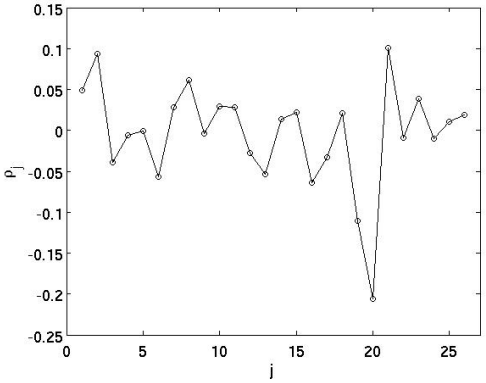

(d) ρ_j against j.

Figure 2.23: Results of sensitivity analysis on apoptotic and survival pathways in model version A. ρ_i correlates perturbations of initial concentration (2.49) and $\Delta m_{21}/m_{21}(\text{off})$ whereas for ρ_j this correlation is with rate constants (Appendix B).

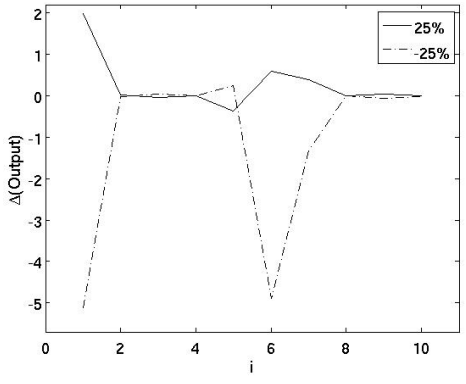

(a) Δ(Output) against i.

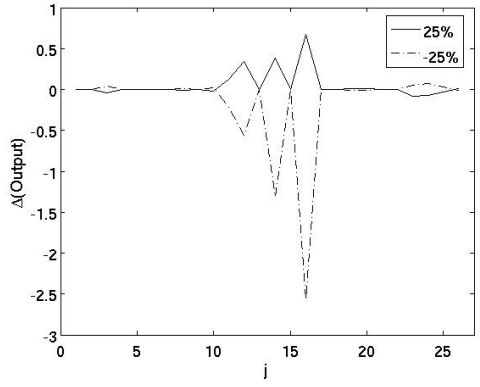

(b) Δ(Output) against j.

Figure 2.24: Δ(Output) is the difference between value of $\Delta m_{21}/m_{21}(\text{off})$ obtained when increasing or decreasing a single initial condition i (2.49) or a single rate constant j (Appendix B) and the unperturbed value of $\Delta m_{21}/m_{21}(\text{off})$. Δ(Output)=perturbed-unperturbed.

2.4.3 Summary of Model A

When apoptotsis is inhibited by c-IAP, the consequence of the condition that caspase-3 has to be reactivated once it is released is that Δm_{21} has a limited maximum value. It was found that if $\Delta m_{21}/m_{21}(\text{off})$ is maximised then the value of $\Delta m_{21}/m_{21}(\text{off})$ is invariant for all $m_1(0) > 12$. The initial concentration of the extracellular signal has relatively little effect on the steady state concentration of DNA fragmentation. Whether this additional amount of DNA fragmentation is oberved or not can be made to be strongly dependent on the levels of ROS in the cell. This can be done by varying k_{90}, k_d and k_8. Varying k_8 by orders of magnitude determines the sharpness of the activation of the MAPK pathway. The order of magnitude of k_d makes a big difference to the timing and rate of the reactivaton of the MAPK pathways after their initial deactivation. k_{90} was used to fine tune this reactivation once k_8 and k_d are set.

The FLIP inhibition of MAP2K* and the deactivation of MAP2K by the ROS sensitive phosphatases can act together to form a very ROS sensitive mechanism. In this mechanism, a sudden reactivation of the MAPK pathway and increase in DNA fragmentation will be observed when the concentration of ROS exceeds a certain level. FLIP acts to capture MAP2K* before it is deactivated by the action of the phosphatases. The relative amount of MAP2K* captured and deactivated depends on the maximum concentration of FLIP relative to the rate of phosphatase deactivation $k_9(m_{32})$. If m_{32} is smaller and k_9 is larger, then more MAP2K* is wasted by being deactivated by the phosphatases, and so Δm_{21} will be smaller.

For the initial conditions introduced in Section 2.4.2.1, $m_{21}(\text{off})$ does not vary much with $m_1(0)$, as demonstrated in Figure 2.12. This means that the concentration of ROS dependent on apoptosis is also approximately the same. As a result, the FLIP/MAP2K* mechanism is sensitive to the ROS produced by nanoparticles inside the cell.

The role of k_{90} and k_{14} in the ROS sensitive FLIP/MAP2K* mechanism is clearer when k_8 is small. In this case the activation of MAP2K is close to a step function with respect to ROS. All the MAPK are activated at approximately the same time as the activation peak is sharp. If the activation peak is broader, then k_9 will decrease in value over the period that MAP2K is activated, so the increase in Δm_{21} will k_{14} will not be so sharp.

If the initial concentration and rate constants in the survival and apoptosis pathways are subject to perturbations from a mean value, to stimulate the environment inside a cell, then $\Delta m_{21}/m_{21}(\text{off})$ is particularly sensitive to only one intitial concentration, that of caspase-8, and one rate constant, the rate at which caspase-3 converts in DNA fragmentation. The results reflect the insensitivity of $\Delta m_{21}/m_{21}(\text{off})$ to TRADD when the initial concentration of TRADD has exceeded a certain value. In this case the extracellular signal acts as a switch rather than having a qualitative effect on the results.

2.4.4 Model B

The difference between model A and model B, as defined in Table 2.3.1 is the in model A FLIP inhibits MAP2K*, while in model B FLIP inhibits TRADD/FADD (m_{14}), which is commonly referred to as the death complex. When FLIP inhibits the death complex, rather than MAP2K*, the behaviour the model captures is qualitatively different. The ROS dependent elements are the ROS dependent acitivation of AP-1 and the ROS sensitive phosphatases, which are interactions A and B in Table 2.3.1. The inhibition of the death complex by FLIP allows, for certain choices in initial conditions of FADD (m_{13}), caspase-8 (m_{15}) and caspase-3 (m_{18}), for $\Delta m_{21}/m_{21}(\text{mid})$ to be much greater and for it to increase with a much greater rate as a function of ($m_1(0)$). As TRADD/FADD (m_{14}) does not have to be reactivated once it is released from FLIP (m_{34}) by ITCH (m_{36}). Δm_{21} is only limited by the amount of caspase-3 (m_{18}) inside the cell.

The rate of increase of $m_{21}(\text{off})$ with $m_1(0)$ can be optimised by maximising the increase in this value for a jump in $m_1(0)$. In a numerical optimisation using the MATLAB *fminsearch*, the difference in Δm_{21}, when $m_1(0) = 20$ and $m_1(0) = 30$, was maximised by allowing the initial concentrations of TRAF2 (m_2), FADD (m_{13}), caspase-8 (m_{15}) and caspase-3 (m_{18}) to be free variables. In Section 2.4.2, TRAF2 (m_2) was not included in the corresponding maximisation problem. However, in this case, the death complex (m_{14}) is the target of the cross-talk between the pathways so the concentration of TRAF2 (m_2) will have an immediate effect on the concentration of the death complex (m_{14}) and so the strength of the cross-talk. In this section, the rate of production of FLIP in Table 2.3 is constant, $k_{FLIP} = 1$ and does not vary from this value in this section.

The results of this optimisation found that if

$$m_2(0) = 0.17, \quad m_{13}(0) = 0.07, \quad m_{15}(0) = 4.22 \text{ and } m_{18}(0) = 38.53, \tag{2.54}$$

then $m_{21}(\text{off}) = 34.57$ and $\Delta m_{21} = 32.38$. Clearly these values are much larger than those found for model version A. These initial conditions are used to find the results in this section. In Figure 2.25, these initial conditions ensure that there is an almost linear correspondence between the initial concentration of TRADD ($m_1(0)$) and Δm_{21}. The value of $m_{21}(\text{off})$ when the FLIP/ITCH interactions are switched off, and so $\text{bind}_E = 0$, is almost constant with respect to $m_1(0)$. This is not the case when the c-IAP/Bidj interaction is switched off in model A, as demonstrated in Figure 2.14(a). As the concentration of DNA fragmentation is continually increasing until it reaches steady state, other sources of ROS, as defined by k_{14} are not considered here. Hence k_{14} would have to be very large to make an observable difference to the results.

As Δm_{21} is so large, then the phosphatases will quickly deactivate. A smaller k_d could be chosen for the phosphatases to deactivate more slowly. However, as the action of the phosphatases were investigated extensively for model version A, the ROS sensitive activation of MAP2K* will be considered the dominant ROS sensitive mechanism in the oxidative stress sensitive pathway.

The form of phosphatase deactivation are taken to be those in Table 2.2. In Figure 2.26, the results show that increasing k_8 by order of magnitude can slow down the rate at which DNA fragmentation reaches its maximum value by making the rate at which MAP2K* is released from TRADD/TRAF2/Thioredoxin/MAP2K more sensitive to ROS. As k_8 is increased, the speed at which MAP2K activates increases. Figure 2.26(b) also shows that the final steady state value of m_{26}, as well as the speed of activation, is also adjusted by k_8. The remaining results in this section are those in the case that $k_8 = 10^7$. This is the largest value of k_8 in Figure 2.25(a) for which the steady state value is not decreased due to the depletion of c-Fos (m_{28}). By choosing this value of k_8, the MAPK pathway is more sensitive to ROS. As the FLIP/ITCH reaction will not be regulating the activation of the MAPK pathway in model B, a larger value of k_8 will allow the activation of the MAPK pathway to be regulated by ROS.

Results from an example solution of model version B can be found in Figures 2.27 and 2.28. Figure 2.27(a) shows that the MAP kinases activate slowly. The amount of FADD ($m_{13}(0)$) is small so that maximum concentration of TRADD/FADD/FLIP (m_{38}) will also be small. Figure 2.27(c) indicates that as the MAP kinases activate, the concentration of TRADD/FADD/FLIP decreases and the concentration of free TRADD/FADD increases. The time taken to reach steady state is longer than that for model version A, as the maximum concentrations of proteins in Figure 2.26 are small. The law of mass action states that the speed of a reaction is proportional to the concentration of the reactants.

The survival pathway in Figure 2.28(b) is activated once only. However, the apoptotic pathway in Figure 2.28(c) is activated twice. After it is deactivated by FLIP, it is reactivated by ITCH, once the MAP pathway reactivates. The survival pathway and oxidative stress pathways are not continually reactivated by TRADD. The initial concentration of TRAF2 (m_2) is small and the protein is soon depleted. This ensures that the extracellular signal is not wasted activating the anti-apoptotic pathway, maximising the value of Δm_{21}.

The solution reaches steady state when the concentration of caspase-3 in Figure 2.28(a) has decreased to zero. As the concentration of caspase-3 decreases, the concentration of m_1 also decreases. As caspase-8 does not need to be reactivated, as is the case for caspase-3 in model version A, the apoptosis pathway can be continually activated by the extracellular signal.

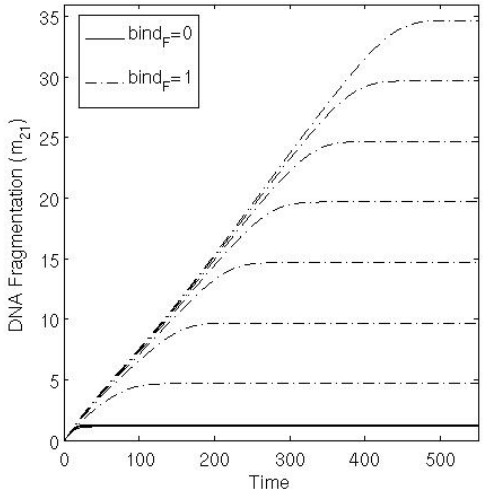

(a) DNA fragmentation (m_{21}) against time when ITCH interaction is switched off and bind$_F$=0 and when it is switched on and bind$_F$=1.

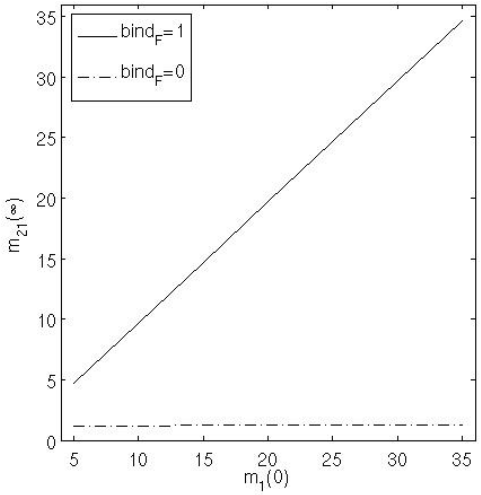

(b) Steady state m_{21}, m_{21}(off), against ($m_1(0)$).

Figure 2.25: Dependence of Δm_{21} on $m_1(0)$ in model version B where initial conditions different from those in Section 2.3 are given in (2.54).

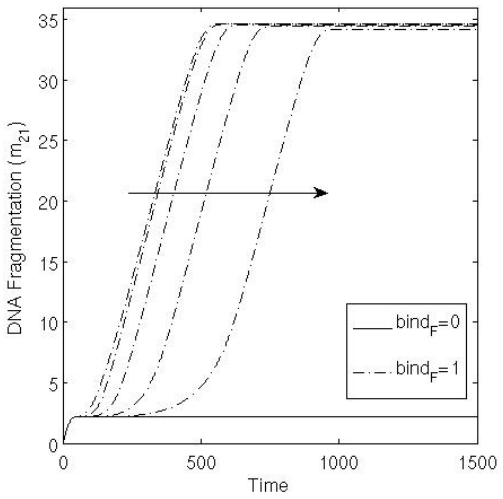

(a) DNA fragmentation (m_{21}).

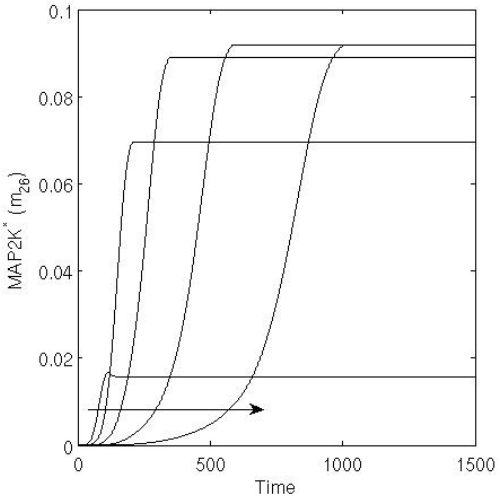

(b) MAP2K* (m_{26}).

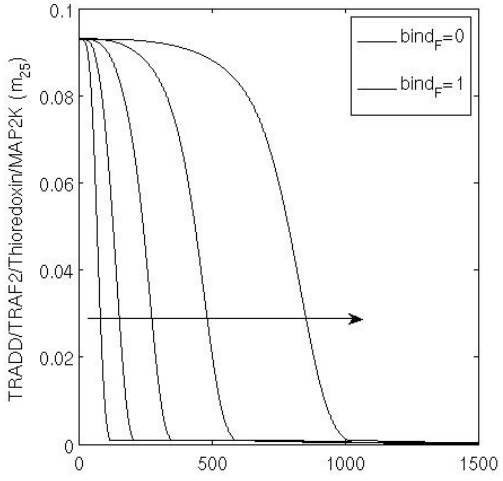

(c) TRADD/TRAF2/Thioredoxin/MAP2K (m_{25}).

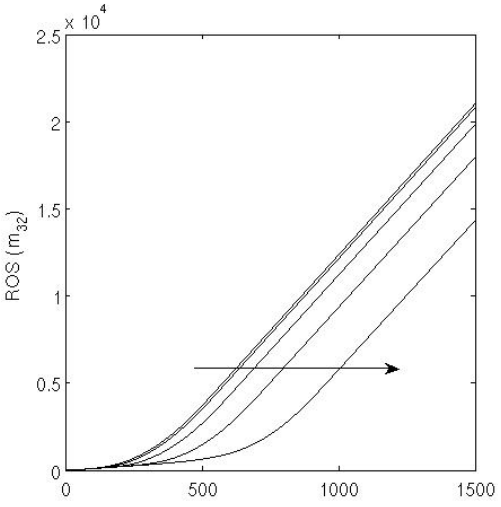

(d) ROS (m_{32}).

Figure 2.26: Dependence of Δm_{21} on disassocation constant k_8 where $k_8 = 10^5$, 10^6, 10^7, 10^8 and 10^9, $m_1(0) = 30$ and bind$_F$=1. Otherwise initial conditions are those in Section 2.3 are given in (2.54). Arrows indicate increasing k_8.

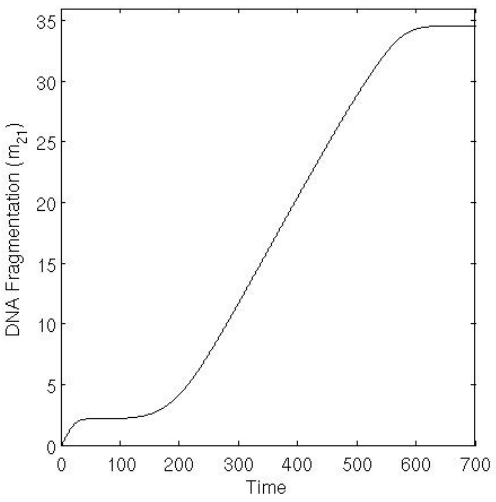

(a) DNA fragmentation (m_{21}).

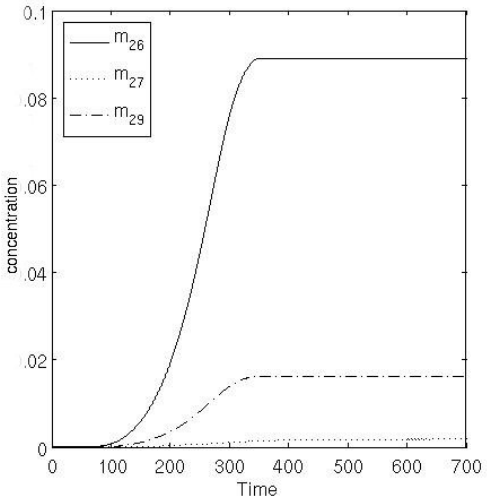

(b) MAP2K* (m_{26}), JNK* (m_{27}) and AP-1 (m_{29}).

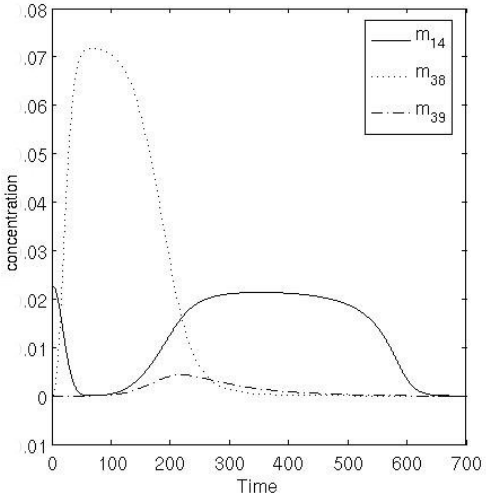

(c) TRADD/FADD (m_{14}), TRADD/FADD/FLIP (m_{38}) and TRADD/FADD/FLIP/ITCH (m_{39}).

Figure 2.27: Results when $m_1(0) = 20$ and $k_8 = 10^7$. Otherwise initial conditions are those in Section 2.3 are given in (2.54).

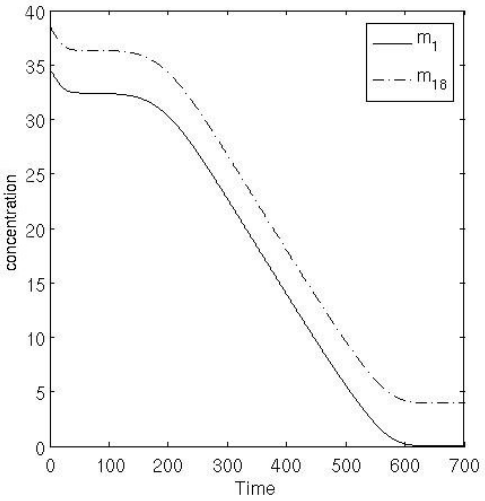

(a) TRADD (m_1) and caspase-3 (m_{18}).

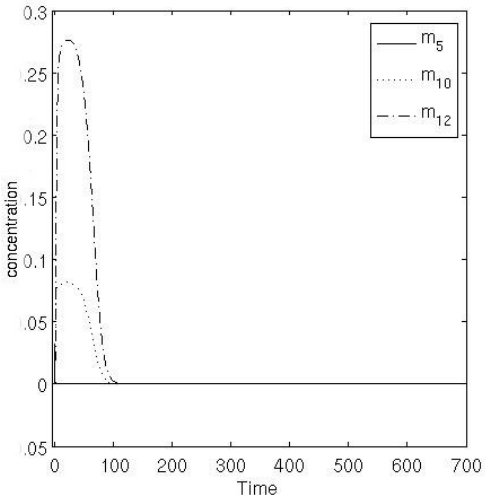

(b) TRADD/TRAF2/RIP-1 (m_5), NF-κ B (m_{10}) and NF-κ B (m_{12}).

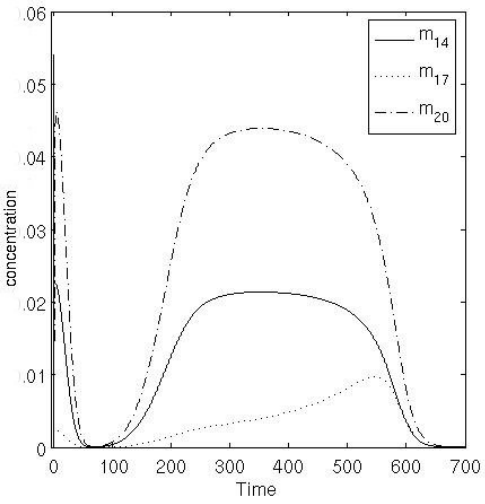

(c) TRADD/FADD (m_{14}), caspase-8* (m_{17}) and caspase-3* (m_{20}).

Figure 2.28: Results when $m_1(0) = 20$ and $k_8 = 10^7$. Otherwise initial conditions are those in Section 2.3 are given in (2.54).

2.4.4.1 Sensitivity Analysis for Model Version B

The sensitivity analysis for model version B follows the method used in Section 2.4.2.5. The number of runs in this case is, $n = 332$. The number of runs in this case is different then that in Section 2.4.4.1. However, in both cases n is of a similar order of magnitude to make the results in this section comparable to those in Section 2.4.4.1. The results of the stochastic sensitivity analysis can be found in Figure 2.29 and those for perturbing initial concentrations and rate constants can be found in Figure 2.30.

The two initial concentration whose values correlate strongly with Δm_{21} are TRADD ($m_1(0)$) and FADD (m_{13}). If either of these initial concentration increase then the value of Δm_{21} increases. Correlation between the other initial concentrations and Δm_{21} is minimal. If either TRADD ($m_1(0)$) and FADD (m_{13}) are increased then Δm_{21} is increased as this increases the peak concentration of the death complex. If the peak concentration of the death complex in increased then m_{21}(off) is increased, increasing Δm_{21}.

If the value of Δm_{21} correlates most strongly with extracellular signal, the results of this sensitivity analysis suggest in Figure 2.29(b) that, when FLIP is the main inhibitor of apoptosis, variation in conditions inside the cell do not significantly influence the decision whether or not a cell undergoes apoptosis. This decision is mainly influenced by the concentration of the extracellular signal. However, the initial concentration of FADD has a moderate influence on this decision which suggests that its concentration inside the cell might still be tightly controlled.

In Figure 2.29(d), the only significant correlation between rate constants and Δm_{21} was found for K_{16}. This is the reaction constant which converts TRADD/FADD/caspase-8 into caspase-8*, TRADD and FADD. If the rate of this reaction is increased, then the reaction cascade by which death complex TRADD/FADD (m_{14}) activates the caspases will be faster than the rate at which TRADD/FADD (m_{14}) is inhibited by FLIP. FLIP will have less opportunity to inhibit the death cascade, so that the maximum concentration of TRADD/TRAF2/FADD/FLIP (m_{39}) will be smaller. This means that if K_{16} is increased, m_{21}(off) will be larger.

If each of the initial concentrations are increased or decreased by 25% then, as for the case where all initial concentration i and rate constants j are stochastic, the output only significantly changes when $m_1(0)$ or $m_{13}(0)$ is increased or decreased. This can be observed in Figure 2.30(a). An decrease in either decreases the perturbed value of Δm_{21} and, to a lesser extent, an increase in either increases the perturbed value of Δm_{21}.

Results in Figure 2.30(b) suggest that the three rate constants which have a significant ability to change Δm_{21} are K_{16}, K_{14} and K_{12}. As previously discussed, increasing the value of K_{16} decreases the amount of time the death complex is available to be inhibited by FLIP. Increasing the rate constant K_{14} increases the rate at which TRADD/TRAF2/FADD (m_{14}) binds to caspase-8 (m_{15}). Increasing the rate constant K_{12} increases the rate at which TRADD (m_1) binds to FADD (m_{13}). Both these rate constants increase the speed of the signal down the apoptotic pathway. The death complex is formed further upstream than FLIP, so if the

speed of the apoptotic pathway is increased then the concentration of the death complex will be well past its maximum by the time the concentration of FLIP is a maximum. This will decrease the maximum concentration of inhibited death complex death complex/FLIP (m_{38}). However, any correlation between K_{14} and K_{12} and Δm_{21} is lost when all initial concentrations i and rate constants j are made stochastic. Their value of ρ_j is not significantly large in Figure 2.29(d). The rate of the reactions, whose rate constants are K_{14} and K_{12}, are proportional to the concentrations of the two associating species. However, the reaction with rate constant K_{16} is self-activating. It is reasonable that the correlation of K_{16} with Δm_{21} is more robust than those with K_{14} and K_{12} as the rate of this reaction is less depedent on other randomly varying factors.

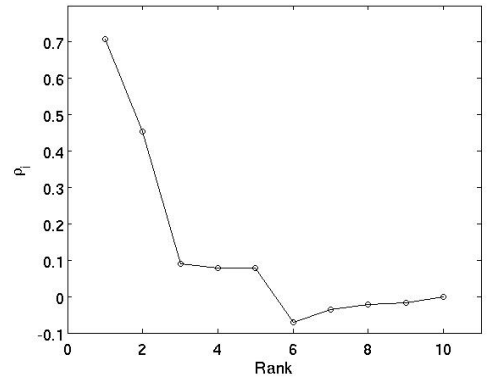

(a) ρ_i ranked by absolute magnitude.

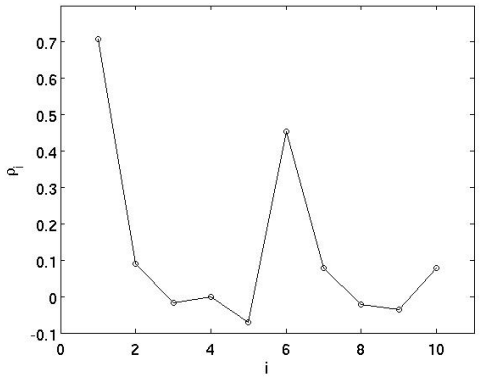

(b) ρ_i against i.

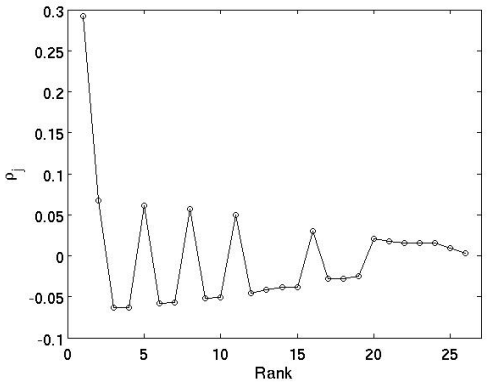

(c) ρ_j ranked by absolute magnitude.

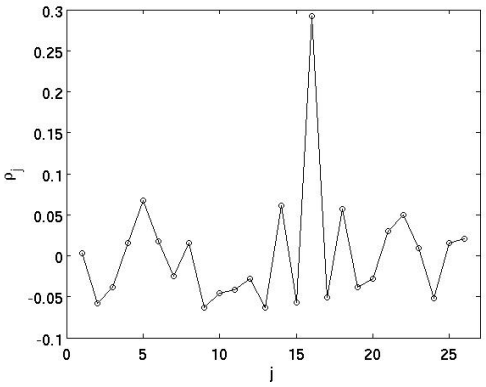

(d) ρ_j against j.

Figure 2.29: Results of sensitivity analysis on apoptotic and survival pathways in model version B. ρ_i correlates perturbations of initial concentration, r_{ni}, with Δm_{21} whereas for ρ_j this correlation is between s_{nj} and rate constants (Appendix B).

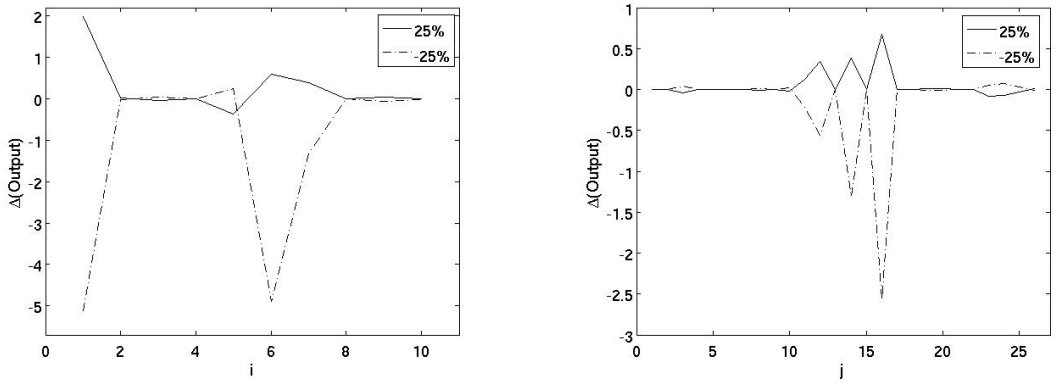

(a) Δ(Output) against i. (b) Δ(Output) against j.

Figure 2.30: Δ(Output) is the difference between value of Δm_{21} obtained when increasing or decreasing a single initial condition i (2.49) or a single rate constant j (Appendix B) and the unperturbed value of Δm_{21}. Δ(Output)=perturbed-unperturbed.

2.4.5 Summary of Model B

When apoptosis is inhibited by FLIP, Δm_{21} is only limited by the initial concentration of caspase-3 inside the cell and the concentration of the extracellular signal. The apoptotic pathway can be continually reactivated until either caspase-3 is depleted or the pro-apoptotic pathway is deactivated. The oxidative stress pathway acts to slow down the rate of increase of DNA fragmentation. By choice of rate constants, this rate is dependent on the rate at which ROS act to disassociate activated MAP2K from Thioredoxin. The anti-apoptotic pathway is prevented from being continually reactivated by a relatively small initial concentration of TRAF2. When this is depleted the survival pathway can no longer be activated by TRADD.

Model B illustrates the case where the inhibition of the death complex allows the rate of activation of the apoptosis pathway to be set by the rate of activation of the oxidative stress sensitive pathway. A concentration of TRADD/FADD (m_{14}) complex is initially formed and rapidly inhibited by FLIP. As the oxidative stress sensitive pathway is activated, it is released by ITCH. The rate at which it is released by ITCH is dependent on the concentration of ITCH and so the steady state concentration of AP-1 in the oxidative stress sensitive pathway.

During the period over which the oxidative stress sensitive pathway is activated the concentration of TRADD/FADD is almost constant as the rate at which is released from FLIP by ITCH is similar to the rate at which it binds to caspase-8. This causes the concentration of m_{21} to increase at a steady rate over the period the oxidative stress pathway is activated. Therefore, the results in this section show how the model can be used to produce results indicating a sustained and steady response to an extracellular signal rather than the sharper response typical of model A.

When the initial concentration and rate constants in the survival and apoptosis pathways are subject to perturbations from a mean value to stimulate the environment inside a cell, Δm_{21} is only particularly sensitive to two initial concentrations and one rate constant. The initial concentration it is most sensitive to is that of TRADD, highlighting the sensitivity of model version B to the extracellular signal. The other initial concentration was that of FADD, which plays a similar role to caspase-3 in model version A. If FADD is increased then Δm_{21} will increase. The rate constant is that which activates TRADD/FADD/caspase-8. Increasing this rate constant, speeds up the rate of reaction down the apoptotic pathway, decreasing the opportunity for FLIP to bind with the death complex.

2.5 Extensions to Immune Response Model

In [107] the effects after the inhalation of CNTs on the lung were studied. The results of this study, along with those of connected studies are summarised in [120]. The observable responses in the lungs on the inhalation of CNTs were found to be direct damage of cells, the formation of granulomas and finally interstitial fibrosis and thickening of the extracellular matrix. The form of the inflammatory response was found to be marked by a rapid induction of proinflammatory cytokines, including TNF-α and other proinflammatory cytokines such as IL-1. Results in [107] show that after a week, the concentration of these cytokines has returned to normal levels while the concentration of Transforming Growth Factor (TGF)-β is greatly increased.

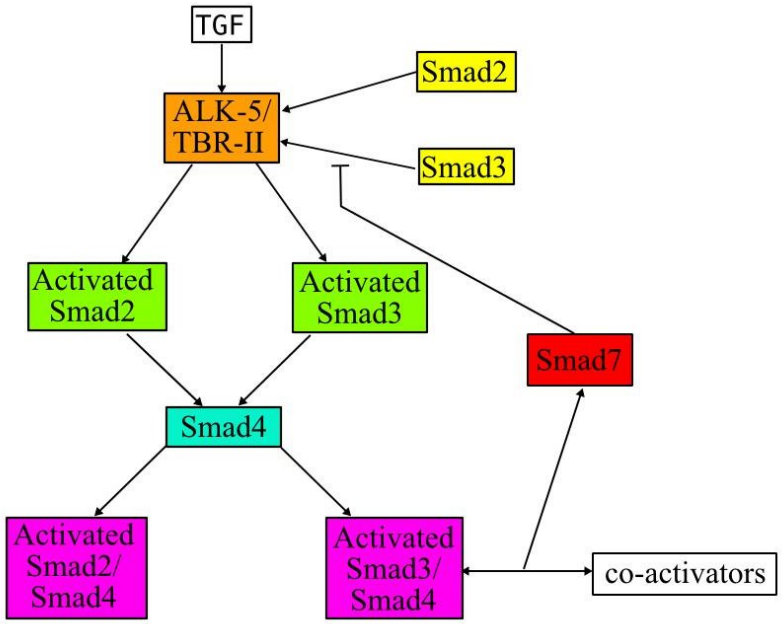

Figure 2.31: TGF-β activation cascade where Smad7 can inhibit the activation of Smad3 by ALK-5.

TGF-β can refer to any protein within the TGF-β superfamily. Like TNF-α, it is an extracellular protein which, in its unactivated form, is found in the extracellular matrix bound to the latency-associated protein. The review paper [114] discusses in detail how mechanical strain on the lung increases the rate of matrix turnover, via integrins and TGF-β, which in turn changes the mechanical properties of the lung. TGF-β is otherwise induced when the epithelium is damaged to attract macrophages and fibroblasts to the site of injury which will then release more TGF-β. Considering the fibrous nature of CNTs and the formation of granulomas, which are a common result of failed phagocytosis, the sustained elevation in the concentration of TGF-β may well be strongly linked to the difficulty of clearing CNTs by macrophages.

The details of TGF-β dependent interactions within a cell are complex and cell dependent.

However, the key elements are well known and are illustrated in Figure 2.31. TGF-β binds to a receptor complex, consisting of one TGF-β type I (ALK5) and one TGF-β type II (TβRII) receptor. ALK5 is activated by TβRII. R-Smads such as Smad2 and Smad3 can then be activated. The activated R-Smads can then bind with Smad4 which allow them to, together with cofactors, upregulate target genes. Smad7 inhibits the activation of Smad2/3 by the ALK-5 receptor. The Smad3/4 complex induces the expression of Smad7, though only with the cooperation of AP-1 and Sp1 transcription factors. Smad3 is essential for the induction of specific genes such as type 1 collagen and connective tissue growth factor (CTGF) which contribute to a TGF-β induced fibrotic response.

In terms of the three pathway model of oxidative stress in this chapter, there is scope to add a pro-fibrosis pathway which is activated by TFG-β. The aim of the three pathway model is to investigate how a cell decides whether to survive, die by necrosis or die by apoptosis. A TFG-β activated pathway adds another option of a fibrotic response where a cell does not die but collagen and other extracellular material.

Specific interactions between TGF-β activated proteins and the apoptotic, anti-apoptotic and pro-apoptotic pathways in Chapter 2 can be found in the literature, some of which are listed below.

- Increased activation of TGF-β inhibitor Smad7 when AP-1 is activated [56], [128].
- Binding of activated c-Jun with Smad3 hindering upregulation of pro-fibrotic genes [56], [122].
- Upregulation of Smad7 by NF-κB [6], [122].
- Activation of TAK1 (TGF-βI-activated kinase I) by TGF-β. TAK1 can activate IKK causing a transient activation of NF-κB in a similar way to TNF-α, [97].
- TGF-β mediated induction of FLIP which can then inhibit activated caspase-8 and activated second tier MAPKs, inhibiting both the anti-apoptotic and pro-apoptotic pathways, [97].

The cell signalling network suggested by these interactions is complex. The scope can be simplified by considering interactions known in specific cell types of interest. Many of the principles used to investigate the three pathway model can be used and developed if another signalling pathway is added. In this case, the model will be a four pathway model with apoptotic, anti-apoptotic, pro-apoptotic and pro-fibrotic pathways. The key inputs will be the extracellular signals for apoptosis and fibrosis as well as the specific stressors on an individual cell, intracellular oxidative stress and mechanical strain. The four pathway model will then decide the balance between survival, apoptosis, necrosis and a fibrotic response.

2.5.1 Chapter Summary

After it was established that a key mechanism of nanoparticle toxicity is often taken to be mediated by the reactive oxidative species (ROS) they produce once inside a cell, a wide-ranging literature review of oxidative stress pathways was undertaken. The outcome of this literature review is the model presented in Section 2.1. The structure of the intracellular oxidative stress sensitive model in Section 2.3 contains many oxidative stress sensitive elements. The complete picture can seem complicated.

The model attempts to answer the question of what a oxidative stress sensitive apoptotic response looks like, given the discussion in many review papers such as [58] and [85]. This model is a numerical representation of all the elements discussed. However, no fine tuning of the model has been attempted. For example, parameters could be chosen so that the time delay between the initial and secondary activation of the caspases, ΔT, could be made either sensitive or insensitive to the extracellular signal $m_1(0)$. However, this would only be justified if the model was used to interpret experimental results.

Results capturing specific behaviours associated with the model are found in Section 2.4. These behaviours are qualitatively different depending on which pairs of inhibitor and inhibitor of inhibitor interactions are switched on. The inhibitor and inhibitor interactions are listed in Table 2.3.1 which indicates the colour-coding in the mathematical model in Section 2.3. In Section 2.4.2 the consequence of the caspase-3*/Bidj/c-IAP interaction was investigated, while in Section 2.4.4 the interaction under investigation was death complex/ITCH/FLIP.

Only one set of initial conditions is used in each of Sections 2.4.2 and 2.4.4. In Section 2.4.2 these initial conditions maximised the Δm_{21}, increase in DNA fragmentation due to the oxidative stress sensitive pathway. In Section 2.4.4, the increase in the value of Δm_{21} when $m_1(0)$ was increased from 20 to 30 was maximised. The initial conditions were chosen to highlight how the outputs of the model are qualitatively different when different interactions are switched on.

Typical results in the case when only the c-IAP/Bidj interactions are switched on can be found in Sections 2.4.2.1, 2.4.2.2 and 2.4.2.3. If c-IAP/Bidj and MAP2K/FLIP/ITCH interactions are both in play then the model is sensitive to ROS in a different way to when only the c-IAP/Bidj are in play. Observations for this case can be found in Section 2.4.2.4.

Generally, when the cross-talk between the anti-apoptotic pathway and the apoptotic pathway targets caspase-3, then the requirement that caspase-3 is to be reactivated results in a transient activation. A minimum concentration of extracellular signal acts to switch on the immune response but has little control over the value of Δm_{21}. In [60] it was discussed how the assumption that extracellular signal has a switch-like effect on the immune response of a cell can be used to build a model of an ensemble of cells. The MAP2K/FLIP/ITCH interaction acts to change the shape of this response, making the reactivation of the apoptosis pathway sharper.

The activation of the oxidative stress sensitive pathway by interactions A and B in Table 2.3.1 do not rely on inter-pathway cross-talk. It was chosen that the rate at which the phos-

phatases deactivate the MAPK pathway decreases as an exponential function with ROS, so that there is a clearly observable point at which there are no longer effective. The rate at which MAP2K* is released from Thioredoxin was taken to be a Hill function with respect to ROS (m_{32}). This sets a maximum rate of activation of MAP2K*, however the rate at which this maximum is reached does depend on ROS. This dependence is more observable for larger orders of magnitude of k_8.

The picture is further complicated when the MAP2K*/FLIP/ITCH interaction is also included. The MAP2K*/FLIP/ITCH interaction delays the second activation of the caspases. This delay increases with the maximum phosphatase deactivation rate k_{90} and decreases with the rate of increase of ROS due to intracellular oxidative stress k_{14}. k_8 determines the range of values of k_{FLIP}, the relative rate of FLIP production, for which the activity of ITCH can not inhibit FLIP inhibition.

The range of interactions acting on the MAPK pathway allow for a variety of possible steady state values of AP-1. The steady state value of AP-1 determines the rate at which Bidj and ITCH are produced, and so that rate at which DNA fragmentation m_{21} reaches its maximum value.

Alternatively, if the TRADD/FADD/FLIP/ITCH interactions the only pair of inhibitors switched on, then Section 2.4.4 suggests that the apoptosis pathway can remain activated for a long time. Its rate of activation being dependent on its sensitivity to ROS. However, the apoptotic and pro-apoptotic pathways are not continually activated as there activation depends on the availability of TRAF2 (m_2) and its initial concentration is chosen to be small. In this case, for a range of extracellular signal, the extent of apoptosis is a linear function of extracellular signal. The MAP2K/FLIP/ITCH interaction is not switched on so that the response is simpler than that in Section 2.4.2. As the increase in apoptosis is slow, then this version of the model may be a good starting point when adding on other cell signalling pathways, such as those for the fibrotic response.

The factors which determine Δm_{21} were found to be separate to those which determine the speed of activation of the oxidative stress sensitive pathway. The maximum possible value of Δm_{21} is determined by the initial conditions and rate constants of the apoptosis and anti-apoptosis pathways. The sensitivity of Δm_{21} to these initial conditions and rate constants was investigated in Sections 2.4.2.5 and 2.4.4.1. These results highlighted the observation that, when the c-IAP/Bidj interaction is switched on, the extent of DNA fragmentation is limited by the concentration of caspase-8 inside the cell. When the ITCH/FLIP/death complex interaction is switched on the extent of DNA fragmentation is mainly limited by the extracellular signal from outside the cell.

The work in this chapter demonstrates how known and accepted oxidative stress sensitive interactions can be used to construct a model. Though there is much discussion on the mechanisms involved in oxidative stress pathways, constructing a numerical model has not previously been attempted. This model is very speculative and serves as an initial attempt of this problem. Any final mathematical model for these complex interactions would require significant scientific collaboration. However, the initial response from the sponsors of this project at the

Health and Safety Laboratory (HSL), in Buxton, has been favourable.

The hypothesis suggested by this model is that the activation of the apoptotic pathway can be either transient or persistent. The activation is expected to be transient when the target of inhibition of the apoptosis pathway is activation caspase-3 and persistant when the target is the death complex, TRADD/FADD.

When the target of the inhibition of the apoptotic pathway by the anti-apoptotic pathway is activated caspase-3 (m_{20}), then the reactivation of caspase-3 after it is released is limited by the initial concentration of caspase-8 (m_{15}). The maximum possible value of Δm_{21} is found by maximising the peak concentration of activated caspase-3 captured by c-IAP (m_{23}) while leaving enough caspase-8 to reactivate the caspase-3 which is later released. The consequence of this limitation is that when the target of inhibition of the apoptotic pathway is activated caspase-3, the activation of the caspases can only be transient.

However, if the target of inhibition is TRADD/FADD (m_{14}) then no such balance is required. As long as there is a large enough initial concentration of both caspase-8 and caspase-3, the extracellular signal can continually activate the apoptotic pathway. It was found that the sensitivity of Δm_{21} to the extracellular signal was maximised when the concentration of the activated proteins was low but the activation persisted over a long period of time.

It will be of interest to see how if any of the results of the model reflect further experimental observations. For this to be possible, the relative concentration of intracellular proteins and the timing of the activation of the MAP kinases needs to be determined when a cell is under different levels of oxidative stress. It will also be useful to understand which proteins are most depleted over the course of response. This will indicate which pathways are most active over the course of oxidative stress and which pathways limit the activation of the apoptotic, anti-apoptotic and oxidative stress sensitive pathways.

Much experimental work has already been done to collect time series data on the concentration of a particular protein of interest within a single cell. For example, [41] reviews studies on the expression of genes which transcribe transcription factors such as NF-κB which are known to oscillate over time.

If the mechanisms by which the apoptotic, survival and oxidative stress sensitive signalling cascades are assumed to interact are found to be valid, then further work could be done to include the signalling pathway which activates the fibrotic response, as has been discussed in Section 2.5. A model linking the oxidative stress and fibrotic response will answer questions on what causes a fibrotic, apoptotic or necrotic response to dominate when a cell is under both mechanical and oxidative stress.

Part II

Pulmonary Toxicity of CNTs

Chapter 3

Review of the Pulmonary Toxicity of CNTs

Research on the toxicity of CNT on inhalation into the lungs has been spurred on by the fact that most of the unregulated exposure to CNTs will be regular inhalation of CNTs during their handling in the workplace. These nanoparticles will be unpurified and will not be designed for human contact. Metal oxides in cosmetics and sunscreens, on the other hand, will be tested for safety by the manufacturer before being brought to the market place. On the discovery that asbestos causes damage to the lung in a way unprecedented by superficially similar materials, research was done to build a new fibre toxicity paradigm to account for this. A fibre toxicity paradigm was constructed which highlighted the importance of a high surface area to mass ratio, a high aspect ratio and a chemical structure which is not quickly broken down by the body. These three factors are shared by CNTs, spurning on the research on their pulmonary toxicity.

The question of whether CNTs are toxic to lungs is complex. An important part of the work in constructing mathematical models on previously untackled topics is to clearly establish what is known and what is quantifiable. The literature review contained in this section presents a comprehensive introduction to the issues at hand as well as justification of the modelling approach taken.

Before any further discussion specific to CNTs is possible, some biological ground needs to be covered. The anatomy of the lungs is introduced in Section 3.1. The steps a macrophage must take to phagocytose a particle are outlined in Section 3.2. Key observations relating CNTs to pulmonary toxicity are summarised in Section 3.3. Visual evidence of the phagocytosis of fibres is given in a series of images in Section 3.4 along with discussion on the investigation of the phagocytosis of high aspect ratio particles. The rationale of how the length of a fibre can be toxic once it is deposited in the lung is summarised in Figure 3.1.

With this background knowledge in place, Section 3.5 introduces the mathematical constructs used in the mathematical models in Chapters 4 and 5. A constant mean curvature model is introduced in Section 3.5.1. This model takes into account volume and surface energies only. The Helfrich energy is introduced in Section 3.5.2 with additional details given

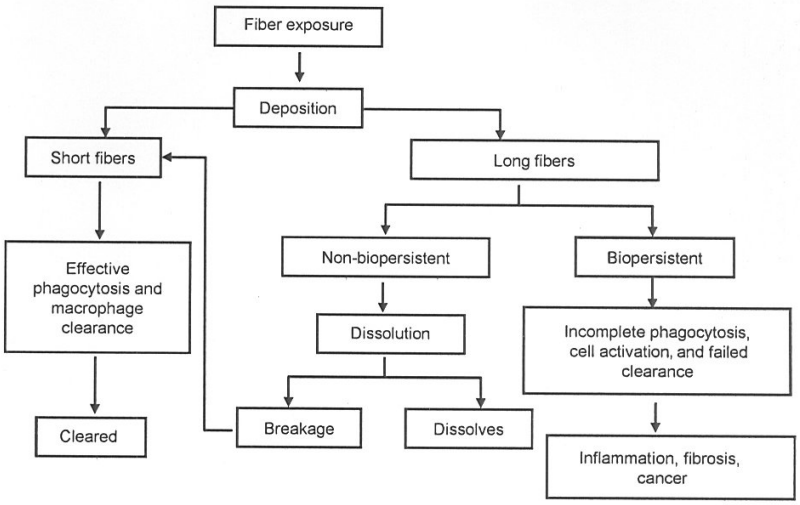

Figure 3.1: Paradigm for the role of long fibres and biopersistence relating to the toxicity of CNTs. Diagram taken from [28].

in Section 3.5.5. It has been used to measure the bending energy associated with a flexible membrane such as the lipid bilayer of a macrophage. Experimental justification for the use of the Helfrich energy is given in Section 3.5.3, while a justification using the theory of liquid crystals can be found in Section 3.5.4. The general conclusion to the phagocytosis models in Chapters 4 and 5 is found at the end of Chapter 5 in Section 6.8.

3.1 Introduction to the Anatomy of the Respiratory Zone

Figure 3.2 is a diagram of the anatomy of the lungs which is familiar to many. The surface of the lung is called the pleura which consists of a thin layer of cells called the mesothelial lining. The trachea is the airway joining the lungs to the throat which divides into the left and right main stem bronchae. Each of these bronchae continue to subdivide into bronchi and then smaller bronchioles. The respiratory bronchioles are the final generation of airways in the lung. The respiratory bronchioles are capped by alveolar ducts which themselves bud into alveolar sacs. Each of the alveolar ducts leads into 3-5 alveolar sacs. This structure can be summarised by Figure 3.3(a). The delicate nature of this region can be appreciated by studying a prepared cross-section of the respiratory zone as in Figure 3.3(b). Adjacent alveolar ducts and sacs form a complicated, interconnected network. The alveoli are the lung parenchyma where air exchange takes place. The alveolar septum divides one alveoli from another.

The alveolar sac walls are made up of a layer simple squamous epithelial cells called type I pneumocytes. Alveolar cell walls are approximately only one cell thick to allow for gas exchange. Type II pneumocytes bulge out from the cell wall and produce surfactant, a lipid rich liquid which reduces the surface energy inside the alveoli which prevents them from collapsing. Respiratory macrophages can also be found inside the alveoli. There are no cilia in the alveolar

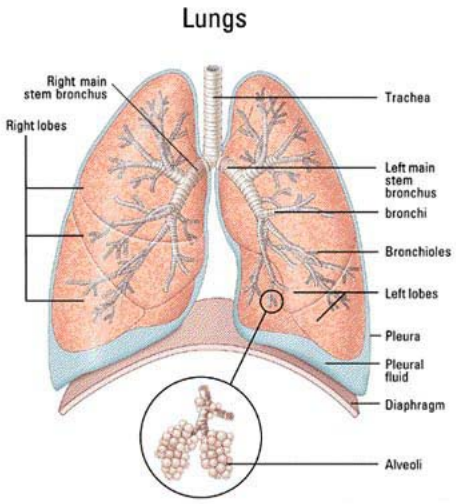

Figure 3.2: A traditional diagram of the anatomy of the lungs. Image publicly available.

regions so macrophages are the only mechanism available for the removal of debris.

The alveoli are encased by a network of capillaries. Between the lung epithelial and capillary endothelial cells is the f matrix (ECM). The molecules found in the ECM largely determine the mechanical properties of the respiratory zone. As is the case for the ECM in most of the body's tissues, the three major components of the ECM are collagen, elastin and the tissue fluid specific to the lung called the ground substance.

Collagen and elastin are key connective and load bearing molecules in the body. In the lung, they serve to support the weight of the lung as well as to support the structure of the lung as it cyclically stretches in normal or tidal breathing. Scanning electron micrographs (SEM) of the human lung can be found in [118]. The lung was treated so that all but the collagen network was washed away. Figure 3.4(a) is an electron micrograph of the remaining collagen network. The surface of the lung and the pleura (P) which surrounds the lung are clearly visible in micrographs A and B. Bundles of collagen fibres can be observed running approximately parallel to the alveolar entrances (AE) in micrograph D. These bundles are made up of individual collagen fibrils. The collagen fibres extend from one AE to another. Some also branch off into the alveolar septa. Figure 3.4(b) contains SEMs of collapsed and inflated lungs. In the collapsed lung the collagen fibres are wavy, while in the inflated lungs the collagen fibres at the alveolar entrances are straight. Most of the inextensibility of collagen is taken to be the result of straightening the wavy structure of the collagen fibres, while the material itself is fairly inextensible.

An established pathway to exposure of the organs to foreign material is the migration of particles trapped in the lung by passing through the pleura. As observed in [30], 'black spots' in the chest wall are commonly found in city dwellers, where exposure to soot particles has led to them passing out of the lungs and into the abdominal cavity.

Integrins are believed to serve as a mechanotransduction device which means that they

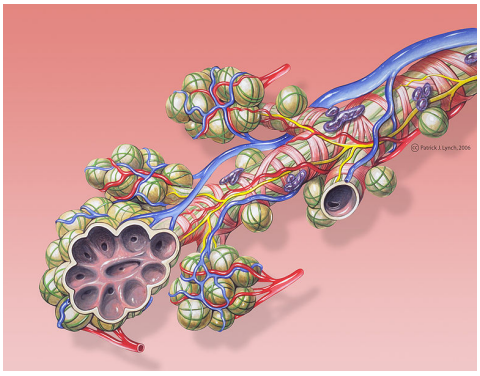

(a) Diagram of a respiratory bronchiole branching off into respiratory bronchioles which bud into alveolar ducts surrounded by alveolar sacs.

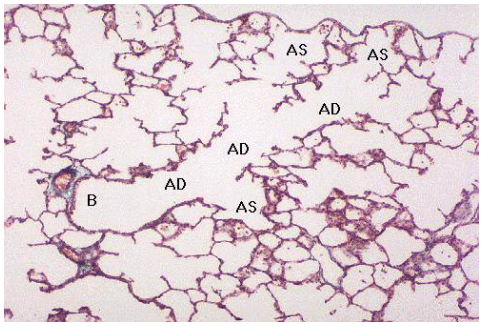

(b) A microscope slide of a slice of lung parenchyma. B - bronchiole. AD - alveolar duct. AS - alveolar sac.

Figure 3.3: Anatomy of the Parenchyma. Images publicly available.

can activate various cellular processes in response to mechanical stress. In [113] and [114] it is described how mechanical forces can induce direct secretion of various growth factors that accelerate the remodelling of the matrix. For example, the force-mediated release of transforming growth factor-beta (TGF-β) increases the upregulation of the procollagen gene which would then increase the production of collagen. The cells and ECM of the alveolar tissues live in a dynamic balance that results in a continuous remodelling of the matrix with a rapid synthesis of collagen in the normal lung of 10% of total collagen per day, 40% of which is immediately downgraded. Mechanical forces and the resulting chemical signals from the ECM are expected to play an important role in regulating such an environment.

Both the structure and functionality of the lung depend on the health of its most delicate parts which are routinely exposed to debris in the air. If the inner surfaces of the lung are not cleared effectively, damage will be done to the epithelium of the alveoli. Due to the dynamic environment of the lung, continual damage, mechanical stress and inflammation may trigger self-perpetuating fibrotic conditions. Though currently poorly understood [102, 115], these conditions leave the interior of the lung scarred and function impaired.

3.2 Introduction to Phagocytosis

All cells have some ability to phagocytose, or engulf, small particles. Phagocytes are those cell types which can ingest larger particles of 1μm or more in diameter. Two important groups of phagocytes are macrophages and neutrophils. Macrophages are all purpose clearers of debris, while neutrophils are more specialised in clearing microbial infection. Alveolar macrophages are the immune system's first line of defence on the lung's surface.

The four main phases of phagocytosis are attachment, ingestion, digestion and disposal. Firstly, macrophages must distinguish foreign substances or damaged cells from healthy cells.

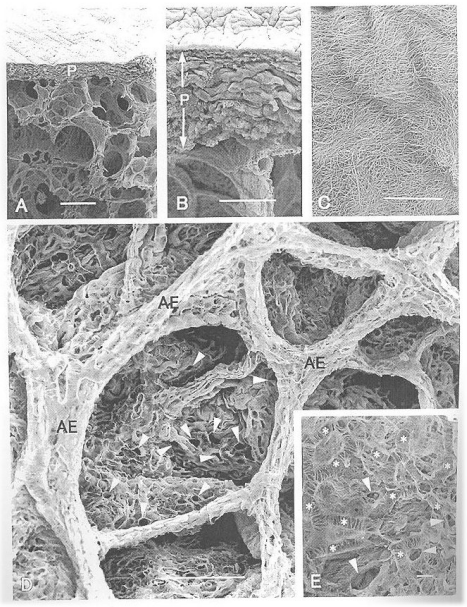

(a) A set of scanning electron micrographs of the collagen fibre network in a human lung. P - pleura. AE - alveolar entrances.

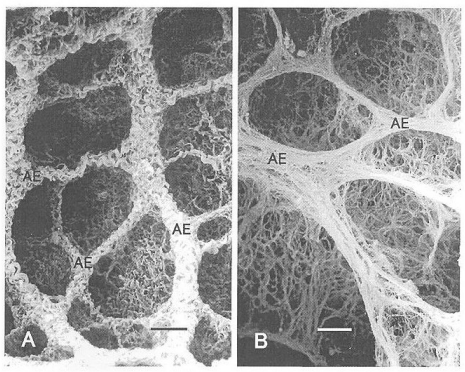

(b) Scanning electron micrographs of collagen fibre networks in a rat lung. Collagen fibres at the alveolar entrances (AE) in the collapsed lung (A) take zigzag or helical courses, while those in the inflated lung (B) are straight. Scale bar $= 100\mu m$.

Figure 3.4: Images taken from [118].

They have surface receptors which recognise structures specific to certain pathogens or damaged cells. They also carry receptors for opsonins, which are antibodies. They belong to a group of proteins found in blood called complement which tag, or opsonise, a pathogen to aid its removal.

Actin is a protein which polymerises to form rod-like structures or microfilaments which are mostly concentrated just underneath the cell membrane, giving the cell shape. Of the three types of cytoskeletal filaments, they are the most dynamic and most active in phagocytosis. After the particle's attachment to the macrophage the cell starts to physically engulf it. By polymerising and depolymerising actin forms protrusions in the cell membrane called pseudopodia which form a cup-like structure around the particle. An above average number of mitochondria provide the chemical energy for such work. The pseudopodia advance over the particle surface until it closes, forming a vesicle called a phagosome.

After the particle has been ingested, the macrophage will then attempt to break up the particle or digest it. Macrophages contain vesicles called lysosomes which are full of enzymes which break chemical bonds, known as hydrolytic enzymes. One of the effects of these enzymes is to increase the pH and create a toxic environment in the phagosome containing the particle. NADPH is an enzyme which reduces oxygen to produce the superoxide anion. The superox-

ide anion is very unstable and produces a cascade of secondary Reactive Oxidative Species (ROS). This mechanism of producing toxic oxygen metabolites is known as the respiratory burst. Lysosomes also contain enzymes which specifically target microbes and bacteria but are ineffective in breaking down CNTs.

Frustrated phagocytosis of fibres deposited on the surface of the lungs by alveolar macrophages has emerged as a key mechanism of toxicity. Macrophages are unable to engulf longer fibres which causes leakage of cytoplasmic enzymes and results in cell death. The natural consquence of damage to cells is the release of the toxic contents of the phagosomes which cause further damage to other cells. The ROS may contribute to the loss of epithelial integrity, allowing various surface proteins and possibly even macrophages and the fibres themselves inside the lung tissue. Even if frustrated phagocytosis does not kill the macrophages it does stimulate an inflammatory response and so the upregulation of cytokines such as TNF-α, which is linked with self-programmed cell death (apoptosis). The inflammatory response can also trigger fibrosis or the formation of scar tissue which damages the tiny and delicate airways of the lungs.

If the cell manages to die in a controlled way by apoptosis the acidic contents of the lysosome are not released. The macrophage can dispose of the indigested material by emptying it into the surrounding medium. It could also store the material within itself until it dies. Alveolar macrophages are often pushed out of the body with mucus from the lung. However, unsuccessful phagocytosis often leads to the acidic and toxic contents being released, causing damage to nearby tissue. The scarring caused by pH 4 acid is a common symptom of asbestosis, the chronic condition caused by prolonged exposure to asbestos.

Even if macrophages are successful in engulfing a fibre they have been shown to have difficulty moving and clearing the fibre out of the lung. Long fibres may interact with several macrophages, which may not then be able to act in concert. The inability of the macrophages to clear the lung surface might then trigger a granulomatous response where a collection of immune cells wall off the foreign substance. Like fibrosis, a granulomatous response will impede the function of the lung.

The information in this section can be found in many immunology textbooks such as [50].

3.3 Factors Relating to the Pulmonary Toxicity of CNTs

The question of whether CNTs are toxic on inhalation can be broken down into a series of more specific concerns. The pattern of deposition of inhaled CNTs in terms of lung anatomy needs to be understood. This may be different from the distribution of CNTs some time after exposure. The distribution of CNTs will depend on the degree of aggregation or agglomeration of them as they enter the lungs. The observed reaction of the lungs to exposure in terms of inflammation, fibrosis or granuloma formation can possibly be linked to the failure of alveolar macrophages to phagocytose the CNTs because of their size and shape. It could also be due to the triggering of particular proteins which form part of a cell's immune response.

Key papers such as [80] allowed the summary in [40] to state that the ability to enter the

lung interstitium from the airspaces is a fundamental property of nanoparticles.

CNTs do not hit any surface of the lung as single fibres [28]. They form loose aggregates in the air which can take the shape of tangled balls of fibres. They are also commonly found in the form of nanoropes, where they twist together to form a fibre with a larger diameter [57].

Findings from [67] and [107] show that on inhalation SWCNTs are deposited into the alveolar region of the lungs. In [67] and [107] it is also suggested how the SWCNTs are deposited depends on how well dispersed they are before inhalation. Samples of well dispersed nanotubes were quickly incorporated into the interstitium and the interstitial fluid. This was found to have the effect of increasing the thickness and collagen content of the alveolar wall. If the sample of SWCNTs were less well dispersed, the agglomerates deposited on the lung epithelium quickly formed granulomatous lesions. Granulomatous lesions are areas of especially fibrous material which serve to isolate potentially harmful contents of that area from nearby cells. In [67] is was reported that the inflammatory response to SWCNT is unusual. It is characterised by a brisk acute phase followed by the early onset of lung fibrosis.

The discussion in [30] put into context the conclusion of [92] that 2-6 weeks following inhalation, CNTs cause subpleural fibrosis. In contrast, carbon black, which is made of the same material as CNTs, was not found in the pleura. Many papers have tried to conclusively prove or disprove whether the pathogenic behaviour of a fibre is length dependent. In [87] this was attempted by counting the number of granulomas and morphonuclear leukocytes, which are a type of white blood cell after exposing the mesothelial lining of the body cavity to samples of predominantly short or predominantly long fibres by injection. The pathogenic response jumped significantly if long fibres were present in the sample.

The pleura are not a common site of damage, even for smokers and coal miners. The natural defences of the lungs, the cilia and macrophages, tend to move particles towards the throat and mouth. Asbestos is the only known material to cause mesothelial cancer and siginificant scarring of the pleura. Due to their irregular shape, it is now suggested [30] that fibrous particles get lodged inside the sensitive pleural tissue, rather than pass through it. Over time this will cause irritation and damage.

In [7] the toxicity of glass microfibres to alveolar macrophages was assessed. The glass microfibres were grouped into samples of five different lengths: 33, 17, 7, 4, and 3μm. The averaged fibre diameter ranged from 0.35 to 0.75μm for the shortest to the longest samples respectively. Lucigenin Chemiluminescence (LC) was measured as an index of cell viability. Also Lactate Dehydrogenase (LDH) release was measured. LDH is an enzyme released when a cell is under toxic stress. The results show that the fibres do negatively effect the viability of macrophages and induce a toxic stress response in a dose dependent manner. Also, the 17 and 33μm samples were significantly more toxic than the 7, 4, and 3 μm samples. The results indicated a cut-off length above which the glass fibre became sigificantly more toxic. The conclusions in [7] suggested that frustrated phagocytosis could be the cause of the length dependent toxicity. The results in [7] agree well with results referenced in [29] which show that marked increased in toxicity is expected when the fibre length is larger than 8-10μm.

In [31] the rate of phagocytosis of vitreous (a type of glass) fibres by either alveolar or

peritoneal macrophages was compared. A key difference between alveolar and peritoneal macrophages is their size. Alveolar macrophages were found to have an average diameter of 13μm, while peritoneal macrophages are slightly smaller with an average diameter of 11μm. Alveolar macrophages could only completely phagocytose fibres with an average length of 8μm, while the average length completely phagocytosed by peritoneal macrophages was only 7μm. The longest fibres completely phagocytosed by alveolar were 24μm and for peritoneal macrophages the longest fibres were 20μm.

In [7] and [29] fibres longer than 10μm were found to be markedly more toxic to alveolar macrophages, this being the average diameter of the macrophages measured in [31]. This suggests that macrophages cannot successfully phagocytose a fiber if they have to significantly extend their length.

The investigation in [129] used only two lengths for their samples of glass fibre: 7 and 17μm. Their work focused on the activity of the cyotkines TNF-α and NF-κB in response to the exposure of alveolar macrophages to the glass fibres. Though their activation was also dose-dependent, the activation of TNF-α and NF-κB was higher for longer fibres. In [129] it was hypothesised that each attempt to phagocytose a fibre is associated with the respiratory burst, discussed in Section 3.2, which releases ROS. The presence of longer fibres would result in repeated frustrated phagocytic events which would generate a larger concentration of ROS. NF-κB is known to be activated by high concentrations of ROS and to stimulate inflammatory cytokines such as TNF-α.

In the investigations [104] and [105], the toxicity of glass microfibres on alveolar macrophages was assessed using cell magnetometry. Due to their relatively high iron content cells can be magnetised and their magnetic field strength can be recorded. The magnetic field strength can again be recorded after a period of exposure to glass fibres. The time taken for the magnetic field to decay was taken to be a measure of the health of the cell's cytoskeleton. The polymerisation and depolymerisation of a healthy cytoskeleton can rapidly move the cell's iron oxide particles and the cell would demagnetise. A slow rate of decay of the magnetic field was linked to high activation of LDH, indicating that the cytokine response of the cell could well be caused by the physical damage done in its attempt to phagocytose a long fibre. The results clearly show how the glass fibres decreased the cell's viability in a dose dependent way.

The studies so far have focused on the consequences of a particle's size and geometry on its toxic effect. More specific biological interactions have also been suggested. It was found in [95] that, despite being a non-organic material, CNT did become coated with complement proteins which would attract phagocytic cells. This opsonisation of CNTs would make their phagocytosis easier. However, [51] suggests that increased opsonisation may also trigger an increased inflammatory response.

Fibroblasts are activated fibrocytes which, when activated, produce many of the components of the ECM such as collagens, elastic fibre and glycoproteins. Experimental work noted in the review of pulmonary toxicity and medical applications of carbon nanotubes [108] suggests that lung fibroblasts may be uniquely sensitive to SWCNTs and increase their rate of collagen production by 70%. In [117] the toxicity of SWCNTs in lung fibroblasts was compared

to the toxicity of active carbon, carbon black, MWCNT and carbon graphite. SWCNTs were found to be the most toxic of these groups. In particular, they were found to induce changes in cell shape and detach cells from their substrate before the cells underwent apoptosis/necrosis.

The study of toxicity of SWCNTs on human fibroblasts found in [117] suggests that the deformation of the cells exposed to SWCNTs, and the observed upregulation of various proteins related to the shape and structure of the cell, was not due a direct chemical interaction of the SWCNTs and the cell's signalling network. Instead a mechanism was suggested where a SWCNT close to the cell membrane caused disruption due to its hydrophobicity.

3.4 Geometry of the Phagocytosis of a Fibre

Several images of macrophages attempting to phagocytose fibres can be found in the literature. The shape of a macrophage is difficult to define due to the number of microvilli on its surface which can be appreciated in Figure 3.5(a). Pseudopodia are clearly visible in Figure 3.5(b). Figure 3.6(a) is a rare image of a macrophage internalising a fibre-like polystyrene particle. The surface is quite smooth as the microvilli have been recruited to engulf the particle. The macrophage itself has been significantly stretched.

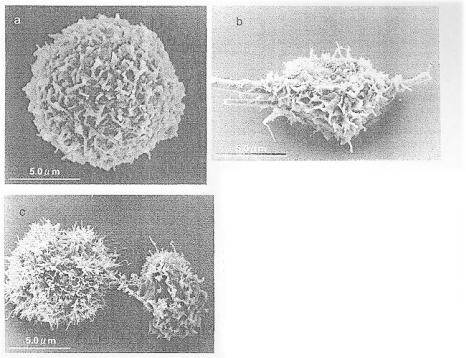

(a) Images taken from [105] of alveolar macrophages exposed to microglass fibres taken by a Scanning Electron Microscope (SEM). The microvilli on the surface of the macrophages are clearly visible.

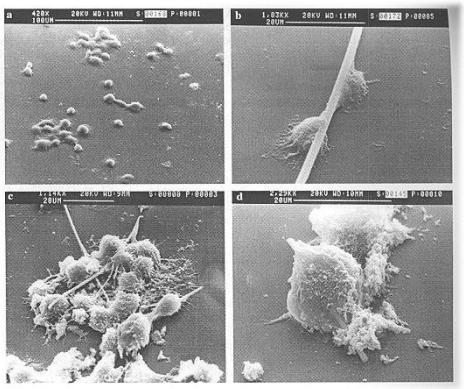

(b) Images taken from [78] of alveolar macrophages exposed to stonewool fibres, taken by a SEM. The microvilli on the surface of the macrophages are clearly visible. Images show how actin protrusions help the cells wrap around the fibre.

Figure 3.5: Images of alveolar macrophages.

In some images the microvilli are not so prominent. From Figures 3.6(b) and 3.7(a) it can be observed that macrophages which have fairly successfully engulfed a fibre are approximately axisymmetric with respect to the fibre. They also have a shape reminiscent of a constant mean curvature droplet shape. This suggests that the effect of macrophage shape is dominated by the cell membrane, while actin remodelling is more important in the energy intensive re-modelling process. In Figure 3.7(b) especially, the effect of increasing fibre length can be clearly seen.

A macrophage is able to engulf several of the smaller (7μm) fibres successfully. However, the shape of the macrophage does not change significantly from its original approximately spherical shape in its attempt to phagocytose the longer 17μm fibres. This image also suggests the importance of the role of the thickness of the fibres. The macrophages were able to bend some of the smaller fibres which may have made the phagocytosis easier. The longer fibres are also thicker and bend less easily, though there is some evidence of the macrophages attempting to bend the fibres. The close-up of the fibre surface in Figure 3.7(a) suggests that there is almost a zero contact angle between the cell membrane and the fibre.

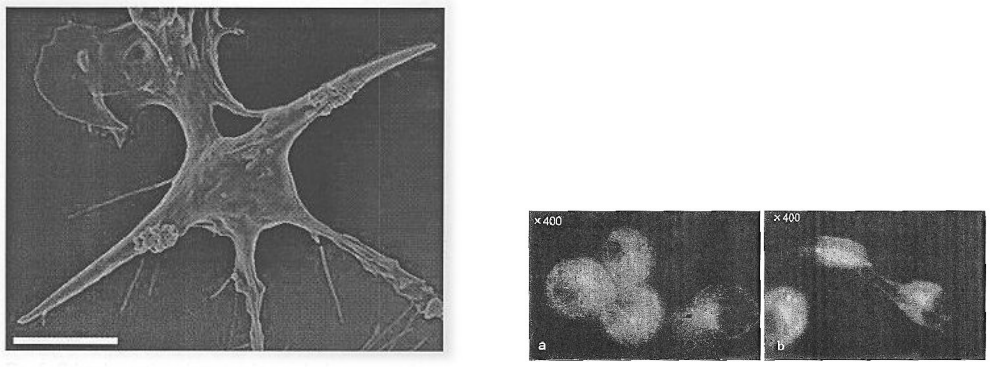

(a) A Scanning Electron Microscope (SEM) image taken from [15] of a macrophage internalising a long, thin particle. Scale bar=5μm.

(b) Immunofluorescent micrographs taken from [105] of alveolar macrophages exposed to microglass fibres.

Figure 3.6: Images of alveolar macrophages internalising high aspect ratio particles.

Detailed investigations on the role of size of particle on phagocytosis commonly limit themselves to spherical particles. However, [14] and [15] focus on the effect of shape on phagocytosis. The investigation in [14] used particles with six geometric shapes. One sample were prolate ellipsoids with a major axis of 2-6μm and an aspect ratio of 1.3-3. Another sample were elliptical disks with a major axis of 3-14μm and an aspect ratio of 1.3-3. The dimensions of these particles are fairly close to the definition of a fibre set by the World Health Organisation which was stated previously. A key finding in [14] was that the success of a macrophage internalising a particle was less dependent on its overall size then its shape at the point of first contact. Series A in Figure 3.9(b) illustrates the successful internalisation of an elliptical disk after an initial attachment by the macrophage at the disk's pointed end. Series B shows the result of an initial attachment along the flat part of the disk. The cell spread along the disk but there is no internalisation. This spreading is also illustrated in series B of Figure 3.9(a).

Actin polymerisation is the principal mechanism by which macrophages push the membrane leading edge to enclose the disk in a phagosome, as discussed in Section 3.2. Initially an actin cup is formed which then transforms into an actin ring which is then pushed along the particle in a uniform and organised way. When macrophages attached to particles along their pointed end, they exhibited an actin cup and ring, while macrophages attaching to the flat end did not.

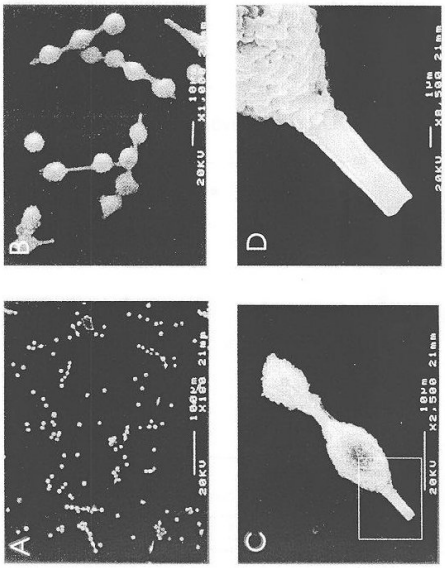

(a) Images taken from [7] of alveolar macrophages exposed to microglass fibres, taken by a SEM.

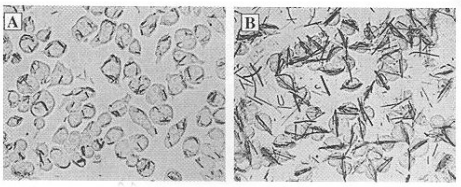

(b) Images taken from [129] of alveolar macrophages exposed to microglass fibres taken using light microscopy.

Figure 3.7: Images of alveolar macrophages exposed to microglass fibres.

It was suggested that as actin remodelling is a metabolically intensive process, phagocytosis is only successful when the actin ring is is only required to be gradual. The first third of the particle takes twice as much time to internalise as the second two thirds due to this remodelling. When an actin cup or ring does not form the macrophage spreads in an unsynchronised way and does not successfully engulf the particle. In [14] an angle Ω is defined which quantifies the difficulty of phagocytosis for a particle of approximately elliptical geometry as

$$\Omega = \langle \int_0^{\theta} \frac{ds}{d\theta} \kappa(\theta) d\theta \rangle_{0,\pi/2}, \tag{3.1}$$

where $\kappa(\theta)$ is the curvature and $ds/d\theta$ is the angular gradient of the arc length s. $\kappa(\theta)$ can be found using the standard curvature for an ellipse. $\theta = 0$ is defined as the point of contact. These parameters are illustrated in Figure 3.8. It was found experimentally that the rate of successful phagocytosis decreases sharply if Ω is greater than 45^0. The rates of successful phagocytosis increased as Ω decreased.

The purpose of [15] was to demonstrate a shape which was almost completely impossible to phagocytose. The result was a worm-like shape illustrated in series B of the images in Figure 3.9(a) which had approximately twice the diameter of the macropahges. No internalisations of the worm-like shapes were captured by time-lapse video microscopy. Successful internalisations of worm shapes were found to be about 6 times less likely than for spheres with the same volume of $3\mu m^3$. This figure increased to 20 when the volumes of the worm-like shapes and spheres was only $1\mu m^3$. The shape of the particle is even more important when the volume of the shape is smaller.

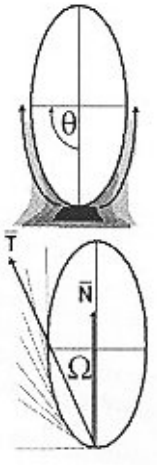

Figure 3.8: Illustration of parameters in (3.1) taken from [14].

Figure 3.6(a) is an image of a worm shape internalised by a macrophage. The cell shape is completely distorted and shows considerable tension along the cell membrane. The shape is not at all close to that of a constant mean curvature shape. The final image of successful internalisation of a spherical particle in series A of Figure 3.9(a) shows that, while the volume of the macrophage might have slightly increased it has retained its near spherical shape. Spherical particles are clearly easier to phagocytose than worm-shaped particles.

Note that despite their extremely elongated geometry all the fibres in series A of Figure 3.9(b) seem to have been engulfed by the macrophages. However, there is no evidence that all the fibres were actually successfully phagocytosed and a proper phagosome was formed. Note that the images of macrophages engulfing longer fibres, for example in Figure 3.7(b), resemble that of the unphagocytosed elliptical disk in series B of Figure 3.9(b). So, while the cells may have successfully engulfed the fibre, the fibre is not necessarily phagocytosised as a lysosome has not been formed.

Figure 3.10 is an image of asbestos fibres on the lung's surface which demonstrates the relative scale of the size of the fibres and the size of the components of the lung.

3.5 Mathematical Models of Phagocytosis

Available mathematical models on phagocytosis are limited. There have been some attempts to model the action of actin on both a molecular level and from a continuum mechanics perspective. The 'Polymerisation Rachet Model' quantifies the force exerted on the load, usually the cell membrane, using thermodynamic principles. In the 'Polymerisation Rachet Model' it is assumed that at some point the load will diffuse forward from the tip of the actin filament, creating a gap large enough for monomers to attach themselves to the actin tip, preventing backward diffusion. A good introduction can be found by reading the review [69] and an earlier paper which includes a comprehensive appendix [70]. A detailed model, using the principles of

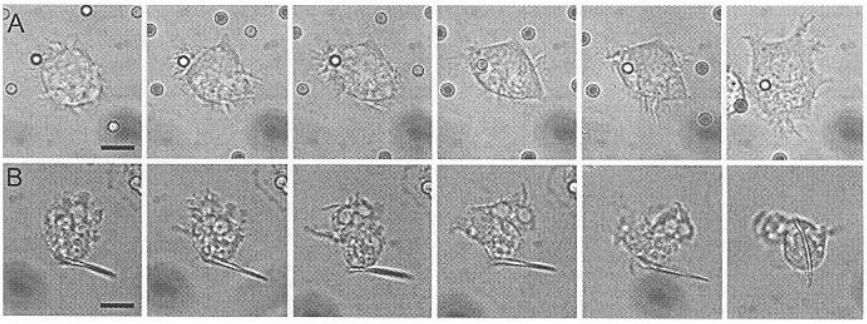

(a) Images taken from [15]. Time-lapse video microscopy clips at 0, 1, 2, 3, 4 and 32 min after initial attachment of alveolar macrophages to opsonised particles. Series A illustrates the phagocytosis of a spherical particle, while in series B the particle has a worm-like shape. Scale bar 5μm.

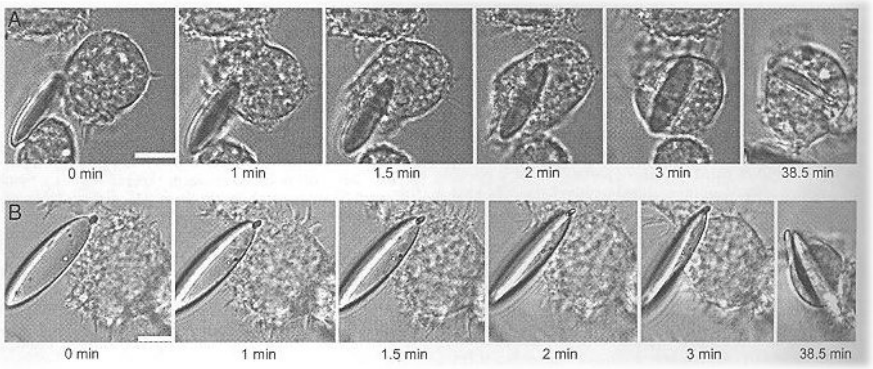

(b) Images taken from [14]. Time-lapse video microscopy clips spanning 39 mins. In series A the phagocytosis was successful, while in series B it was not. Scale bar 10μm.

Figure 3.9: Time-lapse video microscopy clips of the phagocytosis of particles with different geometries.

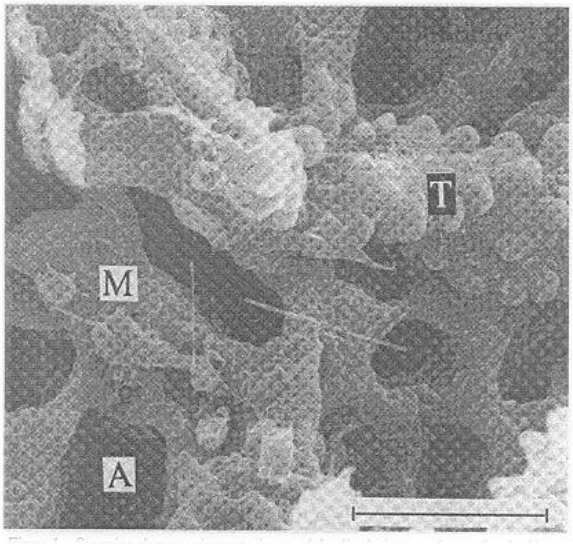

Figure 3.10: A SEM image taken from [29] of the airways of a rat that had been inhaling a cloud of asbestos fibres. The airways are shown on the smallest scale possible. A are openings into the alveoli and T is a portion of bronchial epithelium. Asbestos fibres can be seen free and partially phagocytosed (M).

continuum mechanics can be found in [45], where quantitive results specific to the phagocytosis of small spherical particles were also presented.

3.5.1 Constant Mean Curvature Curvature Model

These models of phagocytosis do not attempt to take into account the geometry of a particle and the macrophage as a complete cell. The geometry of a cell engulfing a fibre can be simplified to a surface of rotation, where the axis of rotation corresponds to the axis of the fibre it is engulfing. Chapter 4 presents an introductory model to this problem. In this model a cell is simply a rotationally symmetric drop of an incompressible, homogenous liquid with a constant surface tension.

The models of phagocytosis employed in this thesis aim to understand possible shapes a macrophage might adopt in order to engulf a long fibre with a small radius. It does not attempt to model phagocytosis as a dynamical process. It is the shape of a macrophage as it engulfs a fibre which is the aspect of phagocytosis most relevant to the question of the toxicity of CNTs on inhalation.

A droplet's shape is the result of an equilibrium between the forces associated with the surface tension, λ, and the pressure difference across its surface Δ_p is defined as

$$\Delta_p = \text{ external pressure } - \text{ internal pressure } . \tag{3.2}$$

Consider the molecules on the surface of the liquid. When inside a liquid a molecule feels equal forces in all directions but on the surface the attractive inter-molecular force is only felt from inside the liquid. The molecules are drawn inside the liquid by this surface tension,

causing the surface to bend to minimise the surface area and so the surface free energy. When a drop is at equilibrium the surface and pressure forces are balanced for a given volume.

The shape of a rotationally symmetric droplet with a given surface tension λ and pressure difference across the surface Δ_p can be found by solving the Laplace-Young equation which is

$$\frac{\Delta_p}{\lambda} = 2 \times \text{ mean curvature.} \tag{3.3}$$

The Laplace-Young equation is derived by minimsing the surface and volume energy of a drop. For a surface which is a solution of (3.3) there are two degrees of freedom which allow the choice of the angle between the droplet and fibre surface at two coordinates. The contact angle of the droplet surface with the surface of the fibre is fixed by the wettability of a particular solid by a particular liquid as determined by the solid-vapour, solid-liquid and liquid-vapour interfacial energies as derived in Apprendix C.2.

Droplets which form on thin fibres have been investigated experimentally. The problem of fluids forming drops around wires of much greater length than the droplet has long interested experimentalists. The work of Carroll in [12] introduced a model for an axisymmetric droplet on a fibre. Whether this model corresponded to observations of droplets forming on a fibre was subsequently investigated in [13, 64, 65]. It was found that for a rotational symmetric "barrel shaped" droplet, the droplet had to be of a minimum value as determined by the radius of the fibre. For smaller volumes, the droplet rolled up to form a "clam shaped" droplet which did not encircle the fibre. The study in [12] did not take into account the disjoining pressure, or the very short range pressure caused by the Van der Waal forces between the surface of the fibre and the droplet. Instead of focusing on the macroscopic description of the droplet shape, Brochard [10] investigated the role of this disjoining pressure in the spreading of a thin film along a cylinder.

The question answered in Chapter 4 is whether an axisymmetric droplet of a given surface tension and volume can engulf a cylinder of a certain length, L, and radius, ρ, as its volume is increased.

3.5.2 The Helfrich Energy

The constant curvature droplet model in Chapter 4 can be taken a step further by enclosing the droplet in a lipid bilayer. Lipid bilayers are the main component of a cell membrane. A single lipid molecule is composed of a hydrocarbon chain which is hydrophobic and a hydrophilic headgroup. A lipid bilayer is formed when two sheets of lipids are arranged so that their hydrophobic components are pointing inwards and their hydrophilic headgroups are left on the upper and lower surface. Figure 3.11 is a diagram of such a lipid bilayer. A cell membrane is soft and incredibly flexible and can conform to extreme curvatures.

In [44] Helfrich introduced the idea that a shape which a lipid bilayer adopts has a bending energy, the energy cost of bending a cell membrane into a specific shape. He suggested that this could be quantified by the Willmore energy. The Willmore energy is proportional to the mean curvature, H, squared integrated over the surface of a shape. The proportionality constant is

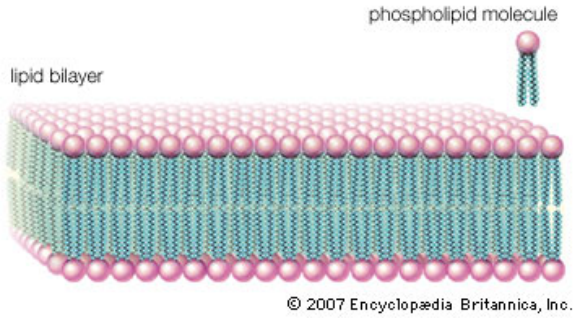

Figure 3.11: A diagram of a lipid bilayer.

k_c, the bending constant, which is a physical property of a particular lipid bilayer. Helfrich introduced a term called spontaneous curvature, c_0, to account for a cell's own ability to change its shape in response to stimuli which was incorporated into the form of the Willmore energy so that

$$\text{Helfrich Energy} = \int (1/2)k_c\,(H - c_0)^2\,dS = \int E_H dS. \tag{3.4}$$

The Helfrich energy is an often used measure to include bending energy for a variety of purposes. Its use in [54] demonstrates a more numerically intensive use of the Helfrich energy, while in [24], the results from its use are more analytically tractable. As the geometry of a surface of rotation is a simple three dimensional geometry which can be mapped to a two dimensional geometry, the results are analytically tractable, allowing for a more detailed discussion of the results.

The Laplace-Young equation of the constant mean curvature model (3.3) can be derived by minimising the surface and volume free energy, which can be written as

$$F = \int \Delta_p dV + \int \lambda dS. \tag{3.5}$$

The total free energy when including the Helfrich energy can now be written as the sum of Helfrich, volume and surface energies so that

$$F = \int (1/2)k_c\,(H - c_0)^2\,dS + \int \Delta_p dV + \int \lambda dS, \tag{3.6}$$

where the physical interpretation of the Lagrange parameters are that Δ_p is the osmotic pressure difference between the outer and inner media already defined in (3.2) and λ is the tensile stress.

It is proposed that as a macrophage phagocytoses a fibre, it has only a limited amount of available energy. The shape of its lipid membrane should be close to one that can be found by solving the Euler-Lagrange equations of the free energy (3.6). The role of actin is not taken into account. It could be assumed that actin is responsible in moving a lipid membrane from one configuration to another, but any stable configuration of a macrophage's membrane should be close to minimising the bending energy with minimal support from actin.

Rotationally symmetric shapes of closed fluid membranes which are solutions to the Euler-Lagrange equations of the free energy (3.6) were computed and discussed in [25]. In this thesis, they are referred to as solutions of the Helfrich boundary value problem. The boundary conditions for the Helfrich boundary value problem are constructed to avoid singularities in the Euler-Lagrange equations at the axis and maximum radius of the rotationally symmetric shape. There are no remaining degrees of freedom.

The solutions to the Helfrich boundary value problem have been used as a guide to find energetically stable shapes which do not have a continuous surface but sit on the surface of a fibre. As the minimum radius is no longer the axis of rotation, some of the parameters of the solution are now free to be chosen to reflect the physical problem at hand.

The 90^o contact angle reflects observations that a macrophage forms a blob around a fibre such as those in Figure 3.7(b). The 0^o contact angle reflects the observation that the macrophage may also spread itself along the fibre as demonstrated in Figure 3.7(a). For both of these contact angles it was investigated how a cell membrane may lengthen along the axis of the fibre, while maintaining a constant volume.

The boundary conditions in Section 6.6 were chosen to investigate how a cell may increase its length under the constraint of constant volume where the contact angle is not fixed. Alternatively, the boundary conditions in Section 6.7 were chosen so that the membrane is parallel to the surface of the fibre so that the contact angle is zero.

Experimental evidence of the validity of the Helfrich energy to find energetically stable membrane conformations is discussed in Section 3.5.3. A physical justification of the form of the Helfrich energy with reference to elastic continuum theory is found in Section 3.5.4. The role of Gaussian curvature with respect to edge effects is dealt with in Section 3.5.5.

3.5.3 Experimental Observations of Vesicles

The axisymmetric shapes found by minimising the Helfrich energy are used as a guide to help understand the various shapes and behaviours exhibited by living cell membranes. There has been some experimental work comparing the shapes and shape transitions of pure lipid bilayers to those predicted theoretically.

In [49] the behaviour of vesicles made of pure synthetic bilayers made out of dimyristoylphosphatidylcholine (DMPC) was observed. In Helfrich's theoretical paper [25] the minimum curvature energy shapes are parametrised by their surface area to volume ratios. The surface area to volume ratios of the vesicles in [49] were controlled by temperature variations.

The shapes predicted by the Helfrich energy were indeed observed. As the temperature was increased the surface area increased so the surface area to volume ratio was greater than that of a sphere. In this case, the condition in the theoretical paper [25] that the vesicle or cell is easily deformable is met. Two major transitions were observed in [49] on heating an approximately spherical vesicle. The vesicle could either become a prolate or oblate ellipsoid. On heating Figure 3.12 shows that a prolate ellipsoid can form a pear shape which then buds to form a secondary vesicle. The budding may never take place and instead the vesicle may alternate between a pear and dumbell shape as illustrated in Figure 3.13. As the surface area

of the vesicle increases the oblate ellipsoid will become a discocyte which is pinched in along its z-axis. Figure 3.14 illustrates how a discocyte transitions into a stomacyte on heating. A stomacyte is an approximately spherical vesicle with an internal vesicle. These sequence of the phase transitions qualitatively agree with [25]. As the normalised volume decreases, the axisymmetrical shapes found on minimising the Helfrich energy move down either the prolate or oblate branches. The prolate ellipsoids form pear shapes which may bud and the oblate ellipsoids form discocytes and possibly stomacytes for very low volumes. These shape transitions depend strongly on the spontaneous curvature c_0.

The emphasis in the papers [27] and [49] was to observe the minimum energy shapes as the surface area to volume ratio increased to its experimental limit. They provide interesting insights on how a cell might form an interior or exterior secondary vesicle as it becomes more deformable. However, this chapter is less concerned with these limit shapes and more concerned with how ellipsoidal vesicles alter to engulf a fibre.

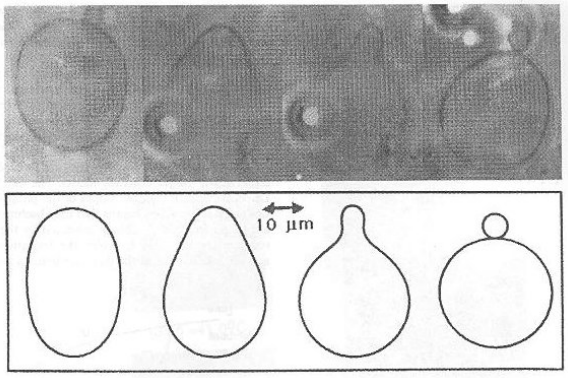

Figure 3.12: A prolate ellipsoid transforms into a pear shape which then buds to form an exterior secondary vesicle as the temperature is increased. The images are of synthetic DMPC vesicles in water taken from [49].

Assuming that a cell can be modelled as a pure lipid bilayer enclosing a homogeneous liquid requires some justification. Figure 3.15 is a cartoon of a cell membrane which highlights the three-layered structure of the cell membrane. The protein bilayer is sandwiched in between the cytoskeleton in the interior of the cell and the glycocalix which contains receptor and binding proteins. Some of the biological complexity of the cell membrane can be grasped by reading the review papers [66] and [93]. In [93] it was stated that the bending stiffness of a red blood cell membrane is roughly equal to that of a synthetic DMPC bilayer used in the experimental paper [49]. This is surprising as a cell membrane is much more complex then a pure DMPC bilayer as it also contains additional proteins, cholesterol and is coupled to the cell's cytoskeleton. In [93] Sackmann allows complex biological interactions which create bending moments along the lipid bilayer to be accounted for by spontaneous curvature. This includes the adsorption of proteins and a change in the surface charge density due a change in the ion concentration.

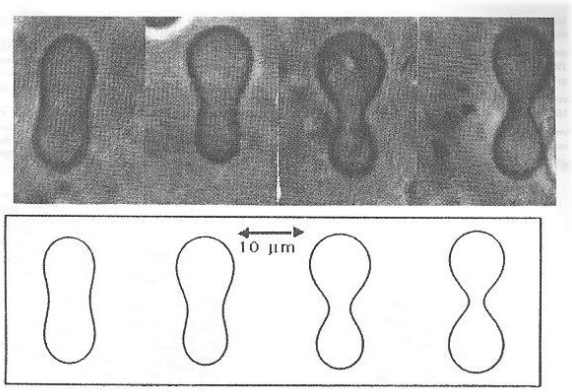

Figure 3.13: A prolate ellipsoid has become a dumbell shape with increased temperature. It then alternates between having a pear and dumbell shape. The images are of synthetic DMPC vesicles in water taken from [49].

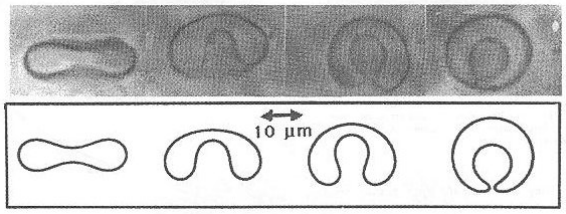

Figure 3.14: An oblate ellipsoid has become a discocyte with increased temperature which then curls round to form a stomacyte with an interior secondary vesicle as the temperature is further increased. The images are of synthetic (DMPC) vesicles in water taken from [49].

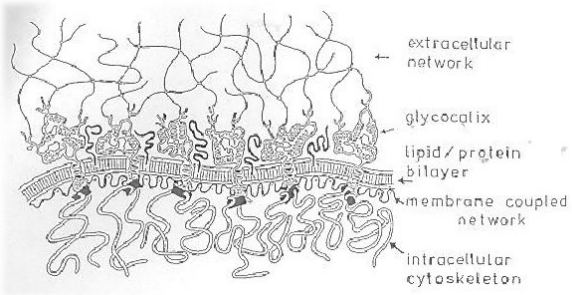

Figure 3.15: A cartoon of the three-layered structure of a cell membrane taken from [93].

3.5.4 Helfrich Energy vs. Shell Theory: a discussion of the physical justifiability of the Helfrich Energy

When drawing-up a model for a system in stationary equilibrium there are always two approaches: either the energy of a system can be defined or a force balance equation can be written down. The energy equation can be minimised using the Euler-Lagrange method which would then result in the implied force balance for a minimum energy equilibrium. Alternatively, the forces can be quantified and balanced which may then be integrated to find the associated energy. Ideally, a force balance equation and its associated energy equation would both be open to physical interpretation and not be a mathematical invention.

Over a decade ago, three attempts at using the Helfrich energy to find axisymmetric surfaces were separately developed and their mutual consistency was questioned in a series of papers, as summarised in [47]. In [130] the Helfrich energy was minimised for a general curvature and then mean and Gaussian curvatures specific to the geometry were later substituted in. In [99] the free energy in terms of Helfrich energy and Lagrange parameters was first written down in an axisymmetric geometry and minimised with respect to (wrt) arclength to find the shape equations. Lastly, [25] found these shape equations with respect to the radius as outlined in Section 5.2.

As can be appreciated from the discussion in Section 5.3, the terms of the Euler-Lagrange equation associated with the Helfrich energy are not easily interpreted as identifiable forces acting on an area element of the cell membrane. The shapes which result from the minimisation of the Helfrich energy match the range of shapes observed experimentally. This will be discussed in more detail in Section 3.5.3.

However, these shapes can also be obtained using shell theory whose starting point is the balance of forces, tension, moments and torques. The results possible using this alternative approach elicits the question of which approach is more physically justifiable. The physical justification of the Helfrich approach lies in the theory of liquid crystals. Liquid crystals are fluids whose molecules have a regular ordering. A lipid bilayer can be thought of as two layer of a smectic crystal whose molecules are aligned in one direction as illustrated in Figure 3.11.

Elastic continuum theory [21] ignores the molecular details of a liquid crystal but instead accounts for the ordering of a liquid crystal by considering three possible deformations. These deformations have been labelled twists, bends and splays. A splay refers to a deformation where a force is applied along the length of the molecule so that it acts as a cantilever. When molecules are twisted, they are deformed in the perpendicular direction. Bends are only possible for liquid crystals if they have multiple layers and are effectively three dimensional so they are irrelevant for lipid bilayers. If $\mathbf{n} = [n_x \; n_y]$, the direction a given molecule points, is written as a function of the two dimensional $x - y$ plane covered by the extent of the liquid crystal then the terms related to the the splay deformation are

$$\frac{\partial n_x}{\partial x} \qquad \text{and} \qquad \frac{\partial n_y}{\partial y} \tag{3.7}$$

and the twist terms are

$$-\frac{\partial n_y}{\partial x} \qquad \text{and} \qquad \frac{\partial n_x}{\partial y}, \tag{3.8}$$

as defined in [36]. In [36] Frank then postulates that the free energy can be written as linear and quadratic combinations of these terms which can then be integrated over the volume of the liquid crystal. As stated in [44] and [21], the deformation should be rotationally symmetric for x and y. This requirement allows only quadratic terms in the free energy. Additionally, in Helfrich [44] specifies that the rotation of the vector field $\mathbf{n}$ is zero or

$$\frac{\partial n_x}{\partial y} - \frac{\partial n_y}{\partial x} = 0, \tag{3.9}$$

so that there is no circulation in the vector field $\mathbf{n}$ as this vector field defines a surface. From the terms listed exhaustively in [36], the remaining terms are a quadratic splay energy

$$E_{splay} = \frac{1}{2}\left(\frac{\partial n_x}{\partial x} + \frac{\partial n_y}{\partial y}\right)^2 \tag{3.10}$$

and a saddle splay energy

$$E_{saddle\ splay} = \frac{1}{2}\left(\frac{\partial n_x}{\partial x}\frac{\partial n_y}{\partial y} - \frac{\partial n_x}{\partial y}\frac{\partial n_y}{\partial x}\right)^2. \tag{3.11}$$

As the principle curvatures in this simple parameter space are

$$c_x = \frac{\partial n_x}{\partial x} \qquad\qquad c_y = \frac{\partial n_y}{\partial y}. \tag{3.12}$$

The term (3.10) can be generalised to $E_{splay} = (1/2)(2H)^2$. $E_{saddle\ splay}$ measures the difference between the curvatures in two perpendicular directions and so can be linked to the Gaussian curvature. Like the Gaussian term to be discussed in Section 3.5.5, its related Euler-Lagrange equation is identically zero and it can only be considered for boundary conditions. In [44] Helfrich took the step of using this bending energy for large deformations, rather than for the close to planar case commonly used for liquid crystals. In conclusion, the Helfrich energy makes some attempt to account for the molecular structure of lipid membranes when used as a free energy term.

Shell theory assumes that a thin shell remains a simple, homogenous two-dimensional surface whose third dimension is infinitesimally small. The governing shape equations are derived by first considering the balance of tensions, torques and momenta on an area element over which there is a pressure difference. These shape equations involve the principal curvatures and are derived for the general and axisymmetric case in [71]. In [8] and [88] standard shell theory was applied to model axisymmetric cell membranes. A particular strain energy function was chosen which implied that the tensions are isotropic. Also it was taken that bending moments acting on the cell membrane can be generalised to

$$m = E_B\left(H - H^R\right)\mathbf{P}, \tag{3.13}$$

where H is the mean curvature and H^R is the resting mean curvature. Here E_B is the scalar bending modulus, quantifying a membrane's resistence to bending, and $\mathbf{P}$ is the elasticity tangential projection operator. The term (3.13) defines a material which has a curvature elasticity and is capable of "remembering" its original curvature, like an elastic band "remembers" its original length. The term (3.13) is a moment which the cell membrane is expected to exert on itself to return to its resting shape. However, a cell membrane is very soft and any tautness is due to the pressure difference across it. However, in order for the cell to be deformable the pressure inside the cell must be decreased.

An alternative isotropic bending moment was used in [34], given here as

$$m = E_B H, \tag{3.14}$$

so that the bending moments are simply proportional to the mean curvature.

The traditional applications of thin shell theory are found in civil and mechanical engineering. The cell membrane model set out in [8] and [88] is similar to that of the buckling of a axisymmetric shape. The scale of a dome used in a building make the assumptions of shell theory justifiable. It is suitable to model such a dome homogenous across its thickness. However, it might be expected that a small-scaled object such as a vesicle might be more sensitive to the ordering of the molecular scale. There is some need to test the assumptions used in applying thin shell theory to cell membranes more thoroughly.

Without a physically justifiable energy function associated with the shape equations derived from shell theory the question of which shape is most stable for a given volume to surface area ratio cannot be answered. On the other hand the are results, such as the ones in [27], which do suggest that the observed transformations of simple lipid vesicles can be mapped onto phase diagrams derived using the Helfrich energy.

3.5.5 Gaussian Constant of Rigidity

A complete quadratic expansion of the free energy in terms of the principal curvatures would include the Gaussian curvature as well as the mean curvature. The mean curvature is defined in (4.6) as

$$H = k_{min} + k_{max}, \tag{3.15}$$

where k_{min} and k_{max} are the principal curvatures. In the same notation, the Gaussian curvature is

$$G = k_{min} k_{max}. \tag{3.16}$$

The Helfrich energy defined in(3.4) can then be extended so that

$$E_H = (1/2) k_c H^2 + \bar{k}_c K, \tag{3.17}$$

where k_c is the bending constant and $\bar{k}_c$ is the Gaussian curvature constant of rigidity. The terms proportional to $\bar{k}_c$ are associated with the liquid crystal saddle-splay term in (3.11) and arise from the resistance of a thin film to bending in two orthogonal directions at the same time.

Lipid bilayers are usually modelled as two-dimensional liquids. As liquids cannot experience shear forces there is a physical justification for their omission in Chapter 5 where they are not considered.

Even if terms proportional to $\bar{k}_c$ were included in the variational problem (5.4) the resulting terms would cancel each other out leaving the Euler-Lagrange equations unchanged. This was mentioned when Helfrich introduced the Helfrich energy in [44] and can be verified for the axisymmetrical case presented in [25].

The Gauss-Bonnet theorem tells us that the integration of Gaussian curvature over a surface reduces to the integration of the geodesic curvature over the boundary of the surface only so $\bar{k}_c$ appears only in boundary conditions. Details of the Gauss-Bonnet theorem can be found in [81]. In the review of cell membrane models [98], the Gaussian term is neglected as it is constant for shapes of the same topology. Very broadly speaking, shapes with the same number of holes share the same topology. All cell on a fibre boundary value problem solutions will share the same topology.

Some numerical work on modelling lipid membranes of different geometries, [79] and [119], reveals that the Gaussian curvature constant primarily effects the leaf-like curling of the membrane at the open edges. The changes in shape when the Gaussian curvature constant was non-zero is localised to the edges. If the interest is in the overall shape of the membrane there is some justification to take the Gaussian constant to be zero.

3.6 Chapter Summary

In this chapter is was established that frustrated phagocytosis of inhaled particles is a mechanism by which nanoparticles, and CNTs in particular, can be toxic. It was found that phagocytosis is more likely to be frustrated when the particles have a larger aspect ratio while having a smaller volume. As CNTs can be described as fibrous while having a small volume, the problem of frustrated phagocytosis is even more relevant to this particular type of nanoparticle. It was found that successful phagocytosis of a particle of high aspect ratio was more likely when the contact angle between the cell membrane of the macrophage and the particle was small. In the review of available mathematical models of phagocytosis, it was found that they were more concerned about the dynamics of phagocytosis at a molecular, rather than a cellular scale. In order to quantify the feasibility of the phagocytosis of a fibre, it was proposed that the geometry of a cell engulfing a fibre is simplified to that where the cell membrane of the macrophage is an axisymmetric surface of rotation where the axis of rotation corresponds to the axis of the fibre. The free energy of this system is the linear sum of the surface and volume free energies, with the possible inclusion of the Helfrich energy which takes into account the energy required to bend a lipid bilayer. The shape of this surface in the case of successful phagocytosis is the solution of this energy minimisation problem. In Chapter 4 the free energy is the sum of the surface and volume free energies only, while in Chapters 5 and 6 the energy minimisation problem is extended to include the Helfrich energy.

Chapter 4

Constant Curvature Droplet Model

4.1 Chapter Summary

Following on from the discussion in Section 3.5.1, this chapter presents an introductory model of a cell engulfing a fibre. The question to be answered is whether an axisymmetric droplet of a given volume and constant mean curvature can engulf a cylinder of a certain length, L, and radius, R, as its volume is increased. The longitudinal profile of the droplet can be found in Figure 4.1(a). The increase in volume can be thought of as being due to condensation where the mass of the droplet slowly increases while the density remains constant. The increase in volume is incremental so that the drop is always at an energetically stable state. It will be discussed in Section 4.6 how the shape of the droplets change as volume is increased. A range of examples of droplet profiles can be found in Figure 4.3.

The basis of the model is the Laplace-Young equation which is

$$\frac{\Delta_p}{\lambda} = 2 \times \text{ mean curvature.} \tag{4.1}$$

This equation relates the physical properties of surface tension, λ, and pressure difference across a droplet surface, Δ_p, to a geometrical property of the shape called the mean curvature. The mean curvature for a surface of revolution is re-derived in Section 4.2. The forces and free energy terms associated with the mean curvature are discussed and expanded on in Section 4.4. The boundary conditions originally given in [12] are presented in Section 4.5.1 and the surface area (S), volume (V) and length (Z) of a drop with these boundary conditions are given in Section 4.5.2. The ODE used to find the profile of the axisymmetric drop is re-derived in Sections 4.5.3 and 4.5.4.

Constant mean curvature droplets are a classical feature of physics. They have been included in this thesis as a limiting case of the Helfrich energy minimisation problem when the bending constant, $k_c = 0$, so that no energy is required to bend the lipid bilayer of the engulfing cell. This chapter serves as an introduction to Chapters 5 and 6. The limited range of solutions in this chapter can be compared to the more varied range of solutions in Chapter 6.

The content in the following sections is original material developed from this problem. Section 4.6 introduces the boundary conditions required to solve the problem of a drop engulfing a fibre of finite length. Sections 4.7-4.9 investigate these solutions so that the engulfment problem can be solved numerically in Section 4.11. Section 4.7 looks at constant mean curvature solutions in general while Section 4.8 looks at the expected solutions in the limit that the radius of the fibre is asymptotically small. It is found that the range of possible solutions could be categorised. In Section 4.9 these groups are parametrised with respect to n and $\cos\theta$, the normalised maximum radius of the droplet and the cosine of the contact angle of the droplet with the fibre. The boundary problem set up in Section 4.5.1 is solved in Section 4.11. The results are interpreted using the knowledge gained from the preceeding sections.

4.2 Mean curvature of an Axisymmetric Drop

This section breifly introduces the concept of mean curvature, H, by first defining the shape operator following [81] and [83]. Firstly, a surface must be defined. A coordinate patch

$\boldsymbol{x} : D \rightarrow \boldsymbol{R^3}$ maps an open set D of $\boldsymbol{R^2}$ onto $\boldsymbol{R^3}$. This mapping is required to be continuous and one-to-one. For a patch to be a proper patch its inverse function is also required to be one-to-one. Roughly speaking, a surface in $\boldsymbol{R^3}$ can be defined as a subset, $\boldsymbol{M}$, of $\boldsymbol{R^3}$ for which a proper patch exists for every small region of $\boldsymbol{M}$. Let a curve be in infinitely differentiable map $\alpha : I \rightarrow \boldsymbol{R^3}$ of on open interval $I = (a, b)$ of real line $\boldsymbol{R}$ into $\boldsymbol{R^3}$, parameterised by its arclength t.

An infinite number of curves cross a point $\boldsymbol{p}$ on this surface. The curvature of each curve $\boldsymbol{\alpha}(t)$ at $\boldsymbol{p}$ is the scalar value

$$k(\dot{\boldsymbol{\alpha}}) = \boldsymbol{U} \cdot \ddot{\boldsymbol{\alpha}}, \tag{4.2}$$

where $\boldsymbol{U}(\boldsymbol{p})$ is the noral to the surface and $\dot{}$ denotes differentiation wrt arclength t. As the tangent and the normal are perpendicular to eachother we have

$$\dot{\boldsymbol{\alpha}} \cdot \boldsymbol{U} = 0, \tag{4.3}$$

which can be differentiated to give

$$\boldsymbol{U} \cdot \ddot{\boldsymbol{\alpha}} = -\dot{\boldsymbol{U}} \cdot \dot{\boldsymbol{\alpha}} = \boldsymbol{S}(\dot{\boldsymbol{\alpha}}) \cdot \dot{\boldsymbol{\alpha}}. \tag{4.4}$$

This expression introduces the shape operator $\boldsymbol{S}(\dot{\boldsymbol{\alpha}})$, as defined in [81] and [83].

It can be found that the shape operator will have principal directions at any point $\boldsymbol{p}$ which are orthogonal eigenvectors $\boldsymbol{e}_1$ and $\boldsymbol{e}_2$ of the shape operator

$$\boldsymbol{S}(\boldsymbol{e}_1) = k_{max}\boldsymbol{e}_1 \quad \text{and} \quad \boldsymbol{S}(\boldsymbol{e}_2) = k_{min}\boldsymbol{e}_2. \tag{4.5}$$

The eigenvalues have been labelled k_{min} and k_{max} as it can be shown that the eigenvalues of the shape operator are the extremal values of curvature at that point. The mean curvature is defined as

$$H = \frac{k_{min} + k_{max}}{2}. \tag{4.6}$$

4.3 Mean Curvature of an Axisymmetric Surface of Revolution

An axisymmetric drop is a surface of revolution around an axis of rotation, which we take to be the z axis in Figure 4.1(a). It is best parametrised in cylindrical coordinates where coordinate x and angle ω are defined in Figures 4.1(a) and 4.1(b). There general form of location of each point on the surface of the droplet is therefore

$$\boldsymbol{x}(\omega, x) = (x\cos\omega, x\sin\omega, z(x)). \tag{4.7}$$

This surface is an example of a two-dimensional space mapped onto a three-dimensional space.

As illustrated in Figure 4.1(c), the function $z(x)$ can be expressed in terms of $\phi(x)$, the angle between the normal at $\boldsymbol{x}(\omega, x)$ and the cylinder axis. The following differential relations

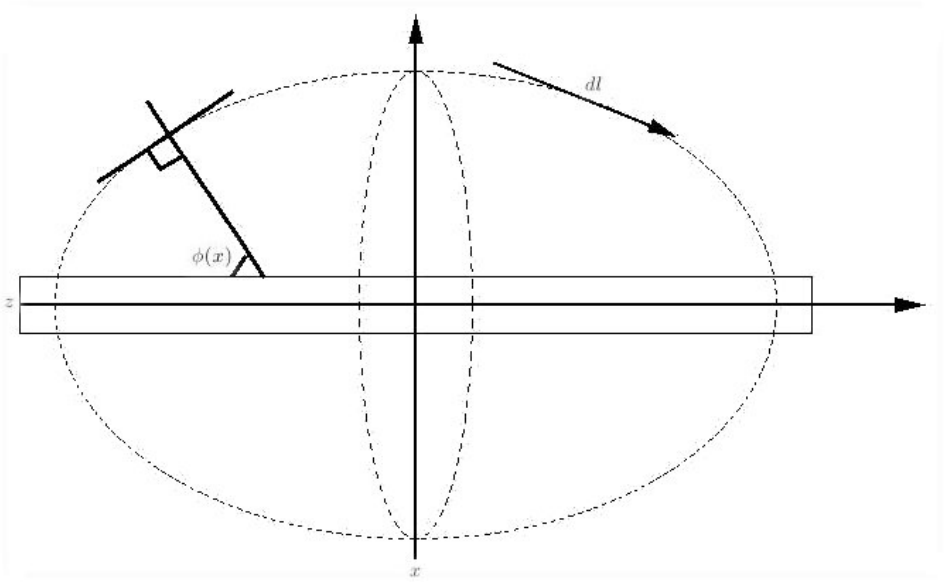

(a) Diagram of the longitudinal cross-section of axisymmetric droplet on which the coordinates x and z, an element of arclength dl and $\phi(x)$ are indicated.

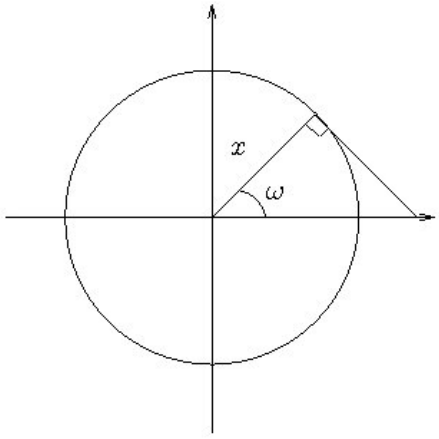

(b) Diagram of coordinates perpendicular to the axis of rotation, parametrised by x and ω.

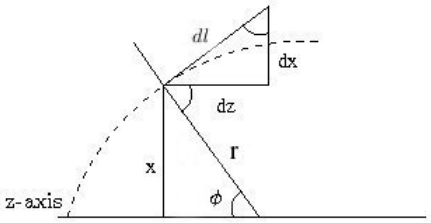

(c) Diagram of $\phi(x)$ and the r, the normal of the surface $z(x)$ (dotted line) and the z and x components of the arclength dl.

Figure 4.1: Diagrams of contact angle θ at the solid/liquid/air boundary point. Illustrated for $\theta < \pi/2$.

can be written down

$$dx = \cos\phi(x)dl, \tag{4.8}$$

$$dz = \sin\phi(x)dl, \tag{4.9}$$

$$\frac{dz(x)}{dx} = \tan\phi(x). \tag{4.10}$$

Equation (4.10) can be used to find a pair of tangent vectors by differentiating along the ω- and x- parameter curves. These tangent vectors are

$$\begin{aligned} \boldsymbol{x}_\omega &= (-x\sin\omega, x\cos\omega, 0)\,, \\ \boldsymbol{x}_x &= (\cos\omega, \sin\omega, \tan\phi)\,. \end{aligned} \tag{4.11}$$

It can be verified that $\boldsymbol{x}_\omega \cdot \boldsymbol{x}_x = 0$. These two tangent vectors are perpendicular to each other. It can be shown that these are the tangent vectors along the principal directions for a axisymmetric surface of revolution. In order to find the principal curvatures the second derivatives and normal vector field must also be found. The second derivatives are

$$\boldsymbol{x}_{\omega\omega} = (-x\cos\omega, -x\sin\omega, 0)\,, \tag{4.12}$$

$$\boldsymbol{x}_{xx} = \left(0, 0, \cos\omega^{-2}\phi(x)\frac{d\phi(x)}{dx}\right). \tag{4.13}$$

The outward-pointing normal vector field can be found to be

$$\boldsymbol{U} = \frac{\boldsymbol{x}_\omega \times \boldsymbol{x}_x}{|\boldsymbol{x}_\omega \times \boldsymbol{x}_x|} = (-\sin\phi(x)\cos\omega, -\sin\phi(x)\sin\omega, \cos\phi(x))\,. \tag{4.14}$$

From (4.2) and (4.4) the principal curvatures can be found to be

$$k_{max} = \frac{\boldsymbol{S}(\boldsymbol{x}_\omega)\cdot\boldsymbol{x}_\omega}{\boldsymbol{x}_\omega\cdot\boldsymbol{x}_\omega} = \frac{\boldsymbol{U}\cdot\boldsymbol{x}_{\omega\omega}}{\boldsymbol{x}_\omega\cdot\boldsymbol{x}_\omega} = \cos\phi\frac{d\phi}{dx}, \tag{4.15}$$

and

$$k_{min} = \frac{\boldsymbol{U}\cdot\boldsymbol{x}_{xx}}{\boldsymbol{x}_x\cdot\boldsymbol{x}_x} = \frac{\sin\phi}{x}. \tag{4.16}$$

Looking at the shape of a droplet whose length is much longer than its maximum radius, it would be expected that the principal direction of the maximum curvature (smallest radius of curvature) is given by the tangent perpendicular to the length of the cylinder. The direction of the minimum curvature (largest radius of curvature) is then parallel to the axis of rotation. In notation found in [44], which will be used from now on, the principal curvatures for an axisymmetric surface of rotation are

$$c_p = \frac{\sin\phi}{x}, \tag{4.17}$$

$$c_m = \cos\phi\frac{d\phi}{dx}. \tag{4.18}$$

The principal directions of curvature for c_m are the meridians and those for c_p are the parallels.

c_p is defined by parameters found in Figure 4.1(c). Substituting in (4.8) it is found that

$$c_m = \frac{d\phi}{dl}, \tag{4.19}$$

so that c_m expresses the rate of change of ϕ with arclength.

4.4 Forces and the Energy for Droplet Model

The Laplace-Young equation in (4.1) can now be given in the form found in Carroll's work [12], namely,

$$\frac{\Delta_p}{\lambda} = c_m + c_p, \tag{4.20}$$

where λ is the surface tension, or interfacial energy, and Δ_p is the pressure difference across the surface. For a liquid drop to be at an equilibrium the Laplace-Young pressure must be constant. A simple derivation which clarifies the relationship between these physical and geometrical properties can be found in Appendix C.1. The radii of curvature in this derivation do not relate to those of an axisymmetric drop. It is the Laplace pressure which causes smaller droplets with smaller radii of curvature to coalesce to form larger droplets with a larger radii of curvature.

In [12], (4.20) is integrated to find the surface forces

$$\begin{aligned}
\frac{\Delta_p}{\lambda} &= \frac{\sin\phi(x)}{x} + \cos\phi(x)\frac{d\phi}{dx} && (4.21)\\
&= \frac{1}{x}\frac{d}{dx}\left(x\sin\phi\right), && (4.22)\\
\lambda K &= \lambda x\sin\phi - (1/2)\Delta_p x^2, && (4.23)\\
& && (4.24)
\end{aligned}$$

where K is a constant of integration. The forces in (4.23) can be labelled as

$$\begin{aligned}
f_1 &= \lambda x\sin\phi, && (4.25)\\
f_2 &= -(1/2)\Delta_p x^2, && (4.26)\\
f_3 &= \lambda K, && (4.27)
\end{aligned}$$

so that $f_3 = f_1 + f_2$. Equation (4.23) can be re-arranged to give an expression for c_p which has two independent parameters, K and $\Delta_p/2\lambda$,

$$c_p(x) = \frac{\Delta_p}{2\lambda} + \frac{K}{x^2}. \tag{4.28}$$

From the form of c_p and c_m in (4.17)-(4.18), the following relation can be drawn

$$\frac{dc_p}{dx} = \frac{c_m - c_p}{x}. \tag{4.29}$$

The known term for c_p in (4.28) can be substituted into (4.29) to find an expression for c_m in terms of the parameters K and $\Delta_p/2\lambda$,

$$c_m(x) = \frac{\Delta_p}{2\lambda} - \frac{K}{x^2}. \tag{4.30}$$

Note that if $K = 0$ then (4.28)-(4.30) are constants and so are each the radius of the resulting sphere.

The dimensions of the surface tension and pressure difference infer the dimensions of K so that

$$\Delta_p = \frac{[\text{Energy}]}{[\text{L}^3]}, \tag{4.31}$$

$$\lambda = \frac{[\text{Energy}]}{[\text{L}^2]}, \tag{4.32}$$

$$K = [\text{L}]. \tag{4.33}$$

It can be checked that the forces (4.25)-(4.27) have the dimension of [Energy]/[L]. f_2 can be recognised as the pressure force and f_1 can be recognised as the capillary force integrated over the surface of the drop. Finally, f_3 is net force over the drop surface. By solving (4.28) and (4.30) it is found that

$$K = (1/2)x^2(c_p - c_m). \tag{4.34}$$

So as $x \to \infty$ then $c_p - c_m \to 0$, where $c_p = c_m$ is the condition for a sphere.

The force conservation equation (4.23) can also be obtained through the minimisation of the surface and volume energy and the energy associated with the force (4.27). Here λ and Δ_p act as surface area and volume Lagrange multipliers. By their dimensions given in (4.31) and (4.32) together with the integrals for surface and volume (4.43) and (4.44), the surface and volume energy is given by

$$\int \lambda ds - \int \Delta_p dV = \int \left\{ \lambda 2\pi \frac{x}{\cos\phi(x)} - \Delta_p \pi x^2 \tan\phi(x) \right\} dx. \tag{4.35}$$

The energy term associated with f_3, defined in (4.27), is

$$-2\pi\lambda K \int \tan\phi(x) dx = -2\pi\lambda K \int dz. \tag{4.36}$$

This term associates an energy cost to an increase in length. The complete free energy term is then

$$F = \int \left\{ \lambda 2\pi \frac{x}{\cos\phi(x)} - \Delta_p \pi x^2 \tan\phi(x) - 2\pi\lambda K \tan\phi(x) \right\} dx. \tag{4.37}$$

Minimising the energy terms in (4.37) would then result in (4.23). The negative sign preceeding the Δ_p term ensures that the signs in (4.37) and (4.23) are the same. A larger value of K would decrease the length of the droplet. As the length would be expected to be small if generally $c_p > c_m$ and larger if $c_m > c_p$ this assumption is consistent with the definition of K in (4.34).

The obvious physical interpretation of the energy term (4.36) is the free energy associated with the solid/liquid interfacial tension, γ_{SL}, and the solid/vapour interfacial tension, γ_{SV}, as defined in Appendix C.2. Such an energy term is expected to take the following form

$$\int 2\pi R \left(\gamma_{SL} - \gamma_{SV}\right) dz. \tag{4.38}$$

Thus K can be given the physical interpretation of the radius of the fibre, R, multiplied by a ratio so that

$$K = -R \left(\frac{\gamma_{SL} - \gamma_{SV}}{\lambda} \right). \tag{4.39}$$

4.5 Boundary Conditions and Parametrisation for a Droplet on a Fibre

4.5.1 Boundary Conditions for a Droplet on a Fibre

The relations (4.28) and (4.30) have two independent parameters which allow $c_p(x)$ and $c_m(x)$ to be fixed at two points. The first point can be chosen to be at the maximum radius of the droplet. ϕ is chosen to make the solution symmetric about its mid-length so that

$$x_{max} = l \quad \text{at} \quad \phi(l) = \pi/2, \tag{4.40}$$

where l is the maximum radius of the droplet. The second point can be chosen to fix the contact angle at the surface of the fibre, θ so that

$$x_{min} = R \quad \text{at} \quad \phi(R) = \pi/2 - \theta. \tag{4.41}$$

A typical solid/liquid/air phase boundary point with contact angle θ is sketched in Figure 4.2(a).

4.5.2 Surface Area, Volume and Length

The physical properties of the droplet are its surface area, S, volume, V, and length Z which are found by integration. The surface element for a cylinder of revolution is by definition

$$ds = |\mathbf{x}_\omega \times \mathbf{x}_x| dx d\omega = \frac{2\pi x}{\cos\phi(x)} dx. \tag{4.42}$$

Surface area can be found by integrating the surface element given in (4.42) and length can be found by integrating (4.10). The relevant integrals are listed here for easy reference:

$$S = 4\pi \int_R^{l-\epsilon} \frac{x}{\cos\phi(x)} dx, \tag{4.43}$$

$$V = 2\pi \int_R^{l-\epsilon} x^2 \tan\phi(x) dx, \tag{4.44}$$

$$Z = 2 \int_R^{l-\epsilon} \tan\phi(x) dx. \tag{4.45}$$

Equations (4.43)-(4.45) will have a value of ∞ at $x_{max} = l$, as boundary conditions (4.40) will set $\cos\phi(l) = 0$. When integrating (4.43)-(4.45) numerically, the upper bound on x must be $x = l - \epsilon$, keeping the boundary conditions (4.40) and (4.41). It would be possible to avoid this singularity by writing these equations as radius as a function of length so that $x(z)$. In this case

$$X = 2 \int_0^L = \arctan\phi(z) dz. \tag{4.46}$$

However, singularities occur if $\sin(\phi(z)) = 0$ for $0 < z < L$, which must then be taken into account. Singularities in both (4.45) and (4.46) can be avoided by matching the solutions of (4.45) to those of (4.43) as $x \to l - \epsilon$ and using (4.43) to find $x(z)$ for $l - \epsilon < x < l$. However,

the limitation of only finding the solution for x in the range $R < x < l - \epsilon$ where $\epsilon = 10^{-4}$ has been accepted.

The key ODE to be solved to obtain these quantities is

$$\frac{dz}{dx} = -\tan\phi(x), \tag{4.47}$$

which will be referred to as the profile equation.

The profile of the droplet can be found by plotting x, the radius of the droplet from the axis of rotation, against $z(x)$, the length of the droplet. The boundary conditions on $z(x)$ are

$$z(l-\epsilon) = 0 \quad \text{and} \quad z(R) = \frac{Z}{2}, \tag{4.48}$$

so that the radius of the droplet decreases as its length is said to increase. If $\phi(R) = \pi/2$ or $-\pi/2$, there is also a singularity at $x = R$ so that x must be integrated in the region $R - \epsilon < x < l - \epsilon$.

4.5.3 The Droplet Model for Arbitrary Contact Angle

The constants in (4.23) can be generalised to

$$x\sin\phi = K_1 x^2 + K_2, \tag{4.49}$$

where

$$K_1 = \frac{\Delta p}{2\lambda} \qquad \text{and} \qquad K_2 = K. \tag{4.50}$$

The boundary condtions (4.40) and (4.41) can be substituted in to find the constants K_1 and K_2 such that

$$K_1 = \frac{l - R\cos\theta}{l^2 - R^2} \quad \text{and} \quad K_2 = Rl\frac{l\cos\theta - R}{l^2 - R^2}. \tag{4.51}$$

By factorising, the profile equation (4.47) can be written as

$$\frac{dz}{dx} = \frac{\sin\phi}{\sqrt{1-\sin^2\phi}} = \frac{x^2 + aRl}{\left[(l^2 - x^2)\left(x^2 - a^2R^2\right)\right]^{1/2}}, \tag{4.52}$$

where

$$a = \frac{l\cos\theta - R}{l - R\cos\theta} = \frac{1}{Rl}\frac{K_2}{K_1}. \tag{4.53}$$

4.5.4 Normalisation of Droplet Model for Arbitary Contact Angle

Set $n = l/\rho$ and $m = R/\rho$ where R is the radius of the fibre and $x_{min} = \rho$ is the minimum radius of the droplet. When the droplet sits on the surface of the fibre then $\rho = R$ and $m = 1$. We make the following normalisations:

$$x = \rho\tilde{x} \quad \text{and} \quad z = \rho\tilde{z}. \tag{4.54}$$

The normalised boundary conditions (4.40) at the mid-length of the drop are now

$$\tilde{x}_{max} = n \quad \text{and} \quad \phi(n) = \pi/2 \tag{4.55}$$

and the boundary conditions at the surface of the fibre (4.41) are now

$$\tilde{x}_{min} = m \quad \text{and} \quad \phi(m) = \pi/2 - \theta. \tag{4.56}$$

The constant (4.53) can also be written as

$$a = \frac{n\cos\theta - m}{n - m\cos\theta} \tag{4.57}$$

and principle curvatures c_p (4.17) and c_m (4.18) can now be written as

$$c_p = \frac{n - m\cos\theta}{n^2 - m^2} + \frac{n}{\tilde{x}^2}\frac{n\cos\theta - m}{n^2 - m^2}, \tag{4.58}$$

$$c_m = \frac{n - m\cos\theta}{n^2 - m^2} - \frac{n}{\tilde{x}^2}\frac{n\cos\theta - m}{n^2 - m^2}. \tag{4.59}$$

Finally, (4.52) can be written in the normalised form

$$\frac{d\tilde{z}}{d\tilde{x}} = -\frac{\tilde{x}^2 + amn}{\left[(n^2 - \tilde{x}^2)\,(\tilde{x}^2 - (am)^2)\right]^{1/2}}, \tag{4.60}$$

which is the form of the general profile equation (4.47) which will be repeatedly referred to in this chapter. The surface area, length and volume of the can be normalised in the same way, as can the length of the fibre L, so that

$$S = \rho^2\tilde{S}, \tag{4.61}$$

$$V = \rho^3\tilde{V}, \tag{4.62}$$

$$z = \rho\tilde{z}, \tag{4.63}$$

$$L = \rho\tilde{L}. \tag{4.64}$$

From now on all variables are assumed to be normalised in this way and the ˜ form is implied.

4.6 The Fibre Engulfment Problem

The next step is to consider what happens to the shape and contact angle of the droplet as it engulfs a cylinder of finite length. Instead of looking at models of a boundary moving with time, it is simpler to start with considering the series of static solutions. This is consistent with the case where vapour slowly condenses onto a fibre, forming a droplet so that rate at which the volume increases is slow enough for the surface tension to maintain the shape of the drop. The relevant contact angle is the dynamic contact angle θ_D, for which the leading edge of the droplet is expected to be moving at a constant speed. Alternatively, the drop might be allowed to reach equilibrium between incremental increases in its volume. In this case, the stationary contact angle, θ_E should be used. For either case, θ_D and θ_E can both be labelled as the critical contact angle θ_c. For more detail see Appendix C.2.

It can be expected that the droplet will engulf the fibre as its volume increases. The problem to be solved is, therefore, how a drop engulfs a fibre of a finite length L and radius 1 as its volume increases, where it is assumed that that these parameters have been normalised as discussed in Section 4.5.4. The steps by which a drop is taken to engulf a fibre are as follows.

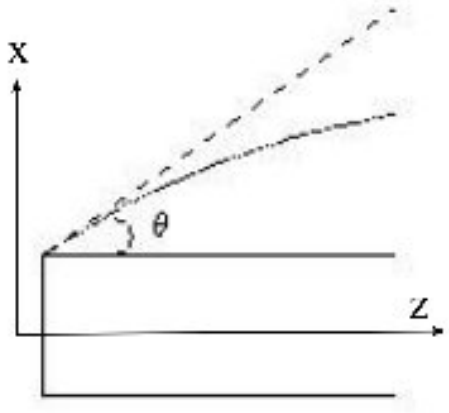

(a) Contact angle between the surface of the droplet (dotted line) and the length of the fibre, θ, at critical volume V_I where $z = L$.

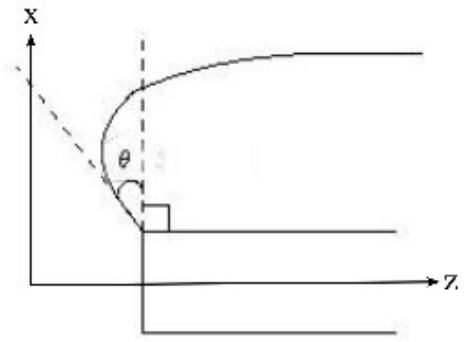

(b) Contact angle between the surface of the droplet (dotted line) and the cross-section of the fibre, θ, at critical volume V_{II} where $z = L$.

Figure 4.2: Diagrams of contact angle θ at the solid/liquid/air boundary point. Illustrated for $\theta < \pi/2$.

Region I

Figure 4.3(a) is a sketch of a droplet in this region. The minimum radius of the droplet is the radius of the fibre and the contact angle is the critical contact angle θ_c. Define $V = V_I$ to be volume at which the length of the drop is the same as the length of the fibre and the contact angle is the critical contact angle. At small volumes $0 < V < V_I$, a droplet's length Z is smaller than the length of the fibre. As its volume increases, the length of the droplet increases. The normalised maximum droplet height n is the only free parameter in the boundary conditions. The boundary conditions for this region can be summarised as

$$x_{max} = n \quad \text{at} \quad \phi(n) = \pi/2, \tag{4.65}$$

$$x_{min} = 1 \quad \text{at} \quad \phi(1) = \pi/2 - \theta_c, \tag{4.66}$$

$$Z = L \quad \text{at} \quad V = VI, \tag{4.67}$$

$$Z < L \quad \text{when} \quad 0 < V < V_I. \tag{4.68}$$

Region II

At the critical volume, V_I the droplet reaches the end of the fibre $Z = L$. At this point the leading edge of the droplet is pinned at that point so its length is fixed as shown in Figure 4.2(a). The normal is not defined at the corner so the contact angle is no longer fixed. An increase in volume results in an increase in contact angle. A sketch of a droplet in this region is in Figure 4.3(b). At the critical volume V_{II} the contact angle has increased by $\pi/2$ so that $\theta = \theta_c + \pi/2$. When $\theta = \theta_c + \pi/2$ the angle between the droplet and the radius of the fibre is the critical angle, θ_c. The boundary conditions in this region can be summarised as

$$x_{max} = n \quad \text{at} \quad \phi(n) = \pi/2, \tag{4.69}$$

$$x_{min} = 1 \quad \text{at} \quad \phi(1) = \pi/2 - \theta, \tag{4.70}$$

$$Z = L \quad \text{when} \quad \theta_c < \theta < \theta_c + \pi/2, \tag{4.71}$$

$$\text{and} \quad V_I < V < V_{II}, \tag{4.72}$$

$$V = V_{II} \quad \text{and} \quad \theta = \theta_c + \pi/2. \tag{4.73}$$

Region III

Figure 4.3(d) is a sketch of a droplet in this region. A droplet at critical volume V_{II} is illustrated in Figure 4.2(b). The contact angle between the droplet and the fibre cross-section is θ_c so that the leading edge of the droplet can move down the end surface of the fibre as the volume is perturbed. The point of engulfment occurs when $V = V_{III}$ as volume is decreased from V_{II} to V_{III}. This point has to be defined slightly differently for long and short fibres. When fibres are short, engulfment will be of type S while when fibres are long, engulfment will be of type L.

For short fibres, a point of engulfment of type S is reached by decreasing x_{min} while θ is fixed until part of the droplet surface rests on the surface of the fibre as shown in Figure 4.3(c).

If a point on the surface of the droplet is given by the coordinates $[z(x),\, x]$ as defined in Figure 4.1(a) then at the point of engulfment of type S we have

$$z(x_{min}) = L/2, \tag{4.74}$$

$$z(1) = L/2. \tag{4.75}$$

x_{min} cannot be decreased after a solution has reached this point.

When the fibre is long, engulfment is of type L. The leading edge of the droplet can move down the cross-section of the cylinder unhindered. As the only possible limiting shape is that of a sphere as $x_{min} \to 0$, the variables θ and x_{min} are no longer independent. For this reason, a series of numerical solutions are found for which x_{min} is decreased, while $\phi(min)$ is fixed, until $x_{min} = \epsilon$ where $\epsilon < 1$. At $x_{min} = \epsilon$ a point of engulfment of type L is reached.

The free parameters are now $x_{min} < 1$ and contact angle. The boundary conditions for this region are

$$x_{max} = n \qquad \text{at} \qquad \phi(n) = \pi/2, \tag{4.76}$$

$$\epsilon < x_{min} < 1 \qquad \text{at} \qquad \phi(x_{min}) = \theta_c + \pi/2, \tag{4.77}$$

$$Z = L \qquad \text{when} \qquad V_{II} > V > V_{III}. \tag{4.78}$$

As $x_{min} \to 0$, Section 4.8 will show that the only possible limit shape is a sphere, which has a smaller volume than any other mean curvature shape of the same length. For this reason, if the leading edge of the droplet moves down the end surface of a fibre, the volume will decrease.

4.7 Delaunay Constant Mean Curvature Surfaces

Firstly, consider the profile equation (4.47) written in terms of $\sin\phi(x)$

$$\frac{dz}{dx} = -\frac{\sin\phi}{\left(1-\sin^2\phi\right)^{1/2}}. \tag{4.79}$$

Recall the geometrical meaning of the z and x co-ordinate axes illustrated in diagram (4.1(c)). The plot of the profile equation $z(x)$ is the cross-section of the droplet.

The force balance equation (4.49) can be re-written as an equation for $\sin\phi(x)$

$$\sin\phi(x) = \frac{K}{x} + \frac{\Delta_p}{2\lambda}x. \tag{4.80}$$

If

$$p = \frac{\Delta_p}{2\lambda}, \tag{4.81}$$

then (4.80) can be substituted into the profile equation so that

$$\frac{dz}{dx} = \frac{px^2+K}{(x^2-(px^2+K)^2)^{1/2}}. \tag{4.82}$$

The denominator of the profile equation is real only when $-1 < \sin(\phi) < 1$. The denominator is quadratic in x so the values of x for which $\sin^2\phi = 1$ are given by

$$x^2 = (px^2+K)^2, \tag{4.83}$$

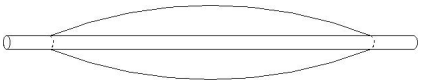

(a) Shape of droplet on the fibre in region I with boundary conditions (4.65)-(4.68).

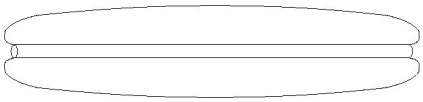

(b) Shape of droplet on the fibre in region II with boundary conditions (4.69)-(4.72).

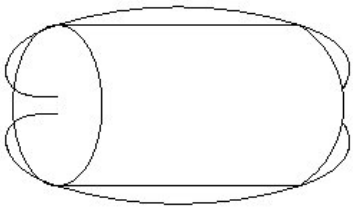

(c) Shape of droplet on the fibre at $V = V_{III}$ for short fibres.

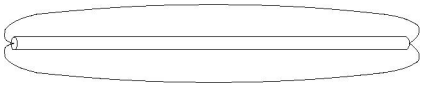

(d) Shape of droplet on the fibre in Region III for long fibres at the point which the contact angle begins to change.

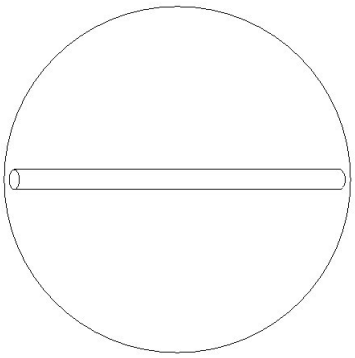

(e) Shape of droplet on the fibre at $V = V_{III}$ for long fibres.

Figure 4.3: Diagrams of fibre and droplet in regions I, II and III in Section 4.6.

or

$$x^2 = \frac{2(1-2pK) \pm 2\sqrt{1-4pK}}{(2p)^2}. \tag{4.84}$$

The positive solutions for x are therefore

$$x_\pm = \frac{1 \pm \sqrt{1-4pK}}{2p}. \tag{4.85}$$

The solutions x_- and x_+ are the minimum and maximum possible droplet radii allowed for any set of parameters p and K.

When $\phi = 0$ the rate of change of the length of the droplet with radius changes sign. The surface of the droplet folds over itself and so it is labelled a turning point. If the contact angle is obtuse so that $\sin\phi(R) < 0$ then there must be a turning point in the solution of $z(x)$ so that the boundary conditions at the maximum radius (4.40) are to be met. From the definition of the maximum curvature c_p, when $\sin\phi$ changes sign then c_p will also change sign.

From the profile equation (4.82), a turning point will occur when

$$x = \sqrt{\frac{-K}{p}} \tag{4.86}$$

if this is real.

When the second derivative of $z(x)$,

$$\frac{d^2z}{dx^2} = -\frac{1}{\cos^2\phi}\frac{d\phi}{dx}, \tag{4.87}$$

is zero there is a point of inflection in the solution. From the definitions of c_m in terms of ϕ this can be re-written as

$$\frac{d^2z}{dx^2} = -\frac{1}{\cos^3\phi}c_m(x). \tag{4.88}$$

From the definition of $c_m(x)$ given in (4.30), an inflection point will occur when

$$x = \sqrt{\frac{K}{p}} \tag{4.89}$$

if this is real. Clearly, the condition for a turning point (4.86) and the condition for an inflection point (4.89) cannot both be true so any solution of the profile equation can have either a turning or inflection point, not both.

From (4.85), (4.86) and (4.89) the following observations can be met. There are no real solutions of (4.85) for $4pK > 1$. When $4pK = 1$ then $x_+ = x_-$ and the solution is that of a cylinder. While $1 > 4pK > 0$ then by (4.86) inflection point solutions are expected. $4pK < 0$ is consistent with the condition for turning point solutions (4.89). (4.28) and (4.30) show that when $K = 0$ the solution is that of a sphere where c_m and c_p are constant. (4.85) confirms that when $K = 0$ $x_{min} = 0$ and $x_{max} = 1/p$ as expected where the radius of the sphere is $1/c_p = 1/p$. These observations confirm well-known properties of surfaces with constant mean curvature called Delaunay surfaces [72].

If the solution has an inflection point, there is a minimum in the function $\phi(x)$. The value of $\sin\phi$ at which an inflection point occurs is

$$\sin\phi_i = 2\sqrt{Kp}. \tag{4.90}$$

As an inflection point occurs when $1 > 4pK > 0$ then $1 > 2\sqrt{pK} > 0$ so $\phi(x)$ will be acute.

4.7.1 An Example Turning Point Solution

For an example of a turning point solution, set the contact angle $\theta = \pi$. The boundary conditions (4.41) and (4.40) are now

$$\phi(R) = -\pi/2 \qquad \text{at} \qquad x = R, \tag{4.91}$$

$$\phi(l) = \pi/2 \qquad \text{at} \qquad x = l. \tag{4.92}$$

These boundary conditions can be substituted into (4.60) in Section 4.5.3 to find the profile equation

$$\frac{dz}{dx} = -\frac{x^2 - Rl}{\sqrt{(l^2 - x^2)(x^2 - R^2)}}. \tag{4.93}$$

Equation (4.93) changes sign at $\sin\phi = 0$ when $x^2 = Rl$, which is the turning point. The solution to the profile equation is plotted in Figure 4.4(b).

4.7.2 An Example Inflection Point Solution

For an example of a turning point solution, set the contact angle $\theta = 0$. The boundary conditions (4.41) and (4.40) are now

$$\phi(R) = \pi/2 \qquad \text{at} \qquad x = R, \tag{4.94}$$

$$\phi(l) = \pi/2 \qquad \text{at} \qquad x = l. \tag{4.95}$$

These boundary conditions can be substituted into (4.60) in Section 4.5.3 to find the profile equation

$$\frac{dz}{dx} = -\frac{x^2 + Rl}{\sqrt{(l^2 - x^2)(x^2 - R^2)}}. \tag{4.96}$$

In this case there is an inflection point when $x^2 = Rl$. The solution to the profile equation is plotted in Figure 4.4(a).

4.8 The Asymptotic Limit $\epsilon = \rho/l \to 0$ for Contact Angle $\theta = 0$

Increasing the volume increases the maximum height, l and so decreases the ratio of the radius of the fibre ρ to the radius of the droplet l. The asymptotic limit where $\epsilon = \rho/l \to 0$ can be investigated and is relevant when considering small bundles of CNTs which have negligable radius. The results from this section show that in the limit $\epsilon \to 0$ the solution is a sphere and corrections of $O(\epsilon)$ add inflection or turning points to the solution.

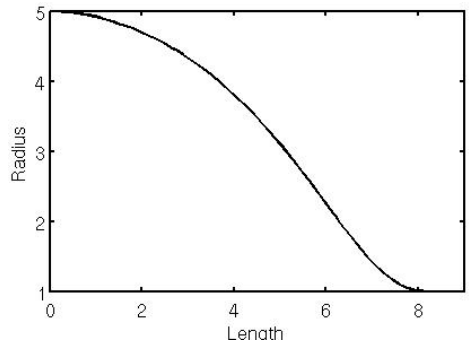

(a) Solution of (4.96) with inflection point. The boundary conditions are given by equations (4.40) (4.41), where $\theta = 0$, $l = 1$ and $R = 0.3$.

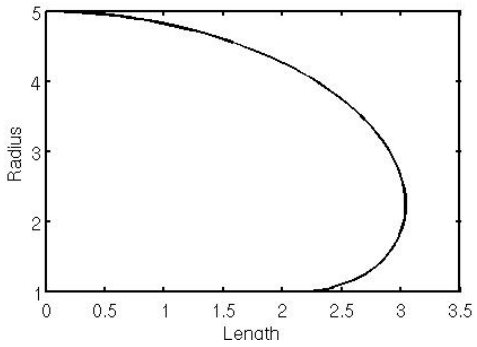

(b) Solution of (4.93) with turning point. The boundary conditions are given by (4.40) and (4.41), where $\theta = \pi$, $l = 1$ and $R = 0.3$.

Figure 4.4: Examples solutions of (4.93) and (4.96).

4.8.1 The Asymptotic Limit $\epsilon = \rho/l$ for an Inflection Point Solution

Scale $z(x)$ and x by the maximum length l so that

$$z(x) = lf(g), \tag{4.97}$$

$$x = lg. \tag{4.98}$$

To find the asymptotic expansion of $z(x)$ and x of an inflection point solution these normalisations are substituted in (4.96) so that

$$\frac{df}{dg} = -\frac{g^2 + \epsilon}{\left[(1-g^2)\left(g^2-\epsilon^2\right)\right]^{1/2}}. \tag{4.99}$$

Using the following asymptotic expansion,

$$f(g) = f_0(g) + \epsilon f_1(g) + \ldots, \tag{4.100}$$

to zero order in ϵ, (4.99) is reduced to

$$\frac{df_0}{dg} = \frac{g}{\sqrt{1-g^2}}. \tag{4.101}$$

This can be integrated to find the normalised length to leading order so that

$$f_0 = -\sqrt{1-g^2} + c \text{ or } 1 = (f_0 - c)^2 + g^2. \tag{4.102}$$

This is a spherical solution. When $c = 0$ the boundary conditions $f_0(0) = 1$ and $f_0(1) = 0$ are met. The first order equation is

$$\frac{df_1}{dg} = \frac{1}{g\sqrt{1-g^2}}, \tag{4.103}$$

which has the solution

$$f_1 = -\text{arctanh}\left(\frac{1}{\sqrt{1-g^2}}\right). \tag{4.104}$$

From the shape of the plot of (4.104) in Figure 4.5 it can be seen how this first order correction adds a turning point to the solution. The first order solution decreases the length for small radius so that the maximum length is not at the minimum radius. Higher order terms are of a similar shape.

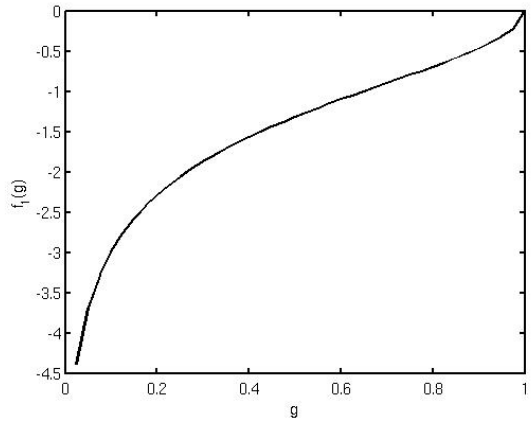

Figure 4.5: Plot of $f_1(g)$ given in (4.104) against g.

4.8.2 The Asymptotic Limit $\epsilon = \rho/l \to 0$ for an Turning Point Solution

Substitution of (4.97)-(4.98) into (4.93) results in

$$\frac{df}{dg} = -\frac{g^2 - \epsilon}{\left[(1-g^2)\left(g^2-\epsilon^2\right)\right]^{1/2}}. \tag{4.105}$$

The zero order solution is the same as (4.102) and the first order solution has the opposite sign of (4.104). This term and higher order terms in f add an inflection point to the solution.

4.9 Types of Solutions in Terms of n and $\cos\theta$

In this section let the boundary condition at the surface of the fibre (4.56) be $m = 1$ as it is for Region I and II solutions defined in Section 4.6. The solutions of the normalised droplet model for an arbitary contact angle introduced in Section 4.5.4 will have turning points when $an < 0$ and inflection points when $an > 0$. For reference, the value of the parameter a (4.57) in terms of n and $\cos\theta$ is again stated below

$$a = \frac{n\cos\theta - 1}{n - \cos\theta}. \tag{4.106}$$

Let x_{ti} refer to the point at which there is either a turning or inflection point. It is useful to quantify the relative placement of the turning or inflection point along the x-axis. This is done by defining

$$F_1 = \frac{x_{ti}^2 - x_{min}^2}{x_{max}^2 - x_{min}^2} \tag{4.107}$$

Parameters	x_{min}^2	x_{ti}^2	x_{max}^2
$w\ p$	$(\frac{1}{p} - w)^2$	$\lvert w(w - 1/p)\rvert$	w^2
$a\ R\ l$	$(aR)^2$	$\lvert aRl\rvert$	l^2
$a\ m\ n$	$(am)^2$	$\lvert amn\rvert$	n^2

Table 4.1: Miminum x_{min} and maximum x_{max} possible radii of solutions and also radius of turning or inflection point x_{ti}.

Type	Bounds on Constants	Bounds on $\cos\theta$ and n
1	$K_1 < 0$ $K_2 > 0$	$1 > n > \cos\theta$
2	$K_1 > 0$ $K_2 < 0$	$1/\cos\theta > n > 1$
3	$K_1 > 0$ $K_2 > 0$	$n > 1/\cos\theta$
4	$K_1 < 0$ $K_2 < 0$	$n < \cos\theta$

Table 4.2: Types of solutions found for solutions parametrised by n and $\cos\theta$. K_1 and K_2 are defined in (4.49) and (4.51). If $K_1K_2 < 0$ then the resulting solution may have a turning point, and otherwise it may have an inflection point.

and

$$F_2 = \frac{x_{max}^2 - x_{ti}^2}{x_{max}^2 - x_{min}^2}. \tag{4.108}$$

It can be checked that $F_1 + F_2 = 1$ so F_1 indicates at what fraction of the maximum radius the turning or inflection point occurs without having to use terms containing square roots.

Four groups of solutions can be found. These groups, which are parametrised by K_1 and K_2 defined in (4.51), are presented in Table 4.2. By 4.49, if $K_1K_2 < 0$ then $\sin\phi$ can change sign and the solution may have a turning point. If $K_1K_2 > 0$ then $\sin\phi$ cannot change sign and the solution may have an inflection point. Solution types 1 and 2 are turning point solutions while types 3 and 4 are inflection point solutions. Type 1 and type 2 solutions will be discussed in Section 4.9.1 and type 3 and type 4 solutions will be discussed in Section 4.9.2.

4.9.1 Turning Point Solutions

The turning point occurs when $x = \sqrt{-an}$ which has been plotted as a function of n in Figure 4.7. $\sqrt{-an}$ increases as n increases. As $n \to \infty$ we have $an \approx n\cos\theta$: for large n, an is directly proportional to n. Figure 4.7 plots $\sqrt{-an}$ and n against n for contact angle

$\theta = 120^o$. The plot demonstrates how an monotonically increases with n. The following discussion indicates how $\cos\theta$ determines whether $\sqrt{-an} < 1 < n$ or $1 < \sqrt{-an} < n$ when $n > 1$. These results are summarised in Table 4.3 with example solutions given in Figure 4.9.

Type 1 solutions from Table 4.2 will correspond to choices of n and $\cos\theta$ for which the inequality

$$1 > n > \cos\theta \tag{4.109}$$

is true, so that $K_1 < 0$. $n > 1$ holds in the normalised model in Section 4.5.4 and so type 1 solutions can be disregarded in the fibre engulment problem.

Type 2 solutions correspond to solutions when $K_2 < 0$, or when $1 - n\cos\theta > 0$. This is always true when the contact angle $\theta > \pi/2$ and $\cos\theta < 0$. When $\cos\theta > 0$ type 2 turning point solutions can be found when

$$\frac{1}{\cos\theta} > n > 1 \tag{4.110}$$

is true. When $\cos\theta > 0$ and (4.110) are true, $|an| = n$ when $n = 1$ and $|an| = 0$ when $n = 1/\cos\theta$, so the turning point will never occur in the region when $1 < x_{ti} < n$ if $n > 1$. Type 2 solutions for which $\cos\theta > 0$ correspond to Group 1 solutions in Table 4.3.

When $\cos\theta < 0$ and (4.110) are true, then $|an| = n$ when $n = 1$. Note that

$$\frac{da}{dn} = (n - \cos\theta)^{-2}\left(\cos\theta(1 - n\cos\theta) + n\cos\theta(n - \cos\theta)\right). \tag{4.111}$$

When $\cos\theta < 0$, both terms on the right hand side of (4.111) are always negative so an will become increasingly negative as n increases. As n increases from 1 the turning point will move away from the surface of the fibre. Type 2 solutions for which $\cos\theta < 0$ correspond to Group 2 solutions in Table 4.3.

As n is increased then the increase in maximum thickness $n - 1$ will ensure an increase in length. Now from (4.107) we have

$$F_1 = \frac{x_{ti}^2 - x_{min}^2}{x_{max}^2 - x_{min}^2} = \frac{an - 1}{n^2 - 1} \to 0 \text{ as } n \to \infty. \tag{4.112}$$

As n increases, less of the droplet doubles back over itself as the turning point moves relatively closer to x_{min}. Increasing the maximum radius of the droplet also moves the turning point closer to the radius of the fibre and both factors work together to increase its length.

4.9.2 Inflection Solutions

The inflection point occurs when $x = \sqrt{an}$ which has been plotted as a function of n in Figure 4.8. $\sqrt{an}$ increases as n increases. Figure 4.8 plots $\sqrt{an}$ and n against n for contact angle $\theta = 60^o$. The plots demonstrates how an monotonically increases with n and $\sqrt{-an} < 1$ for small n. The following discussion indicates how $\cos\theta$ determines whether $\sqrt{-an} < 1 < n$ or $1 < \sqrt{-an} < n$ when $n > 1$. These results are summarised in Table 4.3.

Type 4 solutions will correspond to the case where $K_1 < 0$ and $K_2 < 0$ so

$$n < \cos\theta, \tag{4.113}$$

which are only possible for $n < 1$ which are irrelevant to the normalised model in Section 4.5.4.

Type 3 solutions will correspond to the case where $K_1 > 0$ and $K_2 > 0$ when $n > 1$ and

$$n > \frac{1}{\cos\theta}. \tag{4.114}$$

If $n < 1$ then $\cos\theta > 0$.

When $n = 1/\cos\theta$ then $a = 0$. From (4.111) and the inequalities

$$\begin{aligned} & \cos\theta(1 - n\cos\theta) + n\cos\theta(n - \cos\theta), & (4.115)\\ = \;& \cos\theta(1 + n^2) - 2n\cos^2\theta, & (4.116)\\ > \;& \cos\theta(1 - n)^2 > 0, & (4.117) \end{aligned}$$

it is clear that a will increase with n. When $an = 1$ the inflection point is at the surface of the fibre. The equation $an = 1$ where a is given in (4.57) is a quadratic equation in n and can be solved for n to find

$$n_{\pm} = \frac{1 \pm \sin\theta}{\cos\theta}, \tag{4.118}$$

where $n_- < 1$ belongs to type 4 solutions and $n_+ > 1$ belongs to type 3 solutions. If $1 < n < n_+$ then $\sqrt{an} < 1$ and the solution is a Group 3 solution in Table 4.3. Otherwise, if $n_+ < n$, then it is a Group 4 solution.

The inflection point occurs when $x_i = \sqrt{an}$ and the corresponding value of ϕ_i is given by

$$\tan\phi_i = \frac{2an}{\sqrt{(n^2 - an)(an - a^2)}} = \frac{2\sqrt{an}}{(n - a)}. \tag{4.119}$$

Note that this has a maximum at

$$n_{max} = \frac{1 \pm \sin\theta}{\cos\theta}. \tag{4.120}$$

From (4.118) it is known that when $\tan\phi_i$ is a maximum, the inflection point is at the surface of the fibre. Substituting (4.120) into (4.119) leads to

$$\tan\phi_i(n_{max}) = \pm\frac{\cos\theta}{\sin\theta}. \tag{4.121}$$

Now define the inflection angle to be the value $\theta_i = \pi/2 - \phi_i$ so $\tan\phi_i = \tan(\pi/2 - \theta_i) = \cot\theta_i$. By (4.121) when the inflection point is at the surface of the fibre $\theta_i = \theta$ as required by the boundary conditions.

The limit of $\tan\phi_i$ for large n is $2\sqrt{an}/n \to 0$. As $n \to \infty$ the value of $\phi_i \to 0$. $\phi_i = 0$ is effectively the condition for a turning point. Figure 4.6 clearly shows that the maximum value of ϕ_i is the contact angle and ϕ_i decreases with increasing n. It can be shown to tend to 0^o for extremely large n.

Now consider

$$F_1 = \frac{x_{ti}^2 - x_{min}^2}{x_{max}^2 - x_{min}^2} = \frac{an - 1}{n^2 - 1} \to 0, \tag{4.122}$$

so when $n \to \infty$ the inflection point will move towards the minimum radius as the inflection point angle tends to $\pi/2$. The solution tends to the same spherical limit which was found in Section 4.8.

As n increases, the maximum droplet thickness $n-1$ also increases, which will increase the droplet length. Initially, $\phi_i(x)$ also increases with n which will also increase the droplet length. However, when $n > n_{max}$, $\phi_i(x)$ will decrease with n which will slow the increase in droplet length. A smaller contact angle θ will allow a larger minimum angle so smaller contact angles will allow longer droplets for a given n.

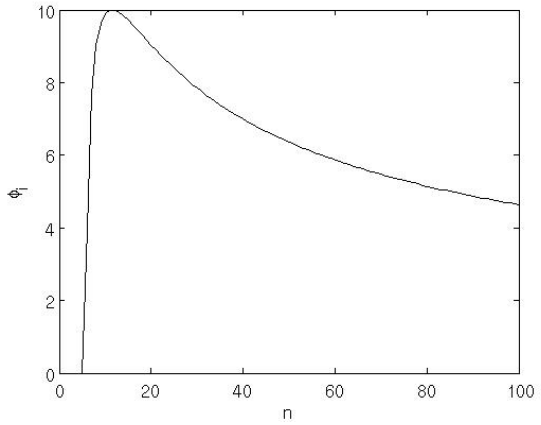

Figure 4.6: Plot of ϕ_i (degrees), $\phi(x)$ at the point of inflection as defined by (4.121), against n for contact angle $\theta = 80^o$. ϕ_i is a maximum when $\phi_i = 90 - \theta$ and $n = (1 + \sin\theta)/\cos\theta$.

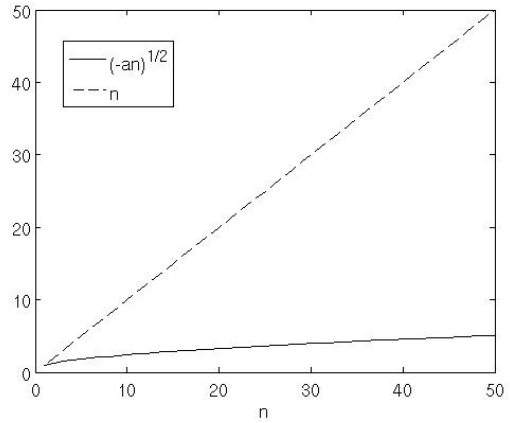

Figure 4.7: Plot of $\sqrt{-an}$ and n against n turning point solutions for $\theta = 120^o$ and $\cos\theta < 0$. Turning points are found when $x = \sqrt{-an}$. Note that as n increases the ratio $\sqrt{an}/n \to 0$ and at $n = 1$ we have $an = 1$.

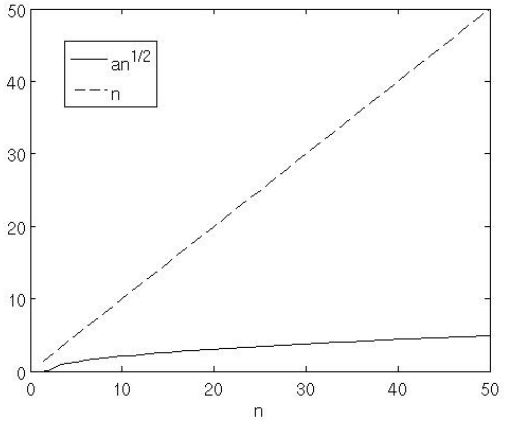

Figure 4.8: Plot of $\sqrt{an}$ and n against n for inflection point solutions for contact angle $\theta = 60^o$. Inflection points are found when $x = \sqrt{an}$. Note that as n increases the ratio $\sqrt{an}/n \to 0$ and at $n = 1$ we have $an = 0$.

4.10 Solutions in the Limit that $m \to 0$

In Region III, a series of solutions is found for decreasing values of m. In Region III all solutions are turning point solutions. If $m \neq 1$, then (4.112) is

$$F_1 = \frac{x_{ti}^2 - x_{min}^2}{x_{max}^2 - x_{min}^2} = \frac{anm - m^2}{n^2 - m^2}. \tag{4.123}$$

Using (4.57) in the limit of $m \to 0$ then clearly $F_1 \to 0$. So as m is decreased then $x_{ti}^2 \approx \cos\theta mn$. When $m = 0$ this corresponds to the solution of a sphere where $x_{ti} = 0$. Note that x_{ti}, and so F_1, also decreases as $\cos\theta$ decreases. Therefore as F_1 decreases, more points are required to find smooth numerical solutions. This will be discussed in more detail in the following discussion.

4.11 Solving the Boundary Value Problem

Constant mean curvature droplets can be used to find numerical solutions to the fibre engulfment problem introduced in Section 4.6. A fibre is engulfed by a droplet by perturbing the volume to move solutions through Region I, to Region II and then to Region III. Critical volumes are found when the solution moves from one region to another.

It is assumed that the wettability of the surface of the fibre by the droplet is relatively high and so the contact angle is acute. This is consistent with the assumption that a cell will not easily engulf an object which is very hydrophobic. A droplet which forms on a fibre with an acute contact angle is called a barrel drop and has been investigated in papers such as [12] and [64]. These droplets have points of inflection and have been successfully modelled by inflection point solutions.

There is therefore some physical justification to use inflection point solutions in Region I.

	Bounds on $\cos\theta$	Bounds on n	Order of turning/ inflection points, x_{min} and x_{max}
Group 1	$\cos\theta > 0$	$1 < n < 1/\cos\theta$	$\sqrt{-an} < 1 < n$
Group 2	$\cos\theta < 0$	all n	$1 < \sqrt{-an} < n$
Group 3	$\cos\theta > 0$	$1/\cos\theta < n < (1+\sin\theta)/\cos\theta$	$\sqrt{an} < 1 < n$
Group 4	$\cos\theta > 0$	$(1+\sin\theta)/\cos\theta < n$	$1 < \sqrt{an} < n$

Table 4.3: Summary of the results of Sections 4.9.1 and 4.9.2. If $\sqrt{-an}$ is real then the solution has an inflection point and if $\sqrt{an}$ is real then the solution has a turning point. An example of a solution from each group can be found in Figure 4.9.

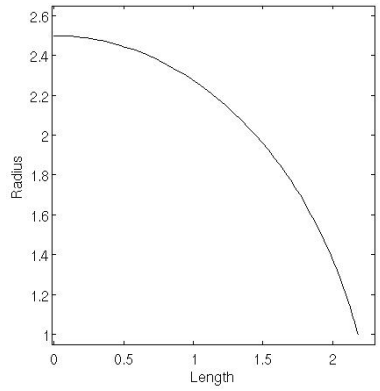

(a) Group 1: $\theta = 70^0$, $n = 2.5$

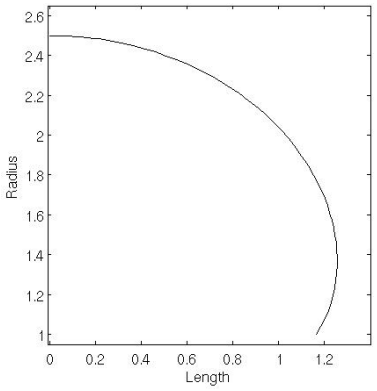

(b) Group 2: $\theta = 120^0$ $n = 2.5$

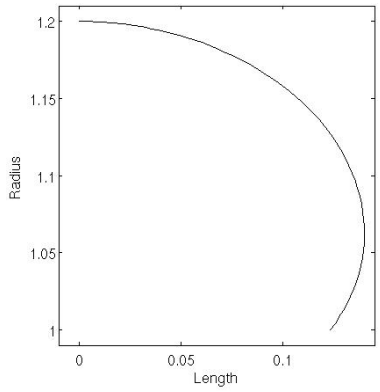

(c) Group 3: $\theta = 120^0$ $n = 1.2$

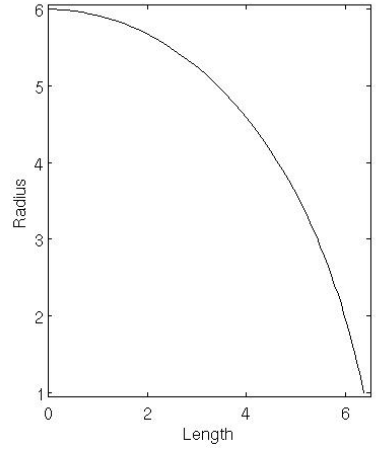

(d) Group 4: $\theta = 70^0$ $n = 6$

Figure 4.9: Examples profiles corresponding to solutions types summarised in Table 4.3.

When the contact angle is variable in Region II, both inflection and turning point solutions will be required while only turning point solutions are useful in Region III.

Solutions of the boundary value problem were found by minimising the output function

$$y = Z/2 - L/2, \tag{4.124}$$

where $Z = z(x_{min})$ and L is the length of the fibre. The minimisation was done using the MATLAB program *fzero* using the default settings. The algorithm uses a combination of bisection, secant and inverse quadratic interpolation methods. The input parameter to this minimisation problem is either n or θ, the required contact angle. The other boundary conditions from Section 4.5.4 are fixed. Z is found by integrating (4.60) between the limits x_{min} to x_{max} using the MATLAB solve *ode45*. The option 'Refine' was increased from a default value of 4 in order to increase the number of points required to find a smooth solution when F_1, as defined in (4.107) is small. The default number of points in a solution is multiplied by a factor of 'Refine'.

Now the critical volumes defined in Section 4.6 can be found. To increase the volume in Region I, the parameter n must be increased as the contact angle is fixed to the dynamic contact angle, θ_c, and also $m = 1$. As the contact angle is increased in region II, an n must be found for every contact angle θ, which will ensure that $Z = L$.

For solutions in Region III, $\theta = \theta_c + \pi/2$ is fixed. Initially m is decreased in steps of 10^{-2} where for each solution a value of n is found for which $Z = L$. If a solution is found such that for

$$\begin{aligned} z(x_{min}) &= L/2, & (4.125)\\ z(x_E) &< L/2, & (4.126)\\ x_E &< 1, & (4.127) \end{aligned}$$

then for those values of $L/2$ and θ_c, engulfment is of type S. The values of m and n which correspond to this point of engulfment can be determined more accurately by allowing m and n to be free parameters while minimising the output vector $\boldsymbol{y} = [y_1, y_2, y_3]$ where

$$\begin{aligned} y_1 &= z(x_{min}) - L/2, & (4.128)\\ y_2 &= z(x_E) - L/2, & (4.129)\\ y_3 &= x_E - 1. & (4.130) \end{aligned}$$

The point $\boldsymbol{p} = [x_E, z(x_E)]$ is the point on the solution curve closest to the point $\boldsymbol{q} = [1, z(1)]$. As the function to be minimised is a vector rather than a scalar, the MATLAB program *fsolve* was used instead of *fzero*. If a point of engulfment of type S is not reached then engulfment is of type L.

4.11.1 Results and Discussion

All results are parameterised by the contact angle θ_c and the length of the fibre L. Critical volumes are normalised using the volume of a sphere whose radius is $L/2$ so that $V_0 =$

$(4/3)\pi(L/2)^3$. Figure 4.10 contains examples of series of solutions in Regions I, II and III for $\theta_c = 45^o$, 10^o and 80^o when $L/2 = 8$. The solutions in Figures 4.10 and 4.12 show the process of the cell engulfing the ends of the fibre. Examples of solutions at $V = V_I$, V_{II} and V_{III} can be found in Figure 4.11.

Numerical solutions for V_I and V_{II} can be found in Figure 4.13. As L is increased and θ_c is decreased then V_{II}/V_0 tends to 1. In this sense it can be said that the solutions at V_{II} approach a spherical limit. As L is increased, then V_I/V_0 also tends to 1. However, when the contact angle θ_c is small, there is a minimum in V_I w.r.t. L. From Figure 4.14, it can be observed that x_{max} is roughly linearly proportional to L. So as L is increased then F_1 decreases as previously discussed. So as F_1 decreases, the normalised volume of the solution tends to 1. In this sense the solutions for V_I and V_{II} tend to the spherical limit as L is increased.

Figure 4.12(a) is a much less smooth solution than that in Figure 4.12(b). The consequence of the lack of smoothness in solutions is that the numerically obtained critical volumes do not vary smoothly with L or θ_c. Both these solutions were found in the case that the MATLAB parameter 'Refine' was set to the default value for *ode45*, which is 4. However, Figure 4.15 indicates that even significantly increasing the value of 'Refine' does not make the numerically found values of V_{III} vary any more smoothly with L or θ_c when engulfment is of type L and $x_{min} = 10^{-2}$. The results in this chapter were found in the case that 'Refine'= 4. Only results not effected by the lack of smoothness of the numerical solutions of the profile equation (4.60) have been included.

Figure 4.16 shows solutions of V_{III} where $x_{min} = 0.1$. x_{min} is large enough for V_{III} to vary smoothly with L and θ_c. As L is increased and θ_c is decreased V_{III} tends to 1. Figure 4.17 indicates how the volume of a solution in Region III varies with x_{min}. As x_{min} is decreased then the volume of the solution also tends to 1. In Section 4.10 it was discussed how $F_1 \to 0$ as $x_{min} \to 0$. In this sense, the solution tends to the spherical limit as x_{min} is decreased.

Results relating to engulfment of type S are found in Figure 4.18. No minimum limit was imposed on x_{min}. The lack of smoothness in these plots has previously been discussed. They have been included to demonstrate the general properties of these solutions. As in the case for engulfment of type L, x_{max} increases approximately linearly with L. x_{min} also decreases as L increases. The trends in x_{min} and x_{max} both ensure that F_1 decreases as L is increased and so the normalised volume tends to 1 as L is increased.

4.12 Summary

The results of this investigation can be summarised by two points. For droplets whose mean curvature is constant,

- the choice in boundary conditions of normalised maximum radius n and contact angle indirectly control the volume of the droplet by determining the placement of points on the droplet surface where the rate of change of length z with radius x is a minimum, which are points of inflection, or zero, which are turning points.

- for a given volume, the type of solution which has the maximum length is the sphere. So by the constant mean curvature model, it is predicted that CNTs will be phagocytosed by macrophages which can be described as perturbations of a sphere.

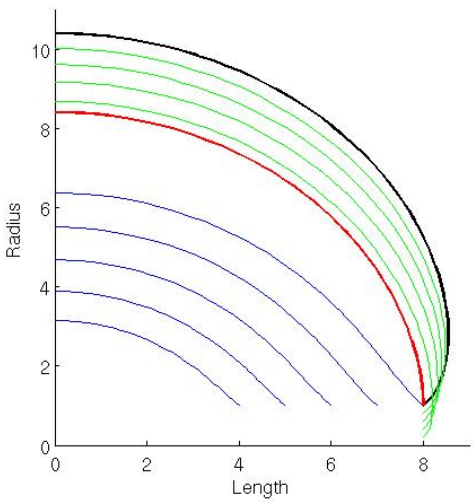

(a) Cell on fibre solutions for which contact angle $\theta_c = 45^o$.

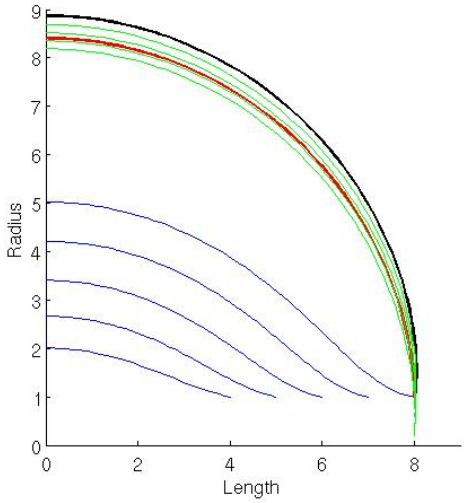

(b) Cell on fibre solutions for which contact angle $\theta_c = 10^o$.

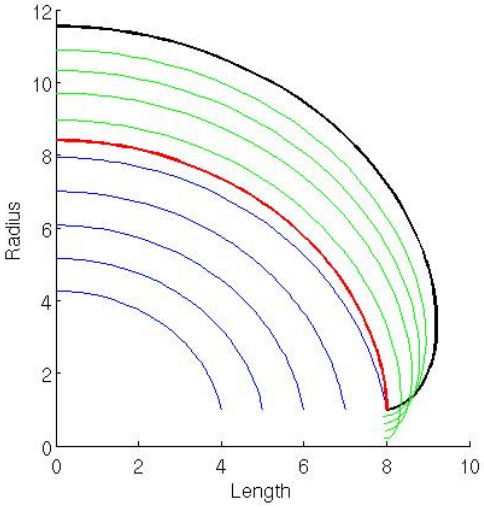

(c) Cell on fibre solutions for which contact angle $\theta_c = 80^o$.

Figure 4.10: Example cell on fibre solutions when $L = 8$. Key: blue - Region I solutions for which $V \leq V_I$, red - solution for which $\theta = 90^o$, black - solution at $V = V_{II}$ and green - solutions in Region III

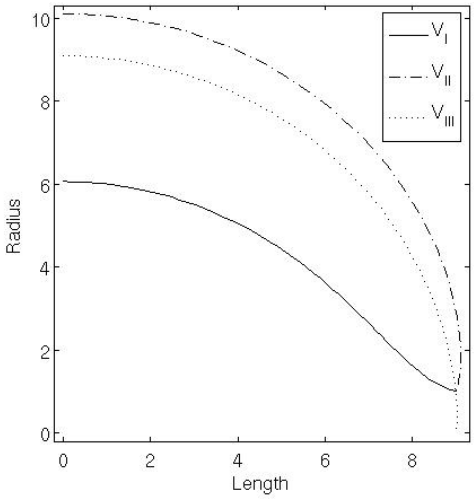

(a) $\theta_c = 15^o$ $L/2 = 9$ $x_{min} = 0.04$. Engulfment of type S.

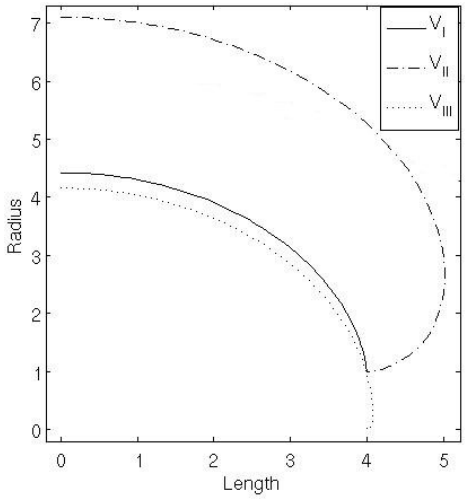

(b) $\theta_c = 90^o$ $L/2 = 4$ $x_{min} = 0.02$. Engulfment of type S.

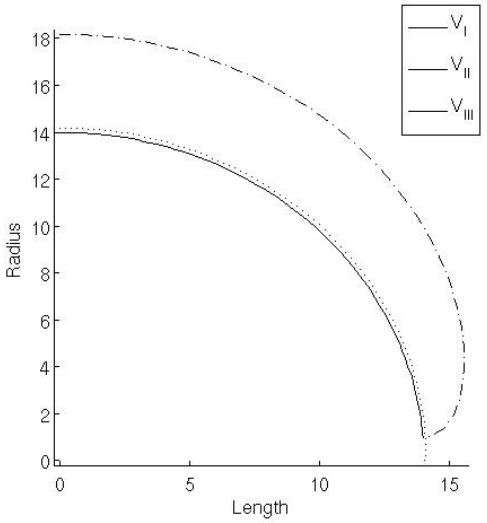

(c) $\theta_c = 90^o$ $L/2 = 14$ $x_{min} = 0.01$. Engulfment of type L.

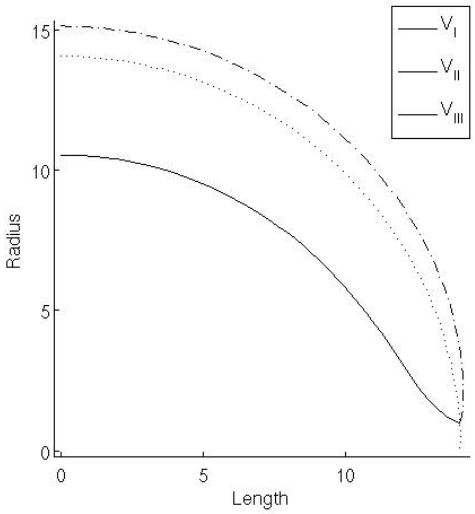

(d) $\theta_c = 15^o$ $L/2 = 14$ $x_{min} = 0.01$. Engulfment of type L.

Figure 4.11: Examples of solutions at which $V = V_I$, V_{II} and V_{III}.

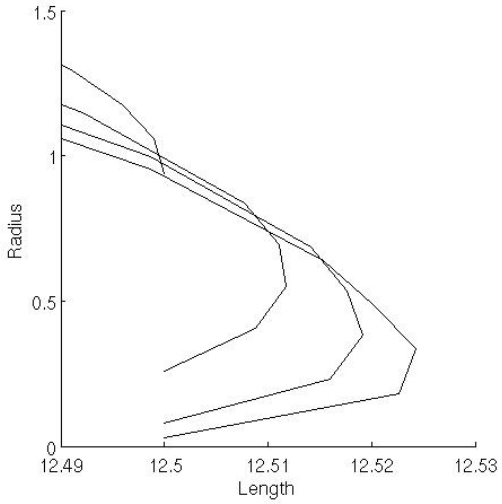

(a) Cell engulfing fibre solutions for $L/2 = 12$ for $\theta = 0$, 5, 10, 15.

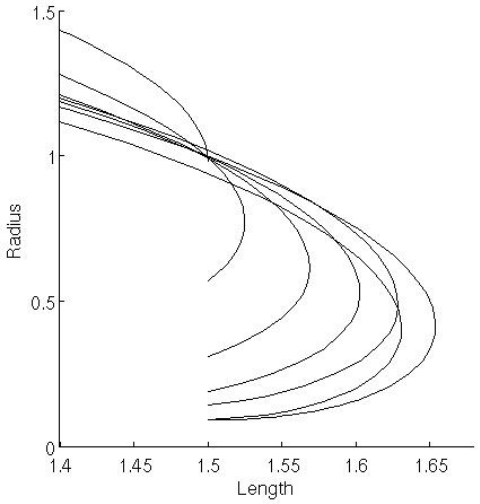

(b) Cell engulfing fibre solutions for $L/2 = 1$ for $\theta = 0$, 15, 30, 45, 60, 75 and 90.

Figure 4.12: Example cell engulfing fibre solutions of type S. For a given fibre length, x_{min} will decrease as θ increases. Note that for the longer fibre the solution is much less smooth.

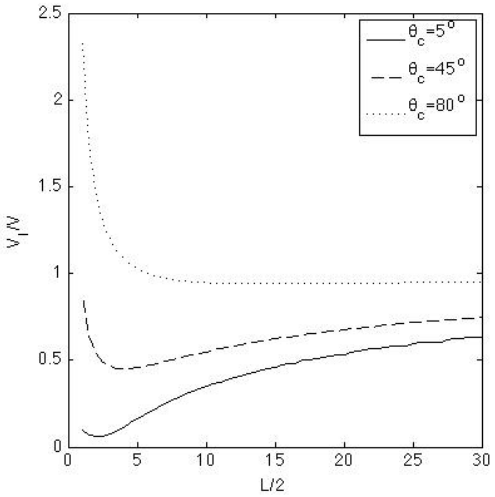

(a) Critical volume V_I/V_0 against L.

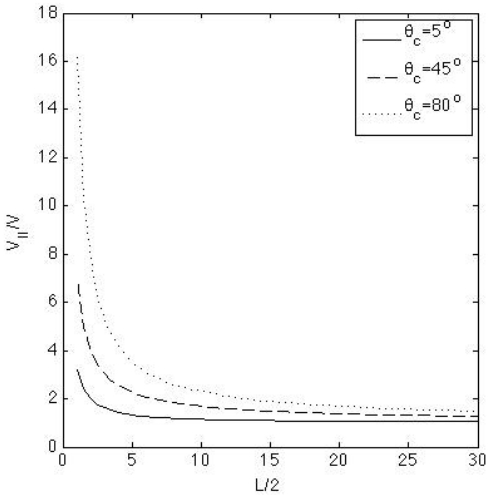

(b) Critical volume V_{II}/V_0 against L.

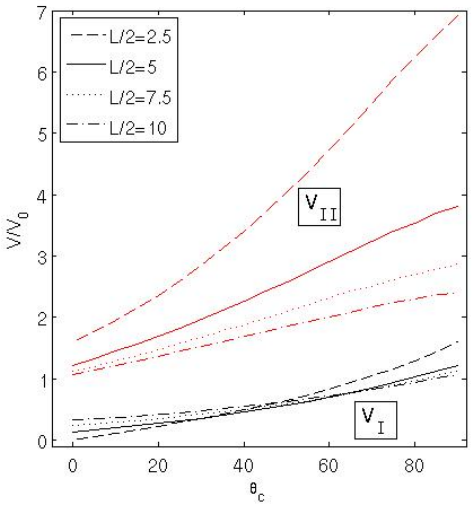

(c) Critical volumes V_I and V_{II} against θ_c.

Figure 4.13: Numerical solutions for V_I and V_{II}.

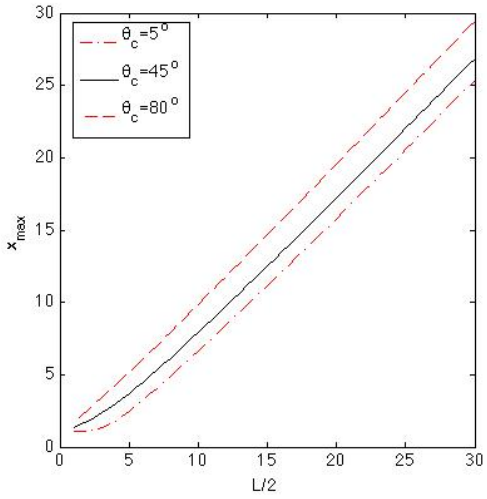

(a) x_{max} against L when $V = V_I$.

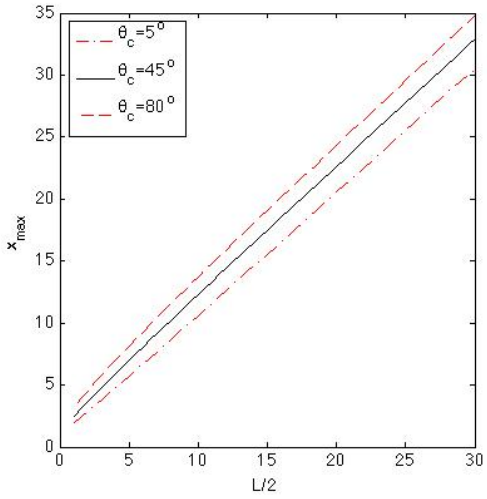

(b) x_{max} against L when $V = V_{II}$.

Figure 4.14: Boundary condition x_{max} as required for critical volumes V_I and V_{II}.

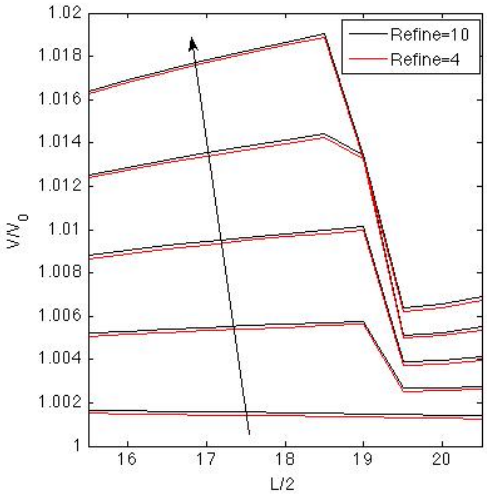

(a) Critical volume V_{III} against L. The arrow indicates increasing θ_c where $\theta_c = 5^o$, 10^o, 15^o, 20^o and 25^o.

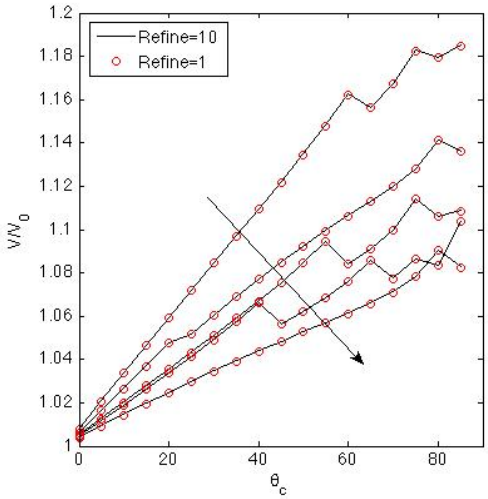

(b) Critical volume V_{III} against θ_c. The arrow indicates increasing L where $L = 1$, 1.5, 2, 2.5 and 3.

Figure 4.15: Numerical solutions for V_{III} when engulfment is of type L and $x_{min} = 10^{-2}$ when the numerical integration was done using the MATLAB solver *ode45*. Results indicate a lack of smoothness numerical results for z and x. 'Refine' is the parameter controlling the number of points in the numerical solution which makes little difference to the numerical results.

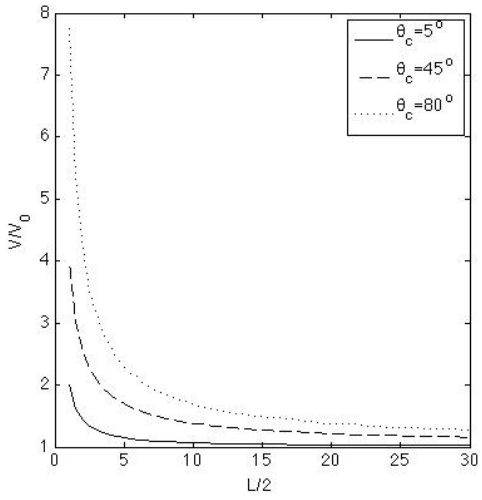

(a) Critical volume V_{III}/V_0 against L.

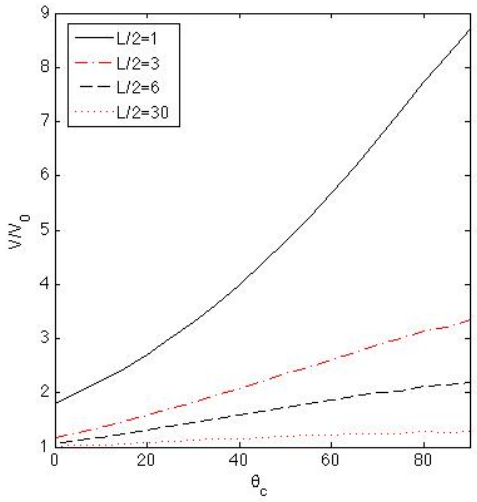

(b) Critical volume V_{III}/V_0 against θ_c.

Figure 4.16: Numerical solutions for V_{III} where engulfment is of type L and $x_{min} = 0.5$.

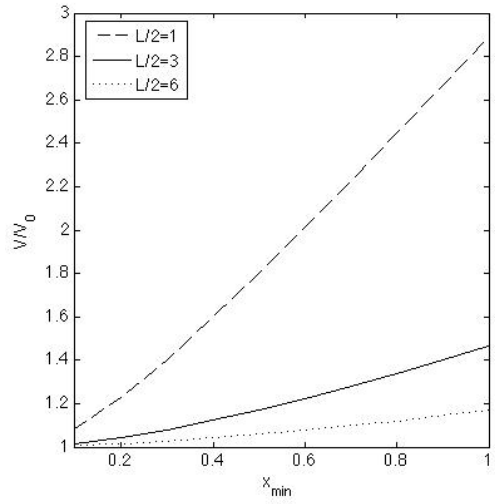

(a) Critical volume V_{III}/V_0 against x_{min} for a range of L where $\theta_c = 0^o$.

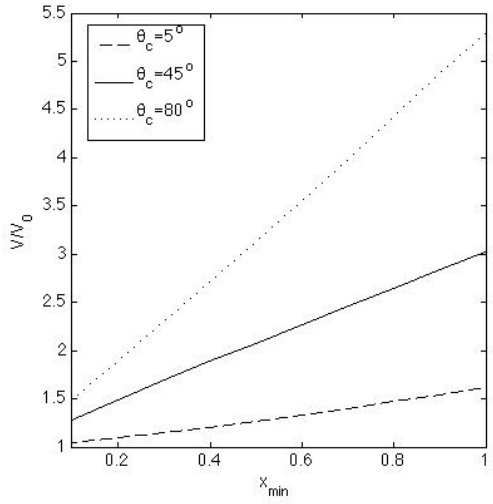

(b) Critical volume V_{III}/V_0 against x_{min} for a range of θ_c where $L = 3$.

Figure 4.17: Numerical solutions for V_{III} where engulfment is of type L and $x_{min} = 0.5$.

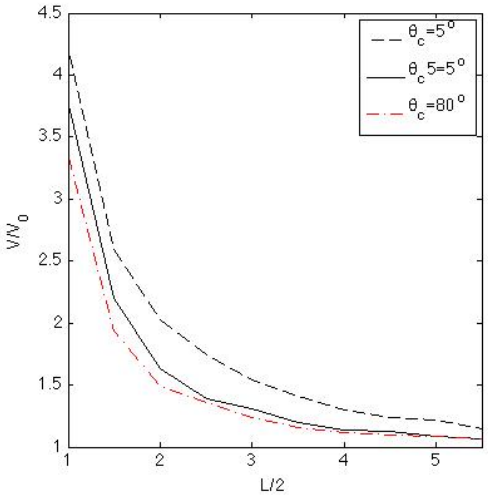

(a) Critical volume V_{III}/V_0 against L.

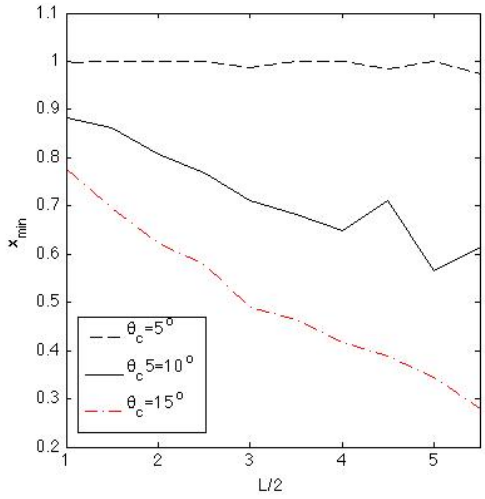

(b) x_{min} against L.

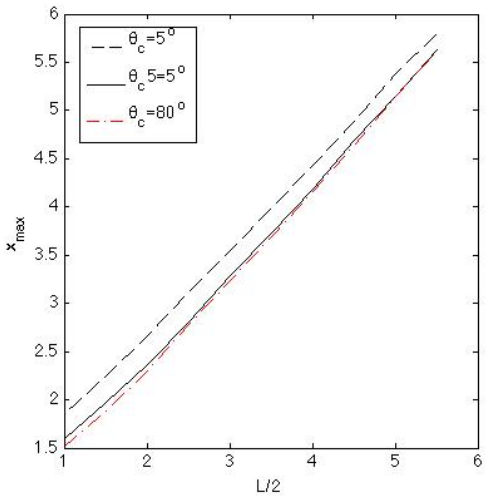

(c) x_{max} against L.

Figure 4.18: Numerical results relating to critical volume V_{III} where engulfment is of type S. Results demonstrate the consequences of the lack of smoothness in solutions when integrating (4.60) numerically when F_1, as defined in (4.107) is small.

Chapter 5

Introduction to the Helfrich Energy Minimisation Problem

5.1 Chapter Summary

The Helfrich energy minimisation problem as outlined in [25] is reviewed in Sections 5.2-5.4. The remaining sections of this chapter present analytical results, which will be referred to when discussing the numerical solutions in Chapter 6. Though plots of numerical solutions to the Helfrich boundary value problem are provided in this Chapter to demonstrate the accuracy of the analytical solutions, full details of how to obtain these analytical solutions will be found in Section 6.3.

The free energy associated with a cell membrane is minimised in Section 5.2. A discussion of the forces implied in the resulting Euler-Lagrange equations can be found in Section 5.3. The boundary conditions of the Helfrich energy minimisation problem are set out in Section 5.4. An introduction to the cell on a fibre boundary value problem is given in Section 5.5 while the normalisation for both the Helfrich boundary value problem and the cell on a fibre boundary problem is given in Section 5.6. The boundary conditions for both the Helfrich boundary value problem and the cell on a fibre boundary problem ensure that the solutions are symmetric about the mid-length. The form of the Helfrich energy used ensures that the solutions are axisymmetric surfaces of rotation.

Analytical solutions found for the Helfrich boundary value problem are given in Sections 5.7-5.11 which have not been found elsewhere. The parameters Δ_p and λ for a spherical solution are found in Section 5.8 for any value of spontaneous curvature c_0. Leading order polynomial solutions for the Helfrich boundary value problem are given in Section 5.9. These solutions are valid when the mean curvature at the axis of rotation κ is asymptotically close to that of a sphere

$$\kappa = 1 + \delta, \tag{5.1}$$

so that δ is small in the case when $c_0 = 0$. These analytical solutions are used to provide initial estimates when numerical solutions for the cell on a fibre problem are found in Chapter 6. These analytical solutions are compared to the solutions found by numerical methods.

In Chapter 6 it will be seen how branchlines of solutions to the Helfrich or cell on a fibre boundary value problems are formed by perturbing certain parameters. These branchlines of solutions end when no further solutions of acceptable error can be found. This numerical error arises from the use of approximations to the Euler-Lagrange equations at $s = 0$ and $s = 1/2$ given in Section 5.4. In Section 5.9.1 it is checked whether the conditions at the singularity at the maximum radius are consistent with the leading order solutions found in Section 5.9. The consequences of numerical error to the leading order solutions is accounted for in Section 5.9.2. Including this numerical error in the analytical solutions improves the fit of the analytically derived boundary conditions with the numerically found solutions.

Numerically calculated higher order corrections to the the leading order solutions found in Section 5.10 were found to be consistent with what can be deduced analytically. Finally, Section 5.11 shows how when the absolute value of spontaneous curvature is small, c_0 dependent terms up to $O(\delta)$ cancel so that the leading order solutions for $c_0 = 0$ are still applicable.

Finally, the Euler-Lagrange equations were examined as a dynamical system in Section

5.13. The discussion in this section is referenced heavily in the discussion of the numerical solutions of the cell on a fibre boundary value problem in Chapter 6.

5.2 Minimisation of the Helfrich Energy

As in the previous chapter, the cell is modelled as a surface of revolution around an axis of rotation. From (4.42) and (4.44) in Chapter 4 we can write

$$ds = \frac{2\pi x}{\cos\phi(x)}dx = 2\pi x(1-(c_p x^2))^{-1/2}dx, \tag{5.2}$$

$$dV = \pi x^2 \tan\phi(x)dx = \pi c_p x^3(1-(c_p x^2))^{-1/2}dx. \tag{5.3}$$

Equations (5.2)-(5.3) and (4.17)-(4.18) can be used to write the free energy of a cell membrane

$$F = \int (1/2)k_c\left(c_m + c_p - c_0\right)^2 dS + \int \Delta_p dV + \int \lambda dS, \tag{5.4}$$

as

$$\pi \int x(1-(c_p x)^2)^{-1/2}\left\{k_c\left(x\frac{dc_p}{dx} + 2c_p - c_0\right)^2 + \Delta_p x^2 c_p + 2\lambda\right\}dx, \tag{5.5}$$

where c_m is eliminated from (5.4) by using the relation

$$\frac{dc_p}{dx} = \frac{c_m - c_p}{x}. \tag{5.6}$$

This relation is identical to (4.29) but has been given here for convenience. In this chapter it will be referred to as the symmetry condition. The terms proportional to k_c in (5.5) are the Helfrich energy E_H, which is

$$\int E_H\, dx = \int (1/2)k_c\left(2c_p + x\frac{dc_p}{dx} - c_0\right)^2 \frac{2\pi x}{\left(1-(xc_p)^2\right)^{1/2}}dx. \tag{5.7}$$

The Euler-Lagrange equation of the Helfrich energy minimisation problem is

$$\frac{\partial E_H}{\partial c_p} - \frac{d}{dx}\frac{\partial E_H}{\partial \dot{c_p}} = 0. \tag{5.8}$$

This integral is minimised w.r.t. $c_p(x)$ or $\phi(x)$. The partial derivatives in (5.8) are

$$\frac{\partial E_H}{\partial c_p} = \pi\frac{x^3 c_p}{\left(1-(xc_p)^2\right)^{3/2}}\left(2c_p + x\frac{dc_p}{dx} - c_0\right)^2 \tag{5.9}$$

$$+ \frac{2\pi x}{\left(1-(xc_p)^2\right)^{1/2}}\left(2c_p + x\frac{dc_p}{dx} - c_0\right) \tag{5.10}$$

and

$$-\frac{d}{dx}\frac{\partial E_H}{\partial \dot{c_p}} = -2\pi\frac{d}{dx}\left(\frac{x}{\left(1-(xc_p)^2\right)^{1/2}}\left(2c_px+x^2\frac{dc_p}{dx}-c_0x\right)\right) \tag{5.11}$$

$$= -\frac{2\pi x}{\left(1-(xc_p)^2\right)^{1/2}}\left(4x\frac{dc_p}{dx}+x^2\frac{d^2c_p}{dx^2}+2c_p-c_0\right) \tag{5.12}$$

$$- \frac{2\pi}{\left(1-(xc_p)^2\right)^{1/2}}\left(2c_px+x^2\frac{dc_p}{dx}-c_0x\right) \tag{5.13}$$

$$- \frac{2\pi c_px(c_px+x^2\frac{dc_p}{dx})}{\left(1-(xc_p)^2\right)^{3/2}}\left(2c_px+x^2\frac{dc_p}{dx}-c_0x\right). \tag{5.14}$$

The lines (5.10), (5.12) and (5.13) can be combined and re-arranged to find

$$-2\pi\frac{x^2}{(1-(xc_p)^2)^{1/2}}\left(\frac{dc_m}{dx}+\frac{dc_p}{dx}\right), \tag{5.15}$$

where by differenting (5.6) we have

$$\frac{dc_p^2}{dx^2} = \frac{1}{x}\left(\frac{dc_p}{dx}-\frac{dc_m}{dx}\right)-\frac{c_m-c_p}{x^2}, \tag{5.16}$$

$$= -\frac{1}{x}\frac{dc_m}{dx}. \tag{5.17}$$

The terms in (5.14) are also be re-arranged to find

$$-2\pi\frac{c_px^3}{(1-(xc_p)^2)^{3/2}}c_m\left(c_m+c_p-c_0\right). \tag{5.18}$$

Writing the Euler-Lagrange equation (5.8) in terms of c_p and c_m results in

$$\begin{aligned}(xc_p)(k_c/2)\left(c_m+c_p-c_0\right)^2-(xc_p)k_c\left(c_m+c_p-c_0\right)c_m& \\ -(1-(xc_p)^2)k_c\frac{dc_p}{dx}-(1-(xc_p)^2)k_c\frac{dc_m}{dx} &= 0.\end{aligned} \tag{5.19}$$

The force associated with the surface energy term has been found in the previous section to be (4.25) and that for the volume energy was found to be (4.26). Recalling that $xc_p=\sin\phi$, these terms can be added to (5.19) so that the balance of forces associated with the Helfrich energy variation problem is

$$\begin{aligned}&x\sin\phi(k_c/2)\left(c_m+c_p-c_0\right)^2-x\sin\phi k_cc_m\left(c_m+c_p-c_0\right)+x\sin\phi\lambda+(1/2)\Delta_px^2 \\ -\;&\cos^2\phi xk_c\frac{dc_p}{dx}-\cos^2\phi xk_c\frac{dc_m}{dx}=0.\end{aligned} \tag{5.20}$$

The bending constant k_c has dimension of [Energy] so it can be checked that each term in (5.20) has dimensions of force [Energy]/[L]. $x\sin\phi\lambda$ is the well-known term for the capillary

force where λ is the curvature-independent tension. The other terms are forces associated with curvature-dependent tensions which have been defined in [44] as

$$\sigma^{iso} = k_c \left(c_m + c_p - c_0\right)^2, \tag{5.21}$$

$$\sigma^{dir} = -k_c \left(c_m + c_p - c_0\right) c_m, \tag{5.22}$$

$$\sigma^{t} = -\cos\phi k_c \frac{dc_p}{dx} - \cos\phi k_c \frac{dc_m}{dx}. \tag{5.23}$$

In (5.20) the tensions (5.21)-(5.23) have been resolved along the axis of rotation which has been labelled the z-axis. For the forces associated with σ^{iso} and σ^{dir} the direction of this force is tangent to the surface as shown Figure 5.1(a). For σ^t the direction of this force is perpendicular to the surface and is resolved along the z-axis as shown Figure 5.1(b).

In Helfrich's paper [44] σ^{iso} is labelled as an isotropic tension while σ^{dir} is labelled as a directed tension. The force associated with the tension σ^t is identified as a torque. In (5.20), the directed tension is offset to some extent by the isotropic tension, resulting in a new combined term

$$\sigma_{net} = (1/2)\sigma_{iso} + \sigma_{dir}, \tag{5.24}$$

$$= (1/2)c_p x \left(\left(c_p - c_0\right) + c_m\right)\left(\left(c_p - c_0\right) - c_m\right), \tag{5.25}$$

$$= (1/2)c_p x \left(\left(c_p - c_0\right)^2 - c_m^2\right). \tag{5.26}$$

The net tension can be interpreted as a kind of shear term associated with the cell membrane being bent in the two perpendicular principal curvature directions. The spontaneous curvature appears as a correction to the principal curvature c_p. A positive spontaneous curvature would favour a larger value of c_p. This would result in a flatter cell profile with a smaller average radius corresponding to a prolate shape. A negative spontaneous curvature would favour a more curved oblate profile.

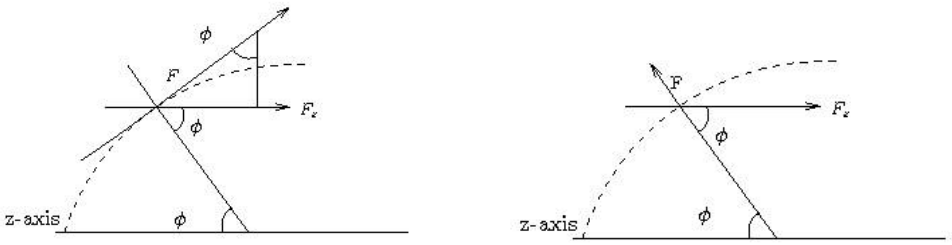

(a) Diagram of a force tangential to the surface F and its component along the z-axis $F_z = F\sin\phi(x)$.

(b) Diagram of a force perpendicular to the surface F and its component along the z-axis $F_z = F\cos\phi(x)$.

Figure 5.1: Sketches of how the forces associated with the tensions (5.21)-(5.23) acting on the surface $z(x)$ (dotted line) are resolved along the z-axis.

5.3 Integration of Forces to find Length and Surface Area

The forces can be integrated w.r.t. x by arranging (5.20) and using the symmetry condition (5.6) as

$$k_c\frac{dc_m}{dx} = x\left(1-(xc_p)^2\right)^{-1}\left\{(1/2)k_c c_p((c_p-c_0)^2-c_m^2)+\lambda c_p+(1/2)\Delta_p\right\} \quad (5.27)$$

$$- k_c\frac{c_m-c_p}{x}, \quad (5.28)$$

$$\frac{dc_p}{dx} = \frac{c_m-c_p}{x}. \quad (5.29)$$

The Weierstrass excess function of the Euler-Lagrange equation (5.8) is always positive (Appendix C.3) indicating that any given function for $c_p(x)$ and $c_m(x)$ will have a larger or equal energy to the solutions found by solving the Euler-Langrange equations (5.28) and (5.29). The Euler-Langrange equation is always a minimiser rather than a maximiser.

Solutions at $k_c = 0$

When the bending constant k_c is set to zero only the surface and volume energy terms in (5.4) remain. The governing equation is

$$\frac{\Delta_p}{\lambda} = c_m + c_p. \quad (5.30)$$

These constant mean curvature solutions have been investigated in depth in the previous chapter.

Solutions as $k_c \to \infty$

The limits of (5.28) and (5.29) are now

$$\frac{dc_m}{dx} = x\left(1-(xc_p)^2\right)^{-1}\left\{(1/2)c_p((c_p-c_0)^2-c_m^2)\right\}-\frac{c_m-c_p}{x}, \quad (5.31)$$

$$\frac{dc_p}{dx} = \frac{c_m-c_p}{x}. \quad (5.32)$$

The first term in (5.31) is the net tension (5.26), which acts tangentially to the surface, resolved along the z-axis. The other terms are an expression of (5.23), the tension acting perpendicularly to the surface.

By (5.2), the surface area for a unit sphere $c_p \equiv 1$ and $0 < x < 1$ is

$$S = \int_0^1 \frac{2\pi x}{(1-x^2)^{1/2}} dx = \pi. \tag{5.33}$$

An assumption first established in [44] is that a bilayer does not stretch and so the surface area, S is fixed. To enforce this assumption it is convenient to write the second-order problem as a third order problem w.r.t. ds. At this point the surface area element (5.2) can be scaled so that the surface area of a sphere with unit radius is 1. Therefore we can write

$$dx = \pm(2/x)\left(1-(xc_p)^2\right)^{1/2} ds. \tag{5.34}$$

In this way x is a function of s. It is convenient to define a new variable $f = x(s)^2$ so that

$$\frac{df}{ds} = 2x\frac{dx}{ds} = 4\left(1-(xc_p^2)\right)^{1/2}. \tag{5.35}$$

The resulting third order problem is

$$\begin{aligned}
\frac{dc_m}{ds} &= \pm\left(1-fc_p^2\right)^{-1/2}\left\{c_p((c_p-c_0)^2-c_m^2)+2(\lambda/k_c)c_p+(\Delta_p/k_c)\right\} \\
&\quad \mp 2(1-fc_p^2)^{1/2}(c_m-c_p)/f, && (5.36)\\
\frac{dc_p}{ds} &= \pm 2(1-fc_p^2)^{1/2}(c_m-c_p)/f, && (5.37)\\
\frac{df}{ds} &= \pm 4(1-fc_p^2)^{1/2}. && (5.38)
\end{aligned}$$

These equations will be referred to repeatedly throughout Part II as the Euler-Lagrange equations. All solutions for the shape of a cell membrane will be found using (5.36)-(5.38), using different boundary conditions are appropriate.

Note that there is a choice of sign in (5.36)-(5.38) from (5.34) and the surface area to be $S = s_{max}$. After integrating (5.36)-(5.38) numerically to find $f(s)$ and $c_p(s)$, length of the fibre $z(s_{max})$, and volume of the droplet $V(s_{max})$ can be found by integrating numerically again. The integrals (4.44) and (4.45) for volume and length and be re-written in terms of c_p, f and ds as defined in (5.34) so that

$$\begin{aligned}
z(s_{max}) &= 2\int_0^{s_{max}} c_p(s)ds, && (5.39)\\
V(s_{max}) &= 2\pi\int_0^{s_{max}} f(s)c_p(s)ds. && (5.40)
\end{aligned}$$

The profile of the droplet is the radius, $x(s) = \sqrt{f(s)}$ plotted against the length, $z(s)$. It is very important to bear this geometry in mind throughout the reading of Chapters 5 and 6.

5.4 The Helfrich Boundary Value Problem

The Helfrich boundary value problem (HBP) is the boundary value problem set out in [44] where there is no fibre at the axis of rotation. Firstly, the surface area of a biological cell does not change significantly as it changes shape so the total surface area can be normalised to a constant value of $s_{max} = 1$. The normalisation of (5.36)-(5.38) is discussed in Section 5.6. We choose the convention that $s = 0$ when $x = x_{min}$. Boundary conditions must also be chosen to avoid singularities in (5.36)-(5.38).

5.4.1 Singularity at $f = 0$ when $\phi(x) = 0$

The right-hand sides of equations (5.36) and (5.37) are finite if the boundary condition

$$f(0) = 0 \quad \text{when} \quad c_p(0) = c_m(0) = \kappa \tag{5.41}$$

is set.

In the limit $s \to 0$, (5.36)-(5.38) are

$$\frac{dc_m}{ds} = \frac{3}{4}\left[c_p\left((c_p - c_0)^2 - c_m^2\right) + 2\lambda c_p + \Delta_p\right], \tag{5.42}$$

$$\frac{dc_p}{ds} = \frac{1}{4}\left[c_p\left((c_p - c_0)^2 - c_m^2\right) + 2\lambda c_p + \Delta_p\right], \tag{5.43}$$

$$\frac{df}{ds} = 4, \tag{5.44}$$

which are derived in Appendix C.4. If $c_p(0) = c_m(0)$ then $\tan\phi(0) = 0$ which implies that $\phi(0) = 0$. The surface of the shape is perpendicular to the axis of rotation, avoiding a corner at that point.

5.4.2 Singularity at $fc_p^2 = 1$ when $\phi = \pm\pi/2$

There is a singularity in (5.36) when $fc_p^2 = 1$ at which point there is either a maxima or a minima in f. The singularities occur when $\phi(s) = \pm\pi/2$ so that the tangent to the surface is parallel to the axis of rotation. (5.36) is finite at $fc_p^2 = 1$ if at that point

$$c_p((c_p - c_0)^2 - c_m^2) + 2(\lambda/k_c)c_p + (\Delta_p/k_c) = 0. \tag{5.45}$$

The limit of (5.36) can be any value depending on the parameters chosen. Take $s = s^*$ when $fc_p^2 = 1$ and

$$\gamma = \frac{dc_m}{ds}|_{s=s^*}. \tag{5.46}$$

The values of $c_m(s)$, $c_p(s)$ and $f(s)$ around this point are found by making the following Taylor expansions

$$c_m(s) = c_m(s^*) + \gamma(s - s^*) + (1/2)\frac{d^2c_m}{ds^2}|_{s=s^*}(s - s^*)^2 + \cdots, \tag{5.47}$$

$$c_p(s) = c_p(s^*) + (1/2)\frac{d^2c_p}{ds^2}|_{s=s^*}(s - s^*)^2 + \cdots, \tag{5.48}$$

$$f(s) = f(s^*) + (1/2)\frac{d^2f}{ds^2}|_{s=s^*}(s - s^*)^2 + \cdots. \tag{5.49}$$

These Taylor expansions can be used to perturb the solution away from the singularity. The second derivatives required for the Taylor expansion are given in Appendix C.5.

Recall that for constant mean curvature surfaces $\phi(s) = \pi/2$ ensures that the solution is symmetric around this point. The Euler-Lagrange equations require an additional condition so that (5.36)-(5.38) are at a stationary point and so symmetric at $\phi(s) = \pi/2$. Referring to (5.47)-(5.49) this condition is

$$fc_p^2 = 1 \quad \text{and} \quad \gamma = 0 \quad \text{at} \quad s^* = 1/2. \tag{5.50}$$

The maximum radius will be at a singularity. Take the maximum radius to be $x_{max} = l$ at which point $s = s^*$. By the definition of c_p in (4.17) we have

$$f(s^*) = l^2, \qquad c_p(s^*) = \frac{1}{l}. \tag{5.51}$$

At the singularity $fc_p^2 = 1$ we have $\phi = \pi/2$, so that $\cos\phi = 0$. Also when $\phi = \pi/2$, $dx/d\phi = 0$, so the value of c_m is the limit

$$c_m = \frac{\cos\phi}{dx/d\phi}|_{\lim fc_p^2 \to 1}, \tag{5.52}$$

which is not necessarily zero.

Singularities are therefore expected at both $s = 0$ and $s = 1/2$. The boundary values can be perturbed away from $s = 0$ using (5.42)-(5.44) and from $s = 1/2$ using (5.47)-(5.49). The solutions can then be integrated towards each other to be matched at some intermediate point. This is discussed in detail in Section 6.3.

5.5 Cell on a Fibre Boundary Value Problem

The boundary conditions at the maximum radius are the same as for the Helfrich boundary value problem (5.51). In this section we define how the boundary conditions on the surface of the fibre relate to the well known definition of a contact angle. The value of $f(0)$ now has a minimum value which is the radius of the fibre, r. The angle of the cell surface can be set at a given contact angle as for the droplet model in Chapter 4. A homogeneous liquid is only at an equilibrium on a surface for a given contact angle at the three phase (liquid/solid/air) boundary. However, in this case, the surface is not defined by an air/liquid boundary but the membrane of the cell so this the condition on the contact angle is not necessary to ensure that the cell model is at a physically justifiable equilibirum. For any contact angle θ, the boundary condition at $x = x_{min}$ are

$$f(0) = f_0 = R^2, \quad \text{when} \quad c_p(0) = \frac{\sin\pi/2 - \theta}{R}. \tag{5.53}$$

There is no singularity at x_{min} so the choice of $c_m(0)$ is independent from $c_p(0)$. There are twelve different individual boundary value problems in Sections 6.5, 6.6 and 6.7 which are best understood in context. The aims of these boundary conditions are summarised in Section 6.1.

5.6 Normalisation of the Helfrich Problem

The surface area S of a cell will be treated as fixed. The variables in (5.36)-(5.38) can be non-dimensionalised according to

$$s = S\tilde{s}, \tag{5.54}$$
$$c_m = \alpha\tilde{c_m}, \tag{5.55}$$
$$c_p = \beta\tilde{c_p}, \tag{5.56}$$
$$f = \gamma\tilde{f}, \tag{5.57}$$

where we now find α, β and γ. The term $(1 - fc_p^2)^{1/2} = \sin\phi$ is dimensionless from which it is known that

$$\gamma\beta^2 = 1. \tag{5.58}$$

Equations (5.38) can be used to find

$$\gamma = S, \tag{5.59}$$

while equation (5.37) implies that c_m and c_p have the same normalisation. The normalised variables are therefore

$$s = S\tilde{s}, \tag{5.60}$$
$$c_m = S^{-1/2}\tilde{c_m}, \tag{5.61}$$
$$c_p = S^{-1/2}\tilde{c_p}, \tag{5.62}$$
$$f = S\tilde{f}. \tag{5.63}$$

The corresponding normalisations for the parameters are

$$\Delta/k_c = S^{-3/2}\tilde{\Delta}, \tag{5.64}$$
$$\lambda/k_c = S^{-1}\tilde{\lambda}. \tag{5.65}$$

Also, by (5.39) and (5.62), the length of the fibre can be normalised so that

$$Z = S^{-1/2}\tilde{Z}. \tag{5.66}$$

Once a solution is found which satisfies the required boundary conditions, its surface area can be scaled to 1.

In Section 5.3 is was stated that the surface area element (5.2) was normalised so that a sphere with a unit radius had a surface area of 1. Therefore, if a solution of the Helfrich ODEs is a sphere and has a surface area of 1, the radius of the sphere (r_0) would also be 1. The maximum possible volume of a shape found as a solution to the Helfrich ODEs (5.36)-(5.38) is the volume of a unit sphere or $V_s = (4\pi/3)r_0^3$. The volume plotted in the numerical results in Section 6.4 is the normalised volume found by the integral

$$V_0 = V/V_{sphere} = (3/2)\int_0^1 f(s)c_p(s)ds. \tag{5.67}$$

This is the integral (5.40) normalised by V_s. In general, any reference to volume can be taken as a reference to this normalised volume. Similarly, the Helfrich energy can be normalised by the Helfrich energy of a sphere

$$E_{H0} = \int_0^1 \frac{(c_m + c_p - c_0)^2}{(2 - c_0)^2} ds. \tag{5.68}$$

This normalisation is particularly useful as it allows the Helfrich energy of shapes with different c_0 to be compared. The length of a sphere given by the integral (5.39) will give a value of $2r_0$ and does not need any further normalisation. As length, volume and Helfrich energy have been non-dimensionalised no units of measurement are used in Chapters 5 and 6.

5.7 Constant Mean Curvature Solutions

In this section we write the solutions for a sphere in terms of parameters c_m, c_p and f in order to clarify how the variables in Chapter 4 relate to those in this chapter and also in Chapter 6. If the boundary conditions in (5.41) are written as

$$c_p(0) = \alpha, \tag{5.69}$$

$$c_m(0) = \alpha, \tag{5.70}$$

then (5.38) can be integrated to find

$$\frac{df}{ds} = \pm\left(1 - f\alpha^2\right)^{1/2}, \tag{5.71}$$

$$f = \frac{1}{\alpha^2}\left(1 - (2s\alpha^2 + \beta)^2\right). \tag{5.72}$$

As the convention $f(0) = 0$ has been adopted, we have

$$f(1/2) = \pm 2 - \alpha^2. \tag{5.73}$$

For a normalised sphere $\alpha = 1$, so $\beta = -1$ will give $f(1/2) = 1$, which is consistent with boundary condition (5.50).

In Chapter 4 the surfaces of rotation all had constant mean curvature. As discussed in the beginning of Section 5.3, if only the terms associated with forces perpendicular to the surface are used in (5.36)-(5.38) the solutions have constant mean curvature. The resulting system of ODEs in terms of c_m, c_p and f is

$$\frac{dc_m}{ds} = \mp 2(1 - fc_p^2)^{1/2}(c_m - c_p)/f, \tag{5.74}$$

$$\frac{dc_p}{ds} = \pm 2(1 - fc_p^2)^{1/2}(c_m - c_p)/f, \tag{5.75}$$

$$\frac{df}{ds} = \pm 4(1 - fc_p^2)^{1/2}. \tag{5.76}$$

5.8 Spherical Solution Parameters

A solution for a sphere has known values of parameters Δ_p and λ. This provides a known set of parameters from which further parameters can be found numerically. Δ_{pc0} and λ_{c0} are the values of Δ_p and λ for a spherical solution when $c_0 = 0$. Δ_{pc} and λ_c are the values of Δ_p and λ for a spherical solution as a function of c_0. By (6.29) it is also known that there is a solution for a sphere when

$$\Delta_{pc} = (12 - 2c_0) \tag{5.77}$$

and (5.45) are true, which can be solved for $c_0 = 0$ to find

$$\lambda_{c0} = -6, \tag{5.78}$$

$$\Delta_{pc0} = 12. \tag{5.79}$$

When $c_0 \neq 0$, then

$$\Delta_{pc} = -2\lambda_{c0} - 2c_0 \tag{5.80}$$

and (5.45) become

$$0 = 2\lambda_c + \Delta_{pc} - 2c_0 + c_0^2, \tag{5.81}$$

which implies

$$\lambda_c = \lambda_{c0} + 2c_0 - c_0^2/2. \tag{5.82}$$

This has a maximum at $\lambda_c = 2$, which is also the point where the normalised Helfrich energy (5.68) is singular.

5.9 Helfrich Boundary Problem Solutions when $c_0 = 0$

The solutions of c_m, c_p and f in Section 5.8 for a normalised sphere can be used to write c_m, c_p and f asymptotic expansions in $\delta << 1$ where

$$c_m(0) = c_p(0) = 1 + \delta. \tag{5.83}$$

Solutions can be said to be close to a spherical solution when $2\lambda + \Delta_p \approx 0$ so define ϵ as

$$\epsilon = 2\lambda c_{p0} + \Delta_p, \tag{5.84}$$

where

$$\begin{aligned} c_{m0} &= 1 + \delta, & (5.85)\\ c_{p0} &= 1 + \delta, & (5.86)\\ f_0 &= 4(s - s^2). & (5.87) \end{aligned}$$

Take c_{m0}, c_{p0} and f_0 to be leading order terms in asymptotic expansions given here as

$$\begin{aligned} c_m &= c_{m0} + \epsilon c_{m1} + \epsilon^2 c_{m2} + \ldots, & (5.88)\\ c_p &= c_{p0} + \epsilon c_{p1} + \epsilon^2 c_{p2} + \ldots, & (5.89)\\ f &= f_0 + \epsilon f_1 + \epsilon^2 f_2 + \ldots\ . & (5.90) \end{aligned}$$

Equation (5.90) follows from the solution for f in (5.72) in the case when curvature is constant. When δ is small, then the solutions found are such that ϵ is of the same order of magnitude. It will be shown how ϵ and δ are proportional to each other. However, initially it is necessary for both terms to be defined separately. The solutions in this section can be compared to corresponding numerical solutions in order to understand how errors in the numerical solutions arise.

If $\delta = 0$ then the solution will be that of a sphere. The term (5.87) is the solution (5.72) in the case that the boundary conditions for a unit sphere have been imposed. When $c_0 = 0$, a solution for a sphere requires $\lambda = -6$ and $\Delta_p = 12$. By (5.84), $\epsilon = 0$, and there will be no $O(\epsilon)$ expansions to c_m, c_p and f. If $|\delta| > 0$ then there will be $O(\epsilon)$ correction terms to the leading order terms.

The parameters λ and Δ_p can also be written as asymptotic expansions with respect to ϵ so that

$$\lambda = \lambda_0 + \epsilon\lambda_1 + \cdots, \tag{5.91}$$

$$\Delta_p = \Delta_{p0} + \epsilon\Delta_{p1} + \cdots. \tag{5.92}$$

Taking λ_0 and Δ_{p0} as unknowns, the known leading order terms in c_m, c_p and f are now used to find them. The conditions required to meet the required boundary conditions to $O(\delta^2)$ are then discussed. Finally, the resulting solutions are compared to the corresponding numerical solutions. Full details on obtaining numerical solutions can be found in Section 6.3. By (5.42)-(5.44), when $s << 1$,

$$c_{m1} \approx \frac{3\epsilon}{4}s, \tag{5.93}$$

$$c_{p1} \approx \frac{\epsilon}{4}s. \tag{5.94}$$

To find c_{p1} and c_{m1} for all s in $0 < s < 1$, then (5.90) can be used to write (5.37) as

$$\frac{dc_{p1}}{ds} = \frac{1-2s}{2(s-s^2)}(c_{m1} - c_{p1}), \tag{5.95}$$

which suggests a solution of the form

$$c_{m1} - c_{p1} = \gamma\left(s - s^2\right). \tag{5.96}$$

So, for large s, (5.93)-(5.94) can be written as

$$c_{m1} = \alpha\left(s - s^2\right), \tag{5.97}$$

$$c_{p1} = \beta\left(s - s^2\right), \tag{5.98}$$

$$\gamma = \alpha - \beta. \tag{5.99}$$

If $c_p(c_p^2 - c_m^2)$ is expanded as a series in ϵ, then we have

$$c_p((c_p - c_0)^2 - c_m^2) = 2\epsilon(c_{p1} - c_{m1}) + O(\epsilon^2). \tag{5.100}$$

Write (5.36) using (5.97) and (5.98) so that

$$\frac{dc_m}{ds} = \frac{2(c_{p1} - c_{m1})}{1-2s} - \epsilon\frac{1-2s}{2(s-s^2)}(c_{m1} - c_{p1}) + O(\epsilon), \tag{5.101}$$

$$\frac{dc_{m1}}{ds} = \frac{2(\beta-\alpha)(s-s^2) + 2\lambda_0\beta(s-s^2) + \epsilon}{1-2s} - \frac{(1-2s)(\alpha-\beta)}{2}. \tag{5.102}$$

Then if

$$\alpha = \alpha_0\epsilon, \qquad \beta = \beta_0\epsilon \tag{5.103}$$

and

$$2(\beta_0 - \alpha_0)(s-s^2) + 2\lambda_0\beta_0(s-s^2) + 1 = (1-2s)^2 + O(\epsilon), \tag{5.104}$$

we have

$$\frac{dc_{m1}}{ds} = \epsilon(1-2s)\left(1-\frac{(\alpha_0-\beta_0)}{2}\right), \tag{5.105}$$

$$\frac{dc_{p1}}{ds} = \epsilon(1-2s)\frac{\alpha_0-\beta_0}{2}. \tag{5.106}$$

Equation (5.104) is satisfied when

$$2(\alpha_0-\beta_0)+2\lambda_0\beta_0=-4. \tag{5.107}$$

By (5.97) and (5.105) we have

$$\alpha_0-3\beta_0=0 \tag{5.108}$$

and by (5.98) and (5.106) we have

$$3\alpha_0-\beta_0=2. \tag{5.109}$$

The three conditions, (5.107)-(5.109) are all true if the three unknowns are

$$\alpha_0 = \frac{3}{4}, \tag{5.110}$$

$$\beta_0 = \frac{1}{4}, \tag{5.111}$$

$$\lambda_0 = -6. \tag{5.112}$$

The leading order term for λ, λ_0, is the same as the value of λ required for a spherical solution. The leading order term for Δ_p can be found by solving

$$2\lambda_0+\Delta_{p0}=0 \tag{5.113}$$

to find

$$\Delta_{p0}=12, \tag{5.114}$$

so that the λ and Δ_p dependent terms cancel to $O(\epsilon)$. The values for α_0 and β_0 are consistent with the limiting values of (5.36) and (5.37) given in (5.42) and (5.43) at $f=0$, and also the condition (5.45) at $fc_p^2=1$, where Δ_p and λ are given by (5.80)-(5.82). Using the initial conditions (5.85)-(5.86) and quadratic solutions (5.97)-(5.98) it is expected that at $s=1/2$ we have

$$c_p(1/2) \approx 1+\delta+\frac{\epsilon}{16}, \tag{5.115}$$

$$c_m(1/2) \approx 1+\delta+\frac{3\epsilon}{16}. \tag{5.116}$$

By (5.86), $c_p(0)=1+\delta$ at $s=0$ so that (5.84) is

$$\epsilon=2\lambda c_p(0)+\Delta_p=-12\delta+O(\delta^2). \tag{5.117}$$

The boundary conditions at $s=1/2$ require that

$$c_p(c_p^2-c_m^2)+2\lambda c_p+\Delta_p=0. \tag{5.118}$$

Using known solutions (5.115) and (5.116), with (5.117) to convert ϵ to δ, we know that

$$c_p(c_p^2 - c_m^2) = 12\delta(s - s^2) + O(\delta^2), \tag{5.119}$$

$$2\lambda c_p + \Delta_p = -12\delta + 36\delta(s - s^2) + 2\lambda_1\delta + \Delta_{p1}\delta + O(\delta^2). \tag{5.120}$$

If

$$2\lambda_1 + \Delta_{p1} = 0, \tag{5.121}$$

then at $s = 1/2$ the required boundary condition (5.118) is met to $O(\delta^2)$ so that

$$c_p(c_p^2 - c_m^2) + 2\lambda c_p + \Delta_p = O(\delta^2). \tag{5.122}$$

λ_1 balances $O(\delta^2)$ terms in c_m and c_p as will be discussed in Section 5.10.1. Their value can be calculated from the numerical solutions in Figure 5.2 so that

$$\lambda_1 = \frac{5}{6} + \frac{3}{100} = \frac{43}{50}, \tag{5.123}$$

$$\Delta_1 = -\frac{86}{50}. \tag{5.124}$$

The method used to find a numerical solution to the Euler-Lagrange equations is given in detail in Section 6.3. In summary, the leading order solutions for the Helfrich boundary value

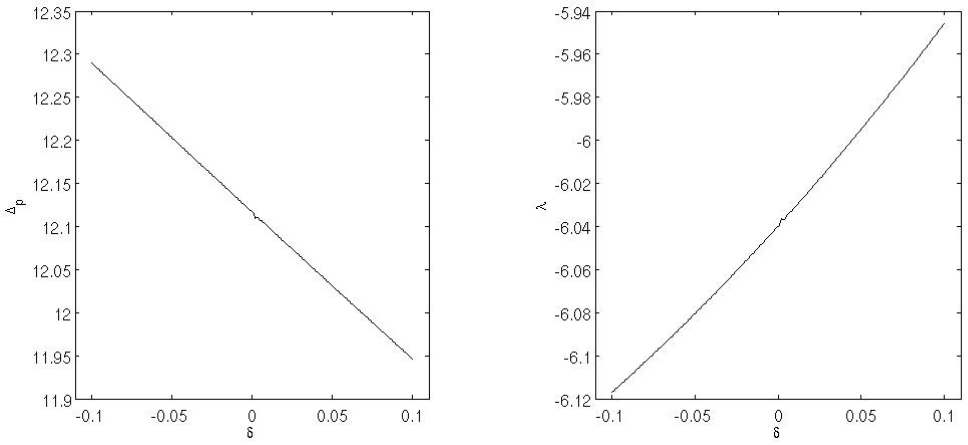

(a) Numerically calculated value of Δ_p against δ.

(b) Numerically calculated value of λ against δ.

Figure 5.2: Dependence of Δ_p and λ on δ.

problem described in (5.4) are

$$c_m = 1 + \delta - 9\delta(s - s^2) + O(\delta^2), \tag{5.125}$$

$$c_p = 1 + \delta - 3\delta(s - s^2) + O(\delta^2), \tag{5.126}$$

$$f = 4(s - s^2) + O(\delta), \tag{5.127}$$

$$\Delta_p = 12 + O(\delta), \tag{5.128}$$

$$\lambda = -6 + O(\delta), \tag{5.129}$$

$$\epsilon = -12\delta + O(\delta^2). \tag{5.130}$$

These solutions have been plotted against the numerically calculated solutions of c_m, c_p and f in Figure 5.3. The solutions are still reasonably accurate when $\delta = 0.1$ is relatively large. Deviation between numerical and analytical solutions is greatest near $s = 1/2$. At $s = 1/2$, the solutions to the Euler-Lagrange equations (5.36)-(5.38) are matched to Taylor expansions of the Euler-Lagrange equations as discussed in Section 5.4.2. The Euler-Lagrange equations are expanded to $O(s^2)$ and therefore there will be some loss of accuracy when the solutions to the Taylor expansions are matched to the solutions of the Euler-Lagrange equations.

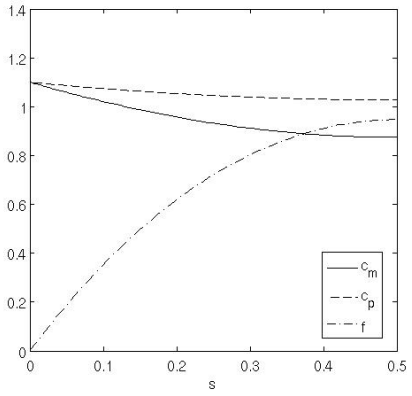

(a) Numerical solutions to c_m, c_p and f.

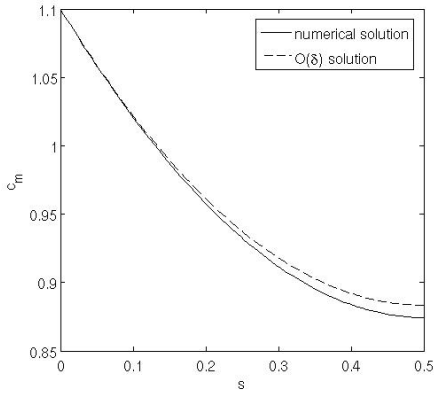

(b) Numerical and leading order analytical solution to c_m.

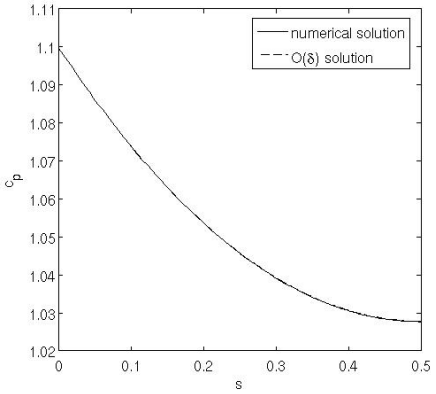

(c) Numerical and leading order analytical solution to c_p

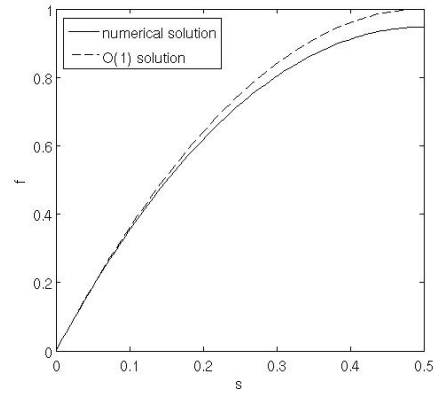

(d) Numerical and leading order analytical solution to f

Figure 5.3: Numerical and leading order solutions to c_m, c_p and f when $\delta = 0.1$.

5.9.1 Polynomial Solutions in the Limit of $fc_p^2 = 1$

In this section it is checked that the asymtotic solutions found in Section 5.9 match the Taylor expansion of the Euler-Lagrange equations at $s = 1/2$ to leading order. The second order derivatives of the Euler-Lagrange equations are listed in Appendix C.5 while the boundary conditions for the Helfrich boundary value problem at $s = 1/2$ are given in full in Section 5.4.2.

When $s = 1/2$, the boundary condition (5.45) and the remaining terms in the Euler-Lagrange equations ensure that

$$\frac{dc_p}{ds} + \frac{dc_m}{ds} = 4\frac{dc_p}{ds}, \tag{5.131}$$

$$3\frac{dc_p}{ds} = \frac{dc_m}{ds}, \tag{5.132}$$

are true. If the solution is to meet the boundary conditions at $s = 1/2$ smoothly, the second order derivatives have to meet the same proportionality conditions as the leading order polynomial solutions, so that

$$\frac{d^2c_p}{ds^2} + \frac{d^2c_m}{ds^2} = 4\frac{d^2c_p}{ds^2}, \tag{5.133}$$

$$3\frac{d^2c_p}{ds^2} = \frac{d^2c_m}{ds^2}. \tag{5.134}$$

The second order derivatives contain many terms. It is not clear how solutions for c_m, c_p and f found by the Taylor expansion smoothly match the values of c_m, c_p and f found by integrating the Euler-Lagrange equations. This will be established in the following discussion. We can write

$$\frac{d^2c_p}{ds^2} = f_1(c_p, c_m, f) + g_1(c_p, c_m, f, \Delta_p, \lambda), \tag{5.135}$$

$$\frac{d^2c_p}{ds^2} + \frac{d^2c_m}{ds^2} = f_2(c_p, c_m, f) + g_2(c_p, c_m, f, \Delta_p, \lambda), \tag{5.136}$$

where, using the terms in Appendix C.5,

$$f_1(c_p, c_m, f) = -\frac{2}{f^2}(3fc_pc_m^2 - c_p - 2c_m), \tag{5.137}$$

$$f_2(c_p, c_m, f) = \frac{2}{f^2}(3fc_pc_m^2 - 3c_p + c_m - fc_m^3), \tag{5.138}$$

$$g_1(c_p, c_m, f, \Delta_p, \lambda) = -\frac{2}{f^2}(2\lambda fc_p + \Delta_p f), \tag{5.139}$$

$$g_2(c_p, c_m, f, \Delta_p, \lambda) = \frac{2}{f^2}(-2\lambda fc_p + 2\lambda fc_m). \tag{5.140}$$

Assume that the leading order corrections to c_{p0}, c_{p0} and f_0 at $s = 1/2$ are also of $O(\delta)$ so that

$$c_p(1/2) = 1 + \delta + \delta A + O(\delta^2), \tag{5.141}$$

$$c_m(1/2) = 1 + \delta + \delta B + O(\delta^2), \tag{5.142}$$

$$f(1/2) = 1 + \delta C + O(\delta^2). \tag{5.143}$$

From (5.41) expect that $B = 3A$. If

$$f(1/2)c_p(1/2)^2 = 1 + O(\delta^2), \tag{5.144}$$

then $C = -2 - 2A$. Using the estimates (5.141)-(5.143) and expanding as a series in δ

$$f_1(c_p, c_m, f) = 16A\delta + O(\delta^2), \tag{5.145}$$

$$f_2(c_p, c_m, f) = -16A\delta + O(\delta^2), \tag{5.146}$$

$$g_2(c_p, c_m, f, \Delta_p, \lambda) = 4\lambda A\delta + O(\delta^2). \tag{5.147}$$

So by proportionality conditions (5.133)-(5.134) and (5.145)-(5.147) we have

$$\begin{aligned} g_1(c_p, c_m, f, \Delta_p, \lambda) &= -8A\delta + O(\delta^2), && (5.148)\\ 2\lambda c_p(1/2)f + \Delta_p f &= -4A\delta + O(\delta^2), && (5.149)\\ -12(1+A)\delta &= -4A\delta + O(\delta^2). && (5.150)\\ A &= -\frac{3}{4}. && (5.151) \end{aligned}$$

Using the leading order solutions to c_m and c_p, (5.125) and (5.126), we have

$$\begin{aligned} c_m(1/2) &= 1 + \delta + \frac{9}{4}\delta, && (5.152)\\ c_p(1/2) &= 1 + \delta + \frac{3}{4}\delta, && (5.153) \end{aligned}$$

so that the value of A found is consistent with this result. By the relation $C = -2 - 2A$ which ensures $f(1/2)c_p(1/2)^2 = 1$ to leading order in δ we have

$$f(1/2) = 1 - \frac{1}{2}\delta. \tag{5.154}$$

However, from the known solution to f in (5.127) we know that $f(1/2) = 1$. This will be discussed further in Section 5.10.

5.9.2 Accounting for Numerical Error in Solutions

Numerical errors arise due to the approximations made when perturbing the solutions of the Euler-Lagrange equations away from the singularities at $s = 0$ and $s = 1/2$. Full details on how to find a solution to the Helfrich boundary value problem numerically can be found in Section 6.3. When $\delta << 1$ the error in the numerical solutions can be expressed explicitly in the solutions found in Section 5.9. For solutions close to that of a sphere, so $\delta << 1$, the numerically calculated solutions to ϵ and $c_p(0)$ can be used to find that

$$\epsilon = -12\delta + \eta, \tag{5.155}$$

which is plotted in Figure 5.4(a). η represents a numerical error which prevents the numerically found values for ϵ, as defined in (5.84), from matching that found analytically in Section 5.9. For small δ, η can be found as a constant of proportionality.

c_m, c_p and f can now be written in terms of δ and η so that

$$\begin{aligned} c_m(1/2) &= 1 + \delta - \delta\frac{9}{4} + \frac{3\eta}{16} + O(\delta^2), && (5.156)\\ c_p(1/2) &= 1 + \delta - \delta\frac{3}{4} + \frac{\eta}{16} + O(\delta^2), && (5.157)\\ f(1/2) &= 1 - \delta\frac{1}{2} - \frac{\eta}{8} + O(\delta^2), && (5.158) \end{aligned}$$

where the $O(\eta)$ term for $f(1/2)$ is again found by requiring $f(1/2)c_p(1/2)^2 = 1$. In Figure 5.4, η is used to correct the fit between the numerically found proportionality constants to $(s - s^2)$ for

c_m and c_p and those expected analytically from (5.125) and (5.126). When $\delta < O(10^{-4})$, then η is of the same order of magnitude. If η is included when numerical solutions are compared to those found in the preceeding work the error of fit is $O(10^{-8})$ or $O(\delta^2)$ so that the analytical solutions are valid to leading order. When $\delta = 0$ the terms (5.137)-(5.140) relating to the boundary conditions at $fc_p^2 = 1$ are dependent on η only so we have

$$\begin{aligned} f_1(c_p, c_m, f) &= -\eta + O(\eta^2), && (5.159)\\ f_2(c_p, c_m, f) &= \eta + O(\rho^2), && (5.160)\\ g_1(c_p, c_m, f, \Delta_p, \lambda) &= \frac{1}{2}\eta + O(\eta^2), && (5.161)\\ g_2(c_p, c_m, f, \Delta_p, \lambda) &= -3\eta + O(\eta^2), && (5.162) \end{aligned}$$

which meet the conditions (5.134) and (5.133). Also, when $\delta = 0$ and $s = 1/2$, use (5.157)-(5.156) to write

$$c_p(c_p^2 - c_m^2) = -\frac{1}{4}\eta + O(\eta^2), \tag{5.163}$$

so that the condition (5.45) implies

$$2\lambda c_p + \Delta_p = \frac{1}{4}\eta + O(\eta^2). \tag{5.164}$$

This is true when $2\lambda + \Delta_p = \eta$, which is consistent with (5.155).

5.10 Corrections Terms to Helfrich Boundary Value Problem

Figure 5.3 gives an example of numerical solutions for c_m, c_p and f together with leading order solutions (5.125)-(5.127). The known leading order solutions (5.125)-(5.127) were substracted from the numerical solutions to c_m, c_p and f. The remaining terms were fitted to a quadratic polynomial wrt s, the coefficients of which were fitted to a polynomial function wrt δ. These numerically obtained correction terms were found to be of the form

$$(A\delta + B\delta^2)s^2(s-1)^2, \tag{5.165}$$

where the coefficients for the correction terms in Figure 5.5 were found to depend quadratically on δ for c_m and c_p and linearly on δ for f. A and B were found for 100 solutions where $0 < \delta < 0.1$. The average value of these coefficients A and B are given in Table 5.1.

The known analytically deduced and numerically calculated solutions for c_m, c_p and f, as asymptotic expansions in δ, of the form

$$\begin{aligned} c_m &= c_{m0} + \delta c_{m1} + \delta^2 c_{m2} + O(\delta^3), && (5.166)\\ c_p &= c_{p0} + \delta c_{p1} + \delta^2 c_{p2} + O(\delta^3), && (5.167)\\ f &= f_0 + \delta f_1 + \delta^2 f_2 + O(\delta^3), && (5.168) \end{aligned}$$

are

$$\begin{aligned} c_m &= 1 + \delta - 9\delta(s - s^2) - 14.5\delta^2(s - s^2)^2 + O(\delta^3), && (5.169)\\ c_p &= 1 + \delta - 3\delta(s - s^2) - 0.4\delta^2(s - s^2)^2 + O(\delta^3), && (5.170)\\ f &= 4(s - s^2) - 8\delta(s - s^2) - 4.7\delta^2(s - s^2)^2 + O(\delta^3). && (5.171) \end{aligned}$$

	A	B
c_m	0	-14.5
c_p	0	-0.4
f	-8	-4.7

Table 5.1: Average value of A and B for $0 < \delta < 0.1$.

The results suggest that there are unknown $O(\delta)$ and $O(\delta^2)$ terms for f and unknown $O(\delta^2)$ terms for c_m and c_p. Note that if the known leading order term (5.127) and calculated correction term are used to write

$$f = 4\delta(s - s^2) - 8\delta s^2(s-1)^2 + O(\delta^2), \tag{5.172}$$

then the expected boundary condition $f(1/2)$ given in (5.154) will be met.

5.10.1 Correction terms for c_m and c_p

If the numerically calculated terms for c_{m2} and c_{p2}, (5.169)-(5.170), are approximated by

$$c_{m2} = -12\delta^2(s - s^2)^2, \tag{5.173}$$

$$c_{p2} = 0, \tag{5.174}$$

then there is no $O(\delta^2)$ term in dc_p/ds, showing that the numerical results can be accounted for.

If f is given by (5.172), then (5.95) is

$$\frac{dc_p}{ds} = \frac{(1-2s)(1-4\delta(s-s^2))(-6\delta(s-s^2) - 12\delta^2(s-s^2)^2)}{2(1-2\delta(s-s^2))}, \tag{5.175}$$

$$= \frac{(1-2s)(1-4\delta(s-s^2))(-6\delta(s-s^2))(1+2\delta(s-s^2))}{2(1-2\delta(s-s^2))}. \tag{5.176}$$

For small δ

$$\frac{1+2\delta(s-s^2)}{1-2\delta(s-s^2)}, = (1+2\delta(s-s^2))(1+2\delta(s-s^2)+O(\delta^2)), \tag{5.177}$$

$$= 1 + 4\delta(s-s^2) + O(\delta^2). \tag{5.178}$$

We also have

$$(1-4\delta(s-s^2))(1+4\delta(s-s^2)+O(\delta^2)) = 1 + 16\delta^2(s-s^2) + O(\delta^3), \tag{5.179}$$

so that, for small δ,

$$\frac{dc_p}{ds} = -3\delta(1-2s)(s-s^2)\left(1 + 16\delta^2(s-s^2) + O(\delta^3)\right), \tag{5.180}$$

so the $O(\delta^2)$ terms cancel out. The numerically calculated correction terms can also be shown to be consistent with what can be deduced numerically. If $c_{m2} \propto (s-s^2)^2$ then $dc_{m2}/ds \propto$

$(1-2s)(s-s^2)$. Only terms of this form will be considered to find the correction term in (5.171). As above, it is approximated that as $c_{p2} \approx 0$. Use (5.171) to make the approximation

$$(1 - f c_p^2)^{1/2} = \frac{1}{4}\frac{df}{ds} \approx (1-2s)(1-4\delta(s-s^2)), \tag{5.181}$$

so that

$$\frac{1}{(1-2s)(1-4\delta(s-s^2))} \approx \frac{1}{1-2s}(1+4\delta(s-s^2)) + O(\delta^2). \tag{5.182}$$

From known $O(\delta)$ terms

$$c_p(c_p^2 - c_m^2) + 2\lambda c_p + \Delta_p \approx -12\delta(1-2s)^2 + O(\delta^2), \tag{5.183}$$

so one $O(\delta^2)$ term in dc_m/ds which is proportional to $(1-2s)(s-s^2)$ will arise by the multiplication of $O(\delta)$ terms in (5.182) and (5.183). So far, we know that

$$c_{m2} = -24\delta^2(s-s^2)^2 + O(\delta^2), \tag{5.184}$$

where the remaining $O(\delta^2)$ arises from the multiplication of the $O(\delta^0)$ term in (5.182) and the as yet unknown $O(\delta^2)$ term in (5.183).

Now if

$$c_m = 1 + \delta - 9\delta(s-s^2) + A\delta^2(s-s^2)^2, \tag{5.185}$$

$$c_p = 1 + \delta - 3\delta(s-s^2) + B\delta^2(s-s^2)^2, \tag{5.186}$$

then by multiplication

$$c_p(c_p^2 - c_m^2) = 12\delta(s-s^2) + 24\delta^2(s-s^2) + (2B-2A)\delta^2(s-s^2)^2 \tag{5.187}$$

$$- \quad 108\delta^2(s-s^2)^2, \tag{5.188}$$

$$2\lambda c_p + \Delta_p = (\delta - 3\delta(s-s^2) + B\delta^2(s-s^2)^2)(-12 + 2\delta\lambda_1), \tag{5.189}$$

$$\tag{5.190}$$

where, $\lambda = -6 + \delta\lambda_1$, $\Delta_p = 12 + \delta\Delta_{p1}$ and $\Delta_{p1} + 2\lambda_1 = 0$. $O(\delta^2)$ terms from (5.187) and (5.189) can be arranged to give

$$\delta^2(s-s^2)\left((24-6\lambda_1) - (108 + 10B + 2A)(s-s^2)\right). \tag{5.191}$$

Using the numerically calculated value of $\lambda_1 \approx 5/6$ from (5.123) and the values of A and B in Table 5.1 it is found that

$$\delta^2 19(s-s^2)\left(1 - 4(s-s^2)\right) = \delta^2 19(s-s^2)(1-2s)^2, \tag{5.192}$$

which is the unknown $O(\delta^2)$ term in (5.183). Multiplying this with the $O(\delta^0)$ term in (5.182) leaves

$$\delta^2 19(s-s^2)(1-2s), \tag{5.193}$$

so that

$$c_{m2} = -24\delta^2(s-s^2)^2 + 9.5\delta^2(s-s^2)^2 = -14.5\delta^2(s-s^2)^2. \tag{5.194}$$

In this way, numerically calculated information on $O(\delta^2)$ terms can be checked to be reasonable.

5.11 Helfrich Boundary Value Problem Solutions when $c_0 \neq 0$

If

$$0 < |c_0| << 1, \tag{5.195}$$

then the c_0 dependent terms in (5.36) cancel using the known polynomial solutions for $c_0 = 0$, so that (5.125) and (5.126) are also solutions in this case. Using the c_0 dependent terms for Δ_p and λ, (5.80) and (5.82) we have

$$2\lambda + \Delta_p = 2c_0 - c_0^2. \tag{5.196}$$

For a sphere where $c_p = 1$ the remaining c_0-dependent terms are

$$-2c_p^2 c_0 + c_p c_0^2 = -2c_0 + c_0^2, \tag{5.197}$$

which cancel with (5.196). If δ is small and c_m and c_p are given by the polynomial solutions (5.125) and (5.126) then using (5.196) we have

$$2\lambda c_p + \Delta_p = 2c_0 - c_0^2 + (2\lambda_{c0} + 4c_0 - c_0^2)(\delta - 3\delta(s - s^2)), \tag{5.198}$$

and (5.197) is now

$$-2c_p^2 c_0 + c_p c_0^2 = -2c_0 + c_0^2 - 4c_0(\delta - 3\delta(s - s^2)) + \delta c_0^2 + O(\delta^2). \tag{5.199}$$

Again all c_0 dependent terms cancel to $O(\delta^2)$.

Referring to Appendix C.5, when $f \equiv c_p \equiv c_m \equiv 1$ then

$$\frac{d^2 c_p}{ds^2} = -2(2c_0 - c_0^2 - 2\lambda_c - \Delta_{pc}) = 0, \tag{5.200}$$

$$\frac{d^2 c_m}{ds^2} = 2(2c_0 - c_0^2 - 2\lambda_c - \Delta_{pc}) = 0, \tag{5.201}$$

so the boundary conditions at $fc_p^2 = 1$ are consistent with that of a sphere when $c_0 \neq 0$.

5.12 Chapter Summary

This chapter introduces the Helfrich energy minimisation problem. The boundary conditions for the Helfrich boundary value value problem have been introduced. The Helfrich boundary value problem has previously been solved in [25]. The boundary conditions for the Helfrich energy cell on a fibre problem are also introduced. In this way the energy minimisation problem is used as a model of phagocytosis in axisymmetric geometry.

Analytical solutions of the Helfrich boundary value problem in Section 5.9 provide initial estimates to parameters when finding numerical solutions. By comparing these analytical solutions and corresponding numerically found solutions, it is found that the numerical error mainly arises from the use of Taylor expansion at $s = 1/2$. This error increases as solutions are perturbed away from the spherical solution until no further solutions can be found.

By investigating the dynamics of the Euler-Lagrange equations, qualitative types of solutions have been identified. The value $|c_m - c_p|$ may increase rapidly as f decreases or c_m and c_p may be wave-like, depending on the value of $(1 - fc_p^2)^{1/2}$. Section 5.11 indicates that when $|c_0| << 1$, c_0 dependent terms are expected to cancel. However, in Section 5.13 it was shown that when $|c_0| > 1$ then c_0 dependent terms can result in sharp maxima and minima in c_m.

By assuming that the shape of a cell membrane minimises a free energy which is the sum of the surface, volume and Helfrich energies, as defined in (5.4), it is found that this model of phagocytosis of a fibre predicts a range of possible observations. The curvatures c_m and c_p could be found to be approximately constant apart from when f is small, or they could be found to be slowly varying across the surface of the cell. A large spontaneous curvature could result in localised areas of the cell where c_m and c_p change rapidly. In the following chapter, solutions to the cell on a fibre problem will be investigated using a range of different boundary conditions. It will be noted which types of solution allow different boundary conditions to be met.

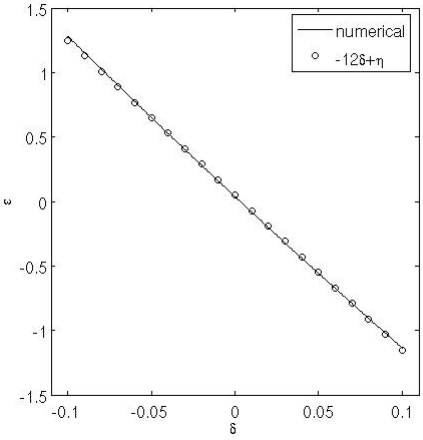

(a) Numerically and analytically calculated values of ϵ against δ.

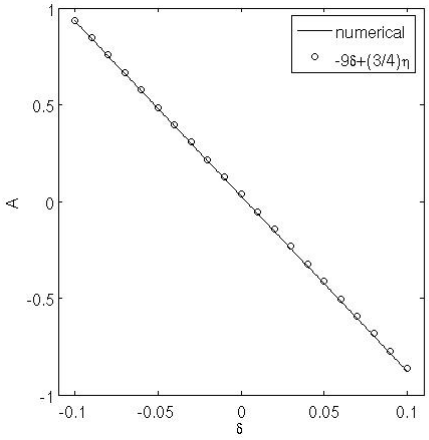

(b) Numerically and analytically calculated value of $A(\delta)$ where $c_m = A(\delta)(s - s^2)$.

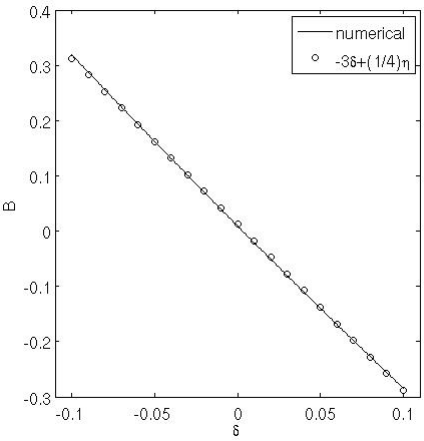

(c) Numerically and analytically calculated value of $B(\delta)$ where $c_p = B(\delta)(s - s^2)$.

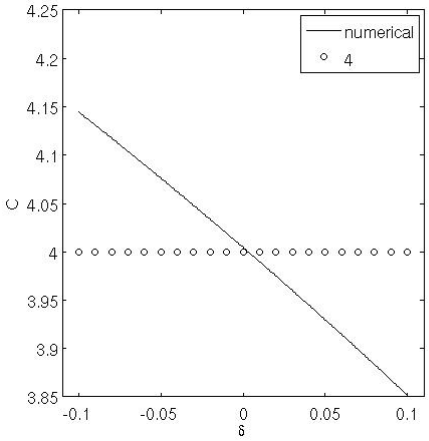

(d) Numerically and analytically calculated value of $C(\delta)$ where $f = C(\delta)(s - s^2)$.

Figure 5.4: Dependence of parameters required for leading order solutions with numerical error, η.

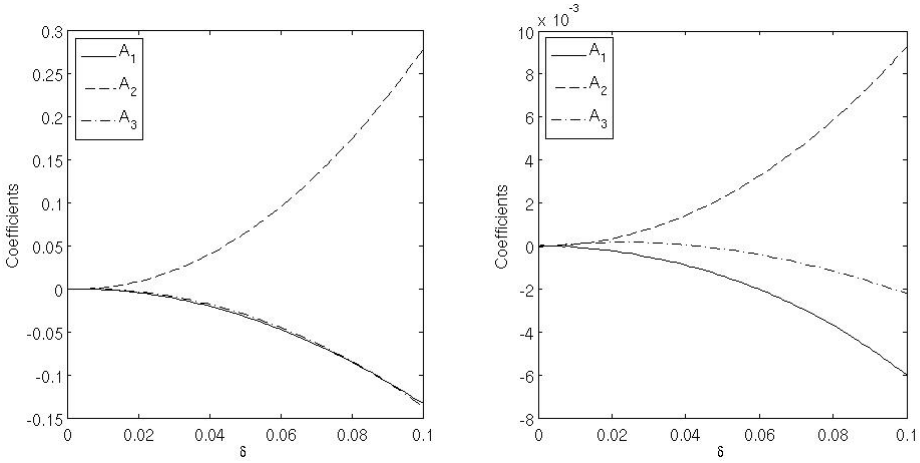

(a) Coefficents for c_m.

(b) Coefficents for c_p.

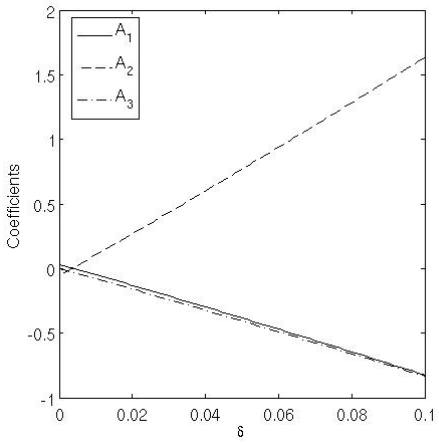

(c) Coefficents for f.

Figure 5.5: Plots of the coefficients from polynomial fits of c_m, c_p and f after the substraction of leading order solutions when fitted to a $O(\delta^4)$ polynomial so that $y = A_1 s^4 + A_2 s^3 + A_3 s^2 + A_5 s + A_5$. Coefficients of the next order terms are quadratic in δ.

5.13 Examination of Euler-Lagrange Equations as a Dynamical System

It is worthwhile examining the Euler-Lagrange equations (5.36)-(5.38) as a dynamical system and understand the role of the terms which appear in them. f will determine the resulting shape of the cell. The shape of a cell will be greatly determined by the placement of turning points, when $c_p = 0$, and inflection points, when $c_m = 0$ as has been discussed for droplets of constant mean curvature in Chapter 4. Whether or not boundary conditions are met at $s = 0$ and $s = 1/2$ will also be determined by the dynamics of the Euler-Lagrange equations.

Two regimes have been identified to write down toy models which do not contain singularities. These regimes are

$$\text{Regime A} \quad (1 - fc_p^2)^{1/2} \approx 1 \quad f = \epsilon, \tag{5.202}$$

$$\text{Regime B} \quad (1 - fc_p^2)^{1/2} \approx \epsilon \quad f \approx 1, \tag{5.203}$$

where $\epsilon << 1$.

Regime A is discussed in Section 5.13.1 and regime B is discussed in Section 5.13.2. In Regime A it is found that $|c_m - c_p|$ increases sharply as $f \to 0$. For convenience, this type of behaviour is referred to as divergence dominated behaviour. In Regime B it is found that solutions of c_m and c_p oscillate with s and there is an attractive steady state. Conclusions from this investigation are summarised in Section 5.13.3. This brief analysis will be useful in interpreting numerical solutions for the cell on a fibre problem. The plots have been obtained by integrating the equations referenced in each caption using *ode45* on default settings.

5.13.1 Eigenvalues of Reduced Euler-Lagrange Equations close to $s = 0$ and $f \approx 0$

When f is close to zero the terms which dominate are those which ensure constant mean curvature so that the Euler-Lagrange equations approximate the constant mean curvature system Section 5.7.

Take $f \approx \epsilon$ and $1 - fc_p^2 \approx 1$ so that (5.36) and (5.37) reduce to

$$\frac{dc_m}{ds} = \mp 2(1/\epsilon)(c_m - c_p), \tag{5.204}$$

$$\frac{dc_p}{ds} = \pm 2(1/\epsilon)(c_m - c_p). \tag{5.205}$$

When (5.204) has a negative sign the eigenvalues of the stationary point are $\gamma_1 = -2$ and $\gamma_2 = 0$ and so this point is unstable. As the system is integrated up from $f = 0$, c_m and c_p converge so that $c_m - c_p \to 0$ as shown in Figure 5.6(a). If (5.204) has a positive sign the eigenvalues are $\gamma_1 = 2$ and $\gamma_2 = 0$ and $c_m - c_p \to \infty$ as shown in Figure 5.6(b). The boundary condition at $s = 0$ for a Helfrich boundary value problem, as given in Section 5.4.1, requires that, when $f = 0$, we have $c_m = c_p$. However, this toy model suggests that this will not be possible if the Euler-Lagrange equations can be approximated by (5.204) and (5.205).

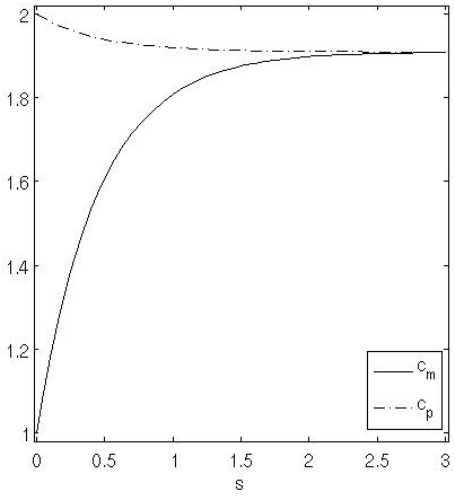

(a) Solutions where (5.204) has a positive sign and f is decreasing, $c_m(0) = 1$, $c_p(0) = 2$ and $\epsilon = 10^{-1}$.

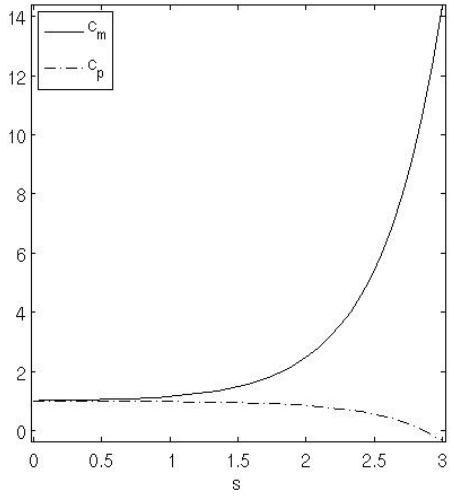

(b) Solutions where (5.204) has a negative sign and f is increasing, $c_m(0) = 1 - 10^{-2}$, $c_p(0) = 1 + 10^{-2}$ and $\epsilon = 10^{-1}$.

Figure 5.6: Numerical solutions of c_m and c_p in regime B where c_m and c_p either converge or diverge.

5.13.2 Eigenvalues of Reduced Euler-Lagrange Equations close to $s = 1/2$ and $fc_p^2 \approx 1$

This section investigates the dynamics of the Euler-Lagrange equations when $fc_p^2 \approx 1$. The sole stationary point of the Euler-Lagrange equations occurs when

$$fc_p^2 = 1 \tag{5.206}$$

$$\underbrace{c_p((c_p - c_0)^2 - c_m^2)}_{\text{shear terms}} + \underbrace{2\lambda c_p}_{\text{surface term}} + \underbrace{\Delta_p}_{\text{volume term}} = 0. \tag{5.207}$$

Equation (5.207) consists of three terms. The surface and volume terms arise from the surface and volume energies in the Helfrich minimisation problem. The first set of terms are here referred to as the shear terms with reference to (5.26) and accompanying discussion. These three sets of terms determine the dynamics of the Euler-Lagrange equations when $fc_p^2 \approx 1$.

The dynamics arising from the surface and volume terms will be investigated separately to those arising from the shear terms. Finally, the resultant dynamics when all terms contribute to the dynamics in the limit $fc_p^2 \approx 1$ are investigated.

Surface and Volume Terms

In the case where $|c_p|, |c_m|$ and $|c_0| << |\lambda|, |\Delta_p|$ the shear terms in (5.36) can be disregarded. Take $f \approx 1$ and $\sqrt{1 - fc_p^2} = \epsilon$ so that, for decreasing s, the Euler-Lagrange equations (5.36)-(5.38) reduce to

$$\frac{dc_m}{ds} = \pm (\Delta_p + 2\lambda c_p), \tag{5.208}$$

$$\frac{dc_p}{ds} = \pm 2\epsilon (c_m - c_p). \tag{5.209}$$

The eigenvalues for the stationary point of (5.208)-(5.209) when the negative signs are chosen are

$$\gamma_\pm = \epsilon \mp \sqrt{\epsilon^2 + 4\epsilon\lambda}. \tag{5.210}$$

When $\lambda = 0$ the eigenvalues are 0 and 2ϵ and so the stationary point is repulsive. When $\epsilon^2 + 4\epsilon\lambda < 0$, then the eigenvalues with have an imaginary part. Oscillations in the solutions for c_p and c_m are expected near the stationary point as in the example in Figure 5.7.

If $\lambda < 0$, the $2\lambda c_p$ term now increases $c_m - c_p$ while the symmetry condition, (5.209), acts to decrease this difference. These opposing factors result in oscillations in c_m and c_p. If $c_0 > 0$ then the frequency of oscillation will also depend on c_0. If $\Delta_p = 0$ and $c_p << c_m$ then (5.208) and (5.209) reduce to

$$\frac{dc_m}{ds} = \pm 2\lambda c_p, \tag{5.211}$$

$$\frac{dc_p}{ds} = \pm 2\epsilon c_m, \tag{5.212}$$

so

$$\frac{d^2c_m}{ds^2} = 4\epsilon\lambda c_m \qquad \text{and} \qquad \frac{d^2c_p}{ds^2} = 4\epsilon\lambda c_p, \tag{5.213}$$

whose solutions are oscillating sine and cosine functions when $\lambda < 0$. The physical interpretation of a negative surface tension is that the free energy increases with increasing surface area. This idea is consistant with a negative surface energy causing undulations in the solutions.

By the eigenvalue (5.210), the stationary point is unstable for decreasing s but can be stable when (5.208)-(5.209) both change sign so that s is increasing. In this case the eigenvalues are

$$\gamma_\pm = -\epsilon \pm \sqrt{\epsilon^2 + 4\epsilon\lambda}. \tag{5.214}$$

This means that perturbations close to the boundary condition at $fc_p^2 = 1$ correspond to larger changes further away as the undulations increase in amplitude as shown in Figure 5.7.

The frequency of these undulations increase as $|\lambda|$ increases as shown in Figure 5.8. There are two values of c_m at which (5.38) is at a stationary point

$$c_{ms}^\pm = \pm\sqrt{\frac{c_p(c_p - c_0)^2 + 2\lambda c_p + \Delta_p}{c_p}}. \tag{5.215}$$

As the amplitude of undulations in c_m are bigger than those in c_p, then the maximum and minimum values of c_m will be largely determined by the boundary conditions at $fc_p^2 = 1$.

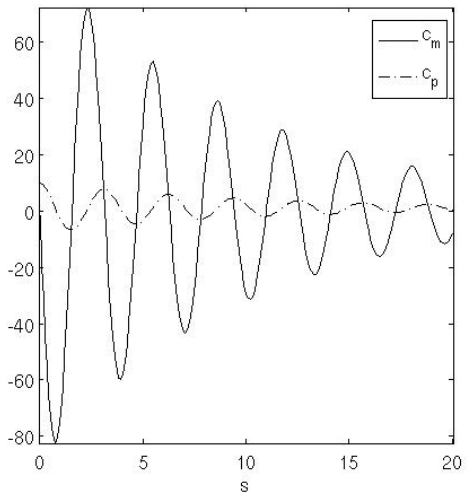

(a) Solutions where (5.208) has a positive sign and f is increasing, $c_p(0) = 10$, $c_m(0) = -1$ and $\epsilon = 10^{-1}$.

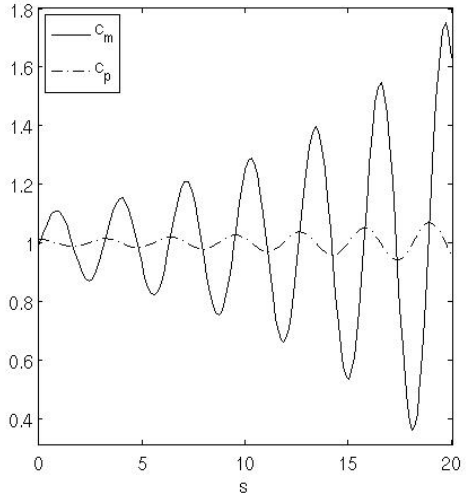

(b) Solutions where (5.208) has a negative sign and f is decreasing, $c_p(0) = 1+10^{-2}$, $c_m(0) = 1-10^{-2}$ and $\epsilon = 10^{-1}$.

Figure 5.7: $c_m(0) = 1$, $c_p(0) = 2$, $\lambda = -10$, $\Delta_p = -\lambda c_p(0)$. Solutions to toy model where surface and volume terms dominate, (5.208)-(5.209).

However, even if the undulations in c_p have a smaller amplitude, they are significant as they results in undulations in fc_p^2.

Shear Terms

Instead of looking at the surface and volume terms as in (5.208), (5.216)-(5.217) have only the shear terms to approximate (5.36)-(5.38) in the case where $|c_p|, |c_m|$ and $|c_0| >> |\lambda|, |\Delta_p|$,

$$\frac{dc_m}{ds} = \pm c_p((c_p - c_0)^2 - c_m^2), \tag{5.216}$$

$$\frac{dc_p}{ds} = \pm 2\epsilon\,(c_m - c_p)\,. \tag{5.217}$$

Take $c_0 = 0$ so that at the stationary point is at $c_{ms} = c_{ps}$. The eigenvalues of (5.216)-(5.217) when the positive sign is chosen are

$$\gamma\pm = -(c_m^2 + \epsilon) \pm \sqrt{(c_m^2 + \epsilon)^2}. \tag{5.218}$$

The eigenvalues are zero and negative and $c_m - c_p \to 0$ as f increases. If the signs of (5.216)-(5.217) are reversed then the eigenvalues will be zero and positive and $c_m - c_p \to \infty$ as f decreases. The shear term therefore contributes to the same convergent and divergent behaviour as the torque terms in Section 5.13.1 as can be observed in Figure 5.9. If $c_0 \neq 0$ then when taking the positive sign in (5.216)-(5.217) the eigenvalues are

$$\gamma\pm = -\frac{\epsilon}{2} - \frac{c_0^2}{4} + \frac{1}{4}\sqrt{c_0^4 - 4\epsilon c_0^2 - 16\epsilon c_0 + 4\epsilon^2}, \tag{5.219}$$

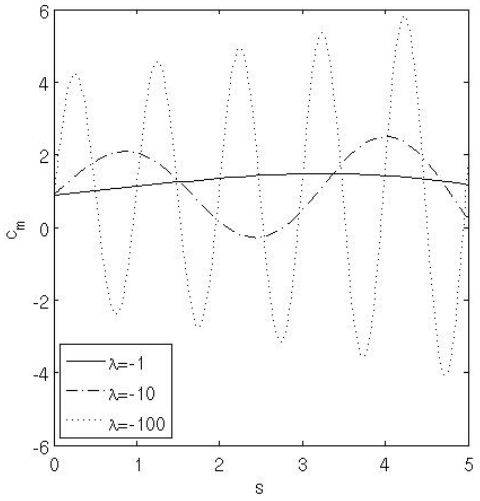

Figure 5.8: Numerical solutions for c_m when $c_p(0) = 1 + 10^{-2}$ and $c_m(0) = 1 - 10^{-2}$ where (5.208) has a positive sign. Frequency of undulations decrease as λ increases.

where at the stationary point $c_m = c_p = \frac{1}{2}c_0$. When $\epsilon = 0$ the stationary point is attractive and real and will be attractive and real as long as $O(\epsilon) << 1$.

There is a maximum or a minimum in c_m when either $c_p = 0$, or $(c_p - c_0)^2 = c_m^2$. There is a maximum or a minimum in c_p when $c_p = c_m$. In Figures 5.9, 5.10 and 5.11 are examples of how a solution may reach a stationary point. In Figure 5.9(a) there is neither a maximum nor a minimum in c_m or c_p. As $c_0 = 0$, the stationary point $c_m = c_p$ will be reached as long as

$$c_p(0)c_m(0) > 0, \qquad c_m(0)\frac{dc_m}{ds} \mid_{s=0} < 0, \quad \text{and} \quad c_p(0)\frac{dc_p}{ds} \mid_{s=0} < 0. \tag{5.220}$$

In Figure 5.11(a), initial conditions are such that

$$c_p(0)c_m(0) < 0, \qquad c_m(0)\frac{dc_m}{ds} \mid_{s=0} > 0, \quad \text{and} \quad c_p(0)\frac{dc_p}{ds} \mid_{s=0} < 0. \tag{5.221}$$

The initial gradient in c_m, moves c_m off away form c_p. However, one minimum in c_p and a minimum and a maximum in c_m allow the solution to reach steady state. The minimum in c_m occurs when $c_p = 0$, then there is a minimum in c_p when $c_m = c_p$ and, finally, there is a maximum in c_m when $(c_p - c_0)^2 = c_m^2$. Solutions which can reach steady state can be simpler. For example, the steady state in Figure 5.10(a) is reached after only one minimum in c_p and no minima in c_m. The steady state in Figure 5.10(b) is reached after only one minima in c_m when $(c_p - c_0)^2 = c_m^2$ and no maxima or minima in c_p.

Whether or not a solution reaches the stationary point for a given set of initial conditions depends on whether or not the solution reaches the limit where $c_0 + c_m - c_p = 0$ so that

$$\frac{dc_m}{ds} = \frac{dc_p}{ds} \quad \text{and} \quad \frac{dc_m^2}{ds^2} = \frac{d^2c_p}{ds^2} = 0. \tag{5.222}$$

If a solution reaches this limit, in Figure 5.11(b), for example, then the solution cannot reach any further maxima or minima which may eventually allow the solution to reach steady state.

The value of ϵ also changes the solution for an given set of initial conditions. For example, compare Figures 5.11(a) and 5.11(b) with 5.11(c) and 5.11(d).

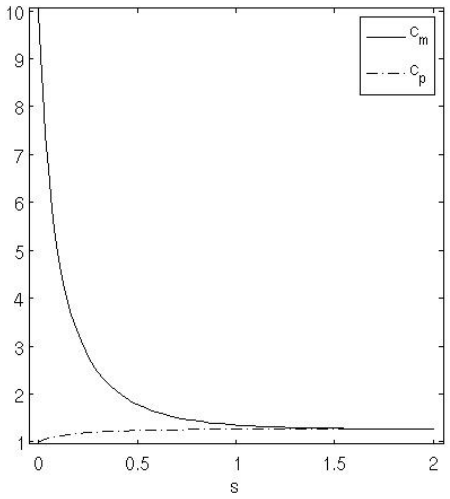

(a) (5.216) has a positive sign and f is increasing, $c_m(0) = 10$, $c_p(0) = 1$, $c_0 = 0$ and $\epsilon = 10^{-1}$.

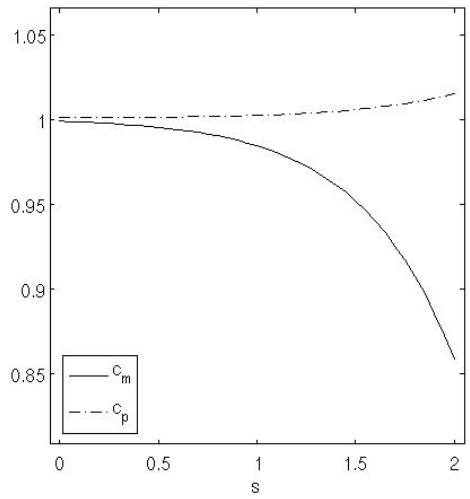

(b) (5.216) has a negative sign and f is decreasing, $c_m(0) = 1 - 10^{-3}$, $c_p(0) = 1 + 10^{-3}$, $c_0 = 0$ and $\epsilon = 10^{-1}$.

Figure 5.9: Numerical solutions to c_m and c_p from (5.216)-(5.217). Shear terms allow c_m and c_p to either converge or diverge.

Surface, Volume and Shear Terms

The surface, volume and shear elements can be combined to give

$$\frac{dc_m}{ds} = \pm \left(c_p((c_p - c_0)^2 - c_m^2) + \Delta_p + 2\lambda c_p \right), \tag{5.223}$$

$$\frac{dc_p}{ds} = \pm 2\epsilon \left(c_m - c_p \right). \tag{5.224}$$

For the positive case and when $c_0 = 0$ (5.223)-(5.224) eigenvalues

$$\gamma\pm = -(c_m c_p + \epsilon) \pm \sqrt{(c_m c_p + \epsilon)^2 - 2\epsilon(c_p + c_m)^2 + 4\epsilon\lambda + 8\epsilon c_p^2}, \tag{5.225}$$

where c_m and c_p satisfy (5.215). If $c_0 \neq 0$ then the eigenvalues are

$$\gamma\pm = -(c_m c_p + \epsilon) \pm \sqrt{(c_m c_p + \epsilon)^2 - 2\epsilon(c_p + c_m)^2 + 4\epsilon\lambda + 8\epsilon c_p(c_p - c_0) + 2\epsilon c_0^2}. \tag{5.226}$$

If $c_p = O(1)$, $c_m = O(1)$, $c_0 = O(1)$ and $\lambda = O(10)$, as suggested in the discussion of parameters in Section 5.8, then whether $\gamma_\pm$ have imaginary parts will depend on λ. If $|c_0| >> 1$, the frequency of these undulations will also depend strongly on c_0.

c_0 dependent terms serve to dampen the undulations in c_m and c_p when $\lambda < 0$. For c_m and c_p to oscillate then $(dc_m/ds)(dc_p/ds) < 0$. In Figure 5.12, the contribution to the initial

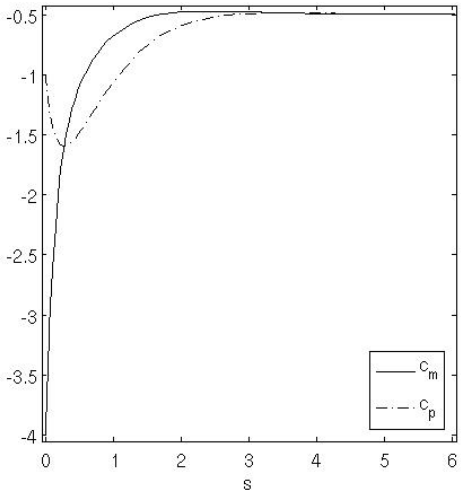

(a) (5.216) has a positive sign and f is increasing, $c_m(0) = -4$, $c_p(0) = -1$, $c_0 = -1$ and $\epsilon = 1$.

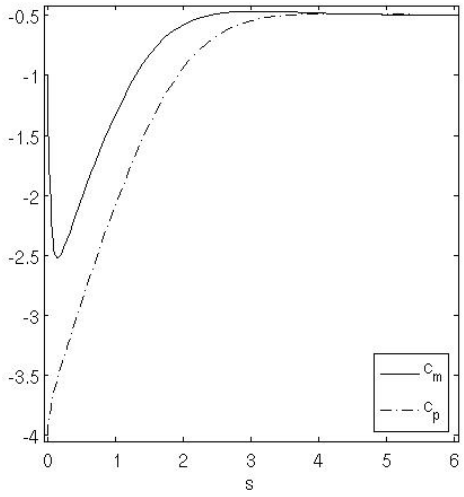

(b) (5.216) has a negative sign and f is decreasing, $c_m(0) = -1$, $c_p(0) = -4$, $c_0 = -1$ and $\epsilon = 1$.

Figure 5.10: Numerical solutions to c_m and c_p from (5.216)-(5.217), demonstrating extrema in c_m and c_p.

rate of change of c_m by the shear terms (C) has the same sign as the contribution from the surface and volume terms (B), so the combined solution has a minimum in c_m. In Figure 5.13, however, this is not the case so in the combined solution there is no minimum or maximum in c_m or c_p. In Figure 5.14, the contribution to the initial rate of change of c_m by the shear terms (C) has the opposite sign to the contribution from the contribution from the surface and volume terms. In this case, there is both a maximum and minimum in c_m due to a minimum in c_m when both shear, surface and volume terms are used, while when the shear terms only are used, there is only a minimum in c_m and maximum.

When $c_0 c_p > 0$, c_0 dependent terms will dampen the undulations in c_m and c_p less than when $c_0 c_p < 0$. The values on the x- and y- axes in Figure 5.15(b) are chosen in order to compare the amplitude of undulations in c_m when $c_0 = \pm\alpha^2$. When $|c_0|$ is large enough, undulations in c_m and c_p will be completely dampened if $c_0 c_p < 0$, while several extrema will still be observed when $c_0 c_p < 0$. In Figure 5.15(b), the sign rather than the magnitude of c_0 has the greatest effect on the solution.

5.13.3 Implications for Boundary Value Problem Solutions

Comparing the observations in Sections 5.13.1 and 5.13.2 leads to the conclusion that the type of solution obtained for c_m and c_p in regime A when $fc_p^2 << 1$ is very different from that observed in regime B when $fc_p^2 \approx 1$. Solutions obtained in regime A show "divergence dominated" behaviour while solutions obtained in regime B show "wave dominated" or "wave-like" behaviour. The terms in quotes will be used to describe numerical solutions as a short

hand way to reference the observations in this section.

For c_m and c_p to oscillate when $fc_p^2 \approx 1$, then $\lambda < 0$. When c_m and c_p oscillate, for each extremum in c_m, there is an extremum in c_p. Whether $c_0 > 0$ or $c_0 < 0$ will also determine the dynamics of the Euler-Lagrange equations. Wave behaviour is more evident when $c_0 c_p > 0$ and less evident when $c_0 c_p < 0$. If the amplitude of their undulations is small, they are not moving towards or away from a stationary point. When c_m and c_p oscillate their mean value is approximately constant. This mean value can be chosen to maximise the length of a solution. In this way, undulations in c_m and c_p provide an extra degree of freedom in the numerical optimisation when searching for cell on a fibre solutions of a certain length and certain fibre radius.

The increase of $|c_m - c_p|$ as $f \to 0$ highlights possible difficulties in finding solutions which meet the boundary conditions at $f = 0$ as given in Section 5.4.1. However, the boundary conditions at $fc_p^2 = 1$ given in Section 5.4.2 could be easily met as a conseqence of the dynamical behaviour of the Euler-Lagrange equations if $c_p(1/2)c_m(1/2) > 0$. The boundary conditions are met when the Euler-Lagrange equations are at an attractive stationary point.

The c_0-dependent shear terms allow an extremum in c_m without a corresponding extremum in c_p. This allows for a greater flexibility in possible solutions.

These observations are useful as broad outlines. The examples in this section also indicate the possible complexity of solutions to the Helfrich and cell on a fibre boundary value problems. Different elements of the dynamics of the Euler-Lagrange equations will be useful to find solutions which meet the required conditions for the cell on a fibre problems in Chapter 6.

Similarly, these observations can be used to understand how a membrane may look like when certain terms of the free energy dominate. When $\lambda < 0$, then undulations in the surface serve to increase the surface area. When f is small and Δ_p is large, so that the volume term dominates, $|c_m - c_p|$ tends to rapidly increase. The rate of this increase may be too large to be representative a real membrane. The only solution for which $|c_m - c_p|$ does not rapidly decrease under these conditions is that of a sphere. This is appropriate as when Δ_p is large the free energy is minimised by minimising the volume. For a given surface area, the shape with the smallest volume is a sphere. Finally, a non-zero value of c_0 alters the solution in a variety of ways. It can act to alter solutions which show undulations in c_m and c_p or rapid increases in $|c_m - c_p|$. These types of solutions have already been discussed. A type of solution which is only found when c_0 is non-zero are those demonstrated in Figures 5.11(a) and 5.11(b). There is sharp change in c_m and so the rate of change of ϕ.

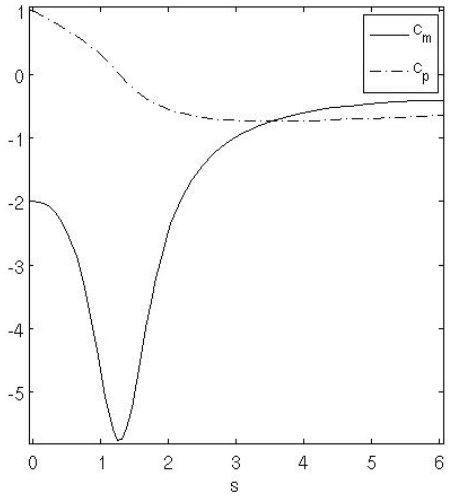

(a) (5.216) has a positive sign and f is increasing, $c_m(0) = -2$, $c_p(0) = 1$, $c_0 = -1$ and $\epsilon = 10^{-1}$.

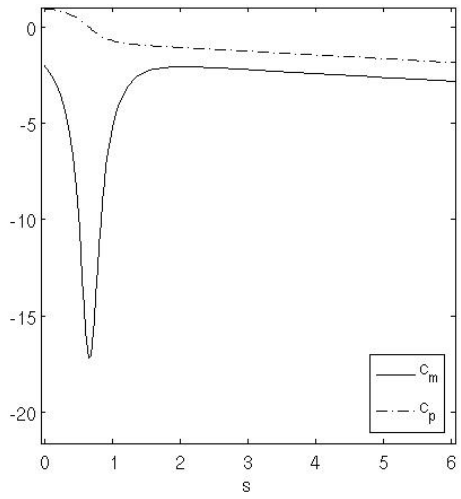

(b) (5.216) has a negative sign and f is decreasing, $c_m(0) = -2$, $c_p(0) = 1$, $c_0 = 1$ and $\epsilon = 10^{-1}$.

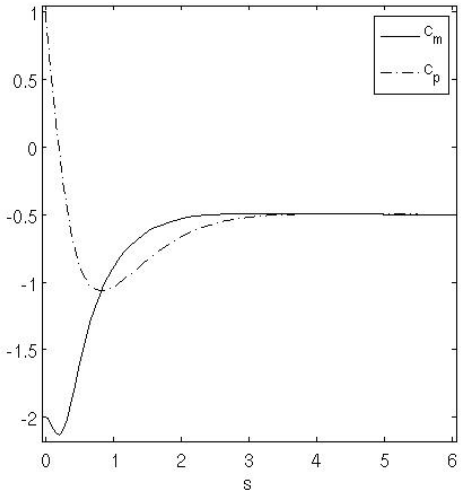

(c) (5.216) has a positive sign and f is increasing, $c_m(0) = -2$, $c_p(0) = 1$, $c_0 = -1$ and $\epsilon = 1$.

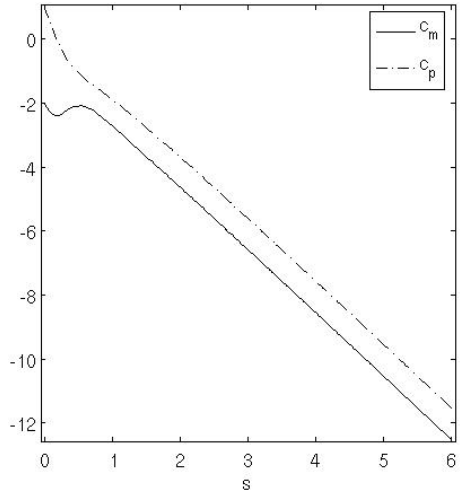

(d) (5.216) has a negative sign and f is decreasing, $c_m(0) = -2$, $c_p(0) = 1$, $c_0 = 1$ and $\epsilon = 1$.

Figure 5.11: Numerical solutions to c_m and c_p from (5.216)-(5.217), demonstrating the effect of the choice of ϵ. Solutions Figures 5.11(c) and 5.11(d) can never reach steady state.

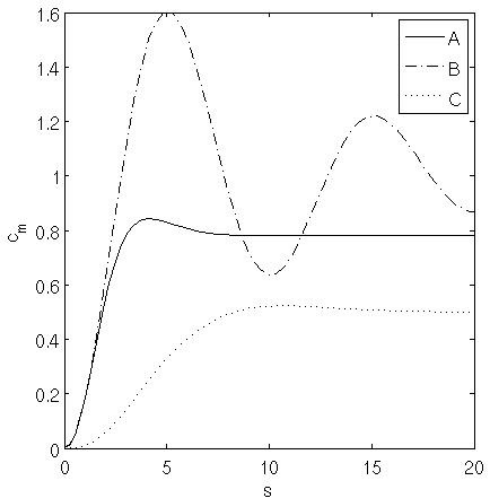

(a) c_m against s.

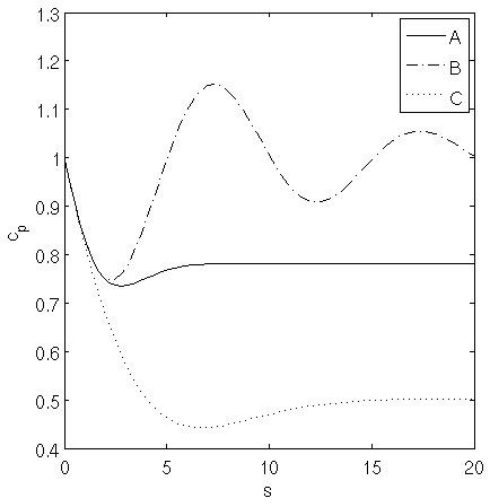

(b) c_p against s.

Figure 5.12: Numerical solutions to c_m and c_p, $\lambda = -1$, $c_p(0) = 1$, $c_m(0) = c_p(0) - c_0$ and $c_0 = 1$. A - (5.223)-(5.224). B - (5.208)-(5.209). C - (5.216)-(5.217). In all figures, where there is a choice in sign, the positive sign is chosen. $c_0 c_p(0) > 0$ and so shear terms can be said to co-operate with the undulations from the surface term.

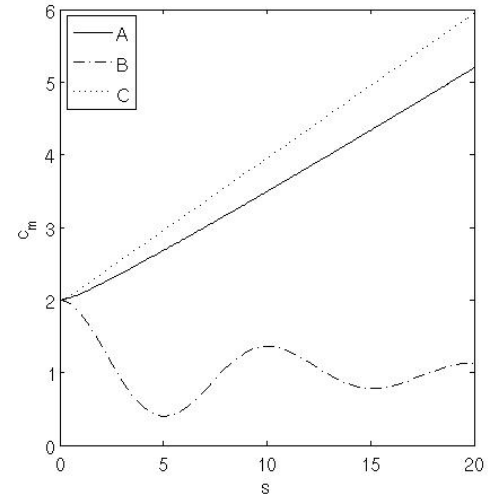

(a) c_m against s.

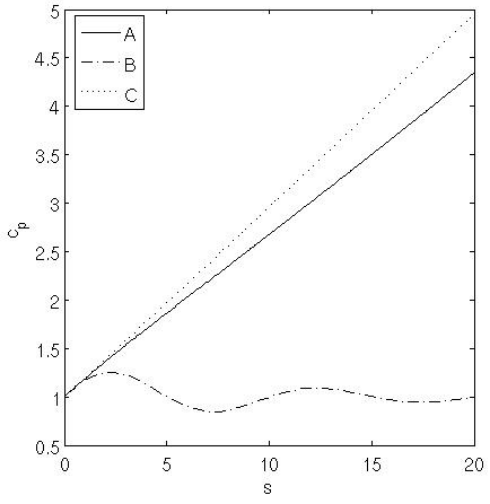

(b) c_p against s.

Figure 5.13: Numerical solutions to c_m and c_p, $\lambda = -1$, $c_p(0) = 1$, $c_m(0) = c_p(0) - c_0$ and $c_0 = -1$. A - (5.223)-(5.224). B - (5.208)-(5.209). C - (5.216)-(5.217). In all figures, where there is a choice in sign, the positive sign is chosen. $c_0 c_p(0) > 0$ and so shear terms cannot be said to co-operate with the undulations from the surface term.

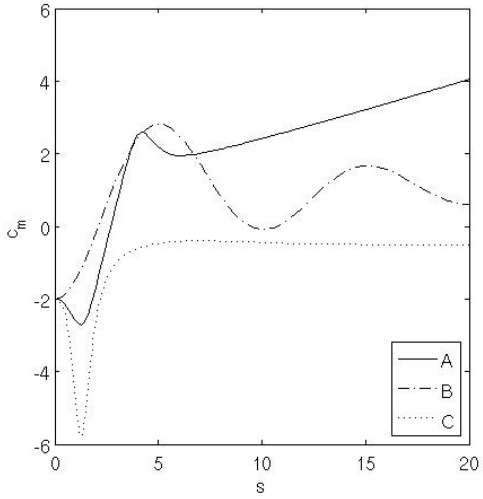

(a) c_m against s.

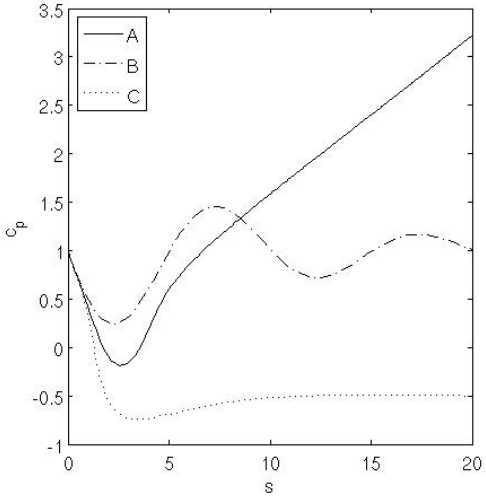

(b) c_p against s.

Figure 5.14: Numerical solutions to c_m and c_p, $\lambda = -1$, $c_p(0) = 1$, $c_m(0) = -(c_p(0) - c_0)$ and $c_0 = -1$. A - (5.223)-(5.224). B - (5.208)-(5.209). C - (5.216)-(5.217). In all, where there is a choice in sign, the positive sign is chosen. Minimum in shear terms allows the shear terms to co-operate with the undulations from the surface term.

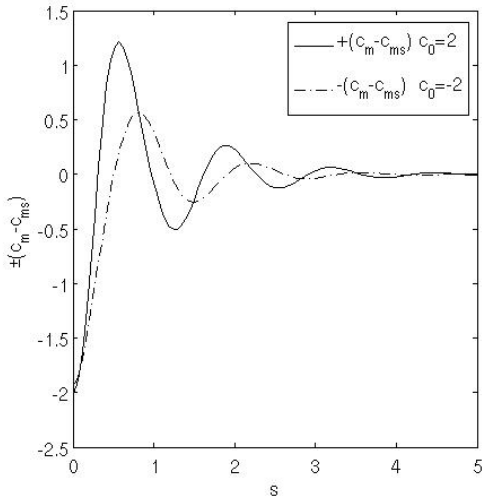

(a) $(c_m - c_{ms})$ against s when $c_0 = 2$, $-(c_m - c_{ms})$ against s when $c_0 = -2$.

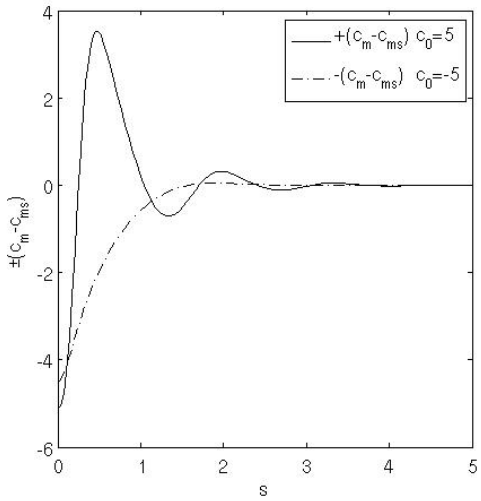

(b) $(c_m - c_{ms})$ against s when $c_0 = 5$, $-(c_m - c_{ms})$ against s when $c_0 = -5$.

Figure 5.15: Numerical solutions to c_m from (5.223)-(5.224), where the positive sign is chosen, $\lambda = -60$, $c_p(0) = 1$ and $c_m(0) = c_p(0) - c_0$. Term for c_{ms} given in (5.215). Sign of $c_p(0)c_0$ determines how much the undulations arising from the surface term are damped by c_0 dependent terms. When $c_p(0)c_0 > 0$ the undulations are less damped than otherwise.

Chapter 6

Numerical Solutions to the Helfrich Energy Minimisation Problem

6.1 Summary of Phagocytosis Models

Section 6.3 contains details of the computational scheme used to find the numerical solutions of the Helfich boundary value problem (HBVP) in Section 5.4. The boundary value problem was solved as a shooting problem where c_m, c_p and f are perturbed away from the boundary conditions and matched at an intermediate point. The matching error is minimised using the MATLAB optimisation function *fsolve* where certain unknown parameters are variables of this optimisation problem.

Results for the HBVP can be found in Section 6.4. Sections 6.5-6.7 contain detailed discussion, numerical schemes and results from the three cell on a fibre boundary value problems. Section 6.5 looks at the zero momentum boundary value problem where boundary term of the first variation in energy is set identically to zero. Section 6.6 looks at cell on a fibre solutions where the length of a cell is increased under the contraint of constant volume. Finally, Section 6.7 looks solutions where the cell membrane is parallel to the fibre surface and the contact angle between the fibre surface and the cell membrane is zero. Conclusions and observations relating to each boundary condition are included at the end of each section. Section 6.8 brings together these conclusions and generalises the observation made for each boundary condition.

The two key parameters of the solutions presented in these sections are the spontaneous curvature c_0, which is the self-induced curvature of the membrane, and the square of the fibre radius, $x_0 = R^2$. It is convenient to refer to the square of the fibre radius due to the variable $f = x^2$ in the Euler-Lagrange equations.

The parameters of interest of the cell on a fibre solutions found are length, volume and Helfrich energy. The Euler-Lagrange equations have been de-dimensionalised in Section 5.6 so no units are in use.

All boundary conditions in this Chapter include the fundamental cell on a fibre boundary condition in Section 5.5. Additional details on the construction of the solutions can be found at the beginning of the corresponding sections.

The discussion of numerical results in Sections 6.5-6.7 uses the analytical insight gained in the previous chapter to understand the results, even if analytical solutions are not available. A section which the reader is advised to be particularly familiar with is Section 5.13.

In its strictly correct use, the term divergent indicates that $|c_m - c_p| \to \infty$. However, it has been used in this current work to summarise the observation that for some solutions there is a rapid increase of $|c_m - c_p|$ as $f \to 0$. Solutions such as this are referred to as "divergent" solutions. Solutions can otherwise be "wave-like" or "undulating".

If solutions are wave-like, then the spontaneous curvature will have a noticable effect on the frequency of the oscillations. If $|c_0|$ is large then maxima and minima may arise due to the shear terms, as introduced in Section 5.13, and further demonstrated for HBVPs in Section 6.4.3.

6.2 Inflection Points, Turning Points and Types of Solution

There are five types of solution to the HBVP: spheres, oblate spheroids, prolate spheroids, discocytes and dumbells. The types of solution and their relationship with volume is summarised in Figure 6.1. Examples of numerical solutions of a prolate spheroid and a dumbell solution can be found in Figure 6.3. For these solutions c_m and c_p monotonically decrease over the interval $0 < s < 1/2$. Examples of numerical solutions of a oblate spheroid and a discocyte solution can be found in Figure 6.2. Some observations on how these types of solutions relate to choice of boundary conditions will now be made. Full details of the boundary conditions of the HBVP can be found in Section 5.4. They will be discussed in the context of the analytical solutions to the perturbation of a sphere given in Section 5.9.

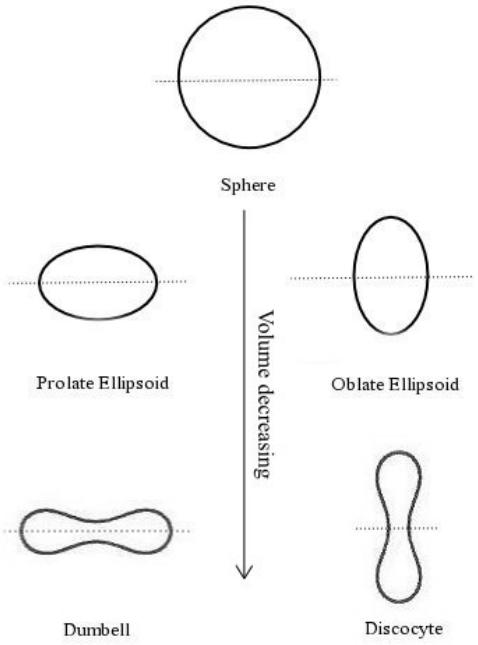

Figure 6.1: Profiles of dumbells and discocytes available solutions on their axis of rotation (dotted line). Shapes of dumbells and discocytes are similar, however, their orientation to the axis of rotation is different.

By (4.17) and (4.18) and the discussion in Chapter 4, a turning point occurs when $c_p = 0$ and an inflection point occurs when $c_m = 0$. From

$$\frac{d(fc_p^2)}{ds} = 4(1 - fc_p^2)^{1/2} c_p c_m, \tag{6.1}$$

it is found that when there is either a turning or an inflection point, by the Euler-Lagrange equations, $f_0 c_{p0}^2 = \sin^2\phi$ is an extremum. By the leading order terms, (5.125)-(5.127), of the solutions found in Section 5.9 we can write

$$f_0 c_{p0}^2 = 4(s - s^2)\left(1 + \frac{\epsilon}{4}(s - s^2)\right)^2, \tag{6.2}$$

Sphere	$\kappa = 1$
Oblate spheroid	$0 < \kappa < 1$
Discocyte	$\kappa < 0$
Prolate spheroid	$1 < \kappa < \kappa_{max}$
Dumbell	$\kappa > \kappa_{max}$

Table 6.1: Types of Helfrich Boundary Problem solutions as defined by $\kappa = c_p(0) = c_m(0)$.

if this is differentiated wrt S so that

$$\frac{d\left(f_0 c_{p0}^2\right)}{ds} = 4(1-2s)\left(1+\frac{\epsilon}{4}(s-s^2)\right)\left(1+\frac{3\epsilon}{4}(s-s^2)\right), \tag{6.3}$$

$$= 4(1-2s)c_{p0}c_{m0}, \tag{6.4}$$

then the result is found to be consistent with (6.1).

Whether a solution with Helfrich boundary conditions is oblate, prolate or spherical depends on the value of $c_m(0)$ or $c_p(0)$ at the axis of rotation which is represented by the variable κ, defined here as

$$\kappa = c_p(0) = c_m(0). \tag{6.5}$$

For Helfrich boundary solutions close to a spherical solution, c_m and c_p will increase or decrease monotonically depending on the signs of ϵ, as defined in (5.84), and δ, as defined in (5.85) and (5.86). If $\delta < 0$, then by the leading order solutions found in Section 5.9, (5.125)-(5.127), $\epsilon > 0$, which implies that $c_m > c_p$. The curvature along the length of the fibre is greater than around the radius. This causes the profile to be flattened along the axis of rotation so that the solution is an oblate spheroid.

For small δ, there will be neither a turning nor an inflection point so that the resulting shape is an oblate spheroid. An example oblate spheroid solution can be found in Figures 6.3(a) and 6.3(b). However, when $\delta = O(1)$, when the asymptotic solutions in Section 5.9 are not longer applicable. As the faster changing variable, c_m, crosses zero there will be an inflection point. Then when the slower changing variable, c_p, crosses zero there will be a turning point. The resulting shape is referred to in [25] as a discocyte. Example discocyte solutions can be found in Figures 6.3(c) and 6.3(d).

If $\delta > 0$, then $c_p > c_m$ and $\epsilon < 0$. In this case c_m is always smaller than c_p and the profile is stretched along the axis of rotation. In this case, the solution is that of a prolate spheroid. Example prolate spheroid solutions can be found in Figures 6.2(a) and 6.2(b). As κ is increased, and the rate of decrease of c_m over the interval $0 < s < 1/2$ increases, there will be a κ_{max} for which $c_m(1/2) = 0$. Solutions for which $c_m(1/2) < 0$ are referred to in [25] as a dumbell. It will be discussed in detail in Section 6.3.2 how the consequence of the boundary condition $c_m(1/2) < 0$ is an additional singularity which results in a maximum in f when $0 < s < 1/2$. Example dumbell solutions can be found in Figures 6.2(c) and 6.2(d). The value of κ_{max} depends on spontaneous curvature c_0. Figure 6.1 demonstrates how the discocytes and dumbells are similar in shape but have a different orientation to the axis of rotation.

6.3 Computational Details in Finding Numerical Solutions for the Helfrich Boundary Value Problem

Details on how to find prolate and oblate spheroids can be found in Section 6.3.1. This section introduces the general method used to find all Helfrich boundary value and cell on a fibre solutions. Details on how the additional numerical challenge of finding a dumbell solution was dealt with can be found in Section 6.3.2. These two sections should indicate the general method used to find cell on a fibre solutions. Further information on the numerical methods used to find cell on a fibre solutions can be found in the corresponding sections.

6.3.1 Spheroid Solutions

Numerical solutions which meet the boundary conditions given in Section 5.4.1 and 5.4.2 can be found in [25] where unknown parameters are listed. To find numerical solutions to the HBVP introduced in Section 5.4 the boundary conditions must first be perturbed away from the singularities at $f(0) = 0$ and $f(1/2)c_p^2(1/2) = 1$ using the appropriate approximations to the full Euler-Lagrange equations (5.36)-(5.38). The Euler-Lagrange equations can then be used to integrate the solutions away from the singularities using the MATLAB solver *ode45*. Parameters which minimise this matching error can be found by solving the corresponding optimisation function numerically. This optimisation is done using the MATLAB program *fsolve* from the optimisation toolbox. In this way, the Helfrich boundary value problem is solved using the shooting method. A general introduction to the shooting method can be found in [90].

The correct approximations of the Euler-Lagrange equations close to the singularity at $f = 0$ were given in Section 5.4.1 to be (5.42)-(5.44). The approximations of the Euler-Lagrange equations close to the singularity at $fc_p = 1$ are given by the Taylor expansions (5.47)-(5.49) and the complete expressions can be found in Appendix C.5. In the case when $c_0 = 0$ (5.47)-(5.49) are given here as a reference:

$$\begin{aligned} c_m(s) &= c_m(s^*) + \gamma(s - s^*) && (6.6)\\ &+ \frac{(c_m(s^*) - c_p(s^*))(4c_p(s^*)c_m(s^*) + 3 - c_m(s^*)^2 + 2\lambda)}{f(s^*)}(s - s^*)^2, && (6.7)\\ c_p(s) &= c_p(s^*) + \frac{2(c_p(s^*) - c_m(s^*))c_p(s^*)c_m(s^*)}{f(s^*)}(s - s^*)^2, && (6.8)\\ f(s) &= f(s^*) - 4c_m(s^*)c_p(s^*)(s - s^*)^2. && (6.9) \end{aligned}$$

Equation (6.9) is generally independent of c_0.

c_m and c_p must be of the same sign at $fc_p = 1$, so that perturbing the boundary conditions of c_p, c_m and f away from $fc_p = 1$ will decrease f. This is consistent with the assumption that the singularity occurs when f is at a maximum. The negative sign must be chosen in (5.38) when integrating the solution away from the singularity at $fc_p = 1$, as f can only increase or decrease monotonically for an spheroidal solution. The positive sign can then be chosen to integrate away from the singularity at $f = 0$. After the solutions are perturbed away from the

singularites at $fc_p = 1$ and $f = 0$ they can then be matched at some intermediate point. For the shape to be symmetric around the mid-length when $s^* = 1/2$ we have $\gamma = 0$ by (5.50).

Define a value ϵ so that if

$$\epsilon \geq 1 - f(s)c_p(s)^2, \tag{6.10}$$

then the solution can be said to be close to a singularity and a Taylor expansion must be used to integrate further. ϵ must be as small as possible while being large enough for c_m, c_p and f to have only real and no imaginary parts when the Euler-Lagrange equations are integrated close to the singularity. It was found that 10^{-9} is a good value for ϵ for which the numerical errors were small. ϵ must be large enough to move the solution sufficiently away from the singularity so that integrating (5.36)-(5.38) does not lead to numerical errors.

The singularity at $f = 0$ as discussed in Section 5.4.1 will now be referred to as point P while the singularity $fc_p = 1$ as discussed in Section 5.4.2 for the boundary will now be referred to as point R as indicated in Figure 6.3(b).

For spheres, oblate spheroids and prolate spheroids, which only have singularities at $s = 0$ and $s = 1/2$, there are five degrees of freedom which uniquely define the boundary conditions of a particular solution. These are

$$c_0 \quad \text{spontaneous curvature}, \tag{6.11}$$

$$\kappa \quad c_p(0) \text{ and } c_m(0), \tag{6.12}$$

$$\Delta_p \quad \text{osmotic pressure}, \tag{6.13}$$

$$\lambda \quad \text{surface tension}, \tag{6.14}$$

$$B \quad f(1/2). \tag{6.15}$$

It is best not to allow c_0 to be a free variable as small changes in c_0 alter the solution of the Euler-Lagrange equations more than small changes in the other free variables (6.13)-(6.12) do. The parameter c_0 is assumed to be fixed for any given branch of solutions. If Δ_p and λ are fixed, then there is one degree of freedom left in the boundary conditions at the axis of rotation given in Section 5.4.1. A useful parameter to define is the value of the principal curvatures at the axis of rotation (6.12), as it determines whether the spheroid solution is oblate or prolate. There remains a degree of freedom in the boundary conditions in Section 5.4.2 when $f(1/2)c_p(1/2)^2 = 1$. The remaining parameter is defined in (6.15) to be the value of f at $s = 1/2$.

The Euler-Lagrange equations are solved using the shooting method, where unknown parameters in the boundary conditions are varied in order for the solutions for c_m, c_p and f to be matched at an intermediate point. Either c_0 and Δ_p or c_0 and κ are fixed while the remaining parameters were used as variables in order to minimise the matching error numerically. A new solution is found using the variables of a known solution as initial estimates, while perturbing the value of one of the fixed parameters. In this way a series of solutions can be found.

The difference between the solutions integrated from point P at $s = 0$ and point Q at $s = 1/2$ at $s = s_m$ using the Euler-Lagrange equations (5.36)-(5.38) is the output of the

function to be minimised which is

$$\begin{aligned} \mathbf{R_1} = [c_{m+}(s_m) &- c_{m-}(s_m), \\ c_{p+}(s_m) &- c_{p-}(s_m), \\ f_+(s_m) &- f_-(s_m)]. \end{aligned} \tag{6.16}$$

This vector will be referred to as the residual of the optimisation problem. A vector of this type will be referred to as the residual and clearly states what is minimised in each optimisation. $c_{m+}(s)$, $c_{p+}(s)$ and $f_+(s)$ are the solutions to c_m, c_p and f found by integrating away from point P. The solution is initially perturbed away from the boundary conditions at $s = 0$ to $s = \epsilon$ by the Euler-Lagrange equations in this limit. Solutions for the interval $\epsilon \leq s \leq s_m$ are found by integrating the Euler-Lagrange equations (5.36)-(5.38) using the inbuilt MATLAB function *ode45*. This solver uses the Runga-Kutta method and ϵ was typically given the value 10^{-3}. An acceptable numerical error to this optimisation problem was taken to be when all components of the residual are of $O(10^{-6})$ or less.

This optimisation is done using MATLAB function *fzero* with the default settings. An accurate solution depends less on the settings associated with *fzero* then on a good choice of initial conditions. The best way of finding a good solution is my making the perturbation to the fixed parameter sufficiently small. The value of this perturbation was usually 10^{-2}. When this does not result in a sufficiently small error in the optimisation problem, then the perturbation was reduced to 10^{-3}. However, if this smaller perturbation did not result in a good solution to the optimisation problem, then no further attempts at finding a further solution was made. In certain cases, it is found that the matching error is improved when the optimisation is run several times, using the parameters found in the previous optimisation as initial estimates for the next optimisation.

$c_{m-}(s)$, $c_{p-}(s)$ and $f_-(s)$ are the solutions to c_m, c_p and f found when integrating away from point R. The Taylor expansion in Sections 5.4.2 was used to perturb the boundary conditions from $s = 1/2$ to $s = 1/2 - \epsilon$. The Euler Lagrange equations were then integrated numerically over the interval $1/2 - \epsilon \geq s \geq s_m$. For a good solution to the minimisation problem, any change in s_m in the range $0.25 < s_m < 0.75$ does not change the value of the residual.

In this minimisation problem there are four unknowns and three matching conditions. Typically the final absolute value of the residuals was between $O(10^{-6})$ and $O(10^{-8})$ where a smaller value is reflected in more continuous values of c_m, c_p and f. One a solution is found, the a single fixed parameter, c_0, κ, Δ_p, is perturbed and the next solution is found. The magnitude of this perturbation was fixed at $\epsilon = 10^{-2}$. The end of a solution branch is taken to occur when there is a sudden jump in the absolute value of the residual. Typically, the absolute value of the residual after the jump will be $O(10^{-3})$. The jump in error is sudden, clearly indicating the end of the solution branch.

6.3.2 Dumbell Solutions

Dumbell solutions have an additional singularity at the point when f is at its maximum. From (5.38) it is clear that at this point $fc_p = 1$. The singularity unique to dumbell solutions will be referred to as point Q. These points are indicated in Figure 6.3(d).

As prolate spheroids are perturbed away from a spherical solution by increasing κ and finding the other parameters using *fsolve*, the minimum value of c_m, c_m^{min}, decreases. The transition point between prolate spheroid and dumbell solutions is when $c_m^{min} = 0$ at point R. The singularity is at a point of inflection. As the second order terms are identically zero the Taylor series used to perturb the boundary conditions away from the singularity must be extended to the fourth order. The effect of further increasing κ is to increase the distance along the z-axis between the point Q and point R.

For dumbell solutions $c_m = 0$ at some point between the points Q and R so at Q we have $c_m c_p > 0$ while at R we have $c_m c_p < 0$. From (6.9), it is clear that point Q is a maximum in f and R is a minimum in f. The signs in (5.36)-(5.38) must be chosen so that f increases between point P and Q and decreases between Q and R.

Generally, for prolate spheroids and dumbells c_m and c_p have a maximum value when $s = 0$ and decrease in value over the interval $0 < s < (1/2)$. As κ is increased, the minimum value of c_m and c_p decreases. Prolate spheroids are found when $c_m|_{min} > 0$ while dumbell solutions are found when $c_m|_{min} < 0$. The rate of change of c_m is generally larger than that for c_p. For the numerical solutions in the current work, c_p is always positive.

By (6.9), if $c_m(0)c_p(0) < 0$ then f is increased when it is perturbed away from its boundary condition at point P. The solutions for f and c_p by integrating the Euler-Lagrange equations then tend towards a singularity $f(s_{m0}c_p(s_{m0})^2 = 1$ where $s_{m0} \neq (1/2)$. At this point $c_m(s_{m0})$ is negative so by (6.9), $f(s_{m0})$ is a maximum. For dumbells, the point at which the solutions found by integrating away from points P and R cannot be matched at an arbitrary point, but at this singularity.

Dumbell solutions must be matched at two points: once between point P and Q and then between Q and R. This means that there are six matching conditions to fill which must correspond to six degrees of freedom. Again, numerical solutions are easier to find if spontaneous curvature c_0 is fixed. Whether the solution is a dumbell or not depends on the value of κ defined in (6.12). By Table 6.1, dumbell solutions are found when $\kappa > \kappa_{max}$. If κ is allowed to be a free variable, small perturbations in κ close to $\kappa = \kappa_{max}$ will shift the corresponding solution from being a prolate spheroid to being a dumbell, which is difficult to account for numerically. For this reason κ and c_0 are fixed while Δ_p, λ and $f(1/2)$ are allowed to be free variables of the optimisation problem.

Two further independent parameters can be defined at point Q. These are

$$C \quad \text{maximum value of } f(s), \tag{6.17}$$

$$\gamma \quad \text{limit of } \tfrac{dcm}{ds} \text{ at point Q.} \tag{6.18}$$

C is the value of f at point Q. At point R, the limiting gradient of c_m is fixed as zero in order

for the resulting shape to be symmetric around the mid-length. However, this condition is not necessary for dumbell solutions.

The choice of the third parameter is determined by the following method used to find the solution. This method is original to this work. If the third singularity, at point Q, occurs at $s = s_{m0}$ then the solutions of (5.36)-(5.38) must be matched at points $s_{\epsilon 1}$ and $s_{\epsilon 2}$ where

$$\epsilon < \quad s_{\epsilon 1} \quad < s_{m0}, \tag{6.19}$$

$$s_{m0} < \quad s_{\epsilon 2} \quad < (1/2 - \epsilon), \tag{6.20}$$

so that, for $0 < \eta < 1$,

$$s_{m0} = \eta \left(s_{\epsilon 2} - s_{\epsilon 1} \right). \tag{6.21}$$

The Euler-Lagrange equations will only be used to find c_m, c_p and f across the intervals $\epsilon \leq s \leq s_{\epsilon 1}$ and $s_{\epsilon 1} \leq s(1/2 - \epsilon)$. If the parameters (6.13)-(6.12) are well chosen then $s_{m0} - s_{\epsilon 1} << 1$ and $s_{\epsilon 1} - s_{m0} << 1$. The integration of c_m, c_p and f between $s_{\epsilon 1}$ and $s_{\epsilon 2}$ can be found using appropriate Taylor expansions. This avoids the problems associated with finding solutions which are invariant when the signs in (5.36)-(5.38) are changed in the region $s_{\epsilon 1} < s < s_{\epsilon 2}$.

Good starting values for parameters Δ_p, λ and $f(1/2)$ for the dumbell branch can be found as follows. The boundary condition at $s = 1/2$, (5.45), requires that the value of c_m at point R is

$$c_m = \pm \sqrt{2\lambda + \Delta_p / c_p + (cp - c_0)^2}. \tag{6.22}$$

For an spheroid solution the positive sign in (6.22) must be chosen at point R. The prolate spheroid branch ends when a real value of (6.22) cannot be found. κ, defined in (6.12), is the parameter which moves the solutions along the prolate spheroid branch line. The best way to find the first point on the dumbell branch line is to fit the parameters Δ_p, λ and $f(1/2)$ to a polynomial solution with respect to κ. The polynomial solutions of Δ_p, λ and $f(1/2)$ can be extended until a κ is found for which (6.22) is real again. For the dumbell branch the negative sign in (6.22) must be chosen.

The problem of accurately finding a dumbell solution is divided into two optimsation problems. Initially, a residual consisting of three conditions is used to find the three parameters Δ_p, λ and $f(1/2)$. The accuracy of the final dumbell solution relies strongly on these parameters. Then a second optimisation programme is run to find the remaining three free variables.

c_m, c_p and f are integrated away from the singularities at point P and point R using the method given in Section 6.3. For the first optimisation, c_{m+}, c_{p+} and f_+ are integrated over the interval $\epsilon < s < (1/2 - \epsilon)$. Similarly, c_{m-}, c_{p-} and f_- are integrated over the interval $(1/2 - \epsilon) < s < \epsilon$. The value of $s_{\epsilon 1}$ is then determined by finding the smallest s for which

$$\text{Real}\left(f_+ c_{p+}^2 \right) < 10^{-10}. \tag{6.23}$$

The value of $s_{\epsilon 2}$ is then determined by finding the largest s for which

$$\text{Real}\left(f_- c_{p-}^2 \right) < 10^{-10}. \tag{6.24}$$

Typically, $s_{\epsilon 1} - s_{\epsilon 2} < 10^{-2}$ so the values of c_p at $s = s_{\epsilon 1}$ and $s = s_{\epsilon 2}$ will be approximately the same. As f and c_p are related by $f c_{p-} \approx 1$, this is also true for f.

As there are three unknowns, three matching conditions are required at $s = s_{m0}$. Solutions cannot be found between $s_{\epsilon 1}$ and $s_{\epsilon 2}$ are not found using Taylor expansions. The required parameters, (6.17) and (6.18) are not included in the minimisation problem as degrees of freedom. However, as $s_{\epsilon 1} - s_{\epsilon 2}$ is so small,

$$c_{p+}(s_{\epsilon 1}) \approx c_{p-}(s_{\epsilon 2}) \qquad \text{and} \qquad f_{+}(s_{\epsilon 1}) \approx f_{-}(s_{\epsilon 2}). \tag{6.25}$$

Close to s_{m0}, the values of f and c_p will almost be constant so their difference across the break in the solution can simply be minimised. As f and c_p are related by $f c_{p-} \approx 1$, it is enough to do this for only for the more slowly varying variable, f.

Across the interval $s_{\epsilon 1} \leq s \leq s_{\epsilon 2}$ c_m can be approximated as a linear function. The solutions to c_m on either side of point Q can be fitted to one continuous polynomial, $x(s)$. It is best to fit a linear polynomial only to values of c_m very close to the singularity. The difference between values of c_m at either side of the singularity and their fitted linear function can then be minimised.

The residual for the first optimisation can now be defined as

$$\begin{aligned} \mathbf{R_2} \quad = \quad & [x(s_{m1}) - c_{m+}(s_{\epsilon 1}), \\ & x(s_{m2}) - c_{m-}(s_{\epsilon 2}), \\ & f_{+}(s_{\epsilon 1}) - f_{-}(s_{\epsilon 2})]. \end{aligned} \tag{6.26}$$

Once this residual is minimised by varying the parameters Δ_p, λ and $f(1/2)$, the values of the other parameters can be found. Firstly, the value s_{m0} at which the singularity at point Q occurs is found as accurately as possible. As discussed, the singularity occurs at the point when the positive sense of (6.22) is true. s_{m0} is found by using the numerical solutions to c_p and f to find the right hand side of (6.22) and fitting a linear polynomial $y(s)$ to it. The value of s at which this polynomial solution equals $x(s)$ was taken to be s_{m0}. The calculated value of s_{m0} can then be used to find η using (6.21). The term (6.17) is the value of a linear polynomial fit of f when $s = s_{m0}$. (6.18) is found by using the simple approximation

$$\gamma \approx \frac{c_m(s_{\epsilon 2}) - c_m(s_{\epsilon 1})}{s_{\epsilon 2} - s_{\epsilon 1}}. \tag{6.27}$$

The parameters Δ_p, λ, $f(1/2)$, $f(s_{m0})$, γ and η are now used as free variables to minimise the residual

$$\begin{aligned} \mathbf{R_3} = [c_{m+}(s_{\epsilon 1}) \quad - \quad & c_{m++}(s_{\epsilon 1}), \\ c_{p+}(s_{\epsilon 1}) \quad - \quad & c_{p++}(s_{\epsilon 1}), \\ f_{+}(s_{\epsilon 1}) \quad - \quad & f_{++}(s_{\epsilon 1}), \\ c_{m-}(s_{\epsilon 2}) \quad - \quad & c_{m--}(s_{\epsilon 2}), \\ c_{p-}(s_{\epsilon 2}) \quad - \quad & c_{p--}(s_{\epsilon 2}), \\ f_{-}(s_{\epsilon 2}) \quad - \quad & f_{--}(s_{\epsilon 2})], \end{aligned} \tag{6.28}$$

where $_+$ denote solutions on integration from point $s = \epsilon$ to $s_{\epsilon 1}$ and $_-$ are solutions on integration from point $(1/2 - \epsilon)$ to $s_{\epsilon 2}$. $s_{\epsilon 1}$ and $s_{\epsilon 2}$ are determined by the same method as in the previous case. The parameter, η, is used to find s_{m0}. Taylor expansions are used to find solutions denoted by $_{++}$ and $_{--}$.

The magnitude of (6.28) found using initial estimates for the free parameters from the first optimisation were found to be $O(10^{-6})$. This value was not improved by further optimisation. The success of finding a dumbell solution relies on good initial guesses and a well chosen residual to find the first three parameters. The dumbell solution branch for a given spontaneous curvature c_0 was continued by increasing κ by $O(10^{-3})$ until the magnitude of (6.28) suddenly increased to $O(10^{-3})$. At this point, no further attempts to find further solutions was made.

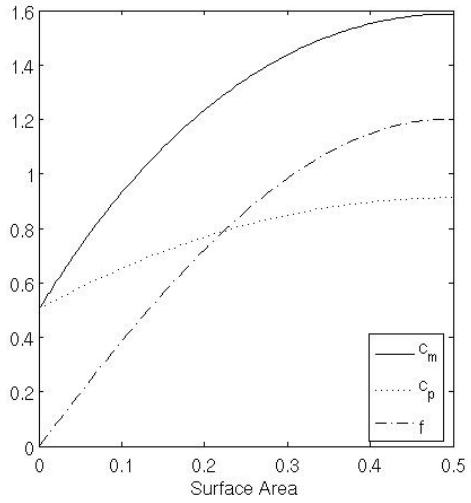

(a) Numerical solutions c_m, c_p and f against s when $\kappa = 1.5$ and solution is a prolate spheroid.

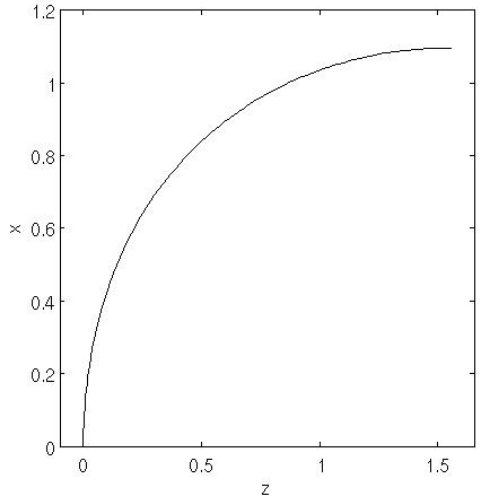

(b) Numerical solution for x against z when $\kappa = 1.5$ and solution is a prolate spheroid.

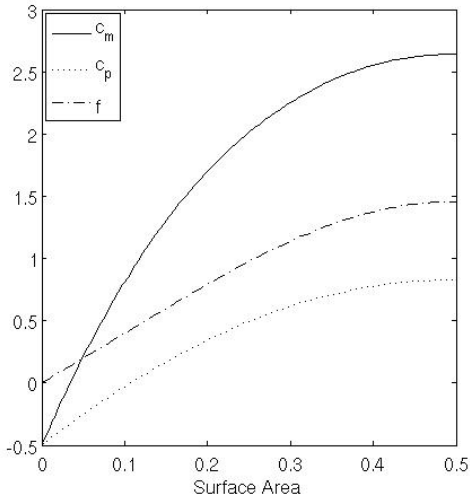

(c) Numerical solutions c_m, c_p and f against s when $\kappa = 1.95$ and solution is a dumbell.

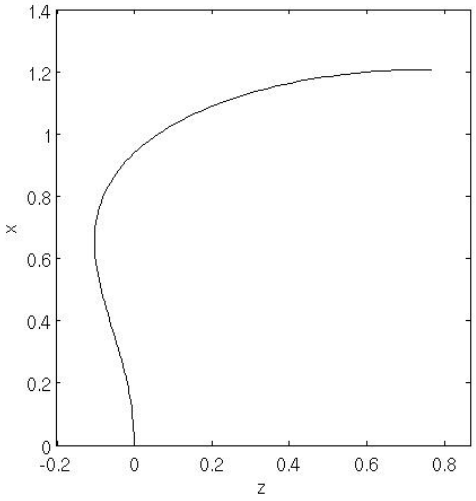

(d) Numerical solution for x against z when $\kappa = 1.95$ and solution is a dumbell.

Figure 6.2: Example prolate solutions when $c_0 = 0$.

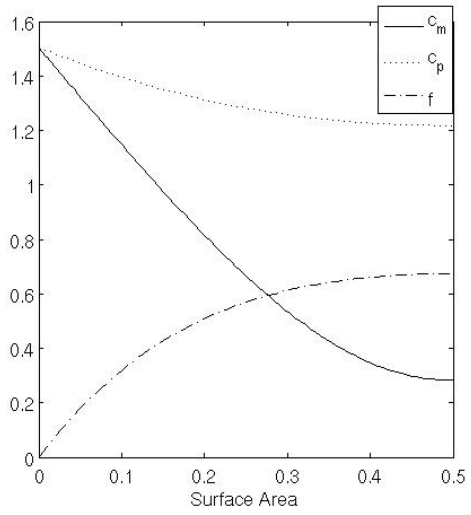

(a) Numerical solutions c_m, c_p and f against s when $\kappa = 0.5$ and solution is a oblate spheroid.

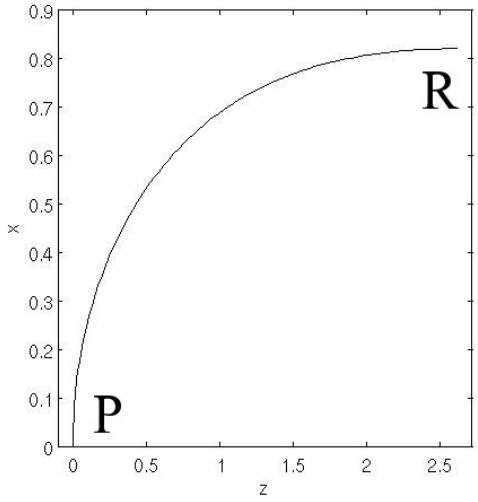

(b) Numerical solution for x against z when $\kappa = 0.5$ and solution is a oblate spheroid.

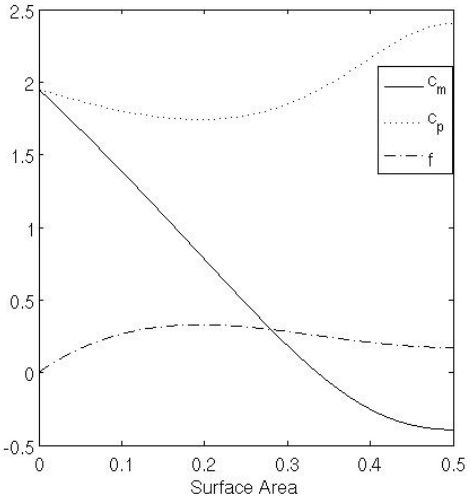

(c) Numerical solutions c_m, c_p and f against s when $\kappa = -0.5$ and solution is a discocyte.

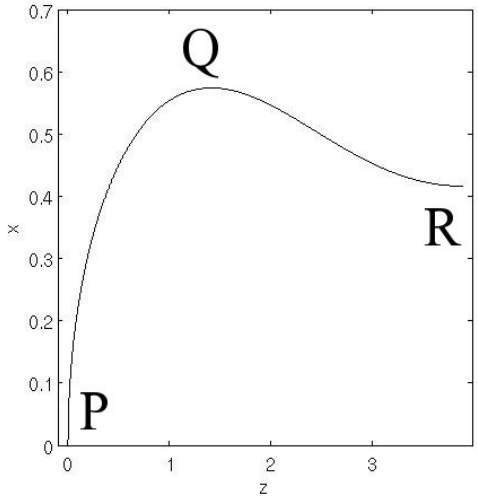

(d) Numerical solution for x against z when $\kappa = -0.5$ and solution is a discocyte.

Figure 6.3: Example oblate solutions when $c_0 = 0$.

6.4 Numerical Results from the Helfrich Boundary Value Problem

How the stability of HBVP solutions depends on Δ_p is examined in Section 6.4.1. Phase diagrams relating κ, Δ_p, length and volume can be found in Section 6.4.2. Finally, specific examples which illustrate the observations in Section 6.4.2 are given in Section 6.4.3. In Section 6.4.3, the types of solutions found for extremely positive and negative κ are described. The solutions in Section 6.4.3 are examples of the sharp maxima and minima in c_m which were introduced in the case of the reduced Euler-Lagrange equations in Section 5.13.

6.4.1 Stability of Solutions with respect to Osmotic Pressure, Δ_p

The Euler-Lagrange equations find shapes which set the first variation of the free energy (5.4) to zero. The form of the second and third variations in free energy for this problem can be found in [130] and [131]. The range of possible shapes which are symmetrical about their mid-length are illustrated in Figure 6.1. For a given surface area, spherical shapes are those shapes with the maximum volume. The critical osmotic pressure Δ_{pc}, is the critical pressure at which there is a phase transition from either an oblate or a prolate spheroid to a sphere. It can be written in terms of c_0 as

$$\Delta_{pc} = 2k_c \left[6 - c_0\right]. \tag{6.29}$$

This result can be found in [130] and again in more detail in [131].

What is observed in the numerical solutions, is that as the osmotic pressure of an oblate or prolate spheroid solution is perturbed towards Δ_{pc}, its volume increases and its Helfrich energy decreases as it reaches the limiting shape of a sphere. In Figure 6.4(a), the spherical limit is reached when $c_p(0)$ and $f(1/2)$ no longer change. The values of Δ_p at which this occurs when c_0 is clearly effected by numerical error. Once a solution has reached the limit of a sphere, further perturbations to Δ_p cannot move the solution away from the spherical limit.

In practice, this means that if the volume of a sphere is decreased, while surface area is constant, then the solution will be a so-called spheroid. When $\Delta_p = \Delta_{pc}$ the second variation in free energy is zero. In [131], the third variation in the Helfrich free energy functional (5.4) was found. It indicated that there is a critical spontaneous curvature,

$$c_{0c} = -1.2. \tag{6.30}$$

This critical spontaneous curvature determines whether an oblate or a prolate spheroid is the stable solution when the normalised volume, V_0, as defined in (5.67) is $V_0 < 1$. When $c_0 < c_{0c}$ it is expected that the oblate spheroids are stable and the prolate spheroids are unstable. Conversely, when $c_0 > c_{0c}$ it is expected that the prolate spheroids are stable and the oblate spheroids are unstable. As the volume of a shape continues to decrease, the shapes deform as summarised in Figure 6.1. Prolate spheroids transition into dumbell solutions and oblate spheroids transition into discocytes.

The expected results for stability are found to be describe numerically calculated results for E_{H0} and c_0. A useful way to compare the Helfrich energy of solutions which have different spontaneous curvature is the normalised Helfrich energy defined in (5.68).

Figure 6.5(a) demonstrates how the normalised Helfrich energy is a minimum at $\Delta_p = \Delta_{pc}$. In Figure 6.5(b), the normalised Helfrich energy of oblate spheroids is less than that of prolate spheroids when $c_0 = 0$. It is also shown that, for $V_0 < 0.94$, the normalised Helfrich energy of oblate spheroids is greater than that of prolate spheroids when $c_0 = -4$, which generally supports the analysis in [130] and [131]. Further results for the dependence of the normalised Helfrich energy on volume can be found in Figure 6.9.

The value of $\Delta_p + 2\lambda c_p(0)$ along the solution branch of spherical solutions in Figure 6.4(b) does not change. In this example $c_0 > c_{0c}$. When $\Delta_p < \Delta_{pc}$ then $\Delta_p + 2\lambda c_p(0) < 0$ whereas when $\Delta_p > \Delta_{pc}$ then $\Delta_p + 2\lambda c_p(0) > 0$. In Figure 6.5(b), the opposite is true. By the analysis in Section 5.9 and discussion in Section 6.2, if $\Delta_p + 2\lambda c_p(0) < 0$ then solutions will be prolate solutions and oblate solutions otherwise. When $c_0 > c_{0c}$, $\Delta_p < \Delta_{pc}$ will result in a prolate solution while $\Delta_p > \Delta_{pc}$ will result in an oblate solution. For $c_0 < c_{0c}$, the converse is true. The observations in the previous discussions imply that the most energetically stable solutions, whether oblate or prolate, will be found when $\Delta_p < \Delta_{pc}$. The membranes will deform from a spherical shape as osmotic pressure is decreased.

6.4.2 Overview of Helfrich Boundary Value Solutions

The parameters in Figure 6.6 were found by perturbing κ rather than Δ_p so both energetically stable and unstable solutions could be found. Solutions were found by perturbing κ in a positive or negative direction until there was a sudden increase in error. HBVP solutions were found for which $-12 \leq c_0 \leq 22$. For what will be termed mid-range solutions, spontaneous curvature lies in the range $-4 \leq c_0 \leq 1$. This is the range in spontaneous curvature in [25]. In the current work, the additional HBVP solutions found are referred to as very positive spontaneous curvature solutions, where $2 \leq c_0 \leq 20$ and very negative spontaneous curvature solutions where $-12 \leq c_0 \leq 2$.

Table 6.1 summarises the types of possible solutions in terms of κ. The break in solutions in the prolate branch ($\kappa \approx 2$) is due the difficulty of finding numerical solutions over the jump between prolate spheroids and dumbell solutions. Oblate spheroid solutions where $\kappa \lesssim -2.5$ cannot be found by perturbing away from a spherical solution. A separate set of initial conditions for the minimisation problem was found by trial and error. These solutions give a more complete picture of the range of possible solutions to the HBVP solutions.

Figure 6.6(a) is a plot of Δ_p against κ for some mid-range values of c_0. The key thing to notice in Figure 6.6(a) is that when $c_0 < c_{0c}$ Δ_p is increasing with κ while for $c_0 > c_{0c}$ it is decreasing with κ. The pressure is below the critical pressure for the oblate spheroid branch when $c_0 < c_{0c}$ and for the prolate spheroids when $c_0 > c_{0c}$. In [130] and [131], the second and third variations of the free energy were only calculated for small deformations of a sphere so these observations are only true close to $\kappa = 1$. In Figure 6.6(b), the trend for $c_0 = 6$ shows a discontinuity at $\kappa = 1.1$. It was found that when $\kappa \gtrsim 1.1$, generally no solutions are found

when $c_0 < 16$. For the cases when $c_0 = 6$ and 7 the solver managed to find solutions past this point. When $c_0 \geq 16$, the prolate branch is again extended. Solutions such as these, for which $|\kappa| \approx O(10)$, are discussed in Section 6.4.3. Solutions such as these are made possible by the c_0 dependent terms.

From the preceeding discussion, the volume of a vesicle is expected to be at a maximum when it is a sphere. All the plots of volume against κ in Figure 6.7 clearly a show a maximum in the volume when $\kappa = 1$. The plots become more distinct for extreme values of κ. Some of the oblate solutions also have minima in volume. When $c_0 = 20$, the prolate branch also has a minimum so that the volume of the solutions is always close to 1.

Figure 6.8(a) shows that the normalised Helfrich energy is at minimum when $\kappa = 1$ for all values of c_0. As c_0 decreases this minima is flattened as the variations in c_p and c_m are small relative to c_0.

A plot of normalised Helfrich energy against volume should indicate whether prolate or oblate solutions are more stable for a given volume. This is plotted in Figure 6.9 for mid-range values of $-4 \leq c_0 \leq 1$. They confirm that oblate solutions are more stable when $c_0 < c_{0c}$ and prolate solutions are more stable when $c_0 > c_{0c}$ for shapes close to the spherical solution. The obvious deviations from this result when $c_0 = -1$, -2 and -4 correspond to oblate spheroid solutions which occur before the minimum in volume in Figure 6.7(a).

As these solutions are to be used to provide initial estimates to solve the cell on a fibre boundary value problem introduced in Section 5.5, the length of the vesicle along the axis of rotation is of interest. Figure 6.10(a) includes solutions with negative length. These solutions fulfill the boundary conditions set out in Section 5.4. However, they have no physical meaning as they cannot be used to plot a continuous profile. Figure 6.10(b) illustrates three separate trends in volume and length in the prolate branch of solutions. In the examples where $c_0 = 6$ and 20 there is a maximum in length. When $c_0 = 6$ the volume then decreases with length while when $c_0 = 20$ it then increases.

6.4.3 Specific Examples

Individual solutions when $c_0 = -12$, -2, 6 and 20 can be found in Figures 6.11-6.14. For each solution branch, the solutions with the maximum and minimum values of κ are plotted, along with a third solution. These figures and the discussion in this section aim to familiarise the reader with the full range of the Helfrich boundary value problem solutions obtained. It is especially important to note how when $|\kappa|$ is large then sharp minima and maxima can be observed in c_m due to the shear terms introduced in Section 5.13. Some of the solutions of the cell on a fibre boundary value problem will also have these maxima and minima, allowing certain boundary conditions to be met.

When $c_0 = -12$ the HBVP solution which has the most negative value of κ is found. This is the discocyte solution in Figure 6.11(a). Solutions of negative length are found when $c_0 = -2$, -1 and 0. An example of such a solution can be found in Figure 6.12(a) when $c_0 = -2$. An example of a dumbell solution is also given here.

Examples of solutions along the solution branch parameterised by $c_0 = -12$, 6 and 20

are of interest as they contain solutions at extreme values of κ. When $c_0 = -12$, there is a sharp maximum in c_0 and when $c_0 = 6$ and 20 there is a sharp maximum. Despite being very different from spheroid solutions, solutions for which there is a sharp minimum c_m are still oblate while solutions for for which there is a sharp minimum c_m are still prolate.

The solution in Figure 6.11(b), when $\kappa < 0$ is very different than the oblate solutions in Figure 6.2. In the interval $0.1 < s < 0.5$, we have $c_p \approx 1$ and $c_m \approx 1$. The boundary condition $c_p(0) = c_m(0)$ is met by the presence a sudden maximum in c_m. A less sharp maximum can also be observed when $c_0 = -2$ in Figure 6.12(b). These solutions can be compared. The solution when $c_0 = -12$ is longer than that when $c_0 = -2$ as the turning point is closer to $x = 0$ and less of the solution turns over itself. In fact the solution when $c_0 = -2$ is negative. Generally length increases when κ is decreased. Referring to Figures 6.7(c) and 6.10(c), such solutions for in which c_m is a maximum account for the solutions which increase in length and volume after a minimum in volume as κ decreases. The solutions which have a maximum in c_m are discocyte solutions as they have one turning and one inflection point.

Similarly, when $\kappa > 0$ the example solutions in Figures 6.13 and 6.14 have minima. These minima are sharper when κ is greater. In these solutions, there are at least two points of inflection which move closer to $x = 0$ as κ increases, which has the effect of decreasing the length. In both cases, length is decreased when κ is increased. Referring to Figure 6.10(b), when $c_0 = 6$, as the length of these solutions increases, their volume decreases. In contrast, when $c_0 = 20$, as the length of these solutions increases, their volume gradually increases.

These results show that when κ is increased not only solutions in which c_m crosses zero once, the dumbell solutions, can be found, but solutions in which c_m crosses zero twice can also be found. For these solutions there is no additional singularity. For very large κ, such as in Figure 6.13(d) when $c_0 = 6$, c_p also crosses zero twice which results in two turning points. However, when $c_0 = 20$ solutions there were no turning points in the prolate solutions. Whether both dumbell solutions and solutions with two inflection points can be found for the same c_0 has not been investigated.

The sharp maxima and minima in these solutions can be compared to those in Figures 5.10 and 5.11 in Section 5.13. These sharp minima and maxima are only found in solutions when $|c_0| >> 1$ when the shear terms are of similar magnitude to the terms proportional to $1/f$. In this case, the minima and maxima do not reflect minima and maxima in c_p due to oscillations arising from the surface terms.

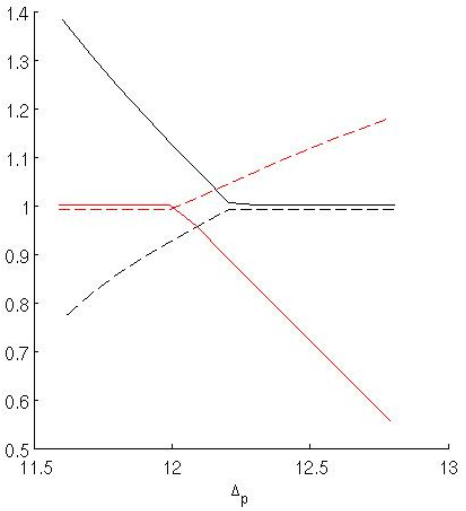

(a) $c_p(0)$ and $f(1/2)$ against Δ_p, $c_0 = 0$. Red - solutions found by incrementally decreasing Δ_p. Black - solutions found by incrementally increasing Δ_p. Solid - $c_p(0)$. Dashed - $f(1/2)$.

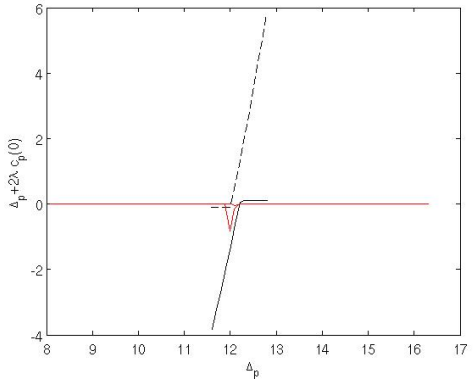

(b) $\Delta_p + 2\lambda c_p(0)$ against Δ_p, $c_0 = 0$. Red - solution moved along the spherical limit. Black solid - solutions found by incrementally increasing Δ_p Black dashed - solutions found by incrementally decreasing Δ_p.

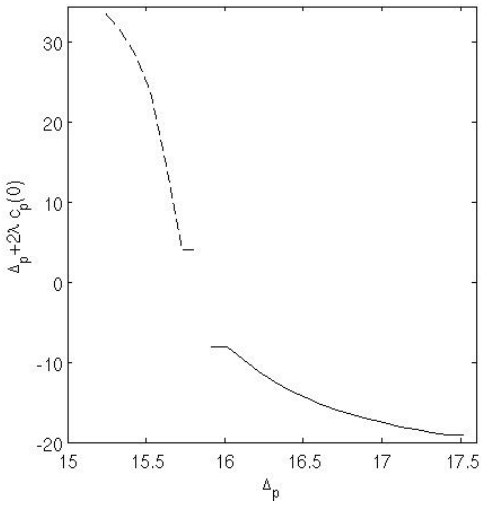

(c) $\Delta_p + 2\lambda c_p(0)$ against Δ_p, $c_0 = 2$. Red - solution moved along the spherical limit. Black solid - solutions found by incrementally increasing Δ_p Black dashed - solutions found by incrementally decreasing Δ_p.

Figure 6.4: Plots of parameters relating to stability in solutions found on incremental changes in Δ_p when $c_0 = 0$.

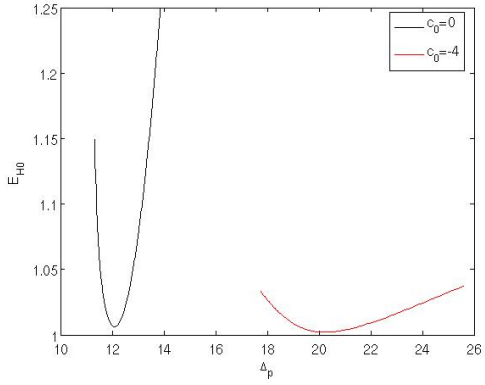

(a) E_{H0} against Δ_p when $c_0 = 0$ and $c_0 = -4$.

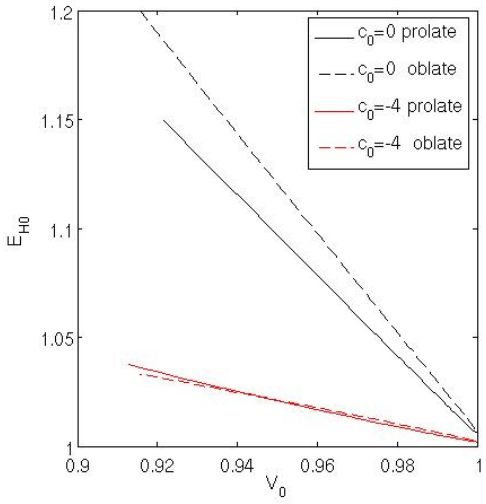

(b) E_{H0} against normalised volume for oblate and prolate spheroids when $c_0 = 0$ and $c_0 = -4$.

Figure 6.5: Dependence of normalised Helfrich energy with Δ_p and c_0.

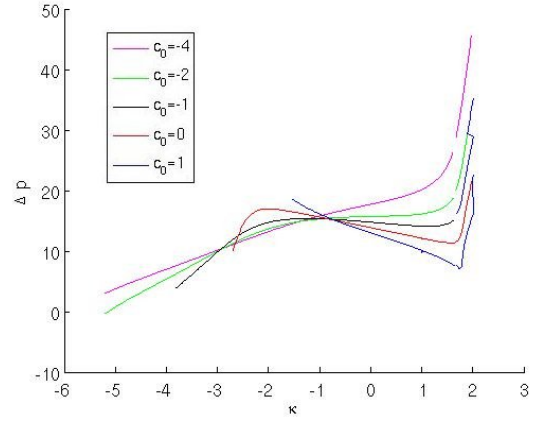

(a) $c_0 = 1$, 0, -1, -2 and -4.

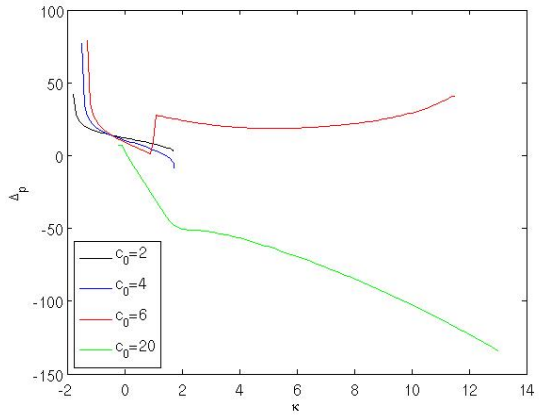

(b) $c_0 = 2$, 4, 6 and 20.

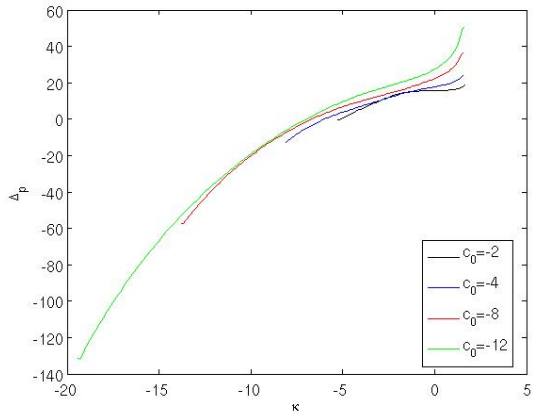

(c) $c_0 = -2$, -4, -8 and -12.

Figure 6.6: Plots of Δ_p against κ, the curvature of the solution at the axis of rotation for a range of values of c_0.

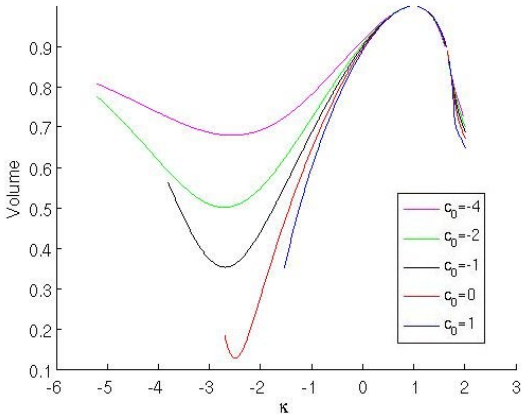

(a) $c_0 = 1$, 0, -1, -2 and -4.

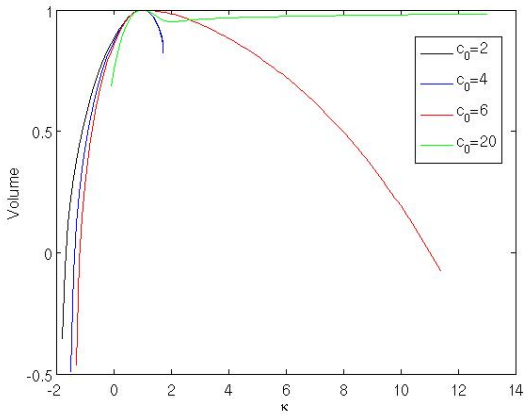

(b) $c_0 = 2$, 4, 6 and 20.

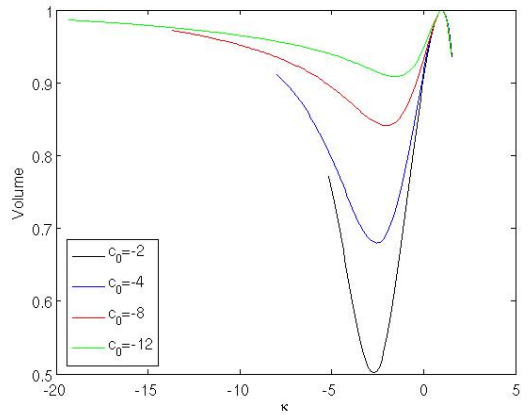

(c) $c_0 = -2$, -4, -8 and -12.

Figure 6.7: Plots of volume against κ, the curvature of the solution at the axis of rotation for a range of values of c_0.

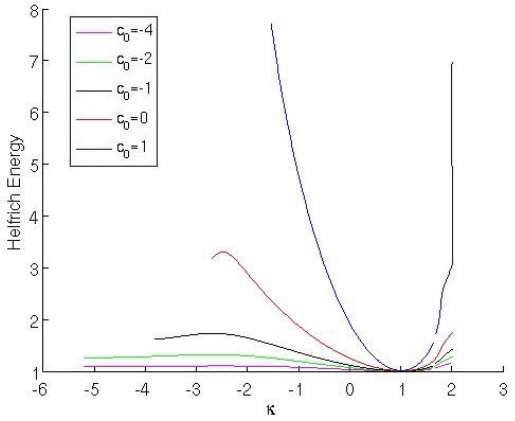

(a) $c_0 = 1$, 0, -1, -2 and -4.

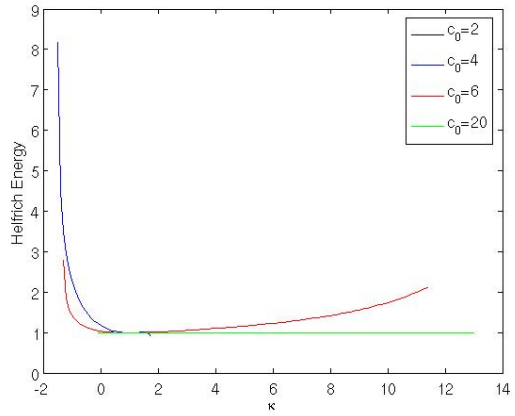

(b) $c_0 = 2$, 4, 6 and 20.

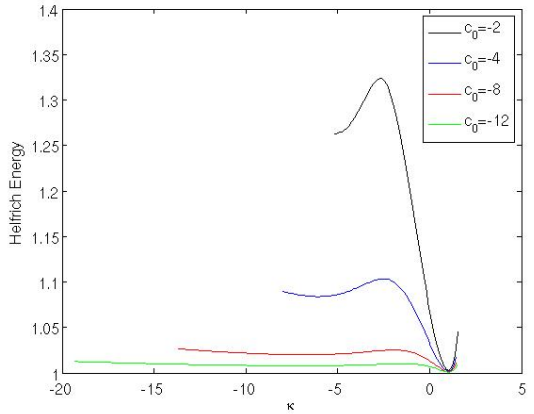

(c) $c_0 = -2$, -4, -8 and -12.

Figure 6.8: Plots of normalised Helfrich energy against κ, the curvature of the solution at the axis of rotation for a range of values of c_0.

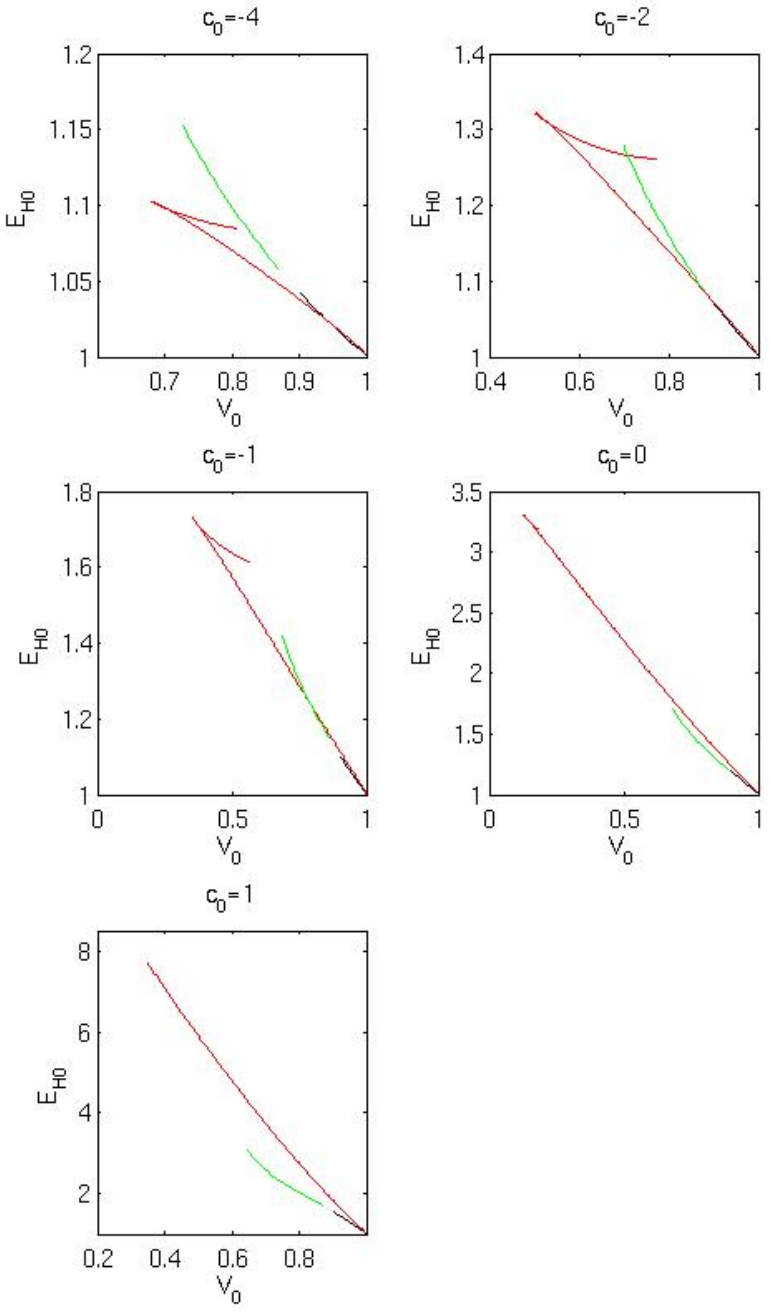

Figure 6.9: Plots of the normalised Helfrich energy against the normalised volume for a range of values of c_0. Black - prolate solutions. Green - dumbell solutions. Red - oblate solutions.

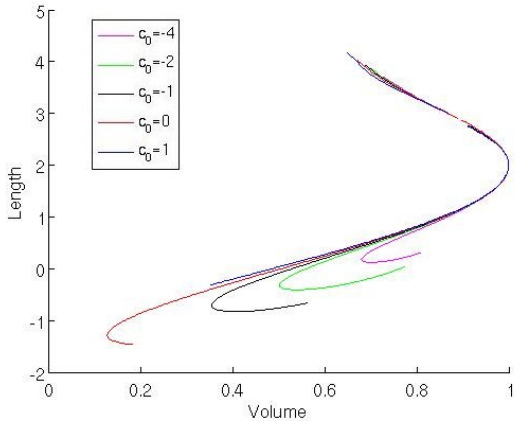

(a) $c_0 = 1$, 0, -1, -2 and -4.

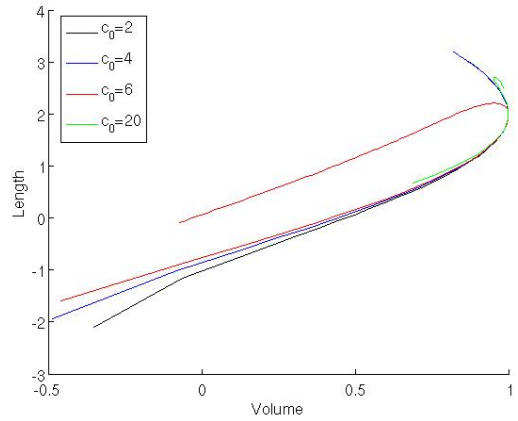

(b) $c_0 = 2$, 4, 6 and 20.

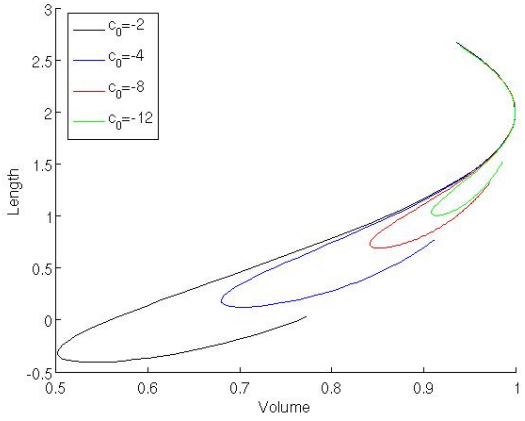

(c) $c_0 = -2$, -4, -8 and -12.

Figure 6.10: Plots of the length of the vesicle against the volume for a range of values of c_0.

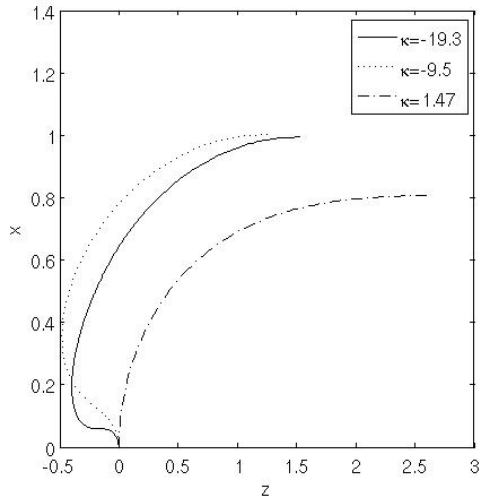

(a) x against z.

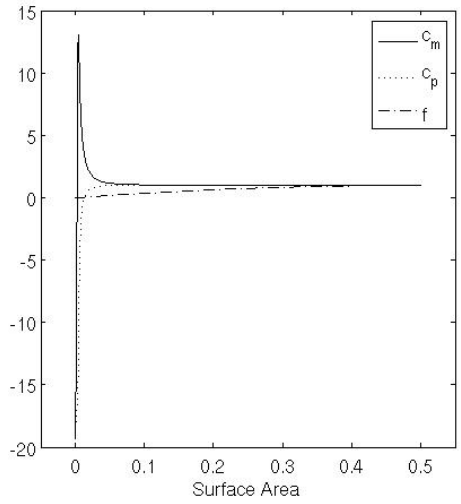

(b) c_m, c_p and f against s, $\kappa = -19.3$.

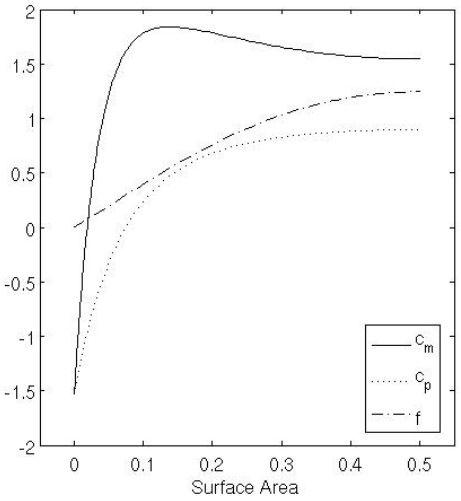

(c) c_m, c_p and f against s, $\kappa = -9.5$.

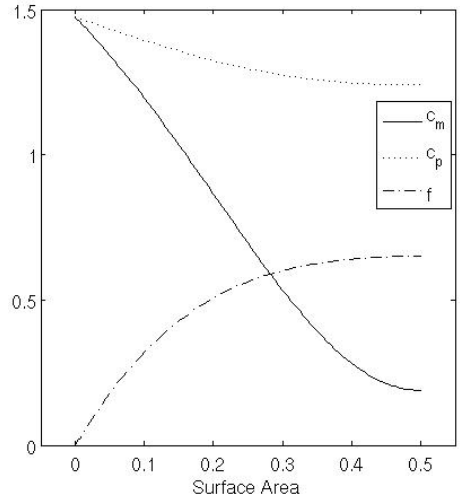

(d) c_m, c_p and f against s, $\kappa = 1.47$.

Figure 6.11: Example HBVP solutions when $c_0 = -12$.

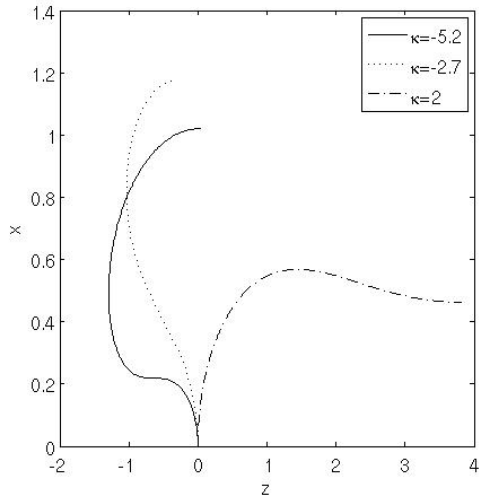

(a) x against z.

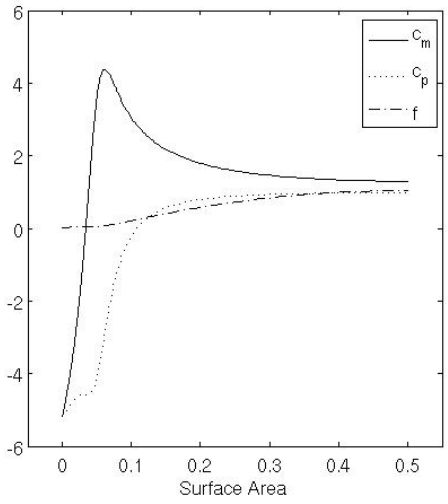

(b) c_m, c_p and f against s, $\kappa = -5.2$.

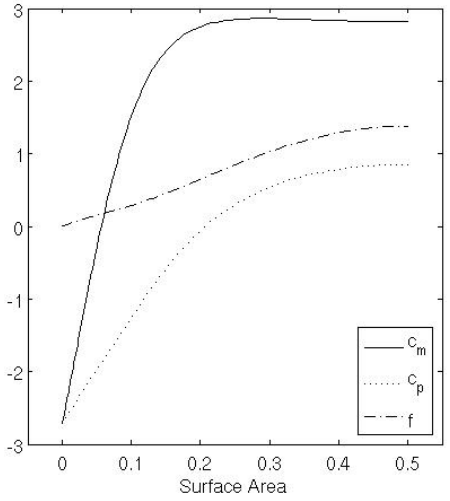

(c) c_m, c_p and f against s, $\kappa = -2.7$.

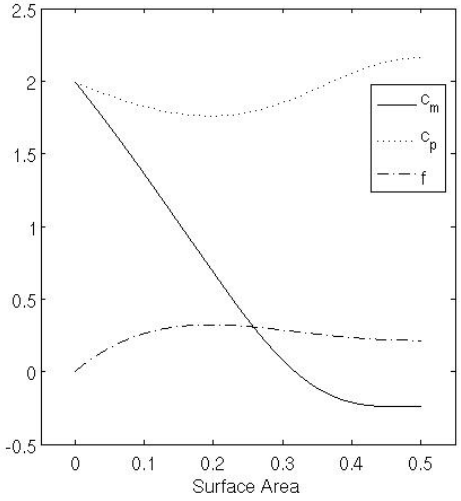

(d) c_m, c_p and f against s, $\kappa = 2$.

Figure 6.12: Example HBVP solutions when $c_0 = -2$. When $\kappa = -2.7$ the solution has a negative length. When $\kappa = 2$, the solution is a dumbell solution.

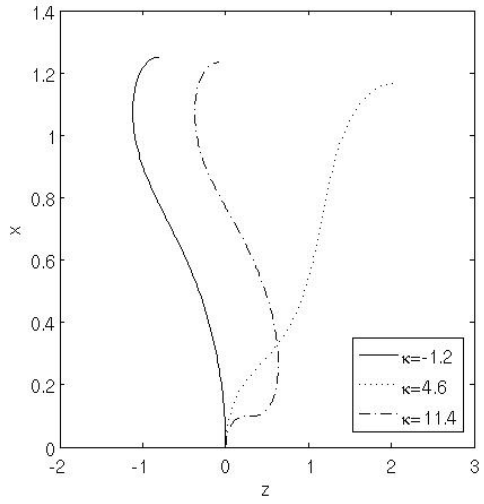

(a) x against z.

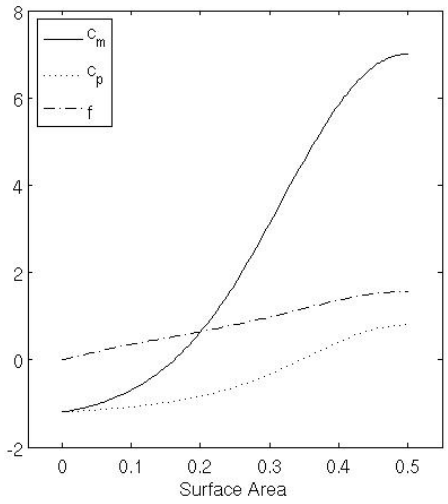

(b) c_m, c_p and f against s, $\kappa = -1.2$.

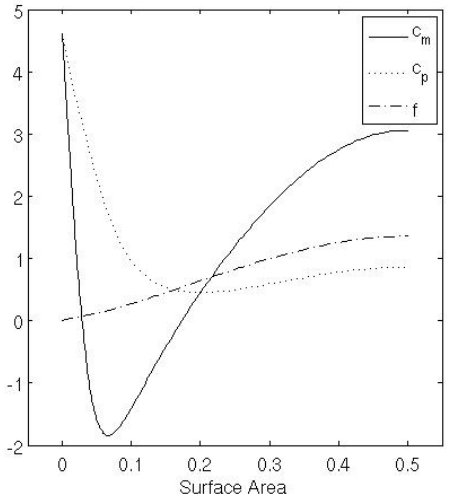

(c) c_m, c_p and f against s, $\kappa = 4.6$.

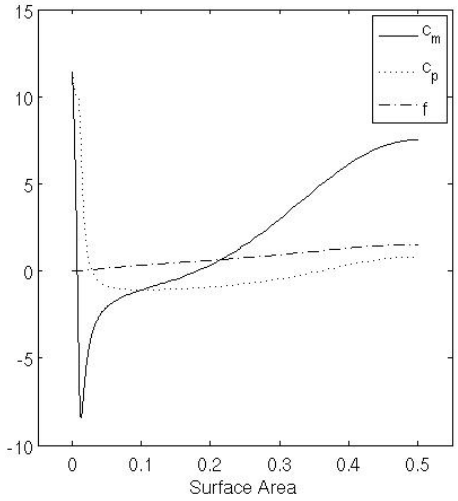

(d) c_m, c_p and f against s, $\kappa = 11.4$.

Figure 6.13: Example HBVP solutions when $c_0 = 6$.

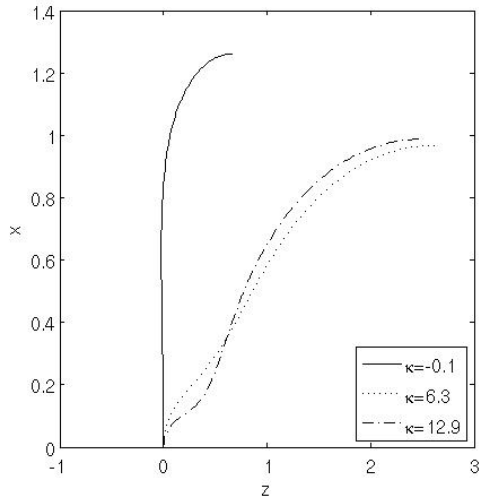

(a) x against z.

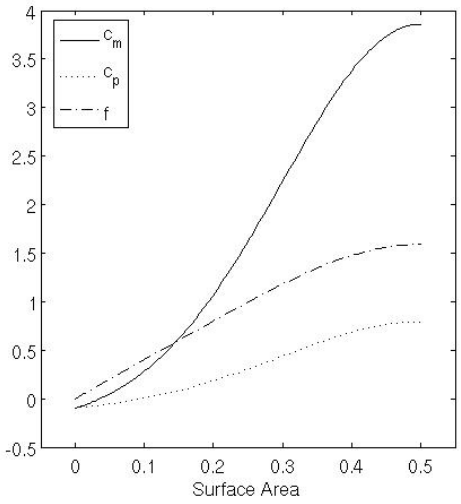

(b) c_m, c_p and f against s, $\kappa = -0.1$.

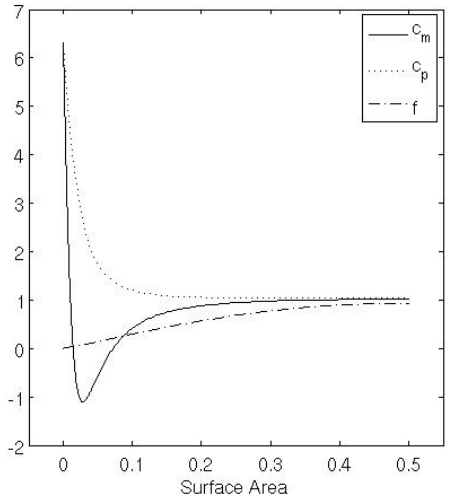

(c) c_m, c_p and f against s, $\kappa = 6.3$.

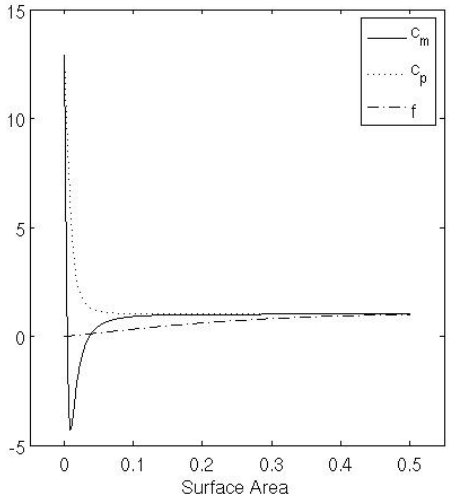

(d) c_m, c_p and f against s, $\kappa = 12.9$.

Figure 6.14: Example HBVP solutions when $c_0 = 20$.

6.5 Zero Momentum Boundary Condition

The boundary conditions given in Section 5.5 are necessary for a solution well-behaved around the singularities. However, as the shape of a vesicle engulfing a fibre is not completely enclosed, additional boundary conditions can be introduced to account for edge effects. The simplest case to consider is to set the contact potential between the cell membrane and fibre to zero and to set the Gaussian bending constant defined in Section 3.5.5 to zero.

By the argument that the energy minimisation is done with respect to ϵ where $c_p = c_{p0} + \epsilon\eta$, so that $\int E_H(x, c_p, \dot{c}_p)dx \geq \int E_H(x, c_{p0}, \dot{c}_{p0})dx$ and $\eta \equiv 0$ at end-points, the boundary term arising from the minimisation of the Helfrich energy,

$$\frac{\partial E_H}{\partial \dot{c}_p}\eta\Big|_{s=0}^{s=1}, \tag{6.31}$$

is usually set to zero. Only solutions of the energy minimisation problem which are symmetric about their mid-length are considered in this chapter. This condition implies that

$$\frac{\partial E_H}{\partial \dot{c}_p}\Big|_{s=0} = \frac{\partial E_H}{\partial \dot{c}_p}\Big|_{s=1}, \tag{6.32}$$

so that (6.31) is met even if η does not vanish at the boundaries. The terms at $s = 0$ and $s = 1$ cancel each other out. Recalling that the Euler-Lagrange equations can be shown to be equivalent to Newton's second law in generalised co-ordinates, a term of the form

$$\frac{\partial E_H}{\partial \dot{c}_p} = \left(2c_p + x\frac{dc_p}{dx} - c_0\right)\frac{x^2}{(1-(xc_p)^2)^{1/2}} \tag{6.33}$$

is referred to as a generalised momentum. How it can be interpreted to represent a generalised form of a particular physical property at a boundary varies between specific examples.

Refer to the balance of forces, (5.20) in Section 5.2, associated with the Helfrich energy minimisation problem. If it is enforced that

$$c_m + c_p - c_0\Big|_{s=0}^{s=1} = 0, \tag{6.34}$$

then forces tangential to the surface dependent on c_m, c_p and c_0, σ^{iso} and σ^{dir}, are set to zero at the surface of the fibre. The remaining force acting tangentially to the surface is the capillary force, so that the forces to balance along the contact line reduce to those for a droplet without a lipid bilayer membrane. Details how forces at a solid/liquid/vapour interface balance are given in Appendix C.2. There are no edge effects specific to the lipid bilayer. The terms perpendicular to the surface remain, but as they are perpendicular to the edge of the membrane, they can be assumed to play little role in the balance of forces at the liquid/solid point of contact.

If the curvature of the solution at $s = 0$ and $s = 1$ plays no role in the balance of forces between the edge of the membrane and the surface of the fibre. This is preferable as forces arising from the bending energy of a lipid membrane along a continuous surface will be very different to the forces associated with a free edge of a lipid membrane.

The condition (6.34) will be referred to as the zero momentum boundary condition for the cell on a fibre problem. It ensures that the generalised momentum is equal to zero at the boundaries $s = 0$ and so, by symmetry about the mid-length, $s = 1$.

6.5.1 Implementation of Zero Momentum Boundary Condition

To explore solution to the zero momentum boundary condition, two approaches were taken. For each value of spontaneous curvature $c_0 = 1$, 0, -1, -2 and -4 a set of solutions parameterised by volume was found. The solutions parameterised by volume can be compared to the HBVP solutions of the same volume. Solutions of this type can only be found for a limited range of f_0. These solutions answer the question of how a cell membrane adjusts its shape on engulfing a fibre when it cannot adjust its volume.

Solutions parameterised by length can be found for a wide range of values of f_0. Solutions of this type were found for $c_0 = -12 \leq c_0 \lesssim 3$. These solutions answer the question of how far a cell membrane can extend down the length of a fibre when it is free to change its volume as necessary. The only limitation to extending length in this case is the condition that the solution meets the zero momentum boundary condition at the surface of the fibre. It is observed that c_0 dependent terms, the shear terms in Section 5.13, play an important role in the resulting solutions.

6.5.2 Zero Momentum Boundary Problem Solutions Parameterised by Volume

For each spontaneous curvature c_0, the possible solutions to the zero momentum boundary problem can be parametrised by their volume V and

$$f(0) = f_0 = R^2, \tag{6.35}$$

where R is the radius of the fibre. The data given in [127] suggests that a fibre is significantly toxic when its radius is in the micron range. Using the data for the diameter of an alveolar macrophage given in [31], it can be found that for these fibres the relative radii of the cell and fibre is approximately 0.1. For these reasons the radius of a fibre has been set at either $R = 0.01^{1/2}$ or $R = 0.001^{1/2}$. For each value of f_0 and spontaneous curvature c_0 a set of zero momentum solutions were found with the maximum possible range in volume.

Solutions are found by minimising a residual using MATLAB optimisation functions as described in Section 6.3.1. c_0, V and f_0 are fixed for each optimisation. The five variables in this optimisation, or degrees of freedom are

$$\Delta_p \quad \text{osmotic pressure}, \tag{6.36}$$

$$\lambda \quad \text{surface tension}, \tag{6.37}$$

$$B \quad f(1/2), \tag{6.38}$$

$$c_m(0) \quad c_m \text{ at fibre surface}, \tag{6.39}$$

$$c_p(0) \quad c_p \text{ at fibre surface}. \tag{6.40}$$

For these five unknowns there are five conditions so that a solution to the zero momentum boundary value problem minimises the residual

$$\begin{aligned}
\mathbf{R_4} = [c_{m+}(s_m) &- c_{m-}(s_m), && (6.41)\\
c_{p+}(s_m) &- c_{p-}(s_m), && (6.42)\\
f_+(s_m) &- f_-(s_m), && (6.43)\\
v &- V, && (6.44)\\
c_m(0) &+ c_p(0) - c_0]. && (6.45)
\end{aligned}$$

The first three conditions and corresponding notation were the matching conditions introduced in Section 6.3.1. The fourth condition minimises the difference between the value of a fixed parameter V and that of the volume of a particular solution v. The fifth condition ensures that the zero momentum boundary (6.34) condition is met.

It is expected that the solution to the Helfrich boundary value problem where $2\kappa = c_0$ would provide a good initial estimate for the unknown parameters (6.13)-(6.15). As the values of c_0 chosen to represent the possible range of spheroid solutions have been chosen to be $c_0 = -4$, -2, -1, 0 and 1, the initial estimates are taken from oblate rather prolate spheroid solutions when $\kappa < 1$. Estimates for the two additional parameters (6.39)-(6.40) can be found by assuming that if the radius of a fibre R is small then

$$\begin{aligned}
s_0(R) &= \frac{R^2}{4}, && (6.46)\\
c_m(0) &= \kappa + \frac{3}{4}(\kappa(c_0^2 - 2\kappa c_0) + 2\kappa\lambda + \Delta_p)s_0(R), && (6.47)\\
c_p(0) &= \kappa + \frac{1}{4}(\kappa(c_0^2 - 2\kappa c_0) + 2\kappa\lambda + \Delta_p)s_0(R), && (6.48)\\
f(0) &= R^2. && (6.49)
\end{aligned}$$

In this case $c_m(0)$ and $c_p(0)$ are not independent. The variable s_0 is only used to find $c_m(0)$ and $c_p(0)$ and is not counted towards the surface area of the solution. For this cell on a fibre problem, there is no singularity at $s = 0$ so Euler-Lagrange equations only can be used to find c_{m+}, c_{p+} and f_+. As for the Helfrich boundary value problem, there remains a singularity at $s = 1/2$. Solutions are perturbed away from this point as described in Section 6.3.1.

A solution branch can be found by either perturbing the value of V. Alternatively, a new set of initial estimates can be obtained from a Helfrich boundary value solution for a slightly larger or smaller value of κ. In this case the solutions can also be parameterised by the value of κ from the Helfrich boundary value solution from which the initial estimates of the parameters were derived. Both methods were used together in order to find sets of solutions which had the greatest range in V for each value of spontaneous curvature c_0.

6.5.2.1 Results for Zero Momentum Boundary Condition Parameterised by Volume

The normalised radius of the fibre was taken to be either $R = 0.01^{1/2}$ or $R = 0.001^{1/2}$, about an order of magnitude smaller than the maximum radius of a Helfrich boundary condition

profile, so by (6.35) $f_0 = 0.01$ or $f_0 = 0.001$.

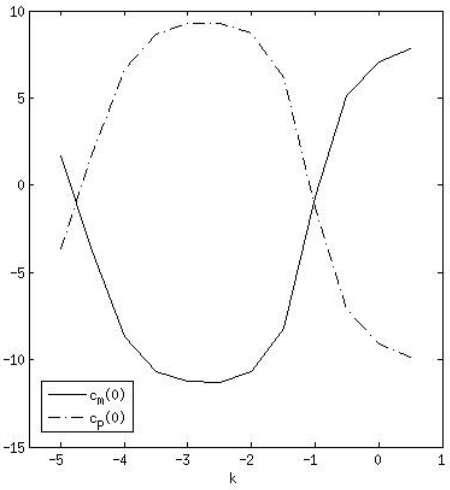

(a) $c_m(0)$ and $c_p(0)$ against κ.

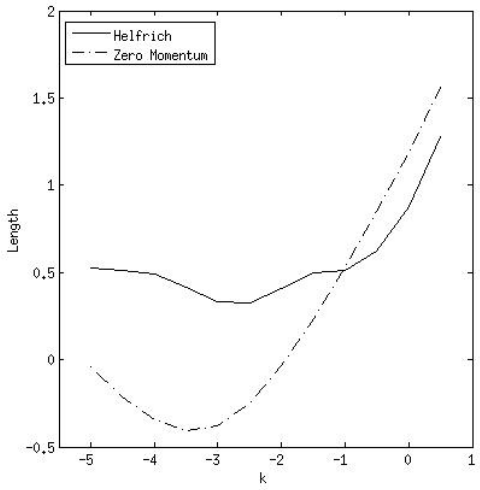

(b) Length against κ.

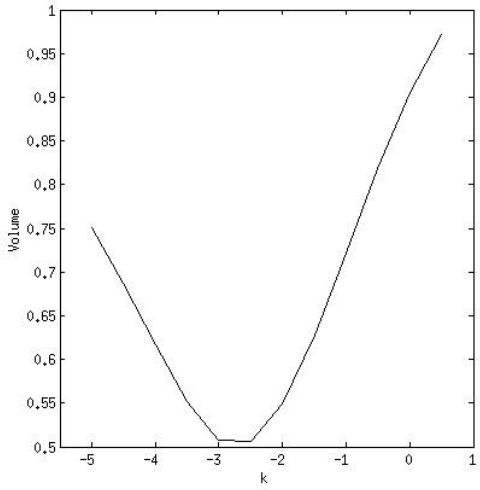

(c) Volume against κ.

Figure 6.15: Dependence of parameters of zero momentum solution on the curvature at $x = 0$, κ, of the Helfrich boundary problem solution used to provide initial estimates. Parameters fixed for this set of solution are $c_0 = -2$ and $f_0 = 0.01$.

Consider a set of solutions for which f_0 and c_0 are fixed and the zero momentum solutions are parameterised by κ. Figure 6.15(a) indicates that there are solutions of the zero momentum cell on a fibre problem for which $|c_m(0) - c_p(0)|$ is a minimum. The values of κ for which $|c_m(0) - c_p(0)|$ is a minimum are referred to as κ_0. The values of κ_0 are given in Tables 6.2 and 6.3 along with the values of $c_p(0)$, $c_m(0)$ and V.

One κ_0 occurs when $2\kappa_0 = c_0$. This is the κ at which the Helfrich boundary value problem itself meets the zero momentum condition. When $c_0 = -2$ and -4 there is another value of

κ_0 for which $|c_m(0) - c_p(0)|$ is of a similar value to $|c_m(0) - c_p(0)|_{min}$. This is possible as, by Figures 6.7(a) and 6.15(c), there is a minimum in volume when κ is negative. Two Helfrich boundary value problems have the same volume. The values of $c_m(0)$ and $c_p(0)$ from the zero momentum solutions found for the second value of κ_0 are similar to those of $c_p(0)$ and $c_m(0)$, respectively, found for the first value of κ_0. These results in Tables 6.2 and 6.3 indicate that the initial estimates of the free parameters do effect the final solution to the optimisation problem.

The values of the parameters λ, Δ_p and $f(1/2)$ found for the zero momentum solutions when $c_0 = -1$ are plotted with those found for the Helfrich boundary condition solutions in Figure 6.23. These parameters for these two sets of solutions are approximately equal when $\kappa = \kappa_0$. When $\kappa = \kappa_0$ the zero momentum solution can be said to be closest to the original Helfrich boundary value problem solution.

It was found that the sign of $c_m(0)$ of a cell on a fibre solution is the same as that of $2\kappa - c_0$. For example see Figure 6.16. See, for example, Figure 6.15(a) in the case that $c_0 = -2$. As $c_m - c_p$ of a cell on a fibre solution increases as $f \to f(0)$, then $c_p(0)$ will be of the opposite sign of $2\kappa - c_0$. Whether or not c_m and c_p crosses zero in the solution determines the number of turning and inflection points.

All oblate spheroids have one turning point. However if $c_p(0)$ is positive then there are at least two turning points in the zero momentum solutions. For example, see Figure 6.16. By the equation for length (5.39) this results in the zero momentum solution being longer than the Helfrich boundary value solution of the same volume. If $c_p(0)$ is negative then the zero momentum solution has only one turning point. As $c_m - c_p$ increases for small f, $c_p(0)$ will be much more negative than the corresponding Helfrich boundary value problem so its length will be smaller than the Helfrich boundary value problem. For example, in Figures 6.17(a)-6.17(b), solutions for which $c_p(0) > 0$ have two turning points which are evident in their solution profiles.

In Figure 6.15(b) zero momentum solutions are longer than HBVP solutions when $\kappa < c_0/2$ as expected. From Tables 6.2 and 6.3, when $\kappa = c_0/2$ and $c_0 = -2$ or -4, the first value of κ_0, $c_p(0) > c_m(0)$. For the second value of κ_0 $c_p(0) < c_m(0)$. By Figure 6.15(b), the length of the solution at the second value of κ_0 is much smaller than the corresponding Helfrich boundary problem solution.

Generally, when κ is negative enough, turning points are unavoidable. The length of a zero momentum solution derived from a HBVP solution of a very negative value of κ will always be smaller than that HBVP solution. In Figure 6.15(b) this is true whether $c_m(0) > c_p(0)$ or $c_m(0) < c_p(0)$. There is only one κ for which the difference in length between the zero momentum and corresponding HBVP solutions is a minimum.

The results for the zero momentum boundary condition solutions are summarised in Figures 6.19-6.22. Each figure summarises results for a value of spontaneous curvature c_0. Where there are two possible solutions for a given volume, the longer solution, is used. The information in these figures is discussed in the following paragraphs.

These observations in $c_p(0)$ and $c_m(0)$ explain aspects of the results in Figures 6.18-6.22. When $\kappa = \kappa_0$ the difference in volume between the zero momentum and Helfrich boundary

problem solutions is a minimum. When $\kappa > \kappa_0$ the Helfrich boundary problem solution is longer, while when $\kappa < \kappa_0$ the zero momentum solution is longer. The volumes of the zero momentum solutions when $\kappa = \kappa_0$ are listed in Tables 6.2 and 6.3.

What can be clearly observed in Figures 6.18-6.22 is that the zero momentum solutions are longer than the HBVP solutions when volume is small.

The plots in the top left of Figures 6.19-6.22 shows that if a zero momentum solution is perturbed away from a solution where $c_m(0) - c_p(0)$ is a local minimum then the value of $(1 - f_0 c_p(0)^2)^{1/2}$ decreases rapidly to 0. This is made possible by the values of $c_p(0)$ and $c_m(0)$ which are plotted in the bottom row of Figures 6.19-6.22. By the discussion in Section 5.13, if a Helfrich boundary value solution is perturbed then when $f \to 0$, $|c_m - c_p|$ will increase. However $c_0 = O(1)$ so $c_m + c_p$ must be $O(1)$. It was found that for some of the solutions $(1 - f c_p^2)^{1/2}$ is small when f is small which slows down the increase of $|c_m - c_p|$.

By the plots in the top right in Figures 6.19-6.22 it is also found that as $(1 - f_0 c_p(0)^2)^{1/2}$ decreases for zero momentum solutions then the value of

$$\epsilon = c_p(0)\left((c_p(0) - c_0)^2 - c_m(0)^2\right) + 2\lambda c_p(0) + \Delta_p \tag{6.50}$$

increases so that the solutions are not tending to the boundary conditions in Section 5.4.2 required for a well behaved solution at $f c_p^2 = 1$. If the boundary condition (5.45) is not zero then the solution is not well-behaved numerically and cannot be used as a possible profile for a cell membrane. This limits the range of Helfrich boundary solutions which can be used as initial profiles to find zero momentum cell on a fibre solutions. Solutions which do meet the boundary conditions for $f c_p^2 = 1$ in Section 5.4.2 at both the fibre surface and at the maximum radius of the solution are discussed in Section 6.7.

The Helfrich energy of each solution is plotted on the mid-right of Figures 6.19-6.22, while the length of each solution is plotted on the mid-left of Figures 6.19-6.22. As is the case for all spheroids, the Helfrich energy of the HBVP solutions decreases as their volume decreases. For oblate spheroids, their length decreases as volume is decreased. The length and Helfrich energy of the zero momentum boundary value solutions are small perturbations of the length and Helfrich energy of these HBVP solutions. Their length increases with volume and their Helfrich energy decreases with volume.

The difference in Helfrich energy between the HBVP solutions and that of the zero momentum solutions is not obviously a minimum when $\kappa = \kappa_0$. The Helfrich energy of a zero momentum solution is always slightly larger than that of the Helfrich boundary value solution of the same volume. When the zero momentum boundary conditions are implemented, a cell on a fibre solution is less energeticall favourable than a Helfrich boundary value solution.

c_0	κ_0	$c_p(0)$	$c_m(0)$	V_0
0	0	-1.21	1.21	0.90
-1	-0.5	-0.41	-0.59	0.80
1	0.5	-2.75	3.75	0.97
-2	-1	-0.68	-1.32	0.72
-2	-4.7	-1.38	-0.62	0.71
-4	-2	-2.00	-1.99	0.69
-4	-3.2	-1.98	-2.02	0.69

Table 6.2: Values for κ_0 for given c_0 together with values of $c_p(0)$ and $c_m(0)$ for cell on a fibre solution where $f_0 = 0.001$.

c_0	κ_0	$c_p(0)$	$c_m(0)$	V_0
0	0	-0.38	0.38	0.90
-1	-0.5	-0.47	-0.52	0.80
1	0.5	0.51	0.49	0.97
-2	-1	-0.85	-1.15	0.72
-2	-4.8	1.32	-3.32	0.73
-4	-2	-2.02	-1.98	0.69
-4	-3.2	-1.79	-2.21	0.69

Table 6.3: Values for κ_0 for given c_0 together with values of $c_p(0)$ and $c_m(0)$ for cell on a fibre solution where $f_0 = 0.01$.

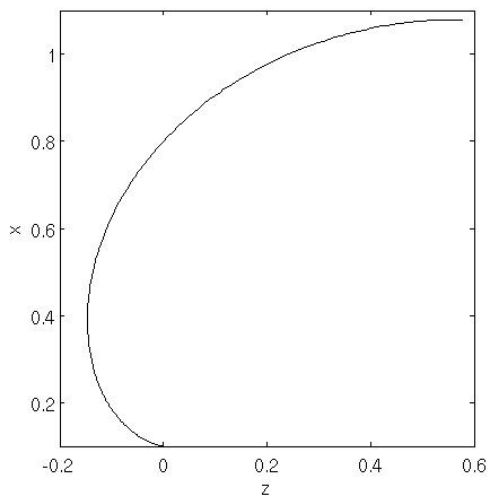

(a) Plot of x against y. Solution has one turning point. $V_0 = 0.96$

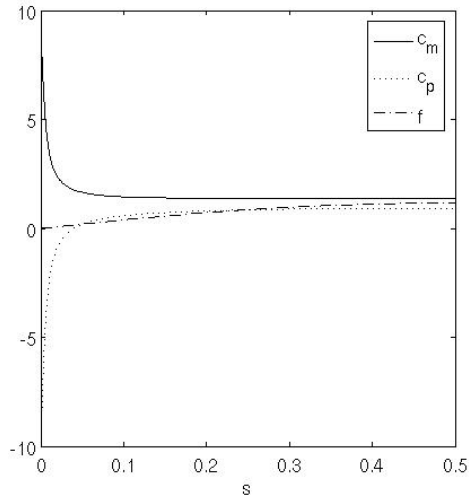

(b) Plot of c_m, c_p and f showing that c_p crosses zero twice. $V_0 = 0.96$

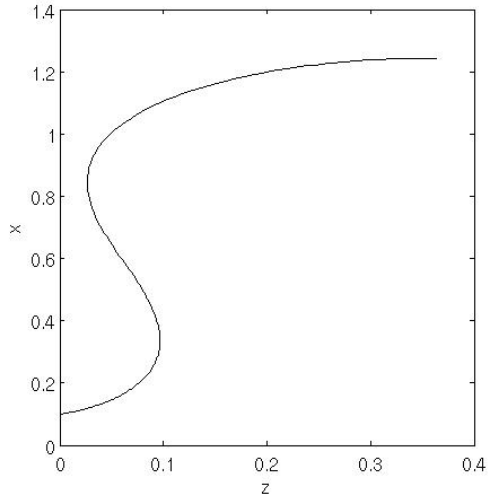

(c) Plot of x against y. Solution has two turning points. $V_0 = 0.66$

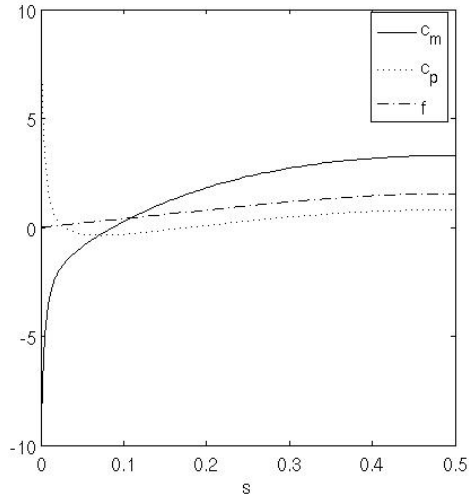

(d) Plot of c_m, c_p and f showing that c_p crosses zero twice. $V_0 = 0.66$

Figure 6.16: Results for a cell on a fibre zero momentum solution parameterised by volume where $c_0 = -1$. Volume of solution determines whether a solution has one or two turning points, which in turn determies the length of the solution.

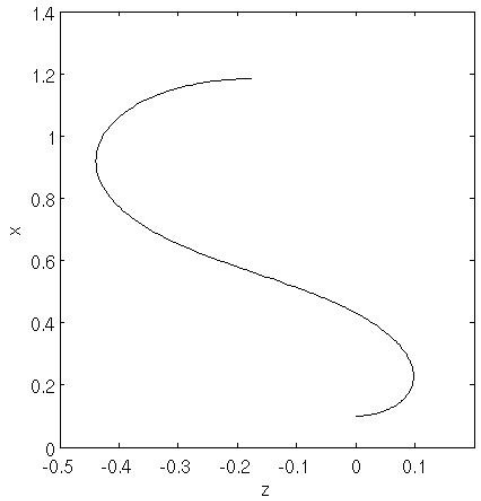

(a) Plot of radius against length. Solution has one turning point. $V_0 = 0.97$ $\kappa = 0.5$

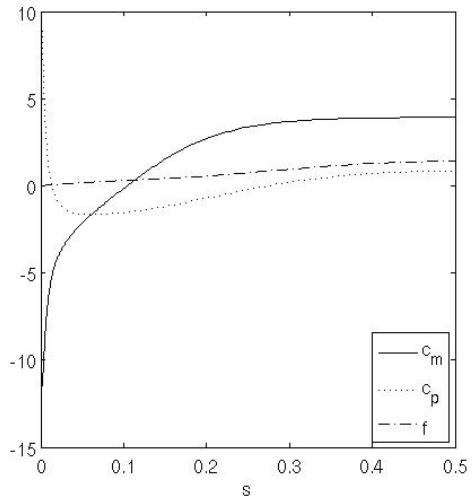

(b) Plot of c_m, c_p and f showing that c_p crosses zero once. $V_0 = 0.97$ $\kappa = 0.5$

Figure 6.17: Results for a cell on a fibre zero momentum solution parameterised by volume where $c_0 = 0$ where solution is of equal volume to a Helfrich boundary value solution with given value of κ. An extreme example of a solution with two turning points.

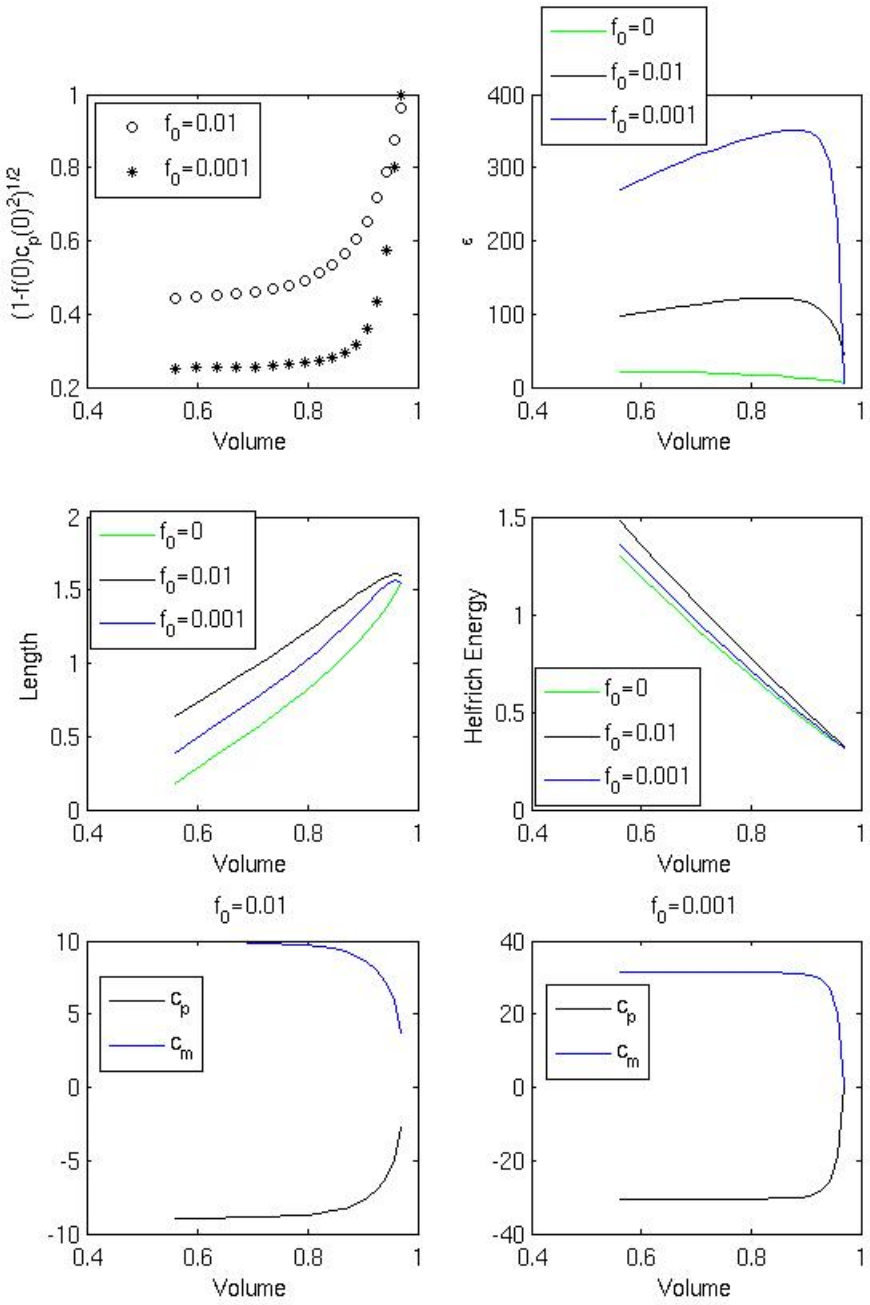

Figure 6.18: Plots associated with cell on a fibre solutions derived from Helfrich boundary problem solutions where $c_0 = 1$. When $f_0 = 0$, parameters from Helfich boundary problem solutions have been used.

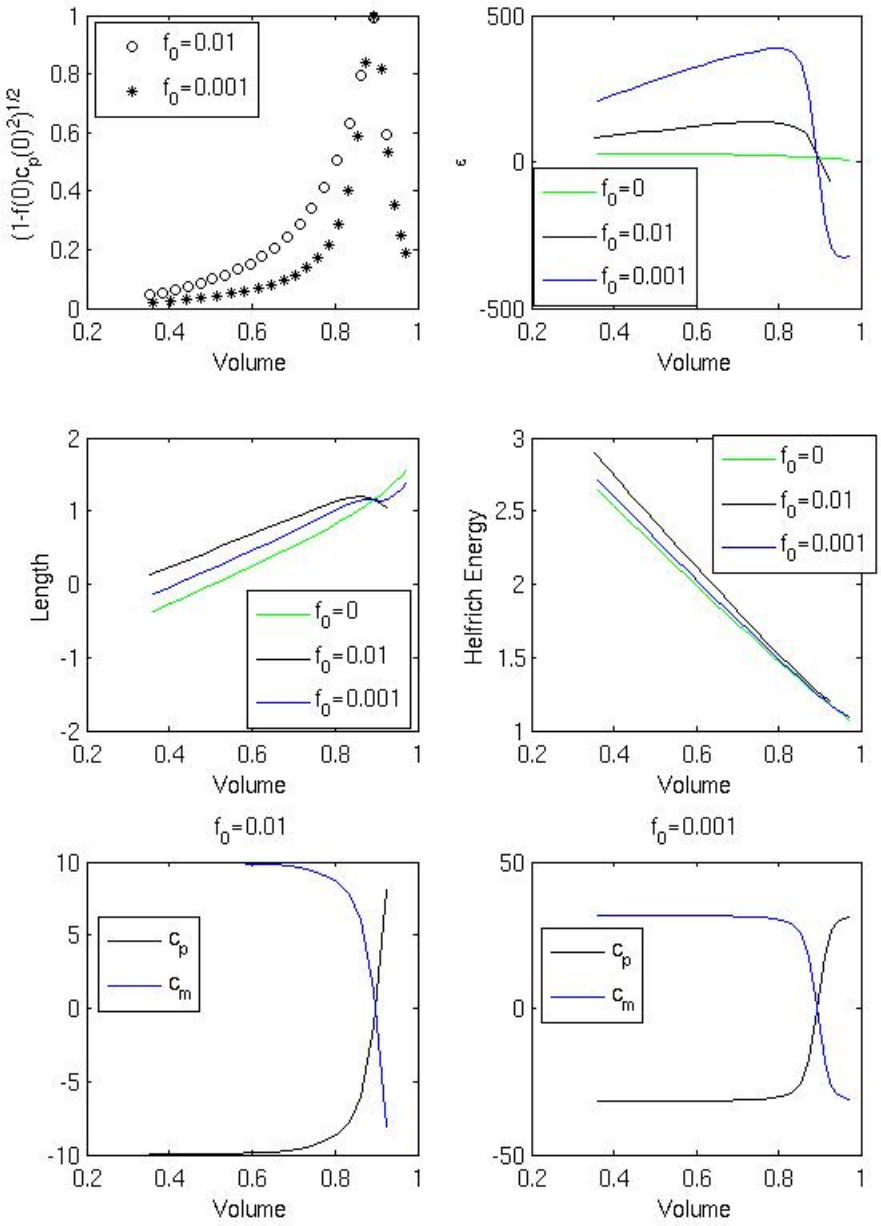

Figure 6.19: Plots associated with cell on a fibre solutions derived from Helfrich boundary problem solutions where $c_0 = 0$. When $f_0 = 0$, parameters from Helfich boundary problem solutions have been used.

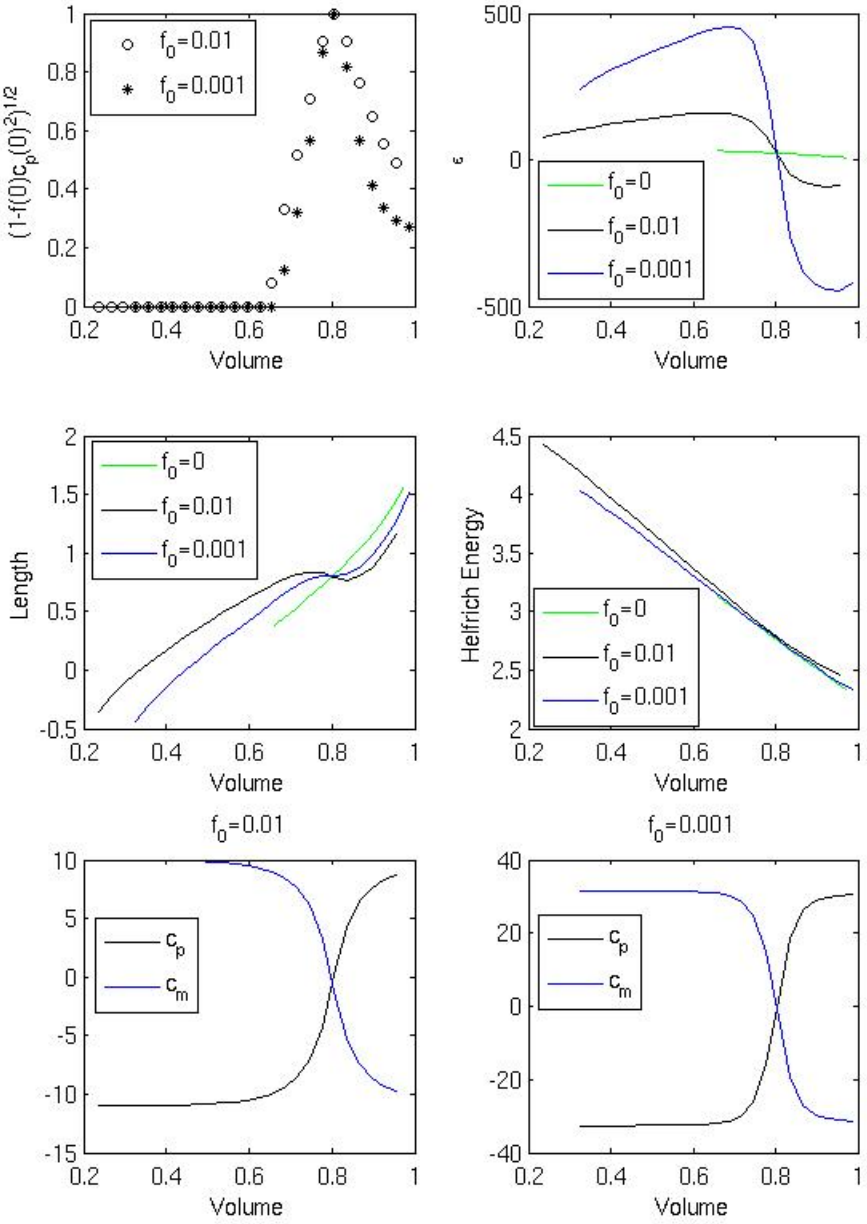

Figure 6.20: Plots associated with cell on a fibre solutions derived from Helfrich boundary problem solutions where $c_0 = -1$. When $f_0 = 0$, parameters from Helfich boundary problem solutions have been used.

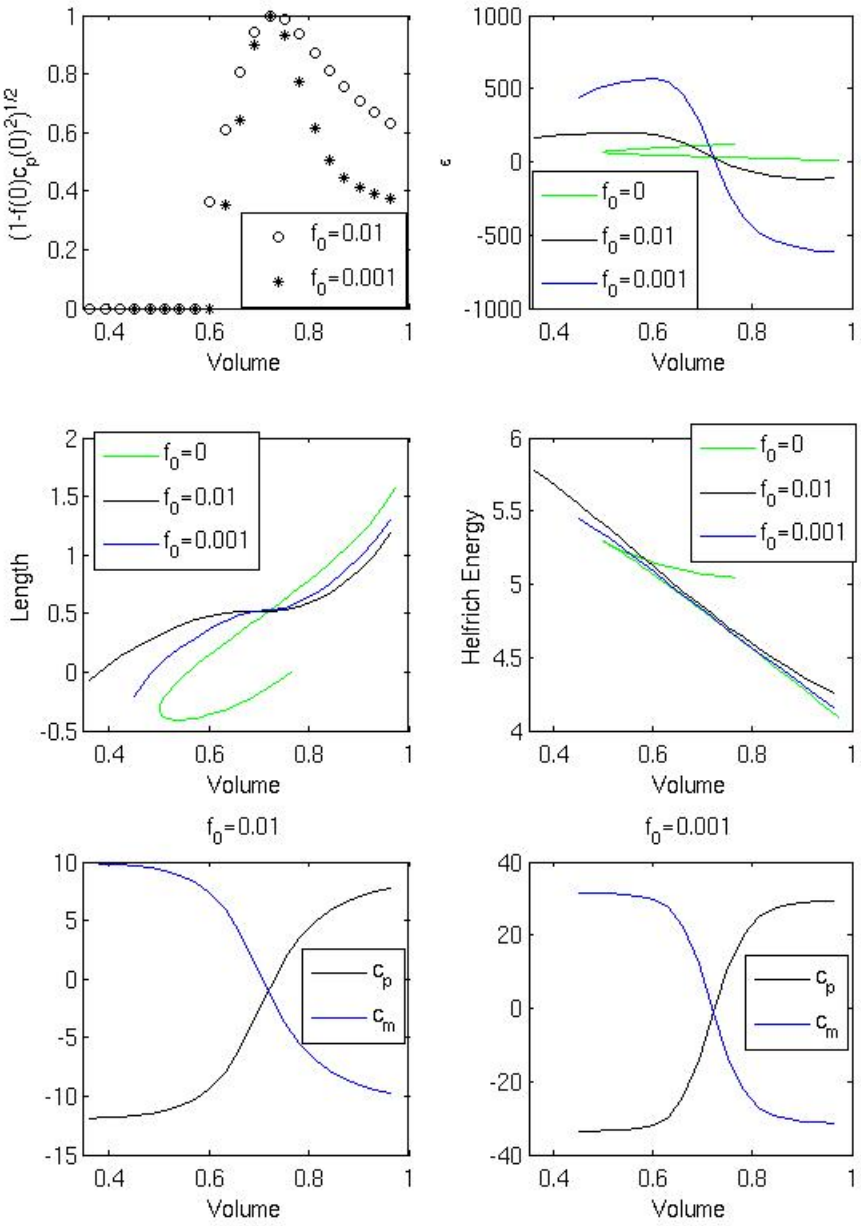

Figure 6.21: Plots associated with cell on a fibre solutions derived from Helfrich boundary problem solutions where $c_0 = -2$. When $f_0 = 0$, parameters from Helfich boundary problem solutions have been used.

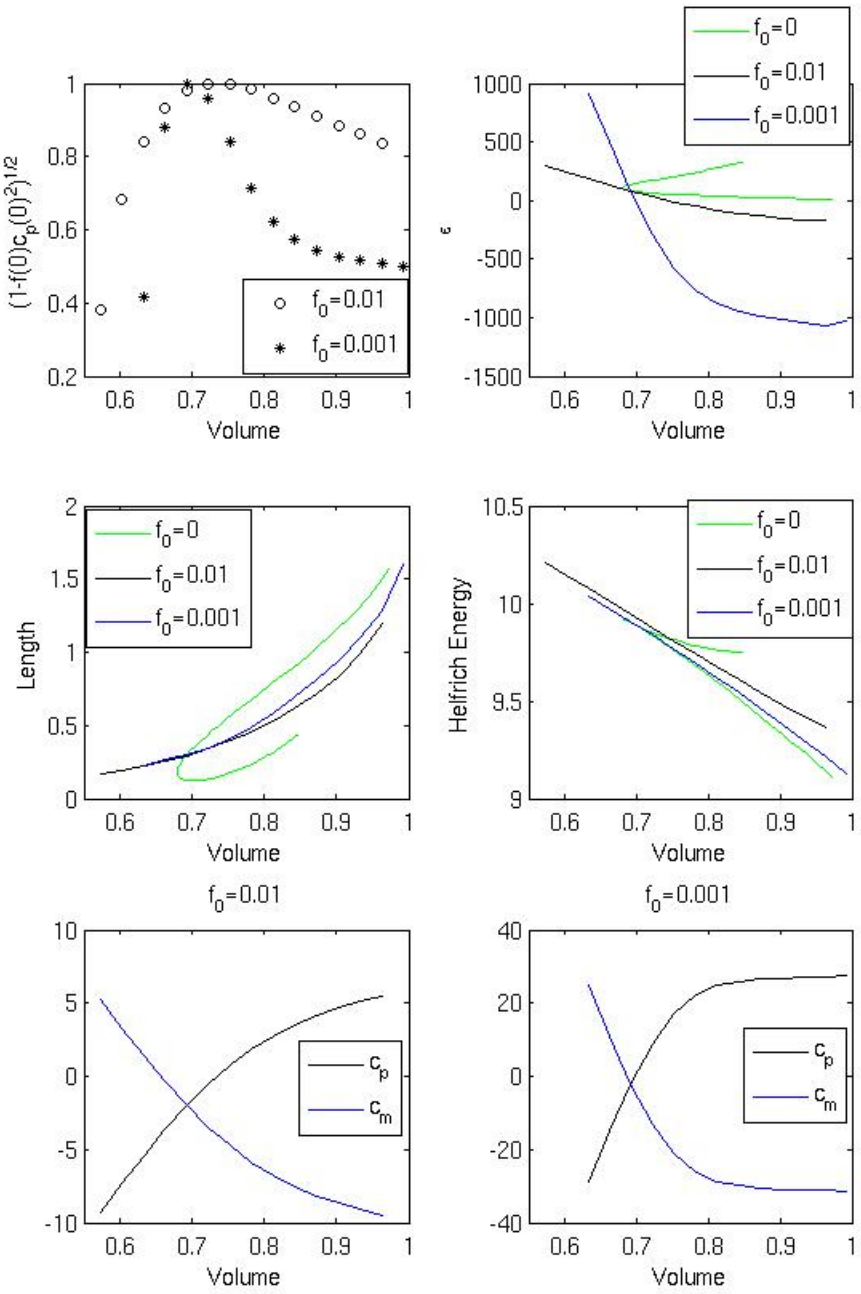

Figure 6.22: Plots associated with cell on a fibre solutions derived from Helfrich boundary problem solutions where $c_0 = -4$. When $f_0 = 0$, parameters from Helfich boundary problem solutions have been used.

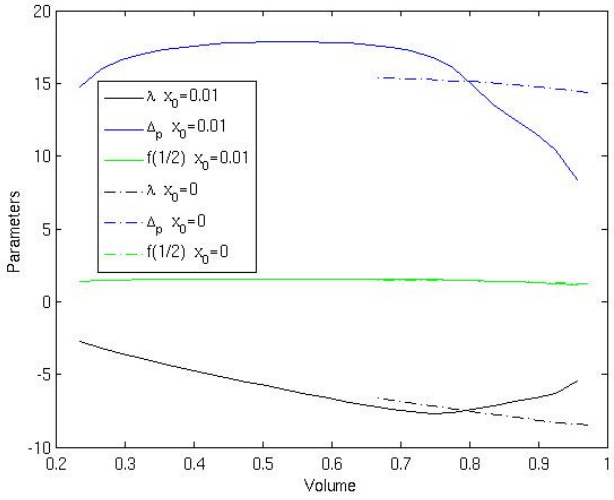

Figure 6.23: Parameters for zero momentum solutions when $f_0 = 0.01$ and HBVP solutions for $c_0 = -1$. unbroken line - Helfrich boundary problem solutions broken line - zero momentum solutions. Parameters coincide when $2\kappa = c_0$.

6.5.3 Numerical Scheme for Zero Momentum Boundary Problem Solutions Parameterised by Length

For a range of values of spontaneous curvature in the range $-12 \leq c_0 \lesssim 3$ a separate series of solutions was found. To find the solutions in this section, a zero momentum boundary condition was found by the method in Section 6.5.1. Again oblate spheroids provided initial estimates of the required parameters. Oblate spheroids of maximum length, for which $\kappa = 1$ were used for this. This zero momentum solution was then perturbed in two directions, that of increasing f_0 and of increasing length. The solution branch is extended for increasing values of f_0 and L until the error suddenly increases by a few order of magnitude.

Solutions of increasing f_0 are found by minimising the residual

$$\begin{aligned}
\mathbf{R_5} = [c_{m+}(s_m) &- c_{m-}(s_m), && (6.51)\\
c_+(s_m) &- c_{p+}(s_m), && (6.52)\\
f_+(s_m) &- f_+(s_m), && (6.53)\\
v &- V, && (6.54)\\
c_m(0) &+ c_p(0) - c_0], && (6.55)
\end{aligned}$$

while keeping f_0 and c_0 fixed for each optimisation. The free variables for this problem are

$$\begin{aligned}
\Delta_p &\quad \text{osmotic pressure}, && (6.56)\\
\lambda &\quad \text{surface tension}, && (6.57)\\
B &\quad f(s) \text{ at } f(1/2)c_p(1/2)^2 = 1, && (6.58)\\
c_m(0) &\quad c_m \text{ at fibre surface}, && (6.59)\\
c_p(0) &\quad c_p \text{ at fibre surface}. && (6.60)
\end{aligned}$$

For each of the solutions found by perturbing f_0, the length can be extended. This was done by minimising the residual

$$\begin{aligned}
\mathbf{R_6} = [c_{m+}(s_m) &- c_{m-}(s_m), && (6.61)\\
c_+(s_m) &- c_{p+}(s_m), && (6.62)\\
f_+(s_m) &- f_+(s_m), && (6.63)\\
l &- L, && (6.64)\\
c_m(0) &+ c_p(0) - c_0], && (6.65)
\end{aligned}$$

where L is incrementally increased by 10^{-2} between each optimisation and l is the length of the solution tested. In this case, the degrees of freedom are

$$\begin{aligned}
\Delta_p &\quad \text{osmotic pressure}, && (6.66)\\
\lambda &\quad \text{surface tension}, && (6.67)\\
B &\quad f(s) \text{ at } f(1/2)c_p(1/2)^2 = 1, && (6.68)\\
c_m(0) &\quad c_m \text{ at fibre surface}, && (6.69)\\
c_p(0) &\quad c_p \text{ at fibre surface}. && (6.70)
\end{aligned}$$

L is increased until the absolute magnitude of the residual suddenly increases from $O(10^{-8})$ to $O(10^{-3})$. The maximum length solution is the longest solution for which the error is $O(10^{-8})$.

6.5.4 Results for Zero Momentum Boundary Problem Solutions Parameterised by Length

Zero momentum cell on a fibre solutions of the greatest length for fixed values of spontaneous curvature c_0 and $f(0) = f_0$ were found. Example results from these maximum length solutions have been plotted in Figures 6.24-6.26. The range in spontaneous curvature for which results were found can be subdivided into three groups: $c_0 < -1$, $-1 < c_0 < 2$ and $2 < c_0$. Solutions with an acceptably small residual of $O(10^{-8})$ were found when $-1 < c_0 < 2$. However, they were discounted true solutions to the zero momentum boundary value problem as numerical error dominated the relationship between length and f_0. Zero momentum boundary value problem solutions for these mid-range values of spontaneous curvature for a smaller range in f_0 are described in detail in Section 6.5.2. The length of solutions in each of the remaining groups is plotted in Figure 6.24, while their volume and Helfrich energy are plotted in Figures 6.25 and 6.26.

The solutions of greatest length can be found when $c_0 > 1.5$. The length of the solutions did not depend strongly on c_0 but increased with f_0.

Finding zero momentum solutions with an acceptably small residual for $c_0 > 2.7$ was not possible using parameters from an spheroid HBVP solution. Dumbell HBVP solution have been used to find a limited range of dumbell cell on a fibre solutions which are discussed in Section 6.6.5. These solutions do not necessarily meet the zero momentum boundary condition.

When $c_0 < -1$ the length of the solutions depends more closely on f_0 than c_0 as is the case when $c_0 > 1.5$. However, when $c_0 < -1$ the length of the solutions decreases with f_0, rather than increases. The range of f_0 for which zero momentum solutions can be found does depend on c_0.

When $c_0 > 1.5$ volume decreases with length, which is the trend for prolate spheroids while when $c_0 < -1$ volume increases with length which is the trend for oblate spheroids.

The Helfrich energy for these two sets of solutions depends on both c_0 and f_0. It increases as f_0 increases. However, for any value of f_0 the solution for which $|c_0|$ is greatest had the smallest Helfrich energy.

When $c_0 < -1$ and $c_0 > 1.5$ then it is found that $\cos\phi = (1 - f(0)c_p(0)^2)^{1/2}$ is $O(10^{-2})$, $\Delta_p/\lambda > 1$ and $\Delta_p < 0$. If these zero momentum boundary problem solutions were perturbations of a sphere, then by Sections 5.9 and 5.11, it would be expected that $\cos\phi = (1-f(0)c_p(0)^2)^{1/2}$ is $O(1)$, $\Delta_p/\lambda \approx -2$ and $\Delta_p > 0$. For the zero momentum boundary value problem solutions, the c_0 terms are of leading order. In Figure 6.27 $c_p \approx c_m \approx 1$ for $0.1 \lesssim s < 1$ and $c_m - c_p$ increases rapidly when $s \to 0$.

A solution where c_m and c_p are mostly constant does not allow much freedom to meet the required boundary conditions. When f_0 is increased, the zero momentum solutions when $|c_0| > 2$ adapt by including a maximum in c_m in the solution. For example, the result of increasing f_0 when $c_0 = -4$ can be observed by comparing Figure 6.27 and 6.28. The maximum

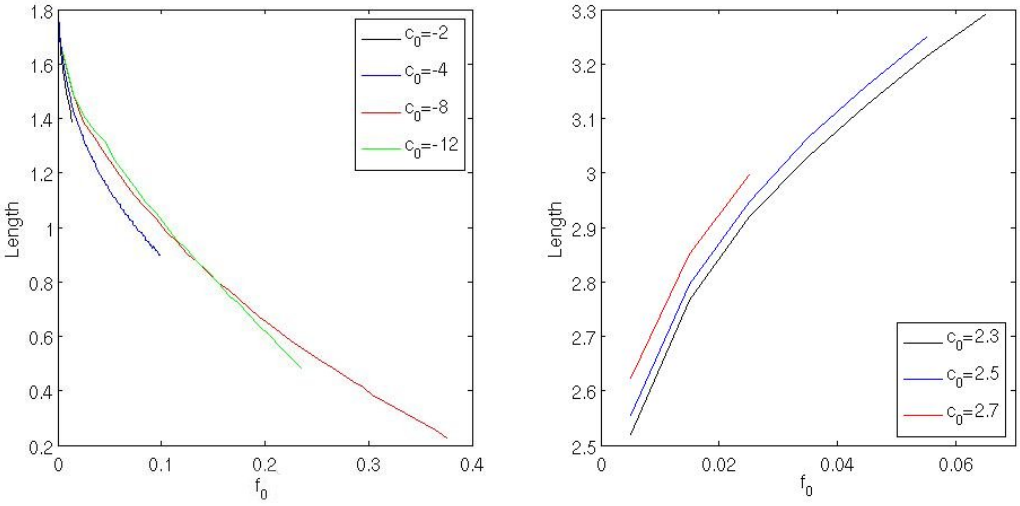

(a) $c_0 = -2$, -4, -8 and -12.

(b) $c_0 = 2.3$, 2.5 and 2.7.

Figure 6.24: Length of maximum possible length of zero momentum solution against f_0.

occurs when

$$\frac{c_p((c_p - c_0)^2 - c_m^2) + 2\lambda c_p + \Delta_p}{(1 - fc_p^2)^{1/2}} - 2\frac{(1 - fc_p^2)^{1/2}(c_m - c_p)}{f} = 0. \tag{6.71}$$

The point at which this occurs can be observed in Figure 6.28(c). $|c_0|$ is large enough for second term not to dominate the behaviour of the solutions for small s. In this way, if $|c_0| \gtrsim 2$, then solutions where the leading order terms are c_0 dependent result in cell on a fibre solutions where length> 2.

HBVP solutions for which there is a maximum or minimum in c_0 were discussed in Section 6.4.3. As is the case in this section, a larger value of $|c_0|$ helped extend the range of possible solutions. It was found that when $|c_0|$ is large enough then oblate and prolate solutions could be found for larger values of $|\kappa|$. The role of c_0 dependent terms in producing maxima and minima in c_m and c_p is discussed in Section 5.13. The maximum in c_m occurs approximately at the same point when $c_p = 0$, which by the discussion in Section 5.13, results in an extremum in c_m in the case where shear terms dominate in Section 5.13.

6.5.5 Conclusions

The results in this section examine zero momentum cell on a fibre solutions in two ways. In Section 6.5.2 these results are parameterised by volume. These results suppose that a cell is pierced by a fibre, so that it has to quickly adjust its membrane until it reaches equilibrium at the point the zero momentum boundary condition is met. The differences in length and Helfrich energy between the original HBVP solutions are not large. These values tended towards those of the HBVP as f_0 decreased. However, valid cell on a fibre solutions for $c_0 = -1$ and $c_0 = -2$ were only found for a limited range in volume as some solutions tended towards a singularity

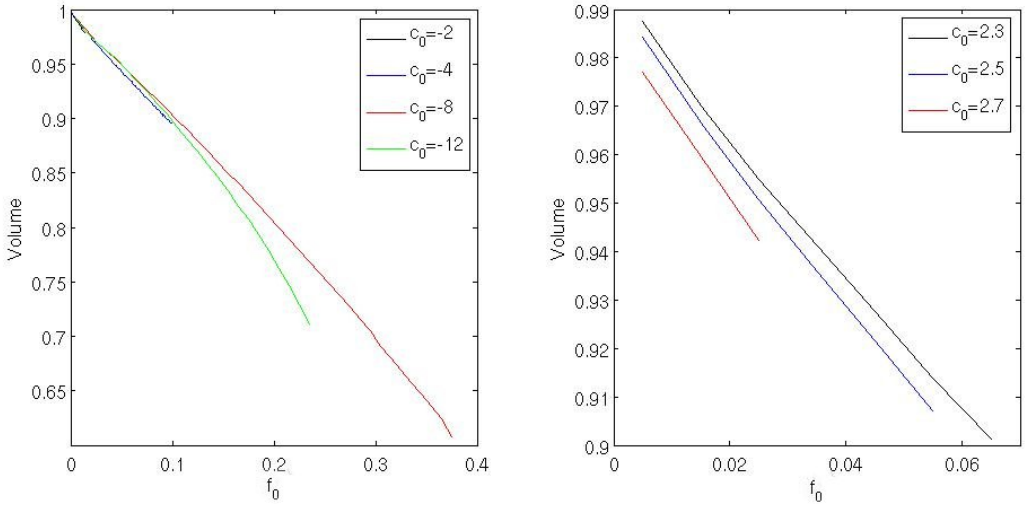

(a) $c_0 = -2$, -4, -8 and -12.

(b) $c_0 = 2.3$, 2.5 and 2.7.

Figure 6.25: Volume of maximum possible length zero momentum solution against f_0.

in $\dot{c_m}$.

The length and Helfrich energy of the HBVP and zero momentum solutions are most similar when for the HBVP solution $2\kappa_0 = c_0$. In this case the solution does not have to greatly adjust to meet the zero momentum boundary condition. If $2\kappa > 2\kappa_0$ then the length of the zero momentum solution is smaller than that of the corresponding HBVP. If $2\kappa < 2\kappa_0$ then the length of the zero momentum solution is greater than that of the corresponding HBVP solution. However, the general trend for both HBVP and zero momentum solutions is for the length to increase with volume which is the general trend for oblate spheroids.

In Section 6.5.3, the zero momentum solutions are parameterised by length. The results can be divided into three groups by spontaneous curvature. For very negative values of spontaneous curvature $c_0 < -1$ the length of a solution can be significantly extended (by more than 0.01) for a limited range in f_0. The length of this maximum length solution then decreases with f_0. No solutions of the cell on a fibre boundary value problem were found for mid-range values of spontaneous curvature $-1 < c_0 < 2$. As for solutions for which $c_0 < -1$, the length of zero momentum solutions for $c_0 > 2$ can be significantly extended. In this case, the length of maximum length solutions for very positive values of spontaneous curvature $c_0 > 2$ increases, rather than decreases, with f_0. If $|c_0| > 2$ then spontaneous curvature adds another degree of freedom which allows zero momentum boundary conditions have a length $L > 2$.

However, the range in possible f_0 of zero momentum solutions for $c_0 \approx 2$ is very small. Prolate HBVP solutions which are not spheroids occur only when $1 < \kappa \lesssim 1.5$. When $c_0 \gtrsim 2$, the initial estimates used to solve for a zero momentum solution must be taken from a dumbell solution. Dumbell solutions have an additional singularity and are discussed in Section 6.3.2. Cell on a fibre solutions with an additional singularity can be found. However, solutions of this type which obey the zero boundary value condition may not be. Some results for these

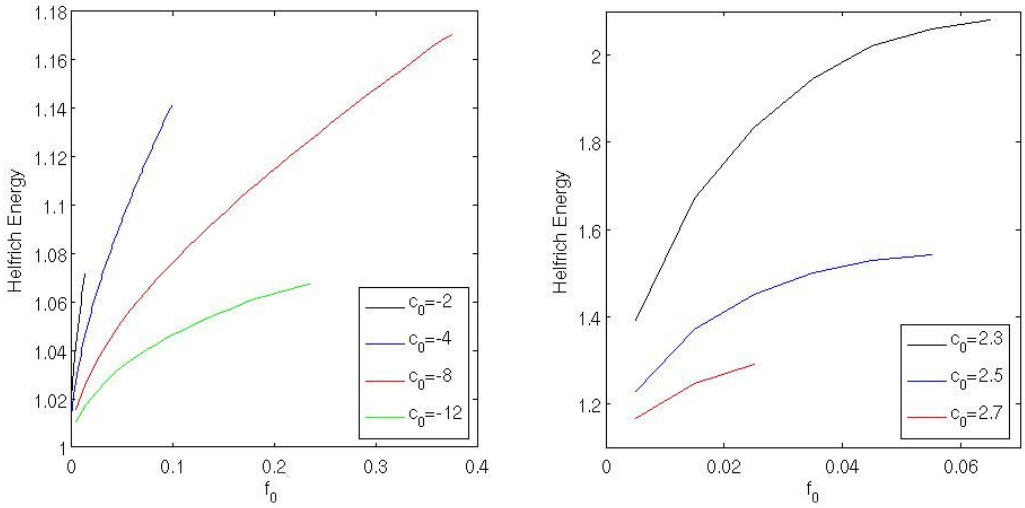

(a) $c_0 = -2$, -4, -8 and -12.

(b) $c_0 = 2.3$, 2.5 and 2.7.

Figure 6.26: Helfrich Energy of maximum possible length zero momentum solution against f_0.

solutions can be found in Section 6.6.5.

The results in Sections 6.5.2 and 6.5.3. In Section 6.5.2, the aim was to find series of solutions with the greatest range in volume for a limited range of f_0, while in Section 6.5.3 the aim was to find series of solutions with the greatest range in length and f_0. In Section 6.5.2, solutions were only found for mid-range values of $-4 < c_0 < 1$. In Section 6.5.3 solutions were found for more negative and also for positive values of c_0. It was found that for positive c_0 and for $c_0 < -2$, zero momentum solutions could be found for a greater range in f_0.

The different numerical schemes find solutions which met the zero momentum boundary condition in different ways. These can be discussed in context of the terminology in Section 5.13. In Section 6.5.2, then $(1 - fc_p^2)^{1/2} \to 0$ as $s \to 0$ in order to control $|c_m - c_p|$ as f decreased. In Section 6.5.3, the zero momentum boundary condition is met by the solution displaying maxima in c_m due to c_0-dependent shear terms. This is only possible for larger values of $|c_0|$. These shear terms allowed zero momentum boundary value solutions to be found when $f_0 = O(10^{-1})$. In both cases, the solutions are dominated by a rapid increase of $|c_m - c_p|$ when f is small.

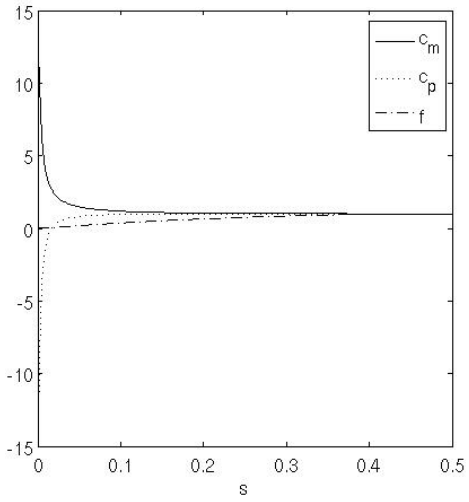

Figure 6.27: c_m, c_p and f against s for maximum length solution to maximum length zero momentum solutions when $c_0 = -4$, $f_0 = 10^{-3}$, $L = 1.62$ and $V = 0.99$. No maximum or minimum in c_m and c_p.

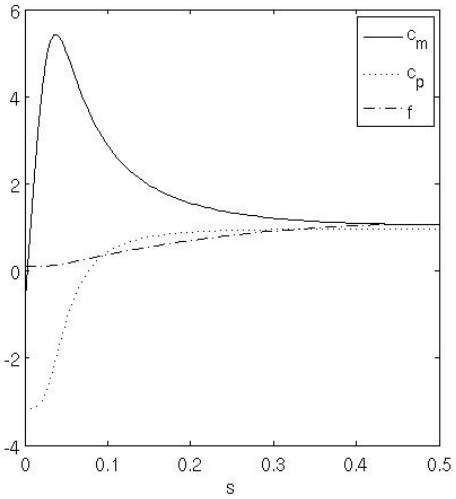

(a) c_m, c_p and f against s.

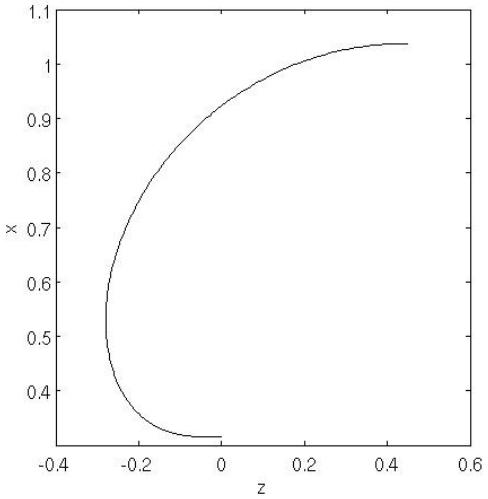

(b) x against z.

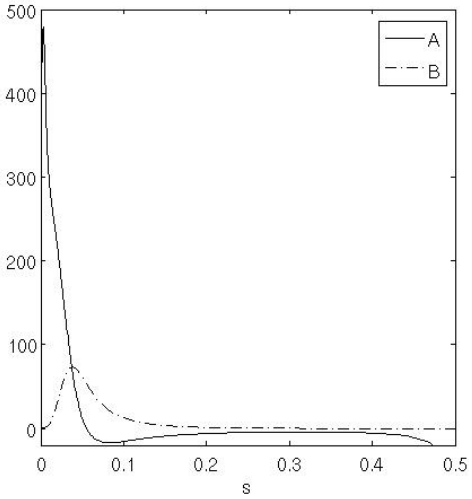

(c) $A = (c_p((c_p - c_0)^2 - c_m^2) + 2\lambda c_p + \Delta_p)/(1 - fc_p^2)^{1/2}$ and $B = 2(1 - fc_p^2)^{1/2}(c_m - c_p)/f$ against s.

Figure 6.28: Solutions to maximum length zero momentum solutions when $c_0 = -4$, $f_0 = 0.1$, $L = 0.90$ and $V = 0.90$. A maximum in c_m and a minimum in c_p.

6.6 Cell Enclosing and Cell Lengthening on Fibre Conditions

The aim of this section is to find the solutions of maximum length for given values of spontaneous curvature, c_0 and $f_0 = R^2$ where R is the fibre radius. In Section 6.5.3, the length of solutions were extended under the constraints of the zero momentum boundary condition. Section 6.6.1 investigates other possible constraints for a cell lengthening on fibre problem. Section 6.6.2 gives details on the final cell lengthening on fibre problem where the length of solutions are maximised under the constraint of constant volume. The results of the cell lengthening on fibre solutions for a wide range of spontaneous curvature and f_0 are given in Section 6.6.3. Further observations on these solutions can be found in Section 6.6.4. It was observed that the sign and magnitude of c_0 plays a key role in determining the range of cell lengthening solutions. In Section 5.13, c_0 was found to effect the frequency of the undulations resulting from the surface, or λ dependent, terms.

6.6.1 Initial Investigation

If the radius of the fibre is small, then the constraint that the membrane must be perpendicular to the fibre surface approximates a solution by which a cell membrane has completely enclosed the fibre. This is an approximation to the cell engulfing fibre solution investigated in Chapter 4. If a cell membrane is perpendicular to the surface of a fibre then the fixed parameters must be

$$c_0 \quad \text{spontaneous curvature}, \tag{6.72}$$

$$f(0) = f_0 \quad R^2, \tag{6.73}$$

$$c_p(0) = 0 \quad c_p \text{ at fibre surface}. \tag{6.74}$$

There are four remaining degrees of freedom which are

$$\Delta_p \quad \text{osmotic pressure}, \tag{6.75}$$

$$\lambda \quad \text{surface tension}, \tag{6.76}$$

$$B \quad f(1/2), \tag{6.77}$$

$$c_m(0) \quad c_m \text{ at fibre surface}. \tag{6.78}$$

A starting cell engulfing fibre solution can be found using parameters from a HBVP and minimising the residual

$$\begin{aligned} \mathbf{R_7} = [c_{m+}(s_m) &- c_{m-}(s_m), \\ c_{p+}(s_m) &- c_{p-}(s_m), \\ f_+(s_m) &- f_-(s_m), \\ v &- V]. \end{aligned} \tag{6.79}$$

The first three conditions are the usual matching conditions first introduced in Section 6.3. The fourth condition minimises the difference between the volume of the solution, v and the volume of the corresponding HBVP solution, V.

For all results in this section, the HBVP was taken to be that for $\kappa = 1$ as it was found to maximise the length of results in Section 6.6.3.

The length of the solution can be maximised as was done in Section 6.5.3. Let L be a fixed parameter and l the length of the solution tested. Solutions of increasing length can be found by minimising the residual

$$\begin{aligned} \mathbf{R_8} = [c_{m+}(s_m) &- c_{m-}(s_m), \\ c_{p+}(s_m) &- c_{p-}(s_m), \\ f_+(s_m) &- f_-(s_m), \\ l &- L], \end{aligned} \tag{6.80}$$

when L is incrementally increased by 10^{-2}.

If $c_p(0)$ is not fixed then there are five degrees of freedom. For an additional constraint, it is set that as solutions solutions are extended in length, their volume must be constant. If volume is to be fixed then the residual (6.80) is extended so that

$$\begin{aligned} \mathbf{R_9} = [c_{m+}(s_m) &- c_{m-}(s_m), \\ c_{p+}(s_m) &- c_{p-}(s_m), \\ f_+(s_m) &- f_-(s_m), \\ l &- L, \\ v &- V]. \end{aligned} \tag{6.81}$$

As an experiment, solutions for which $c_p(0)$ and volume are both free parameters are also extended in length.

6.6.1.1 Results

Figure 6.29 shows how the constraint of volume limits the maximum possible length of the solution less than that of fixed $c_p(0)$. However, when both volume and $c_p(0)$ are free then the maximum length is slightly larger still.

In all solutions in Figure 6.29 the parameters do not vary much from $\Delta_p/\lambda \approx -2$. Figure 6.29 shows that if $c_p(0) = 0$, then at some point both Δ_p and λ change signs. If $\lambda > 0$ then, by discussion in Section 5.13, the solution cannot have wave-like behaviour. The numerical solutions of c_m, c_p and f in Figure 6.30 for the maximum length solution in this case show that the solution is dominated by divergent behaviour. However, when $c_p(0)$ is a free variable, we have $\lambda < 0$ for all solutions found. The numerical solutions for c_m, c_p and f in Figure 6.31 show undulating behaviour.

When volume is allowed to vary, Figure 6.32(b) shows that it does not vary much from 1. However, when volume is allowed to vary a set of solutions with a greater range of length are found. The Helfrich energy for all three sets of solutions of increasing lengths show a minimum in Helfrich energy as plotted in Figure 6.32(a). Solutions with the least Helfrich energy were found when no constraints on $c_p(0)$ or volume were imposed.

Results in this section and those in Section 6.5.3 suggest that, for a cell on a fibre solution, when a boundary condition is imposed at $s = 0$ solutions where c_m and c_p diverge as $f \to 0$ dominate. In order to meet these boundary conditions, the range of solutions found is very limited. In order investigate a broader range of cell on a fibre solutions, a constraint on volume only and not c_p is imposed in Section 6.6.2.

6.6.2 Final Cell Lengthening on Fibre Problem

The constraint on cell lengthening solutions chosen to be investigated for a range of f_0 and c_0 in Section 6.6.3 is that of constant volume, so that the fixed parameters are

$$c_0 \quad \text{spontaneous curvature}, \tag{6.82}$$

$$f(0) = f_0 \quad R^2, \tag{6.83}$$

$$V = 1 \quad \text{Volume of solution}. \tag{6.84}$$

In the constant curvature model in Chapter 4, the only possible way for a cell to engulf a fibre was to increase its volume. Including the bending energy in the energy minimisation problem allows a greater flexibility in solutions. Solutions to this optimisation problem model a macrophage adjusting its shape to spread along a fibre when it is not possible for the cell to greatly change its volume.

There are five degrees of freedom which are taken to be

$$\Delta_p \quad \text{osmotic pressure}, \tag{6.85}$$

$$\lambda \quad \text{surface tension}, \tag{6.86}$$

$$B \quad f(1/2), \tag{6.87}$$

$$c_m(0) \quad c_m \text{ at fibre surface}, \tag{6.88}$$

$$c_p(0) \quad c_p \text{ at fibre surface}. \tag{6.89}$$

Sets of cell lengthening on fibre solutions are found for f_0 in the range $0.01 \leq f_0 \leq 0.1$ and c_0 in the range $-12 \leq c_0 \leq 12$. An initial cell on a fibre solution for a given c_0 is taken to be a cell enclosing fibre solution where $c_p(0) = 0$ when $f_0 = 0.01$. Details are found in Section 6.6.1. Taking c_0, f_0 and V to be fixed over an optimisation, the residual

$$\begin{aligned} \mathbf{R_{10}} = [c_m^1(s_m) &- c_m^2(s_m), \\ c_p^1(s_m) &- c_p^2(s_m), \\ f^1(s_m) &- f^2(s_m), \\ v &- V], \end{aligned} \tag{6.90}$$

is minimised while f_0 is incrementally increased by 10^{-2} between optimisations. These solutions are referred to as the minimum length solutions for fixed f_0 and c_0. The parameters from these solutions provide the initial value of L and the initial estimates for (6.75)-(6.78) which minimise

the residual

$$\begin{aligned}\mathbf{R_{11}} = [c_m^1(s_m) &- c_m^2(s_m),\\ c_p^1(s_m) &- c_p^2(s_m),\\ f^1(s_m) &- f^2(s_m),\\ v &- V,\\ l &- L].\end{aligned} \tag{6.91}$$

v is the volume of the solution tested and l is its length. V remains fixed while L is incrementally increased by 10^{-2} between optimisations, until there is a sudden increase in the absolute value of the residual from $O(10^{-8})$ to $O(10^{-3})$. The longest solution, for which the error in the residual is $O(10^{-8})$ is referred to as the maximum length solution. There are five degrees of freedom and five contraints for each optimisation.

6.6.3 Dependence of Length, Volume and Helfrich Energy on Fibre Radius and c_0

In Figure 6.33(a) the function of contact angle has a minimum wrt length. This indicates that the length of a solution will not always decrease is contact angle is decreased.

In Figure 6.33(b), the Helfrich energy also has a minimum. It could be assumed that the length of a solution will increase as a way to minimise its energy until the solution reaches this minimum in Helfrich energy. This suggests that, under the constraint of constant volume, the most energetically stable solution is not necessarily the longest possible solution. Defining solutions of minimum Helfrich energy to be the end point solutions of the cell lengthening on fibre problem is less arbitrary than simply stretching the capacities of an optimisation function.

The dependence of contact angle and Helfrich energy on length of the solution changes with f_0. In the example in Figure 6.33(a), increasing f_0 has the effect of decreasing the length of the solution which minimises Helfrich energy. How Helfrich energy and length depend on f_0 and c_0 is discussed in detail in the following discussion.

The maximum length solutions and the length of the original cell engulfing fibre solutions for a range of c_0 and f_0 are plotted in Figure 6.34. When $c_0 > 0$, this length decreases smoothly with f_0 when $0.1 \gtrsim f_0 \gtrsim 0.4$. At some point when $f_0 \lesssim 0.1$ there is a maximum in length. This maximum length also decreases smoothly as c_0 increases. These observations are also true when $c_0 < 0$ with an additional observation that at some f_0 the length of the solution suddenly decreases. The value of f_0 at which this switch occurs decreases as c_0 decreases.

The maximum possible length of solution found for each c_0 in Figure 6.34 are plotted in Figure 6.6.3. For these solutions f_0 is inversely proportional to c_0. The maximum possible length inceases as c_0 becomes more negative and as f_0 increases. This suggests that, for these solutions, length increases as wave-like behaviour is more dominant.

Figures 6.35 and 6.36 plot the Helfrich energy of the solutions corresponding to those in Figure 6.34. When $c_0 < 0$ the Helfrich energy decreases with length, while when $c_0 > 0$ the Helfrich energy increases. When $c_0 < 0$, the solution with the minimum Helfrich energy does

not correspond to the solution with the maximum length as there is a minimum in the Helfrich energy as discussed above.

Figure 6.38 shows how (x_{max}/R) decreases with f_0. The ratio of maximum radius over minimum radius (x_{max}/R) is determined by the value of f_0 rather than c_0. For any given piece of information on the comparative size of the radius of a macrophage relative to the radius of a fibre, the best value of f_0 to use for this boundary condition can be picked. For example information relating to Figures 6.38(a)-6.38(b) suggests that $x_{max}/R \approx 10$, which corresponds to the longest cell lengthening on a fibre solutions for which length over fibre radius is $L/R \approx 100$.

If no constraints are put on the contact angle at the fibre surface a smaller choice of fibre radius will result in a larger aspect ratio. Solutions of this type suggest that it is possible for a cell membrane to phagocytose a long fibre, even if the extra structural support provided by the actin filaments just inside the membrane surface are not considered.

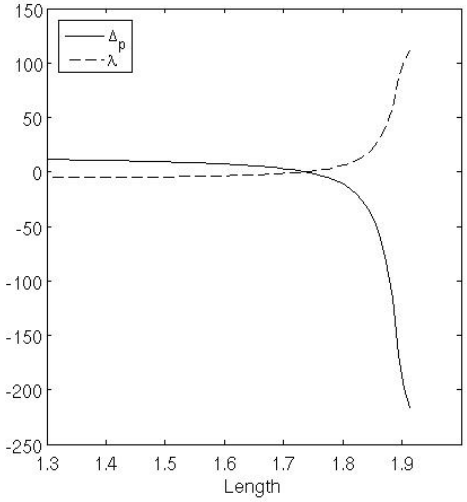

(a) $c_p(0) = 0$ and volume is free.

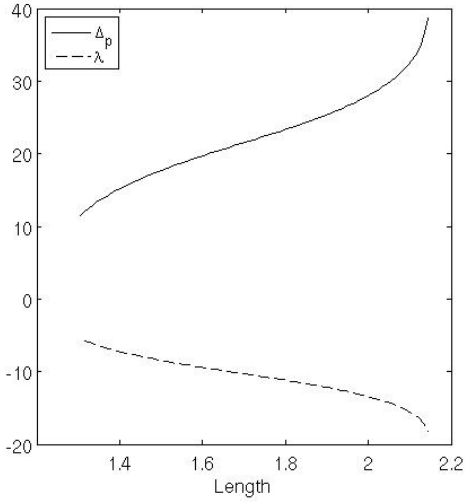

(b) $c_p(0)$ is a free variable while volume is fixed.

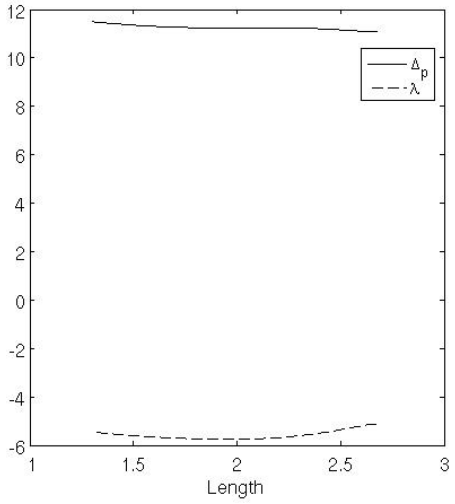

(c) Both $c_p(0)$ and volume are free.

Figure 6.29: Δ_p and λ for solutions of increasing length when $f_0 = 0.1$ and $c_0 = 0$. When boundary conditions are imposed on $c_p(0)$, Δ_p and λ in Figure 6.29(a) change significantly to produce solutions of longer length.

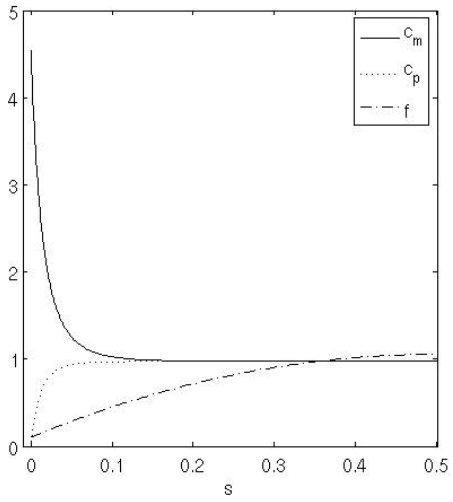

(a) c_m, c_p and f against s.

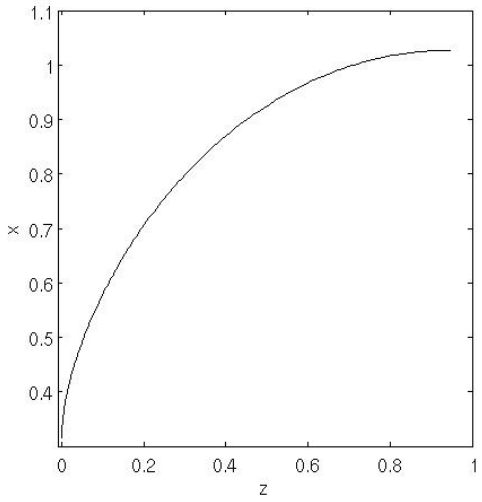

(b) x against z.

Figure 6.30: Solution of maximum length, $L = 1.89$, found when $c_p(0) = 0$ and volume is a free variable, $f_0 = 0.1$ and $c_0 = 0$.

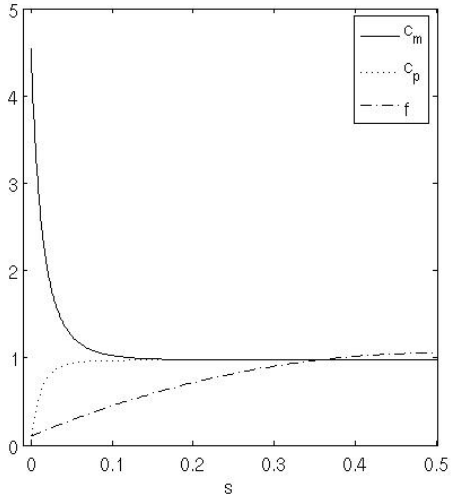

(a) c_m, c_p and f against s.

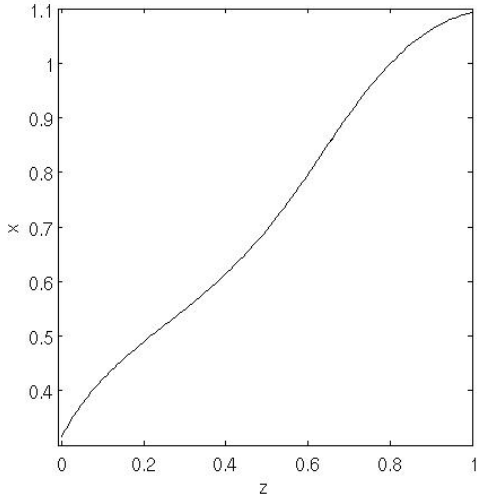

(b) x against z.

Figure 6.31: Solution of maximum length, $L = 2.14$, found when $c_p(0)$ is a free variable and volume is fixed, $f_0 = 0.1$ and $c_0 = 0$.

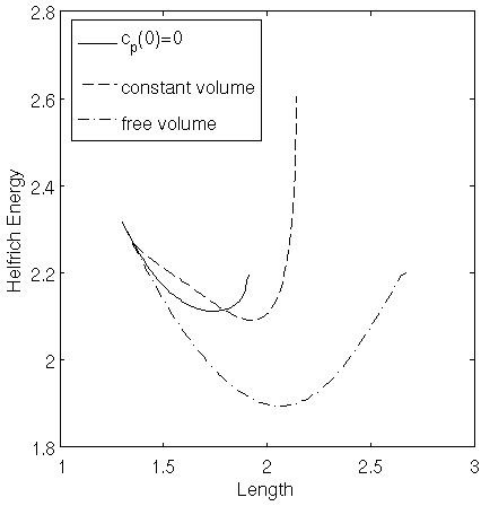

(a) Helfrich energy against length when $f_0 = 0.1$ and $c_0 = 0$.

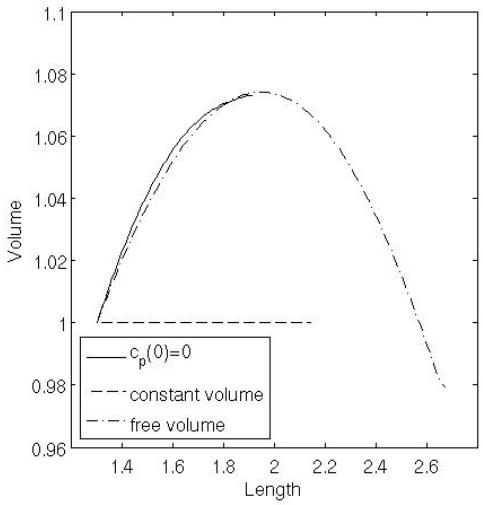

(b) Volume against length when $f_0 = 0.1$ and $c_0 = 0$.

Figure 6.32: Helfrich energy and volume against length for solutions under constraints A - $c_p(0) = 0$ and volume is free. B - $c_p(0)$ is a free variable and volume is fixed. C - $c_p(0) = 0$ and volume are free.

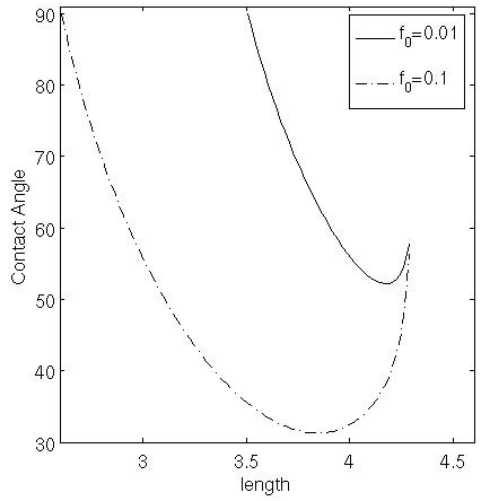

(a) Contact angles against length of solutions.

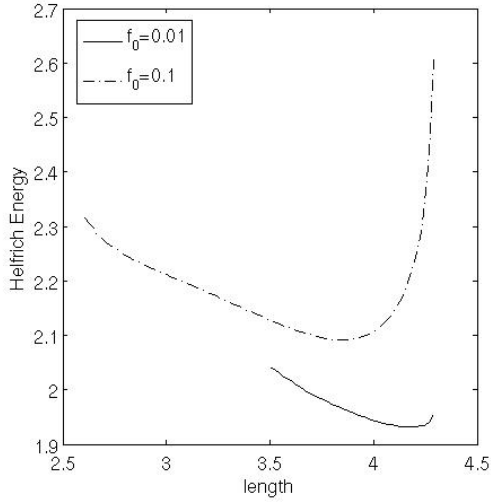

(b) Helfrich energy against length of solutions.

Figure 6.33: Plot of parameters which minimise (6.91) as length is increased from a constant volume cell enclosing fibre solution where $f_0 = 0.1$ and $c_0 = 0$.

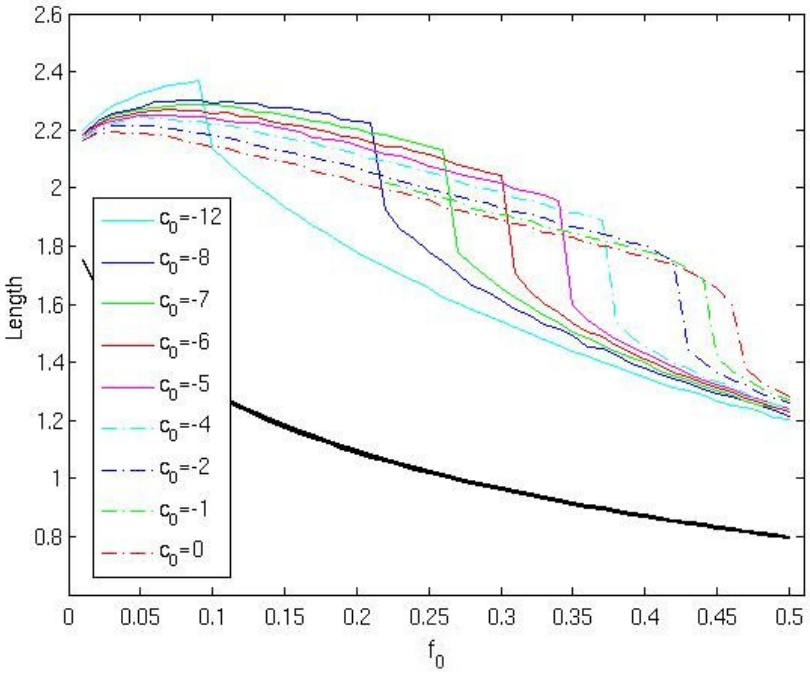

(a) Negative spontaneous curvature c_0.

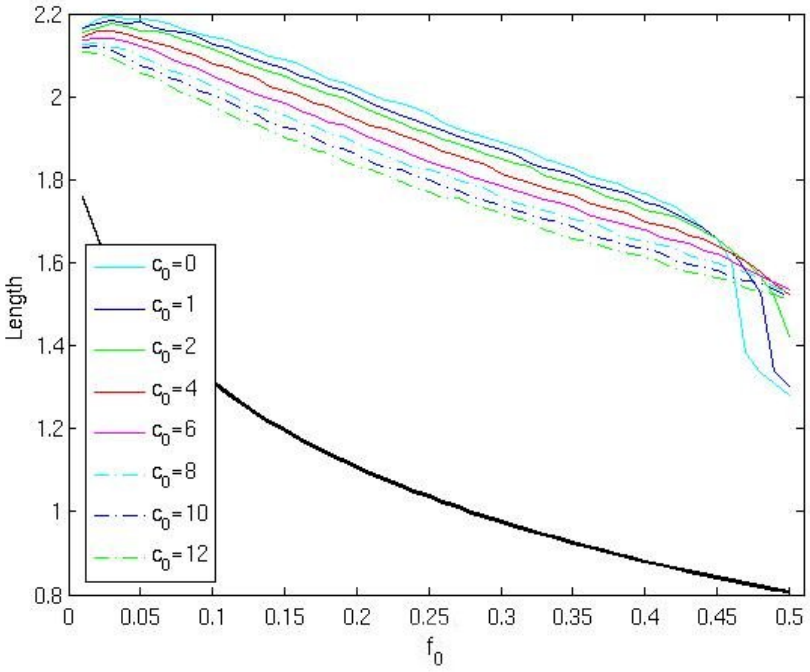

(b) Positive spontaneous curvature c_0.

Figure 6.34: Minimum and maximum lengths of solutions for a range of f_0.

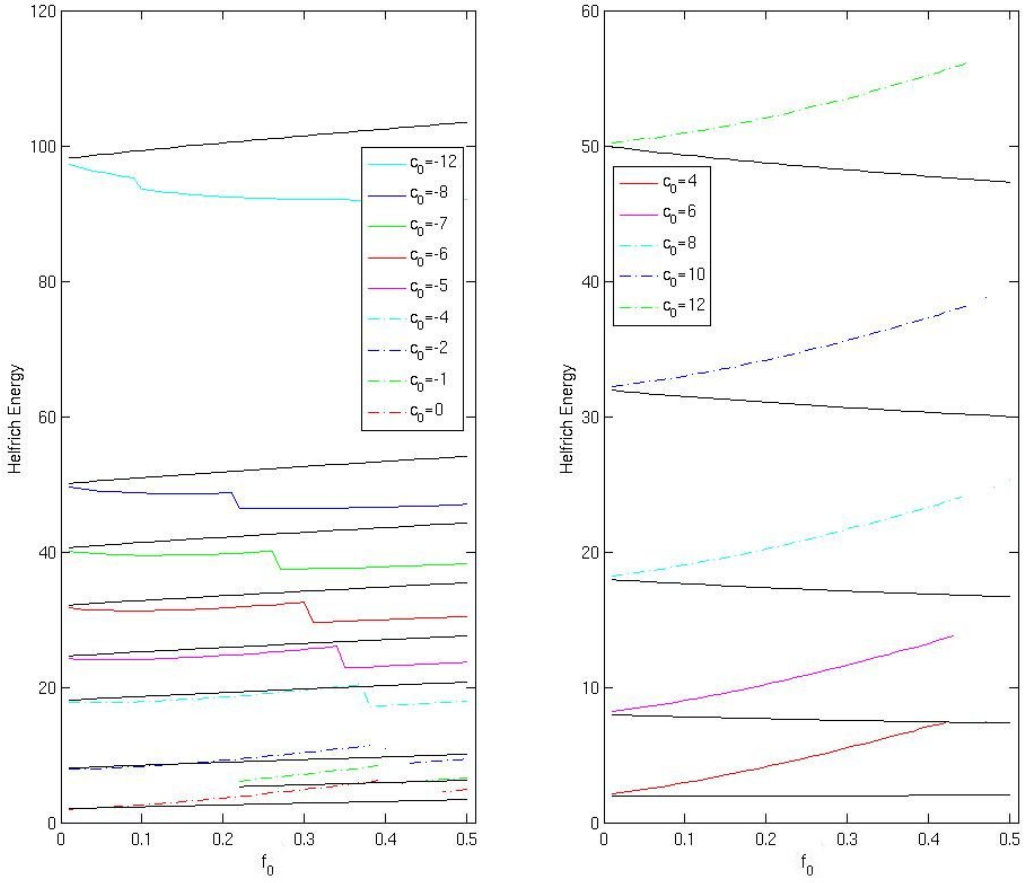

(a) Negative spontaneous curvature c_0.

(b) Positive spontaneous curvature c_0.

Figure 6.35: Helfrich energy of solutions in Figure 6.34. Black line (dashed line) - Helfrich energy of minimum length solution in that set. Coloured line (solid line) - Helfrich energy of maximum length solution in that set.

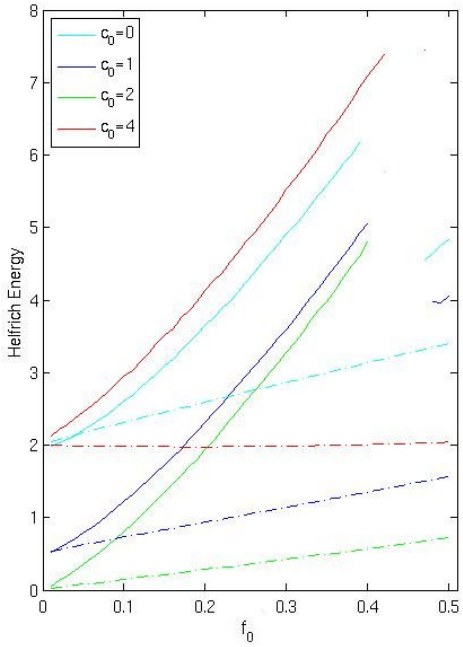

(a) Positive spontaneous curvature c_0.

Figure 6.36: Helfrich energy of solutions in Figure 6.34. Black line (dashed line) - Helfrich energy of minimum length solution in that set. Coloured line (solid line) - Helfrich energy of maximum length solution in that set.

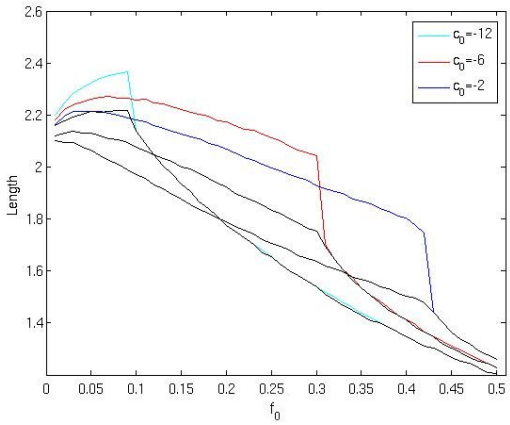

(a) Length of solution with maximum length and length of solution with minimum Helfrich energy as parameterised by c_0 and f_0.

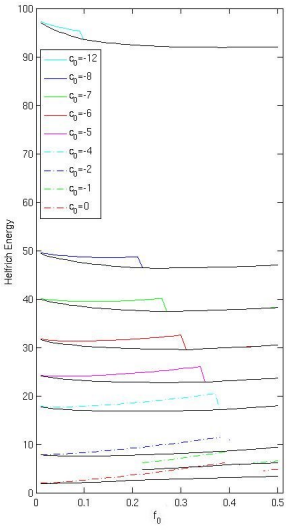

(b) Helfrich energy of solution with maximum length and Helfrich energy of solution with minimum Helfrich energy as parameterised by c_0 and f_0.

Figure 6.37: Comparison of length and Helfrich energy for maximum length and minimum Helrich energy solutions as parameterised by c_0 and f_0. Black line - Solution with minimum Helfrich energy. Coloured line - Solution with maximum length.

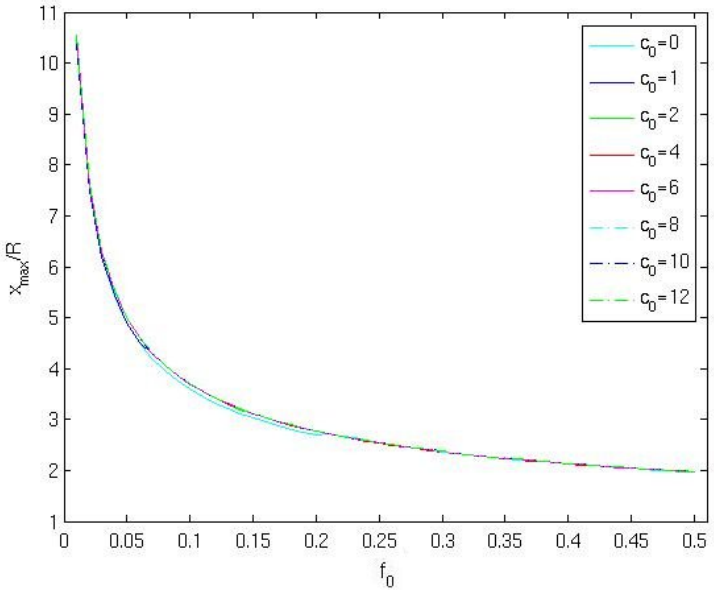

(a) Negative spontaneous curvature c_0.

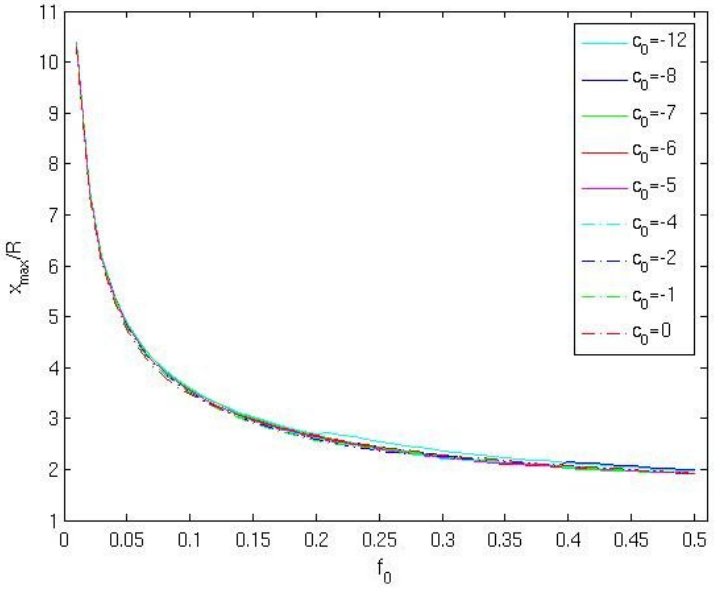

(b) Positive spontaneous curvature c_0.

Figure 6.38: Ratio of x_{max}/R for the solution with maximum length as parameterised by c_0 and f_0.

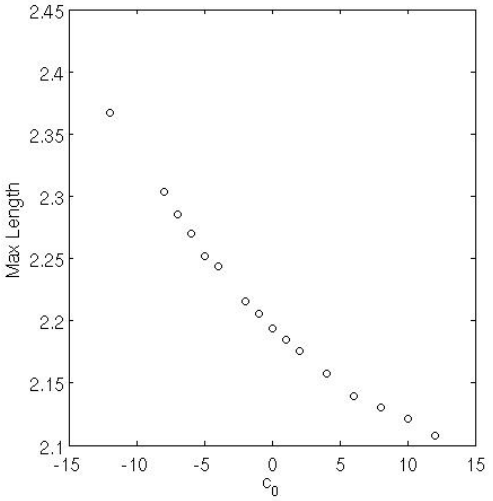

(a) Maximum possible length against spontaneous curvature c_0.

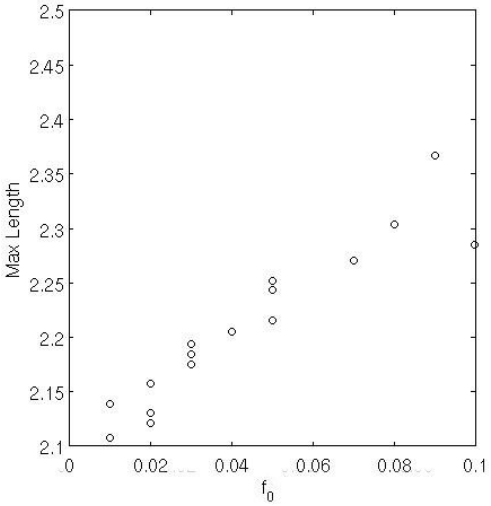

(b) Maximum possible length against f_0.

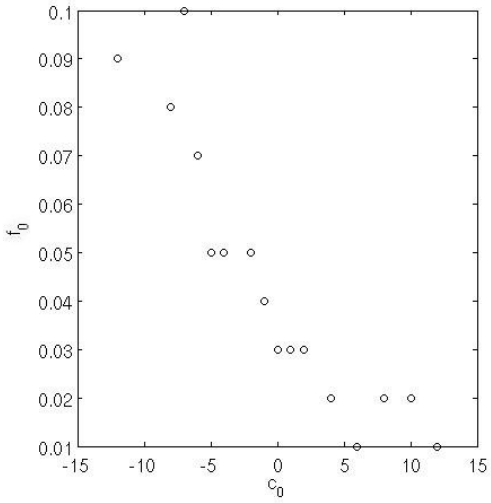

(c) f_0 of maximum possible length solution against spontaneous curvature c_0.

Figure 6.39: Results relating to maximum possible length solutions for cell lengthening on fibre solutions for $-12 \leq c_0 \leq 12$.

6.6.4 Dependence of Free Parameters on Fibre Radius and c_0

Figures 6.42 and 6.43 demonstrate how, for fixed c_0 and $f_0 = 0.09$, the free parameters vary as the length of a solution is increased. The maximum length depends on c_0 in an approximately linear way. λ and Δ_p vary comparatively little compared to the boundary conditions of c_m and c_p at $s = 0$ and $s = 1$. The difference between $c_m(0)$ and $c_p(0)$ increase as $|c_0|$ increases. The length of a maximum length solution increases linearly as $c_p(0)$ increases.

By Figure 6.39(a), it is clear that the maximum possible length of all solutions found for a given c_0 increases as c_0 becomes more negative. The maximum length solution found in this section is found when $c_0 = -12$ where $L = 2.37$. The numerical solutions for c_m, c_p and f from the maximum length solution when $c_0 = 12$ for $0.01 \leq f_0 \leq 0.5$ are plotted in Figure 6.44, while these results for $c_0 = -12$ are plotted in Figure 6.45. In Figure 6.44, c_p undulates, while in Figure 6.45 c_p has one very shallow minimum. The plot of the initial conditions $f(0)c_p(0)^2$ show that $f(0)c_p(0)^2 \approx 0.8$. In Section 5.13.2, it was discussed that when $fc_p^2 \approx 1$ the Euler-Lagrange equations are dominated by wave-like rather than divergent behaviour. The reason that c_p has fewer undulations when $c_0 = -12$ than when $c_0 = 12$ can be found in Section 5.13. A negative spontaneous curvature minimises the undulations induced when $\lambda < 0$ and $c_p > 0$. If c_p does not undulate then its integral, and so the length of the resulting shape, will be larger than if it did undulate. For this reason, the maximum length solution of all solutions when $c_0 = -12$ is larger than that when $c_0 = 12$.

An example of a solution when $c_0 = -12$ is found in Figure 6.44, the extremum in c_m would not occur without the extremum in c_p. However, the first extremum in c_m in Figure 6.45 occurs as c_p monotonically increases. This feature acts to prevent c_m from causing a further extremum in c_p and so maximises length. It also has the effect of increasing the difference $|c_p(0) - c_m(0)|$. As in the examples in Sections 6.4.3 and 6.5.3, a c_0 adds a degree of freedom which allows a solution to be found where there is a maximum or minimum in c_0 without an accompanying maximum or minimum in c_p.

When $c_0 < 0$ the length of the maximum length solutions suddenly decreases with f_0. At this point, Figure 6.40 shows how the value of $f(0)c_p(0)^2$ suddenly increases to ≈ 1. If a solution is to be well behaved when $fc_p^2 = 1$, the solution must meet the boundary condition

$$c_p(0)((c_p(0) - c_0)^2 - c_m(0)^2) + 2\lambda c_p(0) + \Delta_p = 0. \tag{6.92}$$

Figure 6.41 suggests that as $f(0)c_p(0)^2 \to 1$ then $c_p(0)((c_p(0) - c_0)^2 - c_m(0)^2) + 2\lambda c_p(0) + \Delta_p \to 0$. The boundary conditions at $s = 0$ for these solutions are approaching the boundary conditions in Section 5.4.2 which are necessary to avoid at singularity when $fc_p^2 = 1$. Cell lengthening on fibre solutions for which $f(0)c_p(0)^2 \approx 1$ and $c_p(0)((c_p(0) - c_0)^2 - c_m(0)^2) + 2\lambda c_p(0) + \Delta_p \approx 0$ are used an initial estimates to find find solutions of zero contact angle in Section 6.7.

It was found that when L was increased, the solutions found by the optimisation function were such that c_m tends to decrease while c_p monotonically increases as f decreases. Solutions which force $c_p(0)$ to become greater while f_0 is small will push the boundary conditions at

$s = 0$ towards the limit $f(0)c_p(0)^2 = 1$. As $c_p(0)$ does not have to increase as much when f_0 is larger, more maximum length solutions are found for larger f_0.

The toy model in Section 5.13.2 attempts to capture the dynamics of the Euler-Lagrange equations when $fc_p^2 \approx 1$. When s is decreasing and $c_m c_p < 0$ then the conditions $fc_p^2 \approx 1$ and $c_p(0)((c_p(0) - c_0)^2 - c_m(0)^2) + 2\lambda c_p(0) + \Delta_p \approx 0$ correspond to an attractive steady state in the toy model.

At the attractive steady state in the toy model $c_p = c_m$ and $(1 - fc_p^2)^{1/2}$ is fixed at ϵ. In the full Euler-Lagrange equations (5.36)-(5.38), steady state occurs when $(1 - fc_p^2)^{1/2} = 0$ and the limit of the first term in (5.36) is zero so that generally, $c_m \neq c_p$. It is therefore not clear how the attractive steady state of in the toy model in Section 5.13.2 relates to the stationary point in the Euler-Lagrange equations. If $(1 - fc_p^2)^{1/2}$ is small then the full Euler-Lagrange equations will approximate the toy model. The c_m, c_p and f will generally tend towards the condition $c_p(0)((c_p(0) - c_0)^2 - c_m(0)^2) + 2\lambda c_p(0) + \Delta_p \approx 0$. However, as $(1 - fc_p^2)^{1/2} \to 0$, then a comparison between the toy model and the full Euler-Lagrange equations is no longer valid.

Nonetheless, it was found that when no boundary conditions where imposed on c_m and c_p for the cell on a fibre problem, the boundary conditions found for c_m, c_p and f are consistent with those given in Section 5.4.2, which are necessary to avoid a singularity at $fc_p^2 = 1$, and also with the conditions for an attractive steady state in the toy model in Section 5.13.2.

An explanation for this can be found by referring to the analytical solutions for the perturbation of a sphere in Section 5.9. These solutions also have the property that they are invariant to the direction of integration. Integrating away from the boundary conditions at $s = 0$ results in the same solution as when integrating away from the boundary conditions at $s = 1/2$. For a randomly selected range of parameters this is not the case. For a solution to be invariant to the direction of integration towards and away from a potential singularity at $fc_p^2 = 1$, then c_m, c_p and f at $fc_p^2 = 1$ must approximately meet the condition (5.45). In this way, requiring that a numerical solution to the full Euler-Lagrange equations indirectly imposes the condition that when $fc_p^2 = 1$ then (5.45) must also be met.

Figure 6.45 demonstrates that when $c_0 < 0$, solutions are found for which $c_m(0) < 0$ while $c_p(0) > 0$. As there are no restrictions on the specific values of $c_m(0)$ and $c_p(0)$, the numerical solution will tend to such a stationary point at $s = 0$.

In Figure 6.34(b), it can be seen that the value of f_0 for which there is the sudden change in solution is decreased for more negative c_0. This has been observed when $c_0 c_p < 0$, c_0 acts to decrease the frequency of undulations in c_m and c_p. Generally, a solution is pulled to the singularity. If $c_0 c_p > 0$ then the undulations can act as another degree of freedom in order to avoid $|c_m(0) - c_p(0)|$ from being too large so that the steady state can be avoided. This allows a longer solution to be found when spontaneous curvature is positive.

The change in Δ_p/λ across the sudden decrease in length of the cell lengthening solutions plotted in Figure 6.47 can be compared to the change in Δ_p/λ across the sudden decrease in length of the maximum length zero momentum solution plotted in Figure 6.27. This ratio does not change sign for cell lengthening solutions but it does for zero momentum solutions. This indicates that, though the jump in zero momentum solutions indicates a change from a

divergence dominated solution to an undulation dominated solution, all constant volume cell lengthening solutions are undulation dominated.

The observable change in solution across the jump in parameters can be appreciated by comparing the numerical solution of c_m, c_p and f in Figures 6.44 and 6.45 with Figure 6.46. There are no undulations in c_m in Figure 6.46 and the solution is more dominated by the increase of $|c_m - c_p|$ rather than their undulation. For larger f_0, the constraint in volume prevents wave-dominated solutions from being found.

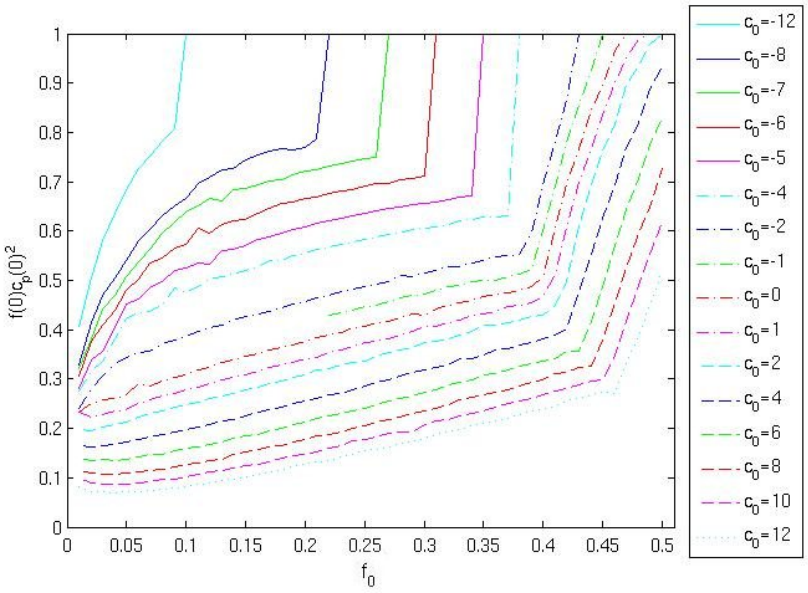

Figure 6.40: $f(0)c_p(0)^2 = \sin^2\phi(s)$ of each maximum length solution as parameterised by c_0 and f_0.

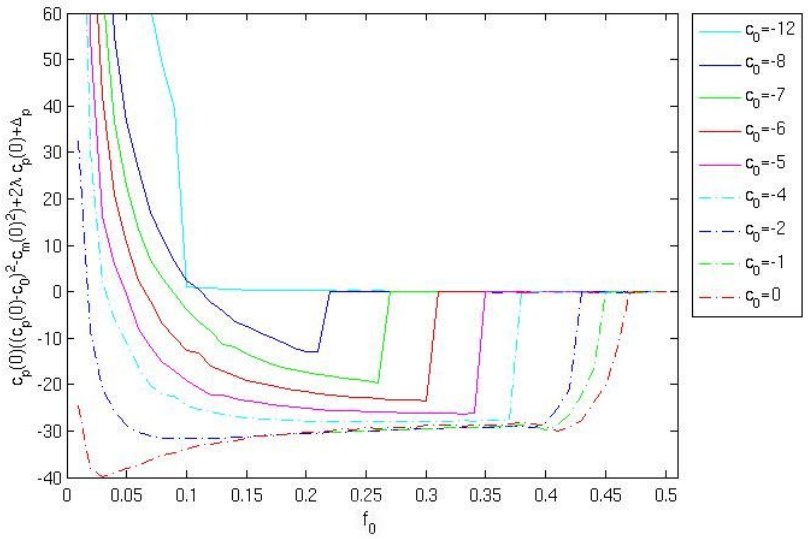

Figure 6.41: $c_p(0)((c_p(0)-c_0)^2-c_m(0)^2)+2\lambda c_p(0)+\Delta_p$ of each maximum length solution as parameterised by c_0 and f_0. When this is zero, the boundary condition at $f(0)c_p(0)^2=1$ in Section 5.4.2 is met.

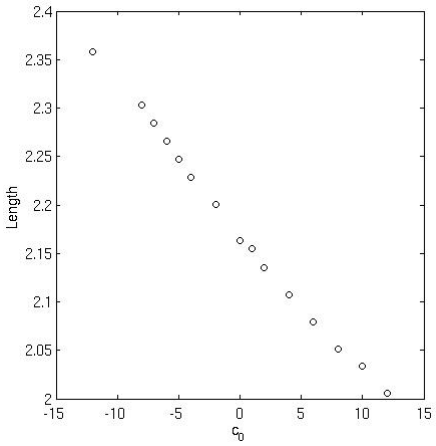

(a) Length against spontaneous curvature c_0 for $f_0 = 0.09$.

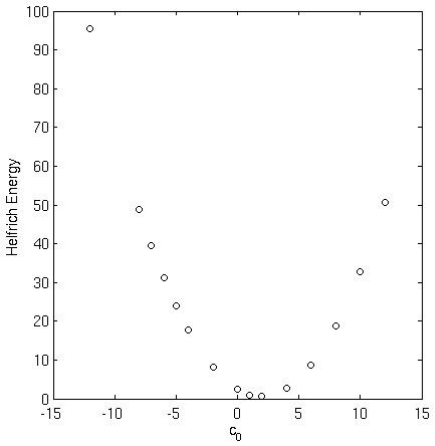

(b) Helfrich energy against spontaneous curvature c_0 for $f_0 = 0.09$.

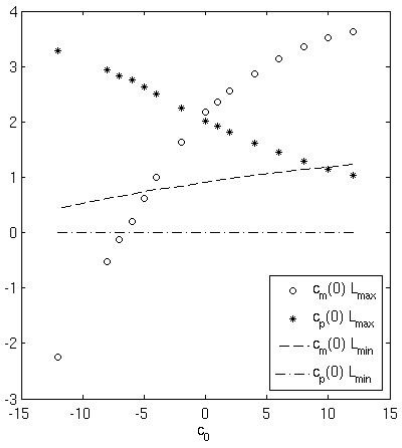

(c) $c_m(0)$ and $c_p(0)$ against spontaneous curvature c_0 for $f_0 = 0.09$.

Figure 6.42: Parameters associated with maximum and minimum length solutions when $f_0 = 0.09$ and $-12 \leq c_0 \leq 12$.

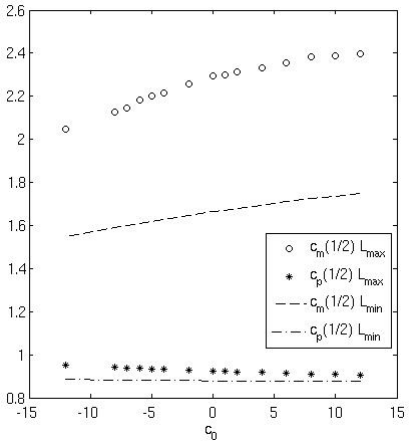

(a) $c_m(1/2)$ and $c_p(1/2)$ against spontaneous curvature c_0 for $f_0 = 0.09$.

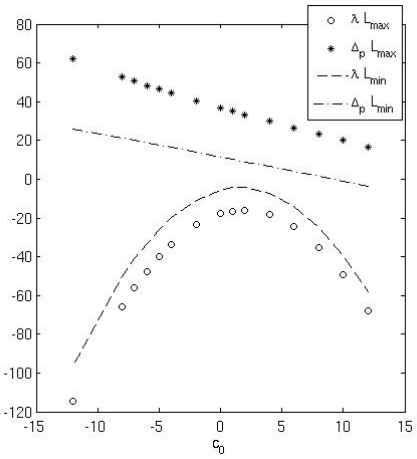

(b) λ and Δ_p against spontaneous curvature c_0 for $f_0 = 0.09$.

Figure 6.43: Parameters associated with maximum and minimum length solutions when $f_0 = 0.09$ and $-12 \leq c_0 \leq 12$.

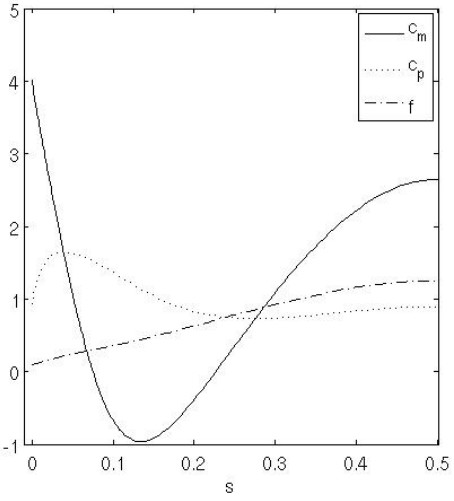

(a) Numerical solutions for c_m, c_p and f against s.

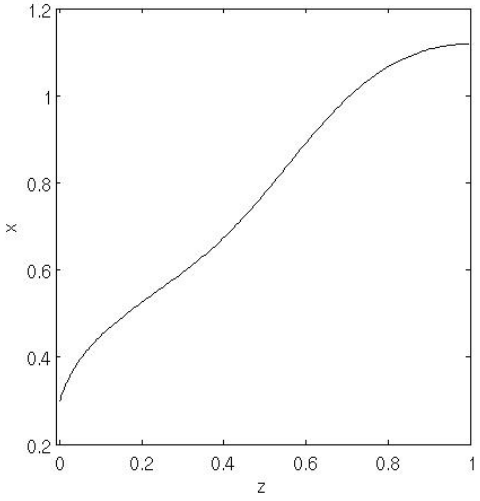

(b) x against z.

Figure 6.44: Maximum length solution $c_0 = 12$ when $f_0 = 0.09$. Generally $c_0 c_p > 0$ so undulations in c_m and c_p dominate solution.

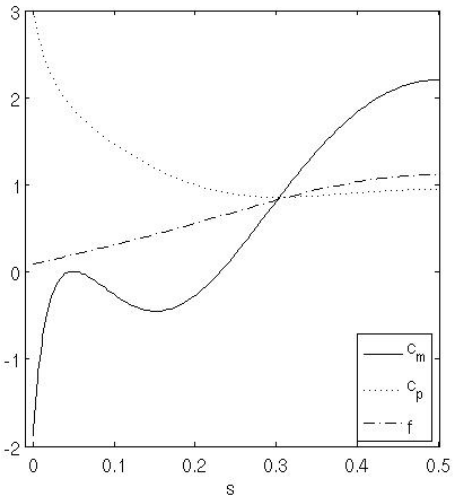

(a) Numerical solutions for c_m, c_p and f against s.

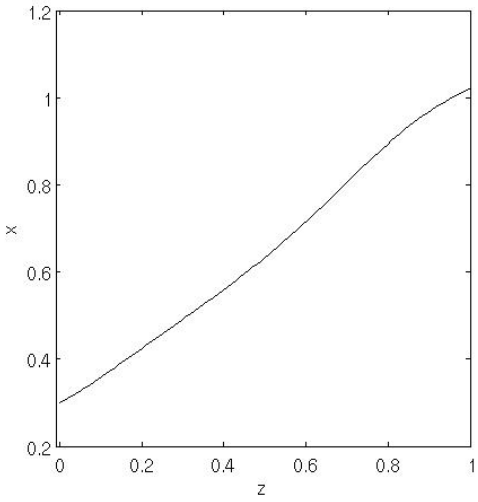

(b) x against z.

Figure 6.45: Maximum length solution $c_0 = -12$ when $f_0 = 0.09$. Generally $c_0 c_p < 0$ so undulations in c_m and c_p dominate solution less than in Figure 6.44.

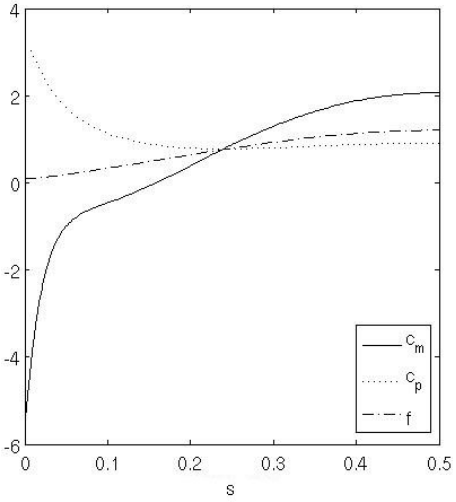

(a) Numerical solutions for c_m, c_p and f against s.

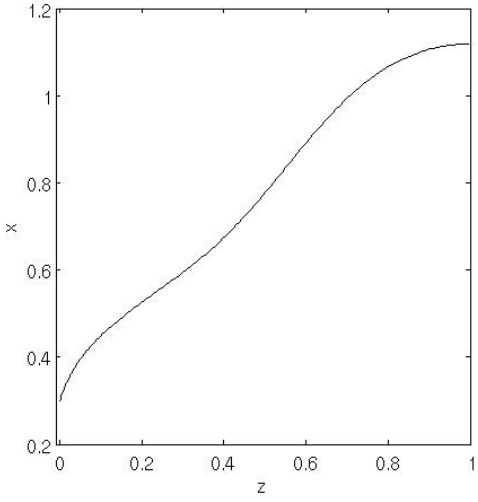

(b) x against z.

Figure 6.46: Maximum length solution $c_0 = -12$ when $f_0 = 0.20$ when $c_p(0)((c_p(0)-c_0)^2 - c_m(0)^2) << 1$ so $f(0)c_p(0)^2 \approx 1$.

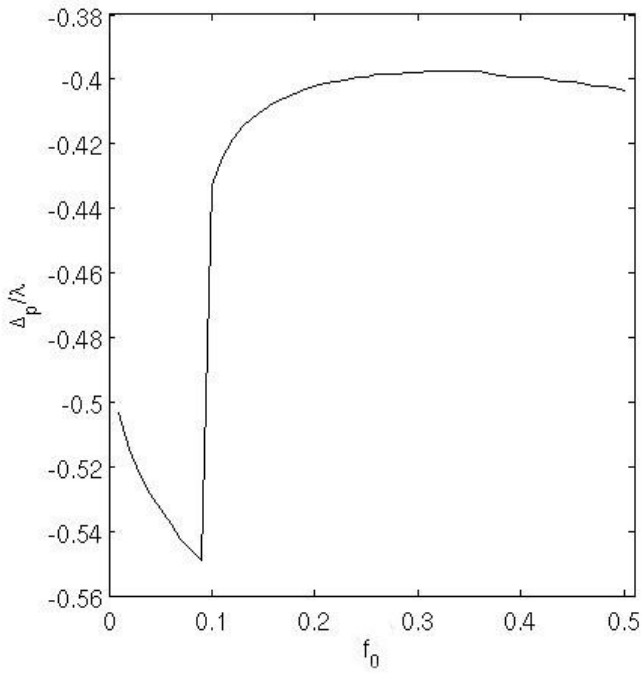

Figure 6.47: Δ_p/λ against f_0 for maximum length solutions when $c_0 = -12$. Sudden change in Δ_p/λ reflects sudden change in solutions. However, Δ_p/λ does not change sign.

6.6.5 Cell on a Fibre Dumbell Solutions

Dumbell solutions which have been introduced in Section 6.2 can be used to find a cell on a fibre solution. Details on how dumbell solutions are found numerically are in Section 6.3.1. Cell on a fibre dumbell solutions share the same boundary and matching conditions at points p and q as the HBVP dumbell solutions. The boundary conditions at point p when $s = 0$ are replaced by the cell on a fibre boundary condition in Section 5.5 only.

For each optimisation the fixed parameters are f_0 and c_0 and the free parameters are

$$\begin{aligned} \Delta_p &\quad \text{osmotic pressure}, && (6.93)\\ \lambda &\quad \text{surface tension}, && (6.94)\\ B &\quad f(s) \text{ at } f(1/2)c_p(1/2)^2 = 1, && (6.95)\\ c_m(0) &\quad c_m \text{ at fibre surface}, && (6.96)\\ c_p(0) &\quad c_p \text{ at fibre surface}, && (6.97) \end{aligned}$$

which are constrained by minimising the dumbell residual (6.26). Once a solution which minimises this residual is found, solutions of increasing length can be found by adding a constraint on length so that

$$\begin{aligned} \mathbf{R_{12}} = [x(s_{m1}) &- c_m(s_{m1}),\\ x(s_{m2}) &- c_m(s_{m2}),\\ f(s_{m1}) &- f(s_{m2}),\\ l &- L], \end{aligned} \qquad (6.98)$$

where L is a fixed parameter and l is the length of the current solution. L can be perturbed by steps of 10^{-3} to find solutions of increasing length.

Parameters relating to three sets of cell on a fibre dumbell solutions are found in Figure 6.48 while four examples of these solutions can be found in Figure 6.49. It was found that cell on a fibre dumbell solutions were easier to find when $f_0 = O(10^{-2})$ rather than $f_0 = O(10^{-1})$. Figure 6.48(d) demonstrates that there is at least one cell on a fibre dumbell solution which is also a zero momentum solution when $c_m(0) + c_p(0) - c_0 = 0$. Of these solutions, the solution with the greatest length was found when $c_0 = 3$ and $f_0 = 0.005$ where $L = 3.8$. Contact angle and volume are primarily dependent on f_0 while the Helfrich energy depends primarily on spontaneous curvature.

The results relating to zero momentum cell on a fibre solutions in Section 6.5.3 show that the solutions with the greatest length were found when $c_0 \approx 3$. These solutions used parameters from prolate spheroid HBVP solutions as initial conditions for the minimisation problem. The cell on a fibre dumbell solutions are another example of the use of a prolate HBVP to find a cell on a fibre solution.

6.6.6 Conclusions

In Section 6.6.1 it was found that imposing if the boundary condition $c_p(0) = 0$ is imposed on the surface of the fibre then the solutions resemble those found in Section 6.5. If no boundary

condition other than that for the length to increase while volume is constant reveals whose length and Helfrich energy depend strongly on f_0 and c_0. These solutions were chosen to be the focus of the investigation.

When spontaneous curvature is negative there is a decrease in Helfrich energy as length increases until a minimum is reached. This shows that it can be energetically favourable for the length of a cell on a fibre to increase in length until this minimum in Helfrich energy is reached. The kinetic, surface, gravitational and dissipation energies were used to model the speed of a spreading droplet in a time dependent system in [39]. In addition to these energies, the Helfrich energy could be used to account for bending energy. If Helfrich energy decreases with length, then by the laws of energy conservation, this energy could then be converted to kinetic energy so the membrane can further extend itself along the fibre.

The maximum length of these solutions falls between the range of the maximum lengths of the zero momentum boundary condition solutions for very negative spontaneous curvature in Figure 6.24(a) and the lengths of the zero momentum boundary condition solutions for very positive spontaneous curvature in Figure 6.24(b). By discussion in Section 5.13, when $c_0 c_p > 0$, c_0 dependent terms will dampen the oscillations in c_m and c_p less than when $c_0 c_p < 0$. The solution of greatest length for all c_0 and f_0 was found when $c_0 = -12$. This can be explained by the observation that when c_0 is negative the undulations in c_m and c_p are dampened. If c_p monotonically increases rather than undulates, then, by (5.39), longer solutions are possible.

When spontaneous curvature is in the range $-12 < c_0 < 2$ then there is a sudden decrease in length, Helfrich energy and associated parameters as f_0 is increased. The discussion in Section 5.13.2 suggests that the Euler-Lagrange equations are attracted to the point where $f c_p^2 = 1$. When $c_0 c_p > 0$, the wave-like behaviour of c_m and c_p prevents the solutions of the Euler-Lagrange equation from being attracted to this point. When $f c_p^2 \approx 1$ then the contact angle is approximately zero. Zero contact angle solutions are investigated further in Section 6.7.

Cell lengthening solutions can also be found which have two singularities where $f c_p^2 = 1$. These solutions are similar in structure to the dumbell solutions to the Helfrich boundary value problem introduced in Section 6.3.2. Such cell on a fibre dumbell solutions have the greatest length of all the cell lengthening solutions found. They can also be found to meet the zero momentum boundary condition when $c_0 \approx 3$. However, due to the numerical difficulty of finding cell on a fibre dumbell solutions they do not make a good candidate for systematic investigation.

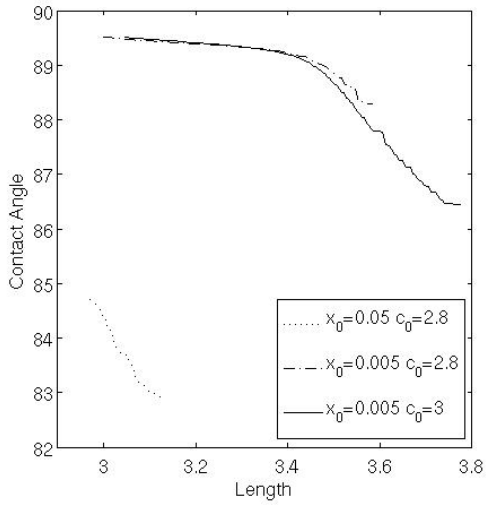

(a) Contact angle against length.

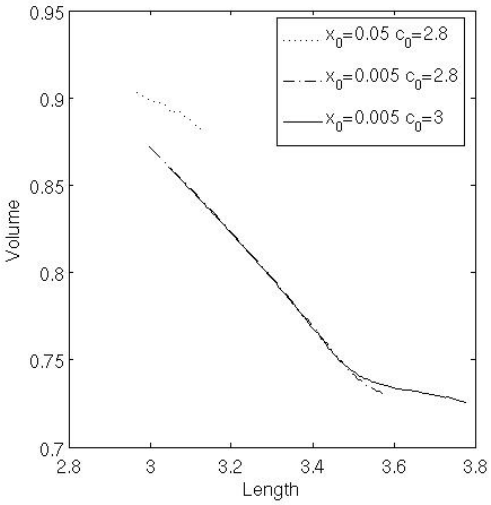

(b) Volume against length.

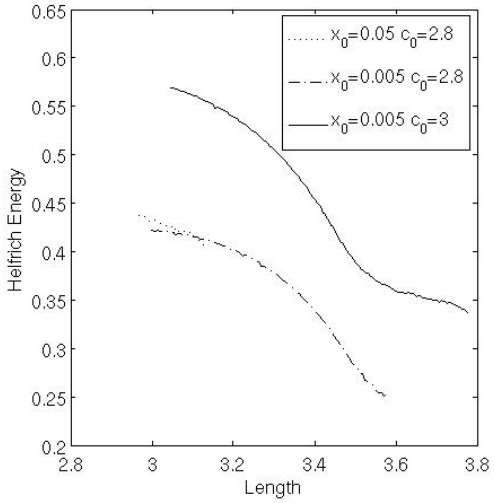

(c) Helfrich energy against length.

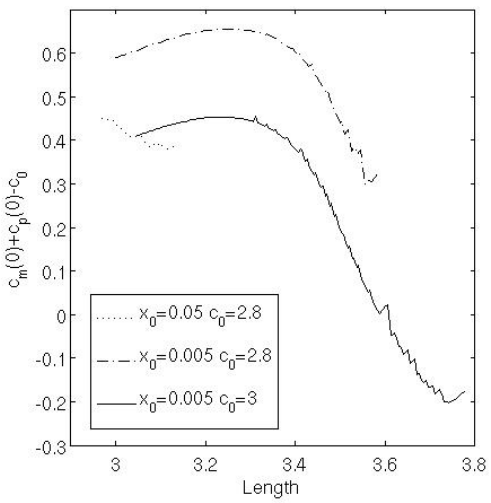

(d) $c_m(0) + c_p(0) - c_0$ against length.

Figure 6.48: Parameters relating to three sets of cell on a fibre dumbell solutions. Trend in Helfrich energy and contact angle can be compared to Figure 6.32.

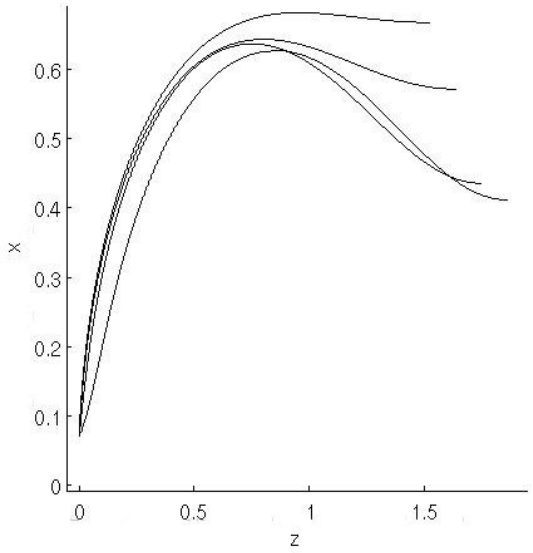

Figure 6.49: Radius against length of four cell on a fibre dumbell solutions, $f_0 = 0.05$, $c_0 = 3$. Solutions indicate how placement of maxima in f changes as length of solution is increased.

6.7 Zero Contact Angle Boundary Condition

Images and accompanying discussion in Section 3.4 suggest that, a cell is expected to spread along the fibre so that its contact angle with the fibre surface is zero. This is reasonable to assume as in order to spread along the fibre, part of the cell surface will be attached to the surface of the fibre by actin filaments.

The results for the cell lengthening on fibre solutions in Section 6.6, with particular reference to Figure 6.33, show that if volume is kept constant, for a set of solution of increasing length, Helfrich energy generally decreases with length as the contact angle between the membrane and fibre decreases. For these results there is some link between increased length and decreasing contact angle.

Solutions for which the contact angle is exactly zero, so that $f(0)c_p(0)^2 = 1$ at the fibre surface are referred to as zero contact angle solutions. $f(0)c_p(0)^2 = 1$ at both the fibre surface, when $s = 0$, and the maximum radius, when $s = 1/2$. The boundary condition (5.45) from Section 5.4.2 is also met at both $s = 0$ and $s = 1/2$ to avoid a singularity in the Euler-Lagrange equations. Such zero contact angle solutions have been found by using solutions found in Section 6.6 as initial conditions.

A range of different solutions where found. However, as f_0 was decreased two limiting sets of solutions were found. When $f_0 \approx 0.1$ then solutions were found with two extrema in c_m and two inflections points when $c_m = 0$. These solutions were very similar in shape for a range of negative spontaneous curvatures. When $f_0 \leq 10^{-2}$ then another set of solutions were found which are referred to as spherical cap solutions. For these solutions $c_m \approx c_p \approx 1$ except when f is very small and $c_p - c_m$ rapidly increases. These solutions have one inflection point.

6.7.1 Numerical Details

The discussion in this section assumes familiarity with Sections 5.4.2 and 6.3.1. A zero contact angle solution is found by perturbing boundary conditions

$$f(0)c_p(0)^2 = 1, \qquad f = f_0 = R^2, \qquad s^* = 0, \qquad \gamma \neq 0 \tag{6.99}$$

and

$$c_m(0) = -\sqrt{\frac{c_p(0)((c_p(0) - c_0)^2 - c_m(0)^2) + 2\lambda c_p(0) + \Delta_p}{c_p(0)}}, \tag{6.100}$$

over the interval $0 \leq s \leq \epsilon$ using the Taylor expansion in Section 5.4.2. The Euler-Lagrange equations are used to integrate over the interval $\epsilon \leq s \leq s_m$. At $s = 1/2$, the boundary conditions in Section 5.4.2 are met. The Taylor expansion in Section 5.4.2 is used to perturb the boundary conditions over the interval $(1/2) \geq s \geq (1/2 - \epsilon)$, and the Euler-Lagrange equations are used to integrate over the interval $(1/2 - \epsilon) \geq s \geq s_m$.

At $s = 0$, (6.100) is negative and so by the discussion in Section 6.3, it is a minimum in f. At $s = 1/2$, (6.100) is positive and so by the discussion in Section 6.3, it is a maximum in f. At $s = 0$, the limit of dc_m/ds can be any value while when $s = 1/2$ it must be zero to ensure symmetry about the mid-length.

As $c_m c_p < 0$ at $s = 0$ and $c_m c_p > 0$ at $s = 1/2$, by discussion in Section 5.13, the stationary point at $s = 0$ is attractive in the direction of s decreasing while the stationary point at $s = 1/2$ is attractive in the direction of s increasing. As solutions are perturbed from their boundary conditions, they are perturbed away from a unstable stationary point, towards a stable stationary point. The dynamics of the Euler-Lagrange equations favours the finding of such a zero contact angle solution.

The parameters of cell lengthening solutions where $f(0)c_p(0)^2 \approx 1$ and $c_p(0)\left((c_p(0)-c_0)^2 - c_m(0)^2\right) \approx 0$, as described in Section 6.6, provide initial esimates for the required parameters.

For each value of spontaneous curvature $c_0^* = -12, -11, -10, -9, -8, -7, -6, -5, -4$ and -2 a solution for which $c_p(0)\left((c_p(0)-c_0)^2 - c_m(0)^2\right) + 2\lambda c_p(0) + \Delta_p \approx 0$ is used to find a set of solutions. Each set of solutions are therefore parameterised by c_0^*.

For each optimisation f_0 only is fixed. The numerical difficulty is finding a zero contact angle solution demands that all remaining parameters

$$\Delta_p \quad \text{osmotic pressure,} \tag{6.101}$$

$$\lambda \quad \text{surface tension,} \tag{6.102}$$

$$f(1/2) \quad \text{maximum value of } f, \tag{6.103}$$

$$\gamma \quad \text{limit of } \tfrac{dcm}{ds} \text{ at } f = f_0, \tag{6.104}$$

$$c_0 \quad \text{spontaneous curvature } c_0, \tag{6.105}$$

must be allowed to be free variables in the optimisation problem for which

$$\begin{aligned} \mathbf{R_{13}} = [c_{m+}(s_m) &- c_{m-}(s_m), \\ c_{p+}(s_m) &- c_{p-}(s_m), \\ f_+(s_m) &- f_+(s_m)], \end{aligned} \tag{6.106}$$

is minimised. Between each optimisation, f_0 can be incrementally decreased.

A solution of greater length can be found by incrementally increasing the fixed parameter L over a set of solutions which minimise the residual

$$\begin{aligned} \mathbf{R_{12}} = [c_{m+}(s_m) &- c_{m-}(s_m), \\ c_{p+}(s_m) &- c_{p-}(s_m), \\ f_+(s_m) &- f_+(s_m)], \\ l &- L], \end{aligned} \tag{6.107}$$

where l is the length of the current solution. Solutions were accepted when the magnitude of the residual was $O(10^{-7}) - O(10^{-8})$.

6.7.2 Results

Figure 6.50 plots c_0 and Helfrich energy against f_0 for all solutions. Figure 6.50(a) is an example of how generally there is not a smooth trend between f_0 and the parameters (6.101)-(6.105), or between f_0 and length and volume. c_0 largely depends on the value of c_0^*. However,

there is a smooth trend between f_0 and Helfrich energy as this depends more on the numerical solutions of c_p, c_m and f than the parameters.

Numerical error in a HBVP solution or a cell on fibre solution mainly arises due to the approximation of the Euler-Lagrange equations to a Taylor expansion which has to be made at $fc_p^2 = 1$. The magnitude of the residuals to be minimised depend strongly on ϵ, the distance over which the Taylor expansion is used to find solutions to c_m, c_p and f. ϵ cannot be too large or too small. The zero contact angle boundary value problem has two singularities. One of which occurs when f is small, when the divergence terms dominate and so the error cannot be adjusted by adjusting Δ_p and λ. The two singularities, one of which occuring for small f result in fewer good solutions being available.

Profiles of solutions in Figures 6.51 and 6.52 demonstrate the range possible solutions which can be found within a dataset. Cell spreading solutions of this type are varied and are not simply small perturbations of a solution which can be defined by, for example, the number of oscillations of c_m and c_p.

In each set of solutions, two solutions are of particular interest. One is the solution with the maximum length. The other is the zero contact angle solution which has a smallest possible value of f_0.

6.7.2.1 Summary of Maximum Length Solutions

Parameters of maximum length solutions obtained for each c_0^* are summarised in Figures 6.53 and 6.55. Figure 6.41 indicates that there are many possible cell lengthening solutions for each value of c_0, from which a zero contact angle solution can be obtained. Whether a zero contact angle solution is possible to obtain from a given set of starting conditions is limited by the ability of the solver used to tackle this numerically challenging problem. For this reason, the results should be taken to represent a sample of possible solutions. It should not be assumed that for the given value of c_0, the maximum length solution found is the longest possible solution would could be found if all possible permutations of starting parameters were tried. However, clear trends in values and parameters associated with these solutions have been observed which are helpful in understanding these solutions.

Figure 6.54(a) indicates that f_0 decreases with c_0 for all solutions. The maximum length solutions for $c_0^* = -12$, -10, -9, -7, -6 and -5 (open circles) also show a clear linear trend between c_0 and volume and a clear linear trend between f_0 and volume which is indicated in Figures 6.53(a) and 6.53(c). The length of these solutions is ≈ 0.3 and has little variation between solutions. However, Figure 6.54(b) does indicate a slight positive trend between length and c_0, which results in a negative trend between length and f_0. Helfrich energy, λ and Δ_p, in Figures 6.53(d), 6.55(a) and 6.55(b), also show linear trends with volume.

The values of the same parameters for the remaining solutions (filled circles), where there are no clear trends with volume, are more scattered. They indicate that a variety of different solutions, with different features, are possible over the same range in f_0 and c_0. Figure 6.50(b) indicates that Helfrich energy depends more closely on f_0 than on length, so there is no straightforward relationship between length and Helfrich energy, which was found for the cell

lengthening solutions.

6.7.2.2 Example Maximum Length Solutions

Once a zero contact angle solution is found, further solutions were found by decreasing the fixed value of f_0. For each value of f_0, solutions were increased in length while keeping f_0 constant. Example solutions in the cases where $c_0^* = -6$ and $c_0^* = -12$ can be found in Figure 6.56. When c_0^* is more negative, and so, by Figure 6.50, c_0 is generally more negative, the solutions found are more varied and have more oscillations in fc_p^2. By discussion in Section 5.13, when $c_0 c_p$ is more negative, the frequency of oscillation increases. This increases the difficulty of meeting boundary conditions at $s = 0$.

Results for maximum length solutions where $L > 2.9$ (open circles) are found in Figures 6.57 which show all these solutions to be very similar in shape. For these solutions, c_m does change sign twice, on either side of a maximum, so that the solutions have two inflection points. The boundary conditions vary little between these solutions at $s = 1/2$. $c_p(0)$ increases slightly as f_0 decreases, which is expected as $|c_m - c_p|$ tends to increase as $f \to 0$. This explains how $c_p(0)$ manages to increase when f_0 is deceased, so that the boundary condition $f(0)c_p(0)^2 = 1$ is met.

As $c_p(0)$ is larger when f_0 is smaller, length is increased slightly as f_0 is decreased, see Figure 6.54(c). When f_0 is decreased, Figure 6.54(a) shows that c_0 is more negative. Also when c_0 is more negative, by discussion in Section 5.13, oscillations are flattened so that the average value of dc_p/ds is greater. This allows the boundary condition $f(0)c_p(0)^2 = 0$ to be met for small values of f_0.

Summary of Spherical Cap Solutions

Cell spreading solutions were found when $f_0 = 10^{-2}$, 10^{-3}, 10^{-4}, 10^{-5}, 10^{-6} and 10^{-7}. When $f_0 = 0.01$, two types of solution were found. Solutions of one type have a length $L \approx 3$ while another group of solutions have a more varied length.

The cluster of solutions with the greatest length in Figure 6.58(a) demonstrate a small range in the values of their volume, λ and f_{max}. These solutions all have a positive value of c_0. These solutions can be used to find the zero contact angle solutions with very small values of f_0 in Figures 6.59(a) and 6.59(b).

Figure 6.59(b) demonstrates that, even for very small f_0, these solutions are numerically well-behaved where there are no discontinuous jumps in $c_m(s)$, $c_p(s)$ or $f(s)$ and that these solutions are real and have no imaginary parts. As $f_0 \to 0$, it is found that $c_0 \to 2$ so that $(1 - c_0)^2 - 1 \to 0$ while $2\lambda + \Delta_p \to 0$. Figure 6.59(c) shows that the length of the solution does increase as f_0 and s_l decreases.

The solutions are tending to the limit that $c_p \approx 1$ and $c_m \approx 1$ over the interval $s \geq s^l$ for smaller and smaller values of s^l. Over the interval $s \leq s^l$, c_p rapidly increases while c_m rapidly decreases. The value of $-\Delta_p/\lambda$ tends to 2 as f_0 is decreased. From Section 5.8 it

is known that $-\Delta_p/\lambda = 1$ for a spherical solution to the HBVP. In this zero contact angle solution $\Delta_p \approx 19$ and $\lambda \approx 9.5$ while for a spherical solution these parameters are $\Delta_p = 12$ and $\lambda = -6$. However, when $s > s_l$ there are enough similarities between this zero contact angle solutions and a solution for a sphere to refer to these zero contact angle solutions as spherical cap solutions. Spherical cap solutions are such that their shape is approximately that of a sphere except close to the fibre surface when c_m and c_p rapidly change in order to meet the zero contact angle condition.

Figure 6.58 indicates that zero contact angle solutions where $c_0 < 0$ and $f_0 = 0.01$ are possible to find. These solutions have a smaller length, volume and f_{max} than those for which $c_0 > 0$. The length and volume of these solutions tends to decrease with increasing c_0. Figure 6.60 is an example of such a solution when $c_0 = -13.9$. The sharp maximum in c_m and associated minimum in c_p, similar to that found in solutions in Sections 6.4.3 and 6.5.3, results in two turning points and one point of inflection which reduces the length of the solution. By discussion in Section 5.13, when $|c_0|$ is too large, it is expected that sharp maxima and minima will arise from the shear terms. These extra maxima and minima may explain why solutions with a similar value of c_0 were not found when $f_0 < 0.01$.

6.7.3 Conclusions

A limited range of zero contact angle solutions were found due to the increased numerical difficulty of the optimisation problem. The lengths of zero contact angle solutions found depend strongly on f_0 and c_0, indicating that this boundary condition may be less useful in finding cell engulfing fibre solutions then the boundary conditions previously found in Section 6.5 and 6.6. In order to find a range of zero contact angle solutions the spontaneous curvature was included as a variable in the residual minimisation problem. However, two interesting sets of solutions were identified.

In Section 6.7.2.1, a set of cell spreading solutions was found in which all solutions had a normalised length of approximately 3. These solutions were found for f_0 in the range $0.01 < f_0 < 0.2$ and where $c_0 < 0$. For these solutions there are approximately linear relationships between c_0, f_0 and volume where f_0 decreases as with increasing c_0. Their solutions for c_m and c_p are very similar with only small adjustments to the height and depth of the maxima and minima. These solutions were characterised by two points of inflection.

If $f_0 \leq 0.01$ then the range of possible solutions in terms of spontaneous curvature length and volume decreases. As f_0 is decreased from any set of initial conditions the solutions will tend towards that of a spherical cap solution. In Section 6.7.2.2 it was found that, for spherical cap solutions, c_0 tends to 2. The length of the spherical cap solution also increased as f_0 was decreased. The solution of maximum length was found when $f_0 = 10^{-7}$ and $L = 3.27$. This is the longest cell on a fibre solution in this chapter.

If f_0 is decreased from any set of initial conditions the solutions will tend towards that of a spherical with a rapid increase of $|c_m - c_p|$ at small f. These limiting solutions have been called spherical cap solutions. The length of these solutions increases as f_0 decreases while c_0 tends to the value of 2. The solution of maximum length was found when $f_0 = 10^{-7}$ and

$L = 3.27$.

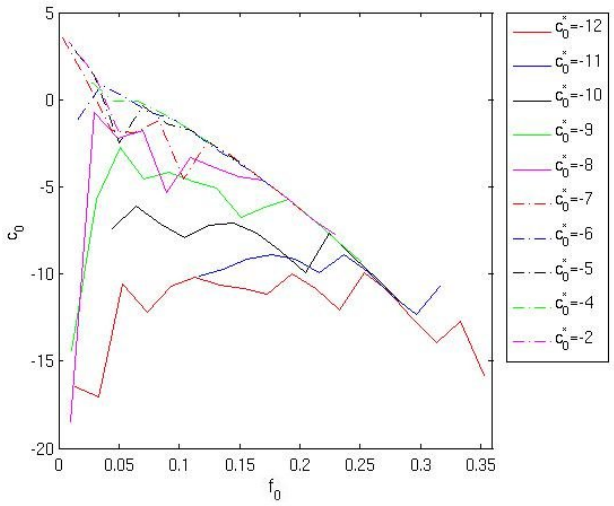

(a) c_0 against f_0.

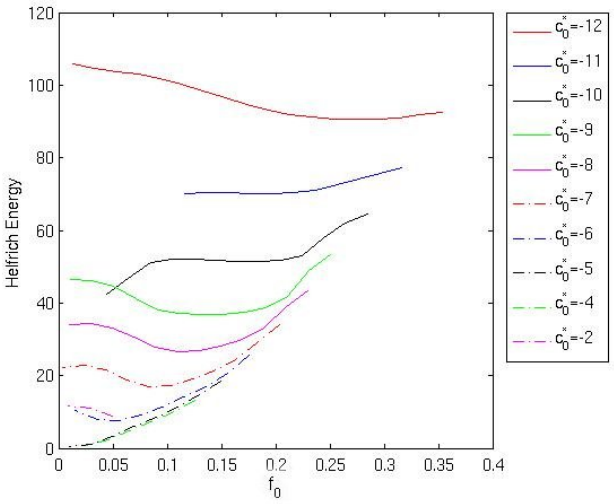

(b) Helfrich energy against f_0.

Figure 6.50: c_0 and Helfrich energy against f_0 for all zero contact angle solutions found in each data set. There is no straightforward relationship between c_0 and f_0. However, the relationship between Helfrich energy and f_0 is much simpler.

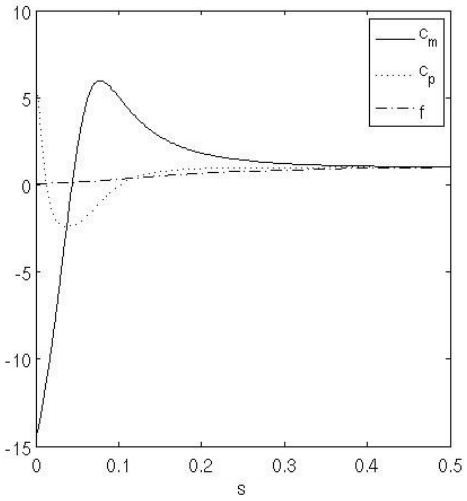

(a) $f_0 = 0.03$

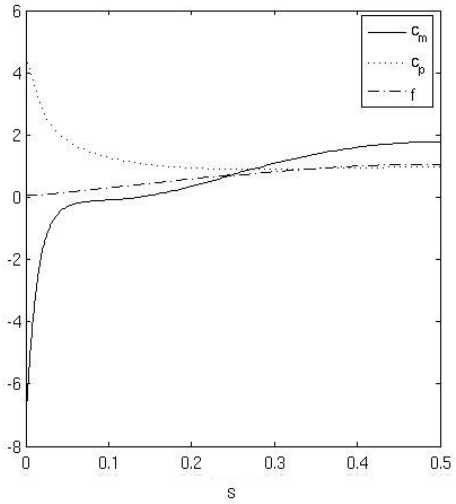

(b) $f_0 = 0.05$

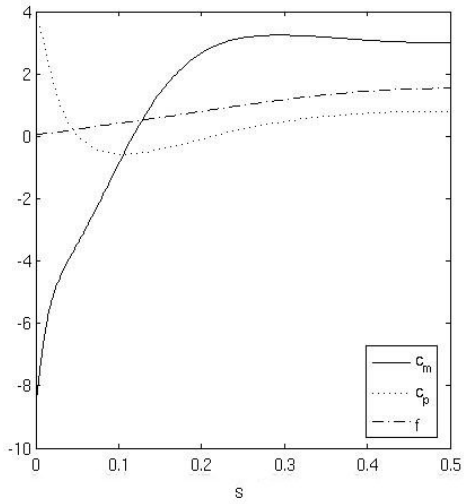

(c) $f_0 = 0.07$

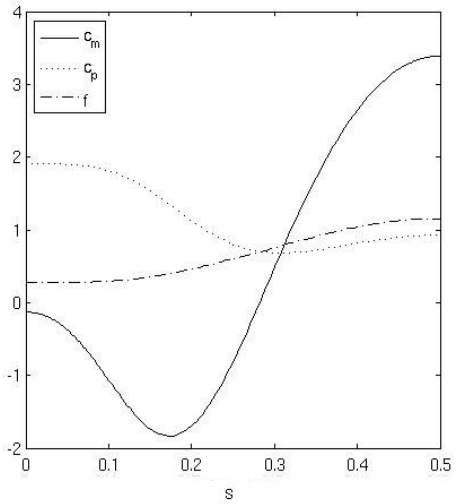

(d) $f_0 = 0.3$

Figure 6.51: c_m, c_p and f against surface area where $c_0^* = 8$. Plots indicate the range in solutions in terms of maxima and minima in c_m and c_p as f_0 is varied.

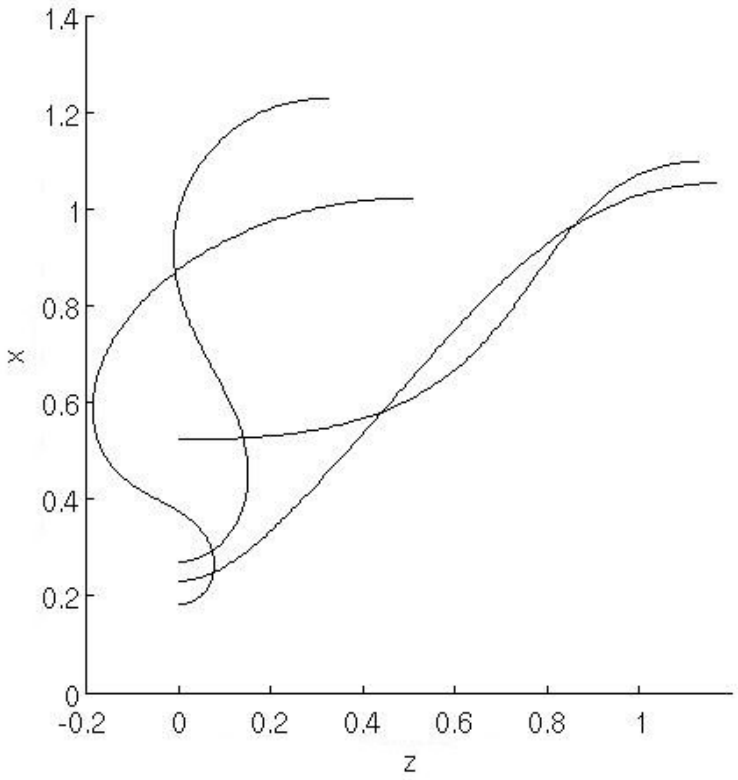

Figure 6.52: Radius against length of solutions in Figure 6.51. Turning points occur when $c_p = 0$ and points of inflection when $c_m = 0$.

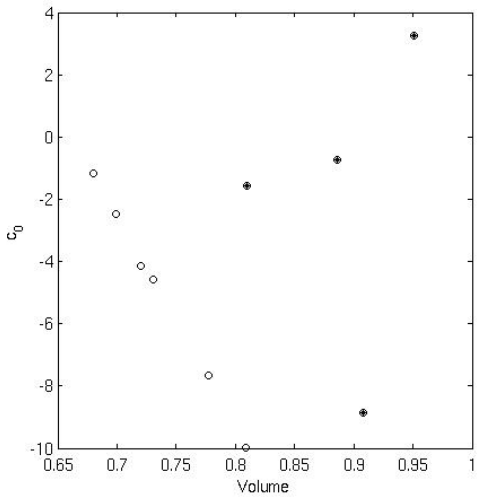

(a) c_0 against volume.

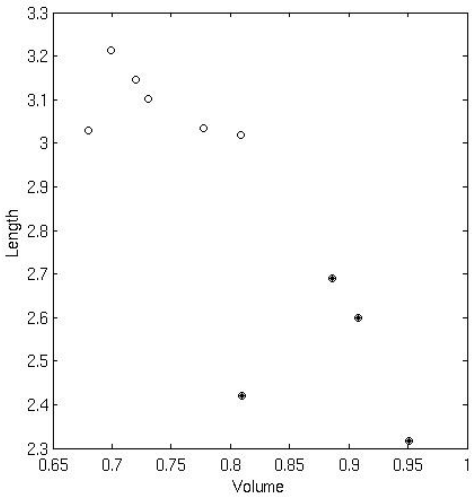

(b) Length against volume.

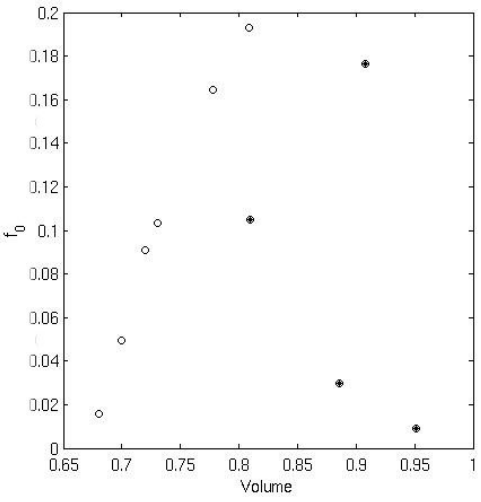

(c) f_0 against volume.

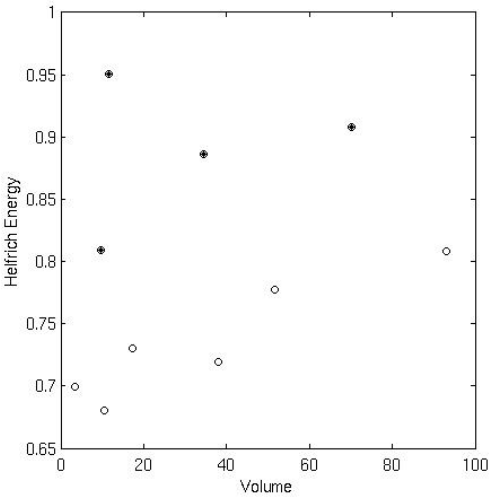

(d) Helfrich energy against volume.

Figure 6.53: Trends in parameters relating to the solution of maximum length in each set and volume. Solutions denoted by o refer to the maximum length solutions where $c_0^* = -12$, -10, -9, -7, -6 and -5 for which certain linear trends with volume are evident. Solutions denoted by $*$ refer to the maximum length solutions where $c_0^* = -11$, -8, -6, -4 and -2.

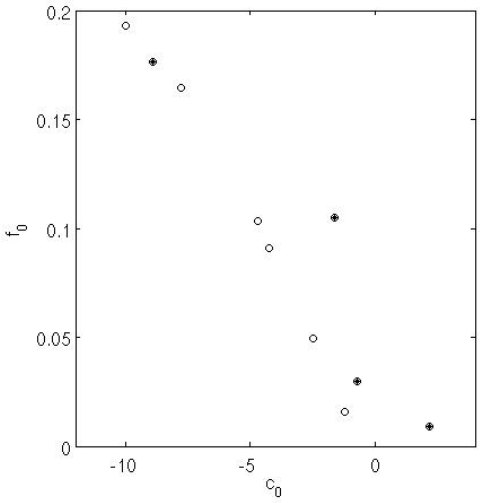

(a) c_0 against f_0.

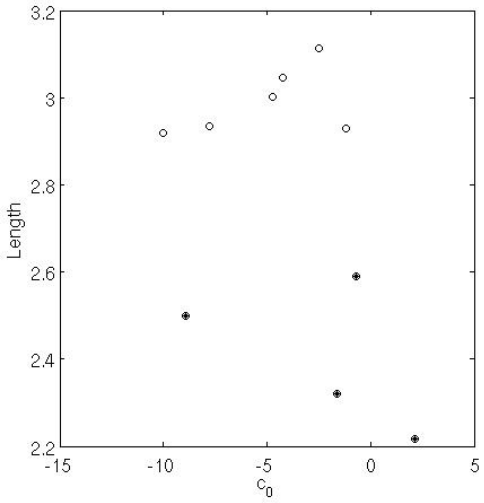

(b) c_0 against length.

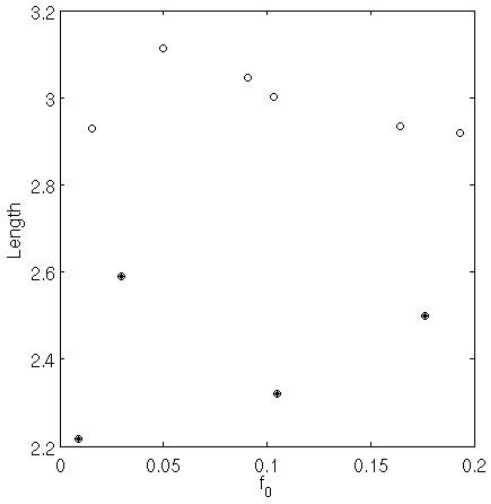

(c) f_0 against length.

Figure 6.54: Trends in parameters relating to the solution of maximum length in each set. Dependence of length on c_0 and f_0. Solutions denoted by o refer to the maximum length solutions where $c_0^* = -12$, -10, -9, -7, -6 and -5 while solutions denoted by $*$ refer to maximum length solutions where $c_0^* = -12$, -10, -9, -7, -6 and -5.

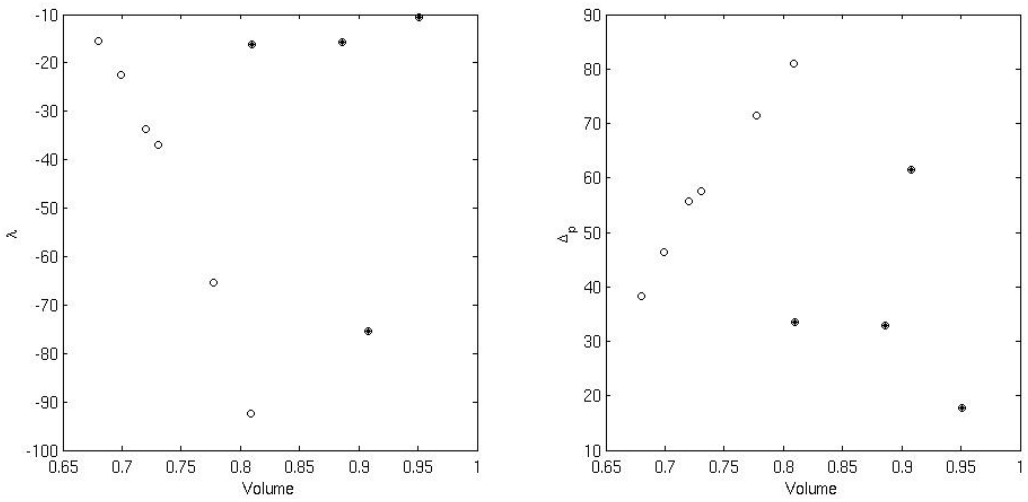

(a) λ against volume.

(b) Δ_p against volume.

Figure 6.55: Summary of parameters relating to the solution of maximum length in each set of solutions. See Figure 6.53.

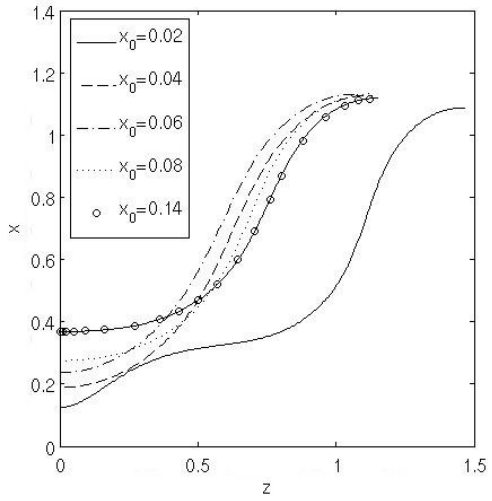

(a) z against x for maximum length solutions where $c_0^* = -6$.

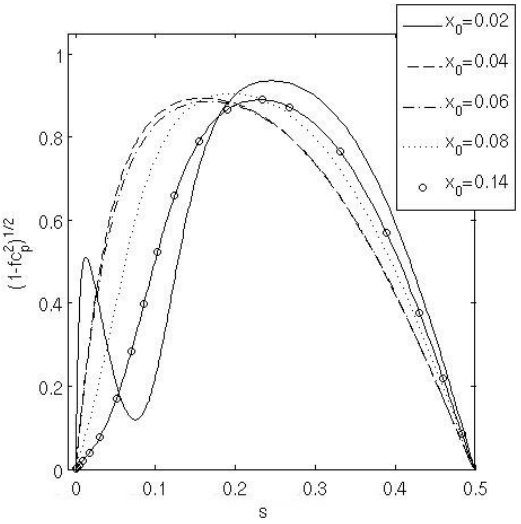

(b) $(1 - fc_p^2)^{1/2}$ against surface area for maximum length solutions where $c_0^* = -6$.

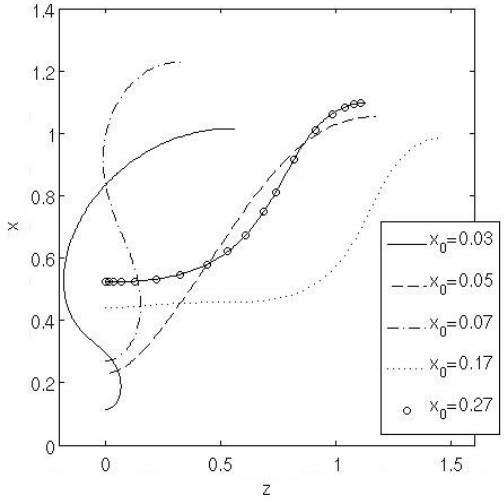

(c) Length against radius for maximum length solutions where $c_0^* = -12$.

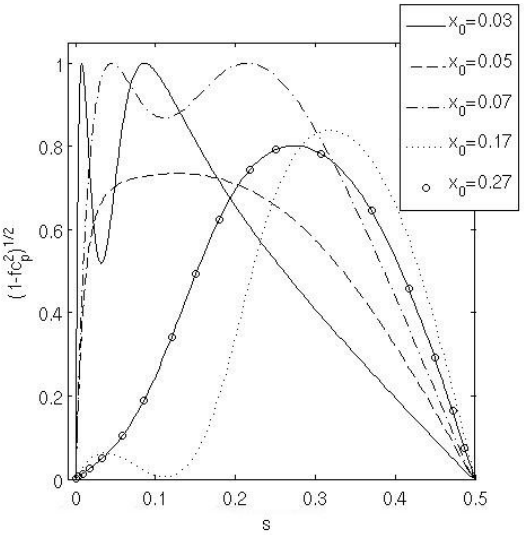

(d) $(1 - fc_p^2)^{1/2}$ against surface area for maximum length solutions where $c_0^* = -12$.

Figure 6.56: Results for maximum length solutions for $c_0^* = -6$ and $c_0^* = -12$ for a range of f_0. When c_0 is more negative, there are more maxima and minima in c_m and c_p when f_0 is small.

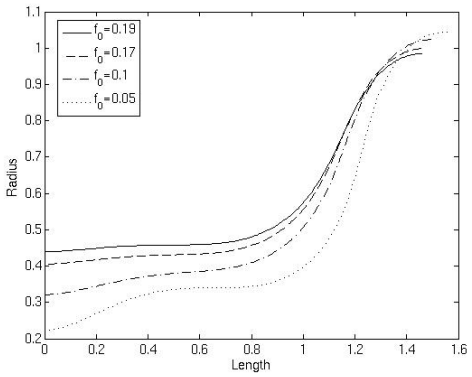

(a) x against z.

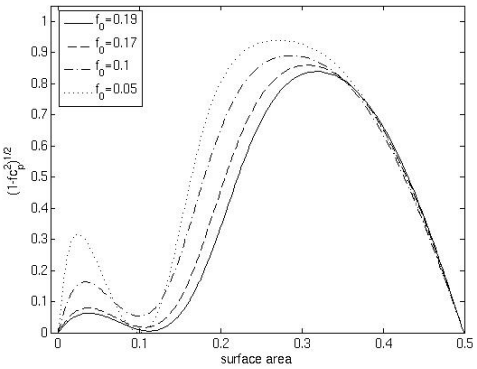

(b) $(1 - fc_p^2)^{1/2}$ against surface area.

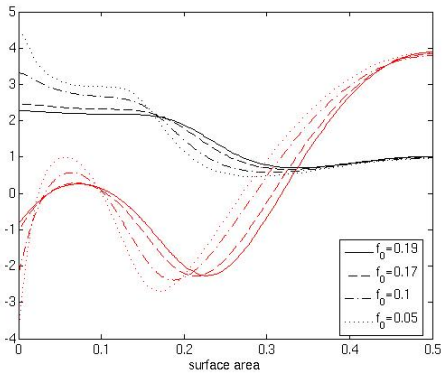

(c) c_m (red) and c_p (black) against surface area.

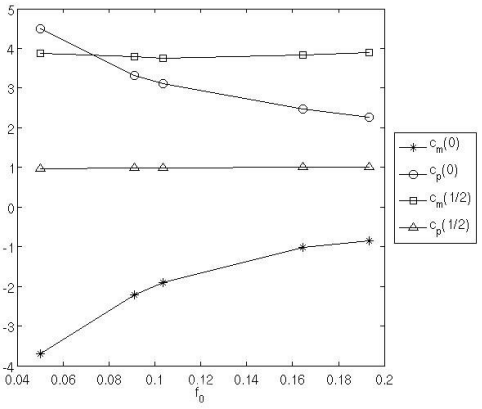

(d) c_m and c_p at $s = 0$ and $s = 1/2$.

Figure 6.57: Results for maximum length solutions for $c_0^* = -12, -10, -9, -7$ and -5 where $L > 2.9$. These are the solutions denoted with an 'o' in Figure 6.53.

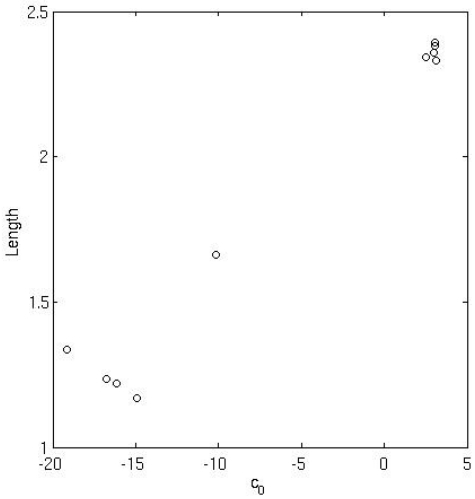

(a) Length against c_0.

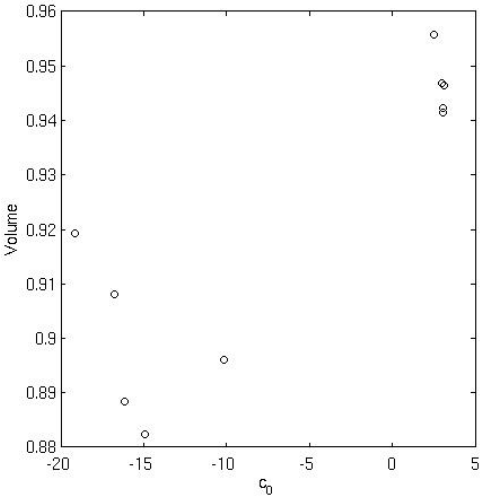

(b) Volume against c_0.

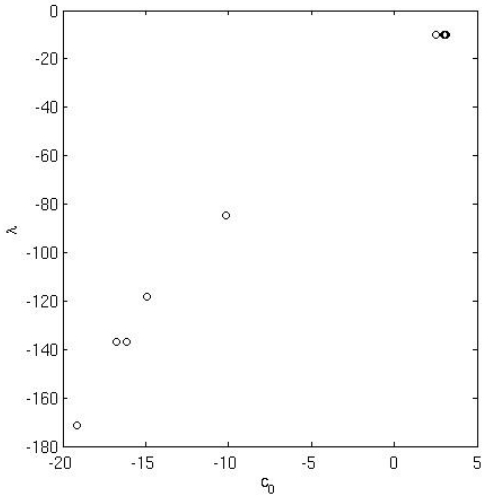

(c) λ against c_0.

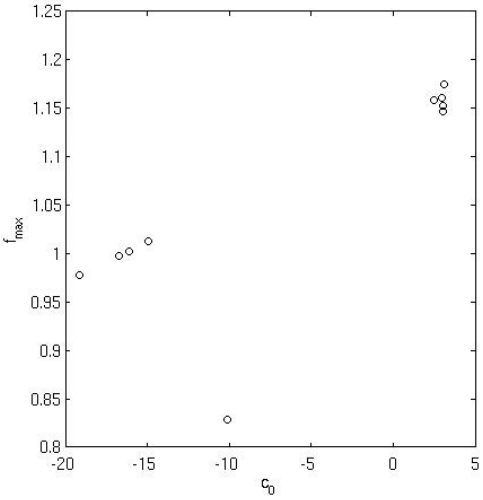

(d) f_{max} against c_0.

Figure 6.58: Summary of parameters relating to solutions where $f_0 = 0.01$. Two groups of solutions emerge where $L > 2$ or $L < 2$.

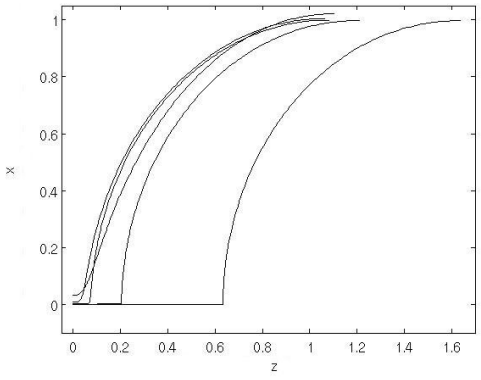

(a) x against z for $f_0 = 10^{-3} - 10^{-7}$.

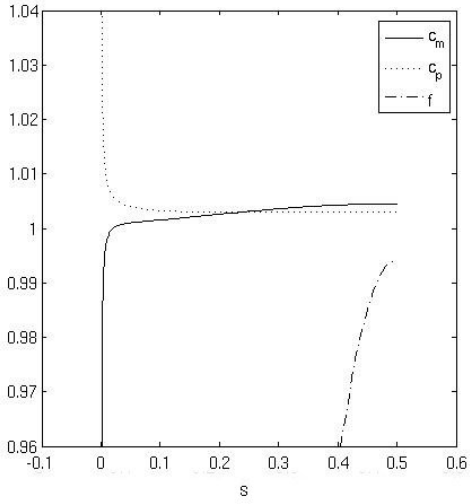

(b) Part of the numerical solution of c_m, c_p and f when $f_0 = 10^{-7}$.

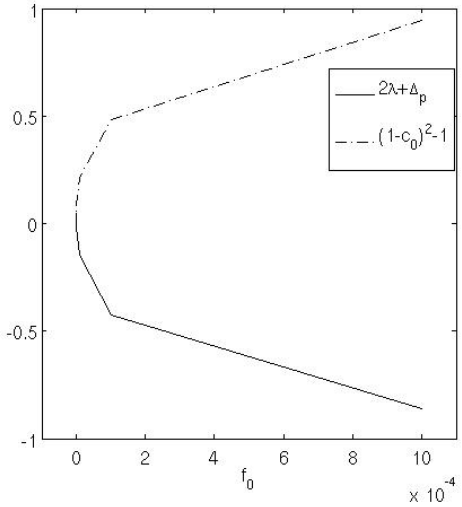

(c) Limit of $2\lambda+\Delta_p$ and $(1-c_0)^2-1$ as $f_0 \to 0$.

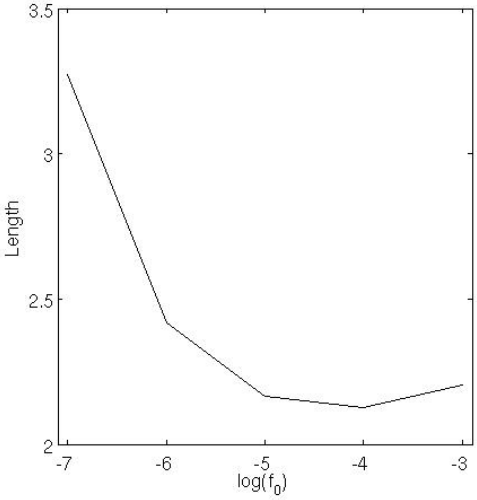

(d) Length against $\log(f_0)$.

Figure 6.59: Summary of parameters relating to solutions in Figure 6.58 where $f_0 = 0.01$.

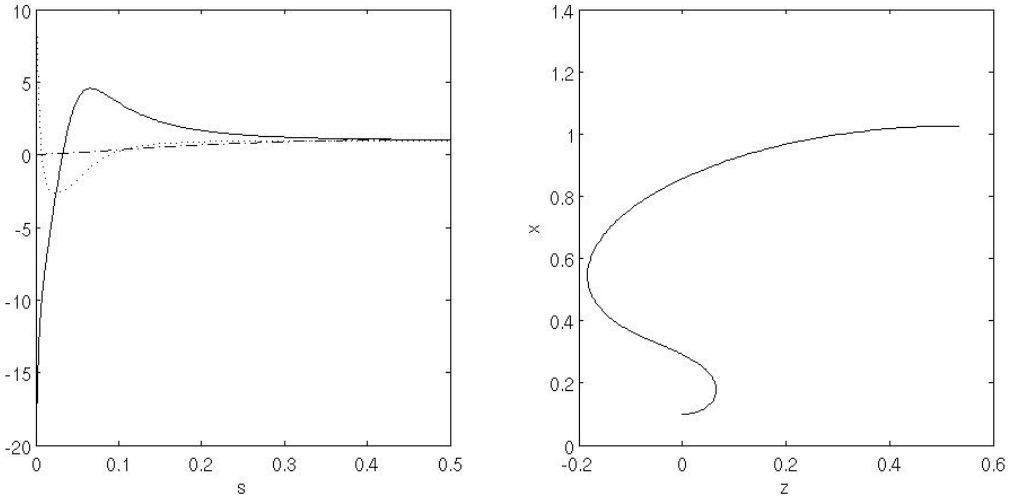

(a) c_m, c_p and f against s.

(b) x against z.

Figure 6.60: An example of a solution with $f_0 = 0.01$, $c_0 = -13.9$ and $L = 1.06$ which indicates that solutions when $f_0 = 0.01$ can be very different from those in Figure 6.59.

6.8 General Conclusions to Helfrich Energy Minimisation Problem

The results of the constant mean curvature droplet model in Chapter 4, summarised in Section 4.11, indicate that the limitation of the droplet model is that the only solutions available in the case that $x_{min} = 0$ are spherical solutions. Imposing boundary conditions which force cell engulfing fibre solutions away from this limit increase the numerical error associated with the integration to find the solutions.

Assuming that a cell engulfing a fibre is spherical does not correspond with any of the experimental results reviewed in Chapter 3. By including the Helfrich energy to the surface and volume free energies in the energy minimisation problem, a greater range of spheroid solutions are available for which $x_{min} = 0$. This allows for a greater range of cell on a fibre solutions.

The analysis contained in Sections 5.9-5.11 on polymer solutions and Section 5.13 on the Euler-Lagrange equations as a dynamical system provide the context required to understand the numerical solutions of the cell engulfing fibre solutions in Sections 6.4-6.7. Section 5.13 suggests that numerical solutions may either be dominated by c_m and c_p diverging as $f \to 0$ or by or by c_m and c_p undulating so that the solution is dominated by wave-like solutions. The wave-like behaviour is typical of a HBVP solution as c_m and c_p cannot diverge in order to meet the condition $c_m(0) = c_p(0)$. If $\lambda < 0$ then c_m and c_p should be wave-like, while when $\lambda > 0$ divergence of c_m and c_p as $f \to 0$ will be more dominant.

6.8.1 Review of Results

The HBVP solutions in Section 6.4 have a much larger range in spontaneous curvature, c_0, and curvature at $x = 0$, κ than those found in [25]. The analytical solutions to the Euler-Lagrange equations in Sections 5.9-5.11 were used to find initial estimates of the free parameters before using MATLAB optimisation tools to minimise the appropriate residual. The range in κ was extended by finding an alternative set of initial estimates, which were not found on perturbing away from the known spherical solutions. In [25] the range in spontaneous curvature is $-4 \lesssim c_0 \lesssim 1$, while in the current work the range in spontaneous curvature is $-12 \lesssim c_0 \lesssim 20$.

The five versions of cell on a fibre solutions introduced in this chapter are the zero momentum solutions in Section 6.5, cell engulfing fibre solutions and cell lengthening on fibre solutions in Section 6.6 and the zero contact angle solutions in Section 6.7. Cell on a fibre dumbell solutions are discussed in Section 6.6.5. The results show that the length, volume and Helfrich energy of all these solutions depend on spontaneous curvature c_0 and the radius of the fibre R, where $f(0) = f_0 = R^2$. The observations for each of the boundary conditions are different in each case.

The zero momentum solutions in Section 6.5 were investigated in two ways. In Section 6.5.2, solutions were found for which a HBVP solution was used as an initial estimate of the parameters. A zero momentum solution of the same volume was then found. Solutions of this

type were only found for very small values of f_0 but their length and Helfrich energy did not vary greatly from that of the corresponding HBVP solution.

In Section 6.5.3, zero momentum solutions were also investigated to find solutions of maximum possible length for a given value of f_0 and c_0. Solutions were only found when $|c_0| > 2$ and $f_0 < O(10^{-1})$. Here $\lambda > 0$ and the solutions were dominated by c_m and c_p diverging when $s \lesssim 0.1$ while $c_m \approx c_p \approx 1$ when $s \gtrsim 0.1$. Maxima in c_m due to c_0 dependent shear terms, as defined in Section 5.13, gave another degree of freedom which allowed the boundary conditions at the surface of the fibre to be met.

Cell engulfing fibre and cell lengthening on fibre solutions were investigated in Section 6.6. Cell engulfing fibre solutions fixed the contact angle of the membrane with the fibre to 90^o by fixing $c_p(0) = 0$. It was found that if $c_p(0)$ is fixed while the length of the solution is increased then solutions where $\lambda > 0$ will be found. However, when $c_p(0)$ is free then $\lambda < 0$ for the solutions found. These solutions could be extended further than those when $\lambda < 0$. For this reason, solutions where $c_p(0)$ is a free variable were investigated in Sections 6.6.3 and 6.6.4.

In Sections 6.6.3 and 6.6.4 cell lengthening on fibre solutions were found for a wide range of c_0 and f_0. The solutions of greatest length were found when $c_0 = -12$, when $L = 2.37$, as the spontaneous curvature term acts to reduce the frequency of the oscillations of the solutions as had been discussed in Section 5.13. When only the volume of a solution is restricted, the remaining restrictions on the length of a solution are due to the dynamics of the Euler-Lagrange equations. The value of c_0, in part, determines the dynamics of the Euler-Lagrange equations.

Cell lengthening on fibre solutions were found for which the Helfrich energy decreased smoothly as length was increased. This result suggests that the bending energy favours the phagocytosis of long fibres. For increasingly negative values of c_0 and increasing values of f_0, there is a point where maximum possible length of such solutions suddenly decreases. The attraction of the Euler-Lagrange equations to a point where $fc_p^2 = 1$ can limit their flexibility to meet set boundary conditions.

The longest zero momentum solutions were dominated by divergence in c_m and c_p while the longest cell lengthening solutions were dominated by wave-like behaviour. The results for the zero momentum and cell engulfing cell solutions in Sections 6.5 and 6.6 suggest that, when the values of $c_m(0)$ or $c_p(0)$ are fixed, wave-dominated solutions may be more difficult to find, so that the solutions found are dominated by divergence rather than wave-like behaviour.

The zero contact angle solutions of maximum length in Section 6.7 have a normalised length of ≈ 3, where length is the normalised length defined in (5.66), which is scaled by the square root of the surface area. The numerical solutions to c_m, c_p and f of all zero contact angle solutions whose length is approximately 3 are similar in terms of the placement of their two inflection points. The value of f_0 for these solutions can be adjusted by changing the spontaneous curvature. The zero contact angle solutions also indicate that a variety of zero contact angle solutions can be found when f_0 is small, $f_0 = 0.01$. However, if f_0 is an order of magnitude smaller than this, then only solutions with two inflection points and $L \approx 3$ can be found.

Finally, cell on a fibre dumbell solutions can be found. These solutions have the greatest

length of all the types of solutions as they use the parameters of prolate dumbells as initial estimates. In Section 6.6.5, solutions with lengths of up to 3.8 were found. However, imposing any kind of volume restriction or boundary condition on these solutions is difficult from a numerical point of view. These solutions were only found for very small values of f_0. If $c_0 = 3$ then the special case of a cell on a fibre solution which meets the zero momentum boundary condition can be found.

6.8.2 Role of c_0 and f_0 in Determining Length

It is not simple to compare the results of the different boundary conditions directly as the solutions have very different properties and can be used for different purposes. When zero momentum solutions are parameterised by volume in Section 6.5.2, the lengths of the zero momentum solutions did not differ greatly from the HBVP solutions of the same volume. However, all cell lengthening solutions in Section 6.6 have the same volume of 1. Implementing the zero momentum boundary condition does not itself greatly increase or decrease the length of a solution, compared to HBVP solutions of the same volume.

Solutions for a range of f_0 were found using zero momentum and cell lengthening boundary conditions in Sections 6.5.3 and 6.6. In Section 6.5.3 the length of the solutions was extended under the condition that the zero momentum boundary condition (6.34) was met. In Section 6.6, this condition was that volume was to remain constant. Length varies significantly with f_0 for zero momentum solutions where $c_0 < -1$ and $c_0 > 1.5$. However, the range in f_0 is very small.

The cell lengthening boundary condition test the flexibility of the Euler-Lagrange equations to find solutions of increasing length for fixed values of c_0 and f_0. Solutions of the zero momentum boundary conditions show how the zero momentum boundary condition limits this flexibility by imposing an extra condition at the boundary.

The maximum possible lengths of the cell lengthening and zero contact angle solutions can also be compared. For both these cases, for the maximum possible length solutions, f_0 and c_0 are inversely proportional. However, for the cell lengthening solutions, maximum possible length decreases with c_0, while for zero contact angle solutions there is a slight increase in length as c_0 increases.

c_0 plays a different role in determining length than in cell lengthening solutions than in zero contact angle solutions. In cell lengthening solutions, the increase in freqency of oscillation when $c_0 < 0$, as opposed to $c_0 > 0$, allows the solution to avoid tending towards a point where $fc_p^2 = 1$ at $s = 0$ so that the solution is longer. However, all zero contact angle solutions have the boundary condition $fc_p^2 = 1$ when $s = 0$ so longer solutions can be found when these oscillations are damped. For example, the zero contact angle solution of maximum length is found when $c_0 > 0$.

The boundary conditions which produced solutions of the greatest length were the zero contact angle solutions and zero momentum cell on a fibre dumbell solutions. The maximum possible length of the zero contact angle solutions is limited. As f_0 is decreased, length increases and the shape tends to that of a sphere will a sharp inflection on the fibre surface. There is a

limit to how sharp the inflection point can be allowed to be, and so which numerical solutions can be accepted as cell on a fibre solutions. A sharp inflection point as is effectively a neat crease in the membrane which is not expected in a lipid bilayer.

The zero momentum cell on a fibre solution is an example of a cell on a fibre solution for which has an additional singularity, as is found in a dumbell HBVP solution. The lengths of these dumbell solutions are limited only by the numerical difficulty of finding solutions of this type. The choice in f_0 is also limited, as longer solutions can only be found for very small f_0.

A cell on a fibre dumbell solution which met the zero momentum solution was found. This was the longest solution featured in the numerical results in this chapter where $L = 3.8$, $c_0 = 3$ and $L/R = 17$. This suggests that very long fibres may be phagocytised by disk-like cells which have a dip in radius at the mid-length. Increasing the number of singularities in the solution, and so finding a shape where there are a number of maxima in f, may be a way to find increasingly longer solutions to the cell on a fibre problem.

6.8.3 General Conclusion

The effect of two key prescribed parameters f_0, the radius of the fibre squared and c_0, the spontaneous curvature on the length of the resulting cell on a fibre solution depend on the boundary conditions used. The sign and magnitude of c_0 plays an important role in determining how a solution meets the required boundary conditions. Spontaneous curvature is a concept which accounts for the natural curvature of a cell membrane due to proteins within the cell membrane and the cytoskeleton just inside the cell membrane. If the spontaneous curvature is non-zero, then the cell membrane has a curvature when no force is applied. If a cell membrane has a spontaneous curvature where $|c_0| >> 1$, then the cell membrane could be described as stiff. Finding an experimental method of quantifying the spontaneous curvature of a cell membrane and validating it as a reasonable concept would be a very useful step in relating solutions in the current work to observations of macrophages engulfing a fibre.

In Sections 6.5 and 6.6 solutions of the longest length were found when $|c_0| >> 1$. In Section 6.7 the spontaneous curvature of solutions was adjusted in order to find cell on a fibre solutions with a given value of f_0. The longest solutions in this section were found when $c_0 \approx 3$. A dumbell cell on a fibre solution can only be found when $c_0 > 2.5$.

A macrophage must be able to somehow "know" how to adjust its spontaneous curvature in order to engulf a fibre of a given dimension successfully. If a macrophage has to significantly change its spontaneous curvature by re-arranging its cytoskeleton or activating or de-activating proteins within its membrane, then phagocytosis will require energy which is not accounted for in the Helfrich energy. In this way, spontaneous curvature provides insight to both the shape of a cell on a fibre solution, and also the energy required for a cell to acheive that shape.

In order for a cell to effectively phagocytose a fibre the membrane may be parallel to the fibre surface, a constraint investigated in the zero contact angle solutions. Also, a cell may not be able to rapidly change its volume, which is a constraint investigated in the cell lengthening on fibre solutions.

The question of how to account for the dynamics involved in phagocytosis can itself lead

to many different avenues of investigation. If length is to increase with time, then the Helfrich energy of solutions of increasing length would be an important property of the solutions. Phagocytosis may be the result of a solution reaching an energy minima.

It is not clear how the forces associated with the Helfrich energy variation problem are applicable when the edge of the membrane is in contact with the surface of the surface. Solutions where the surface forces dependent on curvature are set to zero may give a more realistic idea of how the shape of a cell adjusts as it phagocytoses a fibre.

The problem of modelling a cell phagocytosing a fibre by minimising the Helfrich energy can be tackled by a variety of approaches. Different constraints on a cell on a fibre solution result in solutions with very different properties in terms of length, volume, Helfrich energy and shape. The question to be answered is what feature of a cell on a fibre solution is most important to fix in the boundary conditions. The most appropriate cell on a fibre boundary conditions could then be chosen to reflect experimental observations. Comparing the images of fibres phagocytosed by macrophages in Section 3.4 to the results of this chapter, it appears likely that the zero contact angle spherical cap solutions in Section 6.7.2.2 best describe the profile of these macrophages.

Part III

Extensions

Chapter 7

Concluding Remarks

Section 7.1 of this chapter describes how mathematical models concerning different areas of biology and physics to those in Parts I and II can be applied to the question of nanotoxicology. Section 7.6 is a general conclusion which breifly summarises the work contained in the thesis.

7.1 Part III - Further Modelling Possibilities

In parts I and II, the possible mechanisms of nanoparticle toxicity investigated were oxidative stress and frustrated phagocytosis. Following a literature review, it is found that there is a another key mechanism which is due to the tendency of nanoparticles to form loosely bonded groups or agglomerates. The high surface to volume ratio of nanoparticles in general and the hydrophobicity of CNTs in particular means that they are likely to to aggregate.

Findings from [67] and [107] show that on inhalation SWCNTs are deposited into the alveolar region of the lungs. In [67] and [107] it is also suggested that how the SWCNTs are deposited depends on how well dispersed, or how aggregated, they are before inhalation. Samples of well dispersed nanotubes are quickly incorporated into the interstitium and the interstitial fluid. This was found to have the affect of increasing the thickness and collagen content of the alveolar wall. If the samples of SWCNTs were less well dispersed, the agglomerates deposited on the lung epithelium quickly formed granulomatous lesions. Granulomatous lesions are areas of especially fibrous material which serve to isolate potentially harmful contents of that area from nearby cells. In [67] it was reported that an unusual, and possibly unique, inflammatory response to SWCNT characterised by a brisk acute phase inflammatory response followed by an early onset of lung fibrosis.

Nanotubes are expected to become airborne during the manufacturing process. Filters are set up by HSL at the manufacturing plants to monitor their number. However, the filters do not measure the size of individual agglomerates but measure their cumulative concentration over a number of hours. If the average agglomerate size is a key indicator of how an individual agglomerate will interact with the lung on inhalation, then understanding what affects the size distribution of a sample of airborne nanotubes is important.

As there are no significant experimental results to suggest models, the challenge of this

thesis is to find frameworks for models which have a specific nanoparticle application but do not rely on a set of experimentally found parameters. In Chapter 2 this was done by using established mechanisms from literature reviews to assemble a model and then to investigate and categorise the results of this model. Chapters 4, 5 and 6 do this by introducing specific boundary conditions to find shapes of an appropriate geometry. In both these cases, sets of qualitatively different results were obtained which could help explain a range of behaviour that could potentially be observed experimentally.

There are several different modelling ideas relating to the agglomeration and dispersal of nanoparticles [75]. Looking at dispersed nanoparticles in air as an aerosol is an established way of looking at the nanoparticle problem [100]. Aerosol science examines how small solid particles distribute themselves in air. Aerosols of this type are commonly referred to as ultrafine aerosols. As particles become smaller, the most observable macroscopic consequence of Brownian motion is not diffusion but agglomeration. Agglomerated particles will form on a smaller timescale than they will diffuse over any significant distance. The rate of collision between particles increases as they get smaller. So aggregation is the most important mechanism, over diffusion and gravitational deposition, which effects the concentration of ultrafine aerosols.

7.2 Macroscale Models

The aggregation of ultrafine aerosols can be examined on many scales. The size distribution of a number of particles can be modelled using the mean field Smoluchowski and Becker-Döring equations, while the free energy of a single agglomerate can be evaluated using concepts from polymer physics.

The standard form of a system of Smoluchowski equations is as follows [125]. A cluster composed of r fundamental units has a time-dependent concentration of $c_r(t)$. For an aggregation only model the law of mass action suggests equations of the form

$$\frac{dc_r}{dt} = \frac{1}{2}\sum_{s=1}^{r-1} a_{s,r-s}c_s c_{r-s} - b_{s,r-s}c_r - \sum_{s=1}^{\infty} a_{r,s}c_r c_s - b_{r,s}c_{r+s}, \tag{7.1}$$

where $a_{r,s}$ are the aggregation rate coefficients while $b_{r,s}$ are the fragmentation rate coefficients. Note that the equation of the monomer concentration is

$$\frac{dc_1}{dt} = -\sum_{s=1}^{\infty} a_{1,s}c_1 c_s + b_{1,s}c_{s+1}. \tag{7.2}$$

The aggregation and fragmentation rates can be chosen to encapsulate the particular physical properties of the aerosol in question. The forward (aggregation) rate coefficients can be calculated by considering the particle flux and the probability of collision. This depends on the density, diameter and the Stokes-Einstein diffusion coefficient of the particles. The backward (fragmentation) rates correct for the forward rates, moving the population of aggregates back to a size distribution which minimises the free energy.

A comprehensive introduction to aerosol dynamics can be found in [38]. The mean free path of an ideal gas at ambient pressure is $\approx$ 68nm. Single nanoparticles will have a smaller

maximum dimension than the mean free path of gas (large Knudsen number). In the continuum limit, when there are a large number of particles, and at large Knudson number, the Smoluchowski collision frequency and the Stokes-Einstein diffusion coefficent are commonly used to find a typical collision frequency β_{ij}. Define β_{ij} as

$$\beta_{ij} = \frac{2kT}{3\mu} \underbrace{\left((1/v_i^{1/3}) + (1/v_j^{1/3})\right)}_{\text{Stokes-Einstein Diffusion Coefficient}} \times \underbrace{\left(v_i^{1/3} + v_j^{1/3}\right)}_{\text{Smoluchowski Collision Frequency}}, \quad (7.3)$$

where the diameter of a particle $d_0 \approx v^{1/3}$ and gas viscosity is μ. Van der Waals forces can be specifically included by using an effective diameter, d, rather than the actual diameter d_0 so that

$$d = \int_{d_0}^{\infty} \exp(\Psi(x)/kT)/x^2 dx, \quad (7.4)$$

where $\Psi(x)$ is the potential energy. The form of the Van der Waals potential is dependent on the shape and size of the agglomerate as well as the chemical properties of the material. An appropriate form for this potential can be found in books such as [61].

For a cluster with a large number of nanoparticles, it is useful to define a fractal number d such that

$$N_p = A\left(\frac{R}{a_{p0}}\right)^d, \quad (7.5)$$

where N_p is the number of particles in an aggregate and a_{p0} is the radius of a single unit particle. R is a statistically determined value of the radius of an aggregate with N_p particles. Knowing the fractal number allows the collision frequency to be adjusted, so that in the continuum regime for $N_p >> 1000$,

$$\beta_{ij} = \frac{2kT}{3\mu}\left(\frac{1}{v_i^{1/d}} + \frac{1}{v_j^{1/d}}\right)\left(v_i^{1/d} + v_j^{1/d}\right). \quad (7.6)$$

A variant of the Smoluchowski equations are the Becker-Döring equations where only likewise are allowed to aggregate to clusters and only monomers are allowed to deaggregate from clusters. This model assumes that only monomers are mobile enough to be affected by Brownian motion. This allows the system of ODEs to be written in the limit where r is a continous variable so that the concentration of particles of all sizes is a continuous variable $c(r,t)$. This reduces the system to a two-dimensional PDE. Analysis has shown [125] that the solution will approximate to the fundamental solution to a diffusion equation, the heat kernel. The size of the most frequently occuring aggregate will increase in size with time.

A wealth of knowledge can be used to construct a set of Smoluchoswki or Becker-Döring equations. However, without specific information available, it is difficult to find a way to make these equations specifically represent nanoparticle aerosols in a qualitative fashion. One way would be to extend the range in size of agglomerate which is allowed to aggregate and deaggregate to larger clusters in the Becker-Döring equations. This assumes that nanoparticles are small enough that the movement of small aggregates are dominated by Brownian motion.

However, as approximations are used to convert the Becker-Döring equations into a solvable PDE, this modification does not result in any qualitatively different behaviour.

If specific information is not available then concentrating on the free energy of a population of nanoparticles may be more worthwhile. In [32] it was shown that it was possible to specifically account for the entropy of mixing in a variant of Becker-Döring equations. The rate of fragmentation increased as the free energy relating to the entropy of mixing increased so that the rate of fragmentation acts to bring the mxiture back to equilibrium. The free energy of the entropy of mixing decreases as the concentration of different sized particles equalise. In general, it is difficult to incorporate specific free energies into a system of aggregation-fragmentation equations.

The free energy of a gas [82] can be given as

$$F(N,V,T) = N\mu_0(T) - kT\log Z(N,V,T), \tag{7.7}$$

where $\mu_0(T)$ is the chemical potential given only in terms of temperature while $Z(N,V,T)$ is the partition function. Using the common virial form of the partition function [46] results in the expansion

$$\log Z = N\left(1 + \log(V/N) + (1/2)\beta_1(N/V) + \sum_{2}^{\infty}(1/(n+1))\beta_n(N/V)^n\right), \tag{7.8}$$

which is the term for an ideal gas plus corrections for monomer particles proportional to β_1 and corrections accounting for interactions between n-particles proportional to β_n. In an ideal gas there are no interactions between the ideal point particles or particles and the gas. If forces between particles are attractive then the free energy will decrease from that of an ideal gas, while if forces between particles are negative then the free energy will increase. The strength of interaction depends both on the Van der Waal forces between particles and also their geometry and orientation. The specific interaction between cylinders was derived in [82]. Though nanoparticles are not stiff cylinders, these concepts can be applicable to quantify their ensemble free energy.

7.3 Models of Adsorption of Polymers onto a Surface

The question of how polymers are absorbed onto a curved surface is relevant to the question of how nanoparticles form a protein corona around proteins. This question is discussed in [59] and related papers. A protein which has been found to remain attached to nanoparticles over a long period of time is the apoliprotein A-1. The function of this protein is to wrap around and so transport cholesterol [37]. Like many spherical nanoparticles, cholesterol is hydrophobic and its diameter is at the order of nanometres.

If nanoparticles with a high aspect ratio are treated as polymers, then their absorption onto a spherical particle can be examined using the polymer brush model which is discussed in [68]. The polymers are attached to the particle at one end and the average height from the particle surface can be found by considering the energy balance between configurational

entropy and repulsion between over-lapping chains. If polymers are stretched, then repulsion will be at a minimum while the free energy contribution from entropy will be at a maximum.

It may be more appropriate to build a model from first principles using concepts from polymer physics rather than try to apply an existing model which does not capture the specific problem at hand. The conformation of polymers confined to a surface can be examined using self consistent field theory, a good introduction to which can be found in [22]. For small spatial variations and for a inhomogeneous potential, it is demonstrated that the statistical weight for a polymer to proceed from a point $\mathbf{r}'$ to $\mathbf{r}$ in N steps is given by the solution of the following Schrödinger like equation

$$-\frac{\partial G}{\partial N} = -(a^2/6)\nabla^2 G + [U(r)/T]\, G. \tag{7.9}$$

where $\partial G/\partial N$ is rate of change of the path of a polymer chain with N, the number of steps. If $\partial G \partial N = 0$ then the polymer is straight at that point. $U(r)$ is the energy potential experienced by the polymer. Full details can be found in [22].

The geometry in which this equation is solved and the form of the potential can be freely chosen. Adsorption onto a surface can be accounted for by the choice of boundary conditions. In [86] this equation was used to find the adsorption energy at which it was energetically favourable for a polymer to attach itself onto the surface of a colloidal particle. In [110] this problem was extended by allowing the polymers to have a finite length so that the chain ends were given a separate density. The normalised density was found as an expansion in $1/R$, where $1/R$ is the curvature of the curved surface. The Helfrich bending rigidity, Gaussian rigidity and spontaneous curvature of the adsorbed layer of polymers were found in terms of this density and also the excluded volume, bulk polymer density, adsorption energy and temperature. It was found that longer chains has less effect on the curvature parameters than shorter polymers but longer polymers allowed the density of absorbed polymers to increase. There is potential to extend this model in order to investigate the these results in the limit of large R to reflect the absorption of chain-like proteins onto spherical nanoparticles. In this way, the work in [86] and [110] can be developed into further problems which can be solved analytically.

There is also scope for more numerical work. In [111], self consistent theory was used to study phase transitions of semi-flexible polymers. Much like helical proteins, semi-flexible polymers can bend but there is an energetic cost involved. The study in [33] looked at the adsorption of polymers onto spherical and rod-like particles where all calculations were done fully in spherical and cylindrical coordinates. The two elements in [111] and [33] can be combined to answer the question of how semi-flexible proteins absorb onto nanoparticles. These concepts may also be useful to answer the question of how semi-flexible nanoparticles absorb onto highly curved surfaces such as alveoli in the lung. The resultant bending stiffness is likely to determine how the nanoparticles alter the function of that area of the lung.

In [52] the question was investigated in a Monte Carlo simulation. If a semi-flexible polymer is absorbed onto a curved surface then there is a minimum energy penalty as the polymer cannot lie flat on the surface. The curved surface also restricts the configurational entropy of the polymer so that the free energy is dominated by the bending energy.

7.4 Free Energy of an Individual Agglomerate

In order to calculate the fragmentation probability of a single aggregate using, for example, Weibull statistics, the bond strength between nanoparticles must be known. As [101] notes, this is still an unsolved task. For a given bending rigidity and surface energy the volume of the aggregate can be found by minimising the free energy. The surface energy contribution will decrease for a smaller surface area, while the bending energy contribution will tend to increase for a smaller volume. A mean interaction energy between nanoparticles can also be included.

Taking $\beta = 1/kT$, the ensemble average of the free energy can be given generally as

$$< E >= \frac{\sum_s E_s \mathrm{e}^{-\beta E_s}}{\sum_s \mathrm{e}^{-\beta E_s}} = -\frac{\partial Z}{\partial \beta}, \tag{7.10}$$

where $\sum_s$ indicates a summation over states.

The form of the partition function given in [111] for semi-flexible polymers in 1 dimension is potentially very useful. The angle-dependent excluded-volume interaction between two segments of length Ldt and Ldt' and orientations $\mathbf{u}$ and $\mathbf{u}'$, respectively, is given by $v(\mathbf{u}, \mathbf{u}')dtdt'$, where $v(\mathbf{u}, \mathbf{u}') = 2DL^2|\mathbf{u} \times \mathbf{u}'|$. This refers back to results from [82] for liquid crystals. The partition function for a number density of polymers $\rho = n/V$ is of the form

$$Z = \frac{1}{n!} \prod_{i=1}^{n} \int D\{\mathbf{r}_i, \mathbf{u}_i\} P\{\mathbf{r}_i, \mathbf{u}_i[0,1]\} \exp\left(-\rho G \int d\mathbf{r} \int d\mathbf{u} \int d\mathbf{u}' \psi(\mathbf{r}, \mathbf{u}) \psi(\mathbf{r}, \mathbf{u}') |\mathbf{u} \times \mathbf{u}'|\right). \tag{7.11}$$

The probability density takes into account the semi-flexible property of the polymer

$$P\{\mathbf{r}_i, \mathbf{u}_i[0.1]\} \propto \exp\left[-\frac{1}{2N} \int_0^1 dt \kappa(t) \left(\left|\frac{d\mathbf{u}_i(t)}{dt}\right|^2\right)\right], \tag{7.12}$$

where

$$\mathbf{u}_i(t) = \frac{1}{Na} \frac{d}{dt} \mathbf{r}_i(t) \tag{7.13}$$

and $\kappa(t)$ acts as a bending constant. Full details of the coupled self-consistent field theory equations can be found in [111] where a mean field interaction had also been included. The numerical solutions of the resulting diffusion equations were found as expansions of the spherical harmonic functions.

Solutions in two or three spatial dimensions are yet to be found. A surface term could also be included which, for a spherical agglomerate, would depend on volume only. In [111], the volume of the system and the number of polymers n is fixed per calculation, however, the variation of free energy with n or V could be explored to see how the energy of an agglomerate of CNTs is minimised for a given number of polymers by varying volume. This information would be very useful in the building of aggregation/fragmentation models.

7.5 Summary

The ideas in the preceeding sections offer substantial new avenues in developing mathematical models which are qualitatively, as well as quantitatively, specific to the toxicity of

nanoparticles. These models do not rely on external data in order to be relevant to this question.

Section 7.3 suggests ways to investigate how nanoparticles adsorb onto curved surfaces such as the inside of alveoli and how common proteins adsorb onto nanoparticles. Section 7.4 outlines a way in which to investigate the free energy of an individual aggregate. However, it may be useful to follow the lead of research groups which have initially used a moleculer dynamics approach to uncover specific interactions and behaviour which may then be suitable for further mathematical modelling.

7.6 General Conclusion

The work in this thesis is a first attempt at identifying topics in nanotoxicology suitable for mathematical modelling. The choice of models used is informed by information on specific mechanisms associated with nanotoxicology. In Part I, the mechanism under consideration was the oxidative stress induced by nanoparticles. The model which was developed focused on the TNF-α activated apoptosis pathway and the role of NF-κ B and AP-1 in controlling the timing and extent of DNA fragmentation. In this model different pairs of inhibitors can be switched on or off to produce qualitatively different results in terms of the extent to which and speed at which DNA fragments. The activation of the pathways in the model can be referred to as transient or persistent. Section 2.5 suggests extends to this model to include an oxidative stress sensitive fibrotic response which will also be very relevant to the problem of nanotoxicity.

The mechanism under consideration under consideration in Part II was frustrated phagocytosis. Simple models of phagocytosis were constructed by minimising a given free energy of a shape in axisymmetric geometry. An axisymmetric shape is assumed to approximate the shape of a maxrophage as it phagocytoses a fibre. In Chapter 4, the free energy contains surface and volume terms only, while in Chapter 6 the Helfrich bending energy was also included. The length of solution depends strongly on the spontaneous curvature, c_0. The process by which a cell membrane attains a given spontaneous curvature can be assumed to be energy intensive. Information of the free energy associated with a given solution in terms of surface, volume and Helfrich energies also the spontaneous curvature should indicate the difficulty of a macrophage engulfing a fibre for a given radius and length. The validity of the results in Part II may be tested by comparing them with results from further experimental work.

Section 7.1 suggests ways in which polymer science can be used to assign a free energy of aggregation for airborne nanoparticles, or to understand how protein coronas form around nanoparticles. Self-consistent mean field theory is used as a basis for these models, then extensive numerical work may yield relationships between free energy, number of nanoparticles, volume and contact energy. These relationships will be useful to guide the choice of parameters when constructing models where nanoparticles are inhaled or ingested.

The nature of the work in this thesis is very experimental and wide-ranging. This is a first attempt at capturing the toxicity of nanoparticles in a numerical way and attempts to identify what might be of particular interest. Whether the approaches introduced here are valid will

become clearer once the experimental results relating to the toxicity of nanoparticles becomes more quantifiable.

Appendix A

MAPK Self Activation

The MAPK activation part of the pro-apoptotic pathway can be reduced to an independent self-activating system. The three tiers of MAPK proteins is here reduced to just one, JNK which activates c-Jun which then forms a dimer with c-Fos. The activation terms in (A.1) and (A.2) follow those in [43] and are discussed in Section A.1. It is assumed that the rate-limiting step to form AP-1 is the availability of c-Jun rather than c-Fos so that c-Fos is not included as a separate variable. The activation of AP-1 then stimulates the production of ROS which act as messengers to activate JNK. The concentration of ROS is reduced by the presence of anti-oxidants. When the level of anti-oxidants in the cell is high this can be modelled as self-inhibition so that not separate variable for anti-oxidant concentration is included. The reduced MAPK self-activating system can be given as

$$\begin{aligned} \dot{y_1} &= k_1 y_4(1 - y_1/C_1) - k_3 y_1, && \text{(A.1)} \\ \dot{y_2} &= k_2 y_1(1 - y_2/C_2) - k_2 y_2 - k_3 y_1, && \text{(A.2)} \\ \dot{y_3} &= k_2 y_2 - k_2 y_3, && \text{(A.3)} \\ \dot{y_4} &= k_2 y_3 - y_4 - k_1 y_4(1 - y_1/C_1). && \text{(A.4)} \end{aligned}$$

Variables represent the concentration of the following proteins:

$y_1(t)$	activated JNK MAPK protein,
$y_2(t)$	c-Jun protein,
$y_3(t)$	AP-1 transcription factor which is a dimer of c-Jun and c-Fos,
$y_4(t)$	reactive oxidative species (ROS),

and the constants in (A.1)-(A.3) are defined by

k_1	ROS-associated constant,	
k_2	General activation constant,	
k_3	General deactivation constant.	(A.5)

A.1 Activation of JNK and c-Jun

The signal is mediated by the phosphorylation of the MAPKs where each phosphorylated tier can then phosphorylate the next tier. If the unphosphorylated kinase is written as $\tilde{a}_i$ and an unphosphorylated kinase is written as a_i then from [43] the rate of change of concentration of a phosphorylated kinase can be written as

$$\dot{a_i} = \tilde{\alpha}_i a_{i-1} \tilde{a_i} - \beta_i a_i. \tag{A.6}$$

It is assumed that there is some rate β_i of spontaneous dephosphorylation and the reaction constant of the phosphorylation is $\tilde{\alpha}_i$. If it is assumed that the total concentration of the kinase is constant so $C_i = \tilde{a}_i + a_i$ there is no need for a separate variable for the de-phosphorylated kinase. If $\alpha_i = \tilde{\alpha}_i C_i$ then the above equation can be written as

$$\dot{a_i} = \alpha_i a_{i-1} \left(1 - a_i/C_i\right) - \beta_i a_i. \tag{A.7}$$

ROS are highly unstable [91] so k_1 is chosen to be asymototically larger than the general activation rate constant, while in the presence of ROS the phosphatases are mostly de-activated so they can be taken to be asymptotically smaller than the general activation rate.

The non-dimensionalised variables are then

$$\frac{k_2}{k_1} = \epsilon \qquad \frac{k_3}{k_1} = \epsilon^2 \qquad \tilde{y_i} = \frac{y_i}{C_i} \qquad \tilde{t} = \frac{t}{k_1}, \tag{A.8}$$

where $\epsilon << 1$. Note that the dimensions of k_1 and k_2 are the same as $1 - y_i/C_i$ is a dimensionless term. The resulting equation can be simplified by setting $1 = C_1 = C_2 = C_3 = C_4$.

The normalised system of ODEs is

$$\begin{aligned}
\dot{y_1} &= y_4(1 - y_1) - k_3 y_1, && \text{(A.9)}\\
\dot{y_2} &= \epsilon y_1(1 - y_2) - \epsilon y_2 - \epsilon^2 y_1, && \text{(A.10)}\\
\dot{y_3} &= \epsilon y_2 - \epsilon y_3, && \text{(A.11)}\\
\dot{y_4} &= \epsilon y_3 - y_4 - y_4(1 - y_1). && \text{(A.12)}
\end{aligned}$$

This system of ODEs will be solved by using the asymptotic expansion

$$\begin{aligned}
y_1 &= y_{10} + \epsilon y_{11} + \epsilon^2 y_{12} + \epsilon^3 y_{13} + \cdots, && \text{(A.13)}\\
y_2 &= y_{20} + \epsilon y_{21} + \epsilon^2 y_{22} + \epsilon^3 y_{23} + \cdots, && \text{(A.14)}\\
y_3 &= y_{30} + \epsilon y_{31} + \epsilon^2 y_{32} + \epsilon^3 y_{33} + \cdots, && \text{(A.15)}\\
y_4 &= y_{40} + \epsilon y_{41} + \epsilon^2 y_{42} + \epsilon^3 y_{43} + \cdots. && \text{(A.16)}
\end{aligned}$$

The non-zero steady state of the non-dimensionalised model is

$$y_1 = 1, \qquad y_2 = \frac{1}{2}, \qquad y_3 = \frac{1}{2} \quad \text{and} \quad y_4 = \epsilon\frac{1}{2}. \tag{A.17}$$

The dynamics associated with this model can be used to investigate the difference in the activation of the MAPK pathway in the case of top-down activation via TNF-α compared to bottom-up activation via increased ROS concentration. The limiting case of top-down activation is when $y_1(0) = 1$ and the JNK MAPK is initially maximally activated. When $y_1(0) = 1$, then y_1 decouples from y_4 and (A.1) is a linear equation in y_1 allowing the exact linear solution (A.22)-(A.23) to be found. This is given in Section A.2.

When $y_1(0) \neq 1$ the y_1 and y_4 do not decouple and exact analytical solutions are not found. However, by considering y_1, y_2, y_3 and y_4 as asymptotic expansions, approximate solutions (A.73)-(A.74) in Section A.3 have been found which capture the dynamics of the numerical solutions as they reach steady state.

It was found that when $y_1(0) = 1$ solutions reached their steady state in the limit that $\exp(-\epsilon t) \to 0$ while when $y_1(0) = 1$ solutions reached their steady state in the limit that $\exp(-\epsilon t/4) \to 0$. As demonstrated by comparing the x-axes in Figure A.1, bottom-up activation is slower than top-down activation. The fit of these approximate solutions to the numerical solutions can be improved by addition of correction terms. Examples of results can be found in Section A.5.

This model supports the hypothesis in [58] that, using the standard form of MAPK activation, the activation of the MAPK cascade via TNF-α is faster than that of activation via ROS. However, this model does not support the hypothesis that the speed of activation of the MAPK pathway is not sensitive to the initial concentration of ROS. The leading order solutions to the model in this case show that, to leading order, the term responsible for the activation of the components of the MAPK pathway is linearly independent from the initial concentration of ROS.

In order for the model to be sensitive to the initial concentration of ROS, the pool of anti-oxidants must be finite and the rate of anti-oxidant actions must be fast enough to inhibit the activation of the MAPK pathway. Once this pool of anti-oxidants is depleted then the MAPK pathway is allowed to activate.

A.2 Leading Order Solutions $y_1 \equiv 1$ and $k_3 = 0$

If the initial conditions of this self activating system are

$$y_1(0) = 1, \qquad y_2(0) = A, \qquad y_3(0) = B, \quad \text{and} \quad y_4(0) = C. \tag{A.18}$$

In this case, solutions can be found without using asymptotic expansions. Setting $y_1 \equiv 1$ allows y_2 to be only dependent on itself, so that for an initial condition $y_2(0) = A$, y_2 can be solved for using an integration factor to give

$$y_2 = \frac{1}{2}\left(1 - \exp(-2\epsilon t)\right) + A\exp(-2\epsilon t). \tag{A.19}$$

The solution to (A.11) can then be found to be

$$y_3 = \frac{1}{2} + (\frac{1}{2} - A)\exp(-2\epsilon t) + D\exp(-\epsilon t). \tag{A.20}$$

Constants can be chosen to solve for $y_3(0) = B$ so $D = B - ((1/2) - A) - 1/2 = B + A - 1$. Then the solution to (A.4) is

$$y_4 = \frac{\epsilon}{2} + \frac{\epsilon \exp(-2\epsilon t)}{(1-2\epsilon)}(\frac{1}{2} - A) + \frac{\epsilon C \exp(-\epsilon t)}{1-\epsilon} + E\exp(-t), \tag{A.21}$$

choosing E so that $y_4(0) = C$.

The full set of solutions is therefore

$$\begin{aligned} y_1 &\equiv 1, && \text{(A.22)} \\ y_2 &= 1/2(1-\exp(-2\epsilon t)) + A\exp(-2\epsilon t), \\ y_3 &= \frac{1}{2}(\exp(-2\epsilon t) - \exp(-\epsilon t)) + \frac{1}{2}(1-\exp(-\epsilon t)) \\ &+ B\exp(-\epsilon t), \\ y_4 &= \epsilon\frac{1}{2}(\exp(-2\epsilon t) - \exp(-\epsilon t)) + \frac{\epsilon}{2}(1-\exp(-\epsilon t)) \\ &+ \epsilon B\exp(-\epsilon t) + (C - \epsilon B)\exp(-t), && \text{(A.23)} \end{aligned}$$

where analytical solutions agree closely with the numerical solutions in Figure A.1(a). Notice how the initial conditions are generally proportional to $\exp(-\alpha t)$, for some α, while the steady state solutions are proportional to $(1 - \exp(-\alpha t))$.

A.3 Leading Order Solutions $y_1(0) \not\equiv 1$ and $k_3 = 0$

For the case where y_1 and y_2 are coupled ($y_1 \neq 1$) solutions can be found in the form of asymptotic expansions using iterative integration. In this case the initial conditions for y_2 and y_3 are again given as $y_2(0) = A$ and $y_3(0) = B$. C and E are constants of integration which can be chosen to fit initial conditions, $y_4(0)$ and $y_1(0)$.

In terms of the asymptotic expansion, if $y_{10} = 0$, then the leading order equations to be solved are:

$$\begin{aligned} \dot{y}_{11} &= y_{40}, && \text{(A.24)} \\ \dot{y}_{12} &= y_{41} - y_{40}y_{11}, && \text{(A.25)} \\ \dot{y}_{13} &= y_{42} - y_{40}y_{12} - y_{41}y_{11}, && \text{(A.26)} \\ \dot{y}_{14} &= y_{43} - y_{40}y_{13} - y_{41}y_{12} - y_{42}y_{11}, && \text{(A.27)} \end{aligned}$$

$$\begin{aligned} \dot{y}_{40} &= -2y_{40} + y_{30}, && \text{(A.28)} \\ \dot{y}_{41} &= -2y_{41} + y_{40}y_{11} + y_{31}, && \text{(A.29)} \\ \dot{y}_{42} &= -2y_{42} + y_{40}y_{12} + y_{41}y_{11} + y_{32}, && \text{(A.30)} \\ \dot{y}_{43} &= -2y_{43} + y_{40}y_{13} + y_{41}y_{12} + y_{42}y_{11} + y_{33}, && \text{(A.31)} \end{aligned}$$

$$\begin{aligned}
\dot{y}_{21} &= -y_{20}, && \text{(A.32)}\\
\dot{y}_{22} &= -y_{21} + y_{11}(1 - y_{20}), && \text{(A.33)}\\
\dot{y}_{23} &= -y_{22} + y_{12}(1 - y_{20}) - y_{11}y_{21}, && \text{(A.34)}\\
\dot{y}_{24} &= -y_{23} + y_{13}(1 - y_{20}) - y_{12}y_{21} - y_{11}y_{22}, && \text{(A.35)}
\end{aligned}$$

and

$$\begin{aligned}
\dot{y}_{31} &= y_{20} - y_{30}, && \text{(A.36)}\\
\dot{y}_{32} &= y_{21} - y_{31}, && \text{(A.37)}\\
\dot{y}_{33} &= y_{22} - y_{32}, && \text{(A.38)}\\
\dot{y}_{34} &= y_{23} - y_{33}. && \text{(A.39)}
\end{aligned}$$

By simple integration, the leading order terms for y_4 and y_1 for are then

$$\begin{aligned}
y_{40} &= \frac{B}{2} + Ce^{-2t},\\
y_{11} &= \frac{Bt}{2} - \frac{C}{2}e^{-2t} + E. && \text{(A.40)}
\end{aligned}$$

C and E are chosen to fit the initial conditions for y_1 and y_4. In order for the asymptotic solutions to fully meet the initial conditions for every order ϵ constants would have to be introduced in each term of the expansion. In order to simplify this, we see that the initial conditions only need to be fulfilled to leading order and so no further constants are to be introduced.

The solutions for the terms in y_1 and y_4 are closely related. Firstly, look in detail at the differential equation for and solution to y_{41}:

$$\begin{aligned}
\dot{y}_{41} &+ 2y_{41} = y_{40}y_{11} + y_{31},\\
y_{41} &= \int (y_{40}y_{11} + y_{31})\, e^{2t}dt\; e^{-2t}.
\end{aligned} \qquad \text{(A.41)}$$

Recall that this form of equation yields solutions of the form

$$\int f(t)e^{2t}dt\; e^{-2t} = \frac{1}{2}f(t) - \frac{1}{4}\frac{df(t)}{dt} + \frac{1}{8}\frac{d^2f(t)}{dt^2} - \cdots . \qquad \text{(A.42)}$$

As y_{40} has an exponential decay term, y_{41} will also have polynomial terms multiplied by exponential decay terms. Taking $y_{31} = (A - B)t$, the full solution for y_{41} can then be found to be

$$\begin{aligned}
y_{41} &= (A - B)(\frac{1}{2}t - \frac{1}{2^2}) + \frac{1}{2^3}B^2t - \frac{1}{2^4}B^2 + \frac{1}{2^2}BE,\\
&+ e^{-2t}\left(\frac{1}{4}BCt^2 - \frac{1}{4}BCt + ECt\right) + e^{-4t}\frac{1}{4}C^2. && \text{(A.43)}
\end{aligned}$$

The exponential decay terms will decrease to zero in a few seconds and so are not significant at long timescales. In this case

$$\begin{aligned} y_{40} &\approx B/2, \\ y_{11} &\approx (Bt)/2, \\ y_{41} &\approx (B^2t)/2^3. \end{aligned} \tag{A.44}$$

The find the next order term for y_1, y_{12}, the terms not dependent on y_{30} are

$$\begin{aligned} \dot{y}_{12} &= y_{41} - y_{40}y_{11}, \\ \dot{y}_{12} &= (B^2t/2^2)(\frac{1}{2} - 1), \\ y_{12} &= -\frac{1}{2^3}(1/2)B^2t^2. \end{aligned} \tag{A.45}$$

The factor 1/2 from the polynomial integration has been kept separate from the factor of 1/2 found from the difference between the two terms in $\dot{y}_{12}$. y_{12} is effectively found by integrating y_{11} and multiplying the result by 1/4. Following this example, crunching the numbers for the highest orders of t for the next few terms in y_1 gives

$$\begin{aligned} y_{13} &= -\frac{1}{2^5}(1/3)B^3t^3(1 - 1/2), \\ y_{14} &= -\frac{1}{2^7}(1/4)B^4t^4(1/6 - 1/3), \\ y_{15} &= -\frac{1}{2^9}(1/5)B^5t^5(-1/24 + 1/12 + 1/4). \end{aligned} \tag{A.46}$$

For y_4

$$\begin{aligned} y_{42} &= -\frac{1}{2^5}B^3t^2(1 - 1/2), \\ y_{43} &= -\frac{1}{2^7}B^4t^3(1/6 - 1/3), \\ y_{44} &= -\frac{1}{2^9}B^5t^4(-1/24 + 1/12 + 1/4). \end{aligned} \tag{A.47}$$

The expansion terms of y_1 can be put back together to find

$$\begin{aligned} y_1 &= \frac{1}{2}(\epsilon tB) - \frac{1}{2^3}(\epsilon tB)^2/2 + \frac{1}{2^5}(\epsilon tB)^3/6 - \frac{1}{2^7}(\epsilon tB)^4/24 + \frac{1}{2^9}(\epsilon tB)^5/120 \\ &- \frac{1}{2^5}(\epsilon tB)^3/3 + \frac{1}{2^7}(\epsilon tB)^4/12 - \frac{1}{2^7}(\epsilon tB)^5/60, \\ &= 2\left(\frac{1}{2^2}(\epsilon tB) - \frac{1}{2^4}(\epsilon tB)^2/2 + \frac{1}{2^6}(\epsilon tB)^3/6 - \frac{1}{2^8}(\epsilon tB)^4/24 + \frac{1}{2^10}(\epsilon tB)^5/120\right) \\ &+ \left(-\frac{1}{2^5}(\epsilon tB)^3/3 + \frac{1}{2^7}(\epsilon tB)^4/12 - \frac{1}{2^7}(\epsilon tB)^5/60\right) \\ &\approx 2(1 - \exp(-\epsilon tB/4)) + (\exp(-\epsilon tB/4) - 1). \end{aligned} \tag{A.48}$$

This solution fits the steady state conditions.
For y_4 we have

$$
\begin{aligned}
y_4 &= \epsilon\frac{1}{2}B\left(1+\frac{1}{2^2}(B\epsilon t)-\frac{1}{2^4}(B\epsilon t)^2/2+\frac{1}{2^6}(B\epsilon t)^3/6-\frac{1}{2^8}(B\epsilon t)^4/24\right)\\
&+ \epsilon\frac{1}{2}B\left(\frac{1}{2^4}(B\epsilon t)^2+\frac{1}{2^6}(B\epsilon t)^3/3-\frac{1}{2^8}(B\epsilon t)^4/12\right),\\
&\approx \epsilon\frac{1}{2}B(2-\exp(-\epsilon tB/4))+\frac{1}{4}B(\exp(-\epsilon tB/4)-1). \qquad \text{(A.49)}
\end{aligned}
$$

The steady state condition is not quite fulfilled as the solution when $t \to \infty$ depends on B. However, a term of this kind should capture the dynamics of y_4 as it reaches the steady state so that

$$
y_4 \approx \frac{\epsilon}{2}\left(1-\exp(-\epsilon t/4)\right). \qquad \text{(A.50)}
$$

The important outcome of this method is to establish that the solution will reach steady state on a timescale of $O(\epsilon t/4)$, as shown in Figure A.1. The factor of $1/4$ arises from a factor of $1/2$ in the integration of y_4 and another factor of $1/2$ arising from the difference between y_{4i} and $y_{4(i-1)}y_{1i}$ which originates in the leading order terms. Finding this factor correctly is the key step in finding the correct leading order solution when $y_1(0) \not\equiv 1$.

Using the approach discussed above in the case that $y_{11} = E$ the method above results in the terms

$$
\begin{aligned}
y_{11} &= E,\\
y_{12} &= -\frac{1}{2^2}BEt-\frac{1}{2^4}B^2t,\\
y_{13} &= -\frac{1}{2^4}B^2Et^2-\frac{1}{2^6}(3/2)B^3t^2,\\
y_{14} &= \frac{1}{2^6}(1/3)B^3Et^3+\frac{1}{2^8}B^4t^3 \qquad \text{(A.51)}
\end{aligned}
$$

and

$$
\begin{aligned}
y_{41} &= \frac{1}{2^2}BE-\frac{1}{2^4}B^2,\\
y_{42} &= \frac{1}{2^4}B^2Et-\frac{1}{2^6}B^33t,\\
y_{43} &= -\frac{1}{2^6}(1/2)B^3Et^2-\frac{1}{2^8}2B^4t^2. \qquad \text{(A.52)}
\end{aligned}
$$

Gathering terms for y_1 gives

$$
\begin{aligned}
y_1 &= \epsilon E\left(1-\frac{1}{2^2}(BT)-\frac{1}{2^4}(BT)^2/2+\frac{1}{2^6}(BT)^3/6\right),\\
&+ \epsilon\frac{1}{4}B\left(-\frac{1}{2^2}(BT)+\frac{1}{2^4}3(BT)^2/2+\frac{1}{2^6}(BT)^3\right),\\
&\approx \epsilon\left(E\exp(-\epsilon tB/4)-\frac{1}{4}B\exp(-\epsilon tB/4)\right). \qquad \text{(A.53)}
\end{aligned}
$$

Together with the $-(1/2)Ce^{-2t}$ term in y_{11}, the term proportional to E fulfills the initial condition to first order for y_1 to order ϵ^2. The other term suggests some kind of correction to

the leading order solution found previously. Its contribution to the initial condition could be set to zero with the introduction of another constant.

For y_4 we have

$$y_4 = \epsilon^2 \left(-\frac{1}{4} BE \exp(-\epsilon t B/4) + \frac{1}{8} 3B^2 \exp(-\epsilon t B/4) \right). \tag{A.54}$$

The method works less well here. However, it is clear that the timescale over which the solution will reach steady state is still $O(\epsilon t/4)$.

Now to find solution to y_2 as it approaches steady state. The known solution to y_1 can be used to write

$$\begin{aligned}
y_{20} &= A, \\
y_{21} &= -\int A, \\
y_{22} &= \int\int A + \int y_{11}(1-A), \\
y_{23} &= -\int\int\int A - \int\int y_{11}(1-A) + \int y_{12}(1-A) + \int y_{11} \int A, \\
y_{24} &= \int\int\int\int A + \int\int\int y_{11}(1-A) - \int\int y_{12}(1-A) - \int\int y_{11} \int A \\
&+ \int y_{13}(1-A) + \int y_{12} \int y_{20} - \int y_{11} \left(\int\int A + \int y_{11}(1-A) \right), \\
&\vdots \quad .
\end{aligned} \tag{A.55}$$

The terms are proportional to either A or $(1-A)$. The terms proportional to A can be

regrouped. The terms proportional to $(1-A)$ have been set aside for clarity. For y_2 we have

$$\begin{aligned}
y_2 &= A - \epsilon\int A + \epsilon^2\int\int A - \epsilon^3\int\int\int A + \cdots \\
&+ \epsilon^3\int y_{11}\int A - \epsilon^4\int\int y_{11}\int A + \epsilon^5\int\int\int y_{11}\int A - \cdots \\
&+ \epsilon^4\int y_{12}\int A - \epsilon^5\int\int y_{11}\int A + \epsilon^6\int\int\int y_{11}\int A - \cdots \\
&\vdots \\
&- \left(\epsilon^4\int y_{11}\int\int A - \epsilon^5\int\int y_{11}\int\int A + \epsilon^6\int\int\int y_{11}\int\int A - \cdots\right) \\
&- \left(\epsilon^5\int y_{12}\int\int A - \epsilon^6\int\int y_{11}\int\int A + \epsilon^7\int\int\int y_{11}\int\int A - \cdots\right) \\
&\vdots, \\
&= A\exp(-\epsilon t) + \epsilon^2\int y_1\int A - \epsilon^3\int\int y_1\int A + \epsilon^4\int\int\int y_1\int A \\
&- \epsilon^3\int y_1\int\int A + \epsilon^4\int\int y_1\int\int A - \epsilon^5\int\int\int y_1\int\int A, \\
&= A\exp(-\epsilon t) + \epsilon^2\int y_1 At - \epsilon^3\int\int y_1 At + \epsilon^4\int\int\int y_1 At \\
&- \epsilon^3\int\int y_1 A(t^2/2) + \epsilon^4\int\int\int y_1 A(t^2/2) \\
&- \epsilon^5\int\int\int y_1 A(t^2/2) \qquad \text{(A.56)} \\
&\vdots, \\
&= A\exp(-\epsilon t) + \epsilon A\int(1-\exp(-\epsilon t/4))(1-\exp(\epsilon t)) - \\
&\epsilon^2 A\int\int(1-\exp(-\epsilon t/4))(1-\exp(\epsilon t)) + \cdots . \qquad \text{(A.57)}
\end{aligned}$$

Similarly, y_3 can be derived from the known solution of y_2 so that

$$y_3 = B\exp(-\epsilon t) + \epsilon\int y_2 - \epsilon^2\int\int y_2 + \cdots . \qquad \text{(A.58)}$$

Exact solutions are not possible to find. However, by the preceeding analysis, the following approximate solutions will capture the leading order behaviour in ϵ, well as meet the initial conditions and tend to the correct steady state. These approximate solutions are

$$\begin{aligned}
y_1 &= 1 - \exp(-\epsilon Bt/4) - \epsilon\frac{1}{2}Ce^{-2t} + \epsilon E\exp(-\epsilon Bt/4), && \text{(A.59)} \\
y_2 &= \frac{1}{2}(1-\exp(-\epsilon Bt/4)) + A\exp(-\epsilon t), && \text{(A.60)} \\
y_3 &= \frac{1}{2}(1-\exp(-\epsilon Bt/4)) + B\exp(-\epsilon t), && \text{(A.61)} \\
y_4 &= \epsilon\frac{1}{2}(1-\exp(-\epsilon Bt/4)) + \epsilon Ce^{-2t} + \frac{\epsilon}{2}B\exp(-\epsilon t). && \text{(A.62)} \\
&- \epsilon^2\frac{B}{4}E\exp(-\epsilon Bt/4). && \text{(A.63)}
\end{aligned}$$

The leading order analytical and numerical solutions are shown in Figure A.1(b).

Very simple terms are written down in (A.60) and (A.61) for y_2 and y_3 to capture the decay in initial conditions and the timescale at which y_2 and y_3 reach steady state. If the assumed analytical solution is taken away from the numerical solution then the resulting solution will be zero at $t = 0$ and at steady state. Solutions of this kind can be approximated to terms of the form $\exp(-nt)(1 - \exp(-mt))$ which are expected to arise from the non-linear terms.

A.4 Leading Order Solutions $k_3 = \epsilon^2$

Including the dephosphorylation rate constant changes the steady state of the system.

The non-zero steady state solutions can be found from the following simultaneous equations:

$$\begin{aligned} y_4(1 - y_1) - \epsilon^2 y_1 &= 0, && \text{(A.64)} \\ \epsilon y_1(1 - y_2) - \epsilon y_2 - \epsilon^2 y_2 &= 0, && \text{(A.65)} \\ \epsilon y_2 - \epsilon y_3 &= 0, && \text{(A.66)} \\ \epsilon y_3 - y_4 - y_4(1 - y_1) &= 0. && \text{(A.67)} \end{aligned}$$

Firstly, y_4 can be given in terms of y_1 by using (A.64). Note that $y_2 = y_3$ by (A.66) then y_2 can be found in terms of y_1 by using (A.65). Note that $y_4 = \epsilon Y_4$ which results in the equation

$$-2Y_4\epsilon^3 + (-2Y_4 - 3Y_4^2)\epsilon^2 + (Y_4 - Y_4^3 - 5Y_4^2)\epsilon + (Y_4^2 - 2Y_4^3) = 0. \quad \text{(A.68)}$$

The first four terms of the steady state are then found to be

$$y_4(\infty) = \frac{1}{2}\epsilon - \frac{7}{4}\epsilon^2 + \frac{7}{8}\epsilon^3 + \frac{17}{16}\epsilon^4. \quad \text{(A.69)}$$

By substituting all the terms in (A.67) for terms dependent on y_1 the first four terms of the steady state can be found to be

$$y_1(\infty) = 1 - 2\epsilon^1 - 3\epsilon^2 - \epsilon^3. \quad \text{(A.70)}$$

From the known steady states of y_1 and y_4, the steady states of y_3 and y_2 can be found to be

$$y_3(\infty) = y_4(\infty) = \frac{1}{2} - \frac{3}{4}\epsilon - \frac{9}{8}\epsilon^2 - \frac{31}{16}\epsilon^3. \quad \text{(A.71)}$$

From looking at the first few terms in the expansion of y_1 including the extra terms it is clear that the solution would be

$$y_1 = 1 - \left(2\epsilon^1 - 3\epsilon^2 - 1\epsilon^3\right)(1 - \exp(-\epsilon t)). \quad \text{(A.72)}$$

It is a simple exponential decay term as the decay is proportional to its concentration. New

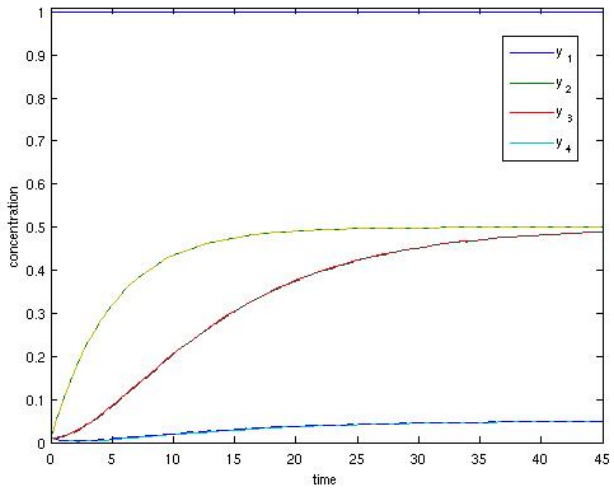

(a) Numerical (solid line) and analytical (dashed line) solutions $y_1(0) = 1$, $y_2(0) = 0.01$, $y_3(0) = 0.01$, $y_4(0) = 0.01$, $k_3 = 0$ and $\epsilon = 0.1$.

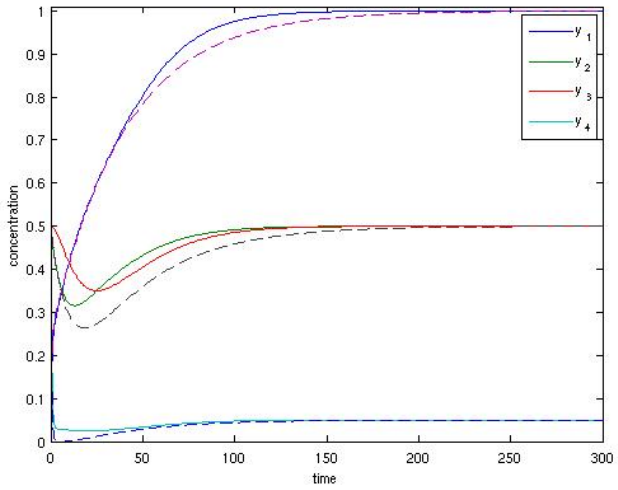

(b) Numerical (solid line) and leading order (dashed line) analytical solutions $y_1(0) < 1$, $k_3 = 0$, $\epsilon = 0.1$, $y_1(0) = 0.01$, $y_2(0) = 0.5$, $y_3(0) = 0.5$, $y_4(0) = 0.5$.

Figure A.1: Numerical Solutions for de-activated case $k_3 = 0$

leading order solutions can be found by modifying the known solutions:

$$
\begin{aligned}
y_1 &= 1 + \left(-2\epsilon^1 - 3\epsilon^2 - 1\epsilon^3\right)(1 - \exp(-\epsilon t))\,, && \text{(A.73)}\\
y_2 &= 1/2(1 - \exp(-2\epsilon t)) + A\exp(-2\epsilon t)\\
&+ \left(-\frac{3}{4}\epsilon - \frac{9}{8}\epsilon^2 - \frac{31}{16}\epsilon^3\right)(1 - \exp(-\epsilon t))\,,\\
y_3 &= \frac{1}{2}(\exp(-2\epsilon t) - \exp(-\epsilon t)) + \frac{1}{2}(1 - \exp(\epsilon t)) + B\exp(-\epsilon t)\\
&+ \left(-\frac{3}{4}\epsilon - \frac{9}{8}\epsilon^2 - \frac{31}{16}\epsilon^3\right)(1 - \exp(-\epsilon t))\,,\\
y_4 &= \epsilon\frac{1}{2}(\exp(-2\epsilon t) - \exp(-\epsilon t)) + \frac{1}{2}(1 - \exp(\epsilon t)) + B\exp(-\epsilon t) + C\exp(-2t)\\
&+ \left(-\frac{7}{4}\epsilon^2 + \frac{7}{8}\epsilon^3 + \frac{17}{16}\epsilon^4\right)(1 - \exp(-\epsilon t))\,. && \text{(A.74)}\\
& && \text{(A.75)}
\end{aligned}
$$

A.5 Fitting solutions when $y_1(0) < 1$

The fit between the assumed analytical and the numerical solutions can be improved by introducing correction terms which do not change the solutions at $t = 0$ or at steady state.

A.5.0.1 $\mathbf{y_1(0) = 1}$ and $\mathbf{k_3 = \epsilon^2}$

In this case, a slightly different selection of correction terms was used. The numerical and final fitted solutions for y_1 and y_4 are plotted in Figure A.2. The numerical and leading order solutions fitted with the correction terms are shown in Figure A.2 for initial conditions $y_1(0) = 1$, $y_2(0) = \epsilon A$, $y_3(0) = \epsilon A$ where $A = 0.112$ and $\epsilon = 10^{-2}$. Figure A.2 demonstrates how y_1 and y_4 tend to a steady state solution when $k_3 > 0$.

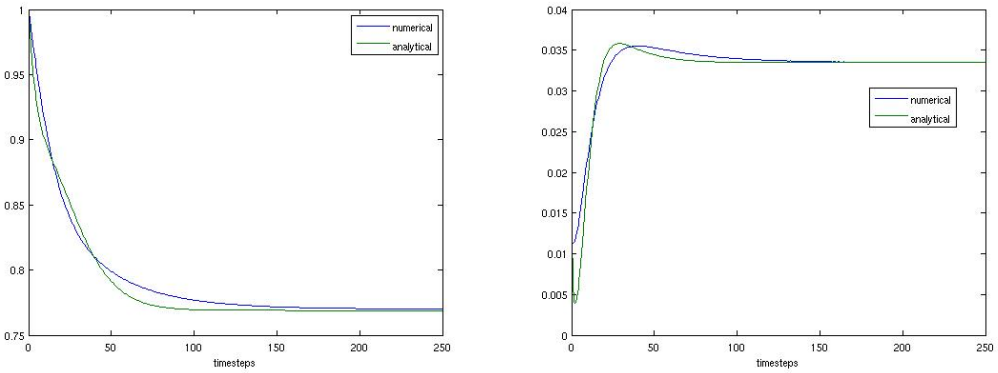

(a) Solutions for y_1.

(b) Solutions for y_4.

Figure A.2: Numerical solutions and leading order solutions with fitted correction terms (analytical) for initial conditions $y_1(0) = 1$, $y_2(0) = \epsilon A$, $y_3(0) = \epsilon A$ and $y_4(0) = \epsilon^2 A$, $A = 112$ and $\epsilon = 10^{-2}$.

Appendix B

Rate Constants for Sensitivity Analysis

This section serves as a reference to Sections 2.4.2.5 and 2.4.4.1. The vector $\mathbf{K}$ is placed in the model in Section 2.3 as follows:

$$
\begin{aligned}
J_1 &= K_1\left(k_1 m_1 m_2\right) - K_2\left(k_2 m_3\right), && \text{(B.1)}\\
J_4 &= K_3\left(k_1 m_3 m_4\right) - K_4\left(k_2 m_5\right), && \text{(B.2)}\\
J_6 &= K_5\left(k_1 m_5 m_6\right) - K_6\left(k_2 m_7\right), && \text{(B.3)}\\
J_3 &= K_7\left(k_3 m_7\right), && \text{(B.4)}\\
J_7 &= K_8\left(k_1 m_8 m_9\right) - K_9\left(k_2 m_{10}\right), && \text{(B.5)}\\
J_8 &= K_{10}\left(k_3 m_{10}\right), && \text{(B.6)}\\
J_9 &= K_{11}\left(k_4 m_{12}\right), && \text{(B.7)}\\
J_{10} &= K_{12}\left(k_1 m_1 m_{13}\right) - K_{13}\left(k_2 m_1 4\right), && \text{(B.8)}\\
J_{11} &= K_{14}\left(k_1 m_{14} m_{15}\right) - K_{15}\left(k_2 m_{16}\right), && \text{(B.9)}\\
J_{12} &= K_{16}\left(k_3 m_{16}\right), && \text{(B.10)}\\
J_{13} &= K_{17}\left(k_1 m_{18} m_{17}\right) - K_{18}\left(k_2 m_{19}\right), && \text{(B.11)}\\
J_{14} &= K_{19}\left(k_3 m_{19}\right), && \text{(B.12)}\\
J_{15} &= K_{20}\left(k_5 m_{20}\right), && \text{(B.13)}\\
J_{16} &= K_{21}\left(k_3 m_{20} m_{22}\right) - K_{22}\left(k_2 m_{23}\right), && \text{(B.14)}\\
J_{17} &= K_{23}\left(k_3 m_{14} m_{34}\right) - K_{24}\left(k_2 m_{39}\right), && \text{(B.15)}\\
J_{18} &= K_{25}\left(k_1 m_3 m_{24}\right) - K_{26}\left(k_2 m_{25}\right), && \text{(B.16)}
\end{aligned}
$$

where the rate of reaction have been written in terms of fluxes the J_i which appear in Sections 2.3.2 and 2.3.3.

Appendix C

Further Details on the Helfrich Minimisation Problem

C.1 Laplace Pressure

The Laplace pressure can be derived by conserving energy in order to demonstrate its physical interpretation. For a drop to maintain equilibrium the total work done on the droplet's surface must be zero. The work done on a surface area by a pressure difference across that surface area is

$$\begin{aligned} \delta W &= \Delta_p \, S \, \delta u, & \text{(C.1)} \\ &= \text{excess pressure} \times \text{surface area} \times \text{displacement}. & \text{(C.2)} \end{aligned}$$

The displacement is perpendicular to the surface.
The surface tension reduces the free energy of the surface so that we can write

$$\begin{aligned} \delta E &= \gamma \delta S, & \text{(C.3)} \\ &= \text{surface tension} \times \text{change in surface area}. & \text{(C.4)} \end{aligned}$$

For a curvature of the 2D surface in 3D space in Figure C.1, this can be written as

$$\delta E = \gamma \left((x + \delta x)(y + \delta y) - xy \right). \tag{C.5}$$

Let the principle directions of curvature be along the x and y axis and let the radii of curvature be r_1 and r_2 respectively. If both r_1 and r_2 increase incrementally by δu then there will be a corresponding incremental increase in surface area. The increase in r_1 by δu can be used to derive how a point on the surface moves along the x-axis by similar triangles see Figure (C.1) so that

$$\begin{aligned} \frac{x + \delta x}{r_1 + \delta u} &= \frac{x}{r_1}, & \text{(C.6)} \\ \left(1 + \frac{\delta u}{r_1}\right) x &= x + \delta x. & \text{(C.7)} \end{aligned}$$

The same principal can be used along the y-axis so that

$$\left(1+\frac{\delta u}{r_2}\right)y = y+\delta y. \tag{C.8}$$

The free energy due to the surface tension is therefore:

$$\begin{aligned}
\delta E &= \gamma\left((x+\delta x)\left(y+\delta y\right)-xy\right), && \text{(C.9)}\\
&= \gamma\left(\left(1+\frac{\delta u}{r_1}\right)x\left(1+\frac{\delta u}{r_2}\right)y-xy\right), && \text{(C.10)}\\
&= \gamma\left(xy\left(1+\delta u\left(\frac{1}{r_1}+\frac{1}{r_2}\right)+\frac{\delta u}{r_1 r_2}\right)-xy\right), && \text{(C.11)}\\
&= \gamma\left(xy\delta u\left(\frac{1}{r_1}+\frac{1}{r_2}\right)+\frac{xy(\delta u)^2}{r_1 r_2}\right). && \text{(C.12)}
\end{aligned}$$

The free energy from the surface tension and the work due to the pressure difference across the surface is now equated so that

$$\begin{aligned}
\delta W &= \delta E, && \text{(C.13)}\\
\Delta_p S\delta u &= \gamma S\delta u\left(\frac{1}{r_1}+\frac{1}{r_2}\right). && \text{(C.14)}
\end{aligned}$$

The change in r_1 and r_2, δu, can be taken to be the distance the surface is displaced by the work done by the excess pressure. This results in the well known Laplace-Young Equation

$$\begin{aligned}
\Delta_p &= \gamma\left(\frac{1}{r_1}+\frac{1}{r_2}\right), && \text{(C.15)}\\
\frac{\Delta_p}{\lambda} &= 2\times\text{mean curvature}. && \text{(C.16)}
\end{aligned}$$

Generally, the energy conservation equation is

$$\begin{aligned}
\delta W &= -\text{pressure inside the drop} - \text{pressure outside the drop} && \text{(C.17)}\\
&+ \text{surface tension}, && \text{(C.18)}\\
\delta W &= -\Delta_p dV + \gamma dA. && \text{(C.19)}
\end{aligned}$$

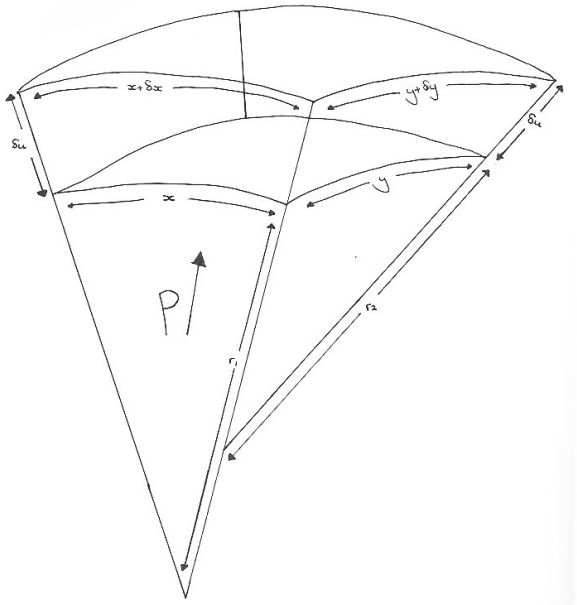

Figure C.1: Diagram of a small element of a surface and the resulting size of the surface element when the radius of curvature is increased.

C.2 Physics of Contact Angles

When a liquid is dropped onto a solid surface the equilibrium angle, θ_E of the forces at the solid/liquid/vapour interface are resolved by the Young Equation which balances the solid-vapour interfacial energy, γ_{SL}, the solid-vapour interfacial energy, γ_{SV} and the liquid-solid interfacial energy, γ. This balance of forces can be written as

$$0 = \gamma_{SV} - \gamma_{SL} - \gamma \cos\theta_E. \tag{C.20}$$

The wettability of a particular surface with a given liquid can be measured by θ_E with θ_E increasing as wettability decreases. If $\theta_E > \pi$ for water then the surface is hydrophobic. The dynamic contact angle , θ_D is defined as the angle for which the three-phase boundary point has constant velocity V. This is because the loss in energy due to viscous forces generally balances that of the rate of change in energy FV. This is discussed in [20] alongside a general derivation from energy conservation principals.

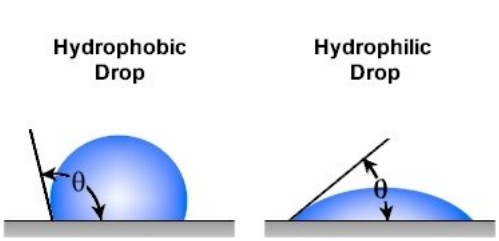

Figure C.2: Diagram of the contact angle of a drop on a solid surface. Image publicly available.

C.3 Weierstrass E-Function

The Weierstrauss E-Function can be used to determine whether the Euler-Lagrange equation minimises or maximises the Helfrich energy. It can be defined as

$$E(x, c_p, \dot{c}_p, q) = f(x, c_p, \dot{c}_p) - f(x, c_p, q) - (\dot{c}_p - q)\frac{\partial f}{\partial q}(x, c_p, q). \tag{C.21}$$

The Helfrich energy can be written in terms of x and $c_p(x)$ only so that

$$\begin{aligned} E_H &= \int x\left(1-(xc_p)^2\right)^{-1/2} f(x, c_p, \dot{c}_p)dx, \\ f(x, c_p, \dot{c}_p) &= \left(x\frac{dc_p}{dx} + 2c_p - c_0\right)^2 dx, \end{aligned} \tag{C.22}$$

so

$$E(x, c_p, \dot{c}_p, q) = \tag{C.23}$$

$$= \left(x\frac{dc_p}{dx} + 2c_p - c_0\right)^2 - (xq + 2c_p - c_0)^2 \tag{C.24}$$

$$-2x\left(\frac{dc_p}{dx} - q\right)(xq + 2c_p - c_0), \tag{C.25}$$

$$= x^2\left(\left(\frac{dc_p}{dx}\right)^2 - q^2\right) + 2x\left(\frac{dc_p}{dx} - q\right)(2c_p - c_0) \tag{C.26}$$

$$-2x\left(\frac{dc_p}{dx} - q\right)(xq + 2c_p - c_0). \tag{C.27}$$

$$= x^2\left(\frac{dc_p}{dx} - q\right)^2 \geq 0 \tag{C.28}$$

If f is written with respect to s, then

$$f(s, c_p, \dot{c}_p) = \left(\frac{f}{2}\left(1 - fc_p^2\right)^{-1/2}\frac{dc_p}{ds} + 2c_p - c_0\right)^2 \tag{C.29}$$

and

$$E(s, c_p, \dot{c}_p, q) = \frac{f^2}{4}\left(1 - fc_p^2\right)^{-1}\left(\frac{dc_p}{ds} - q\right)^2 \geq 0. \tag{C.30}$$

The Euler-Lagrange equation of the Helfrich energy is found to be always always a minimiser of Helfrich energy.

C.4 The Limit of the Euler-Lagrange Equations when $f = 0$

By Hopital's Rule limit of (5.37) at $f = 0$ when $c_m - c_p = 0$ is

$$\lim_{f\to 0}\frac{dc_p}{ds} = 2\lim_{f\to 0}\frac{c_m - c_p}{f}, \tag{C.31}$$

$$= 2\frac{\frac{dc_m}{ds} - \frac{dc_p}{ds}}{\frac{df}{ds}}, \tag{C.32}$$

$$= \frac{1}{2}|\frac{dc_m}{ds} - \frac{dc_p}{ds}|, \tag{C.33}$$

$$\frac{dc_p}{ds} = \frac{1}{3}\frac{dc_m}{ds}, \tag{C.34}$$

$$\tag{C.35}$$

where at $f = 0$ we have $\dot{f} = 4$. As

$$\frac{dc_m}{ds} = \left(1 - fc_p^2\right)^{-1/2}\left\{c_p(c_p^2 - c_m^2) + 2(\lambda/k_c)c_p + (\Delta_p/k_c)\right\} - \frac{dc_p}{ds}, \tag{C.36}$$

then (C.34) can be substituted into (C.36) to find

$$\frac{dc_m}{ds} = \frac{3}{4}c_p\left[(c_p - c_0)^2 - c_m^2\right] + 2\lambda c_p + \Delta_p. \tag{C.37}$$

The correct limits as $f \to 0$ for (5.36)-(5.38) have now been obtained.

C.5 Higher Order Differential Terms of the Euler-Lagrange Equations

In this section contains full details of the second order terms in the Taylor expansion (5.47)-(5.49) in Section 5.4.2. The only stationary point of the third order system given in (5.36-5.38) is at $fc_p^2 = 1$ when $c_p(c_p^2 - c_m^2) + \Delta_p + 2\lambda c_p = 0$. The second order derivatives are

$$\frac{d^2c_m}{ds^2} = -2\left(\frac{-c_m - 4c_p - f\Delta_p - fc_m^3 - 4fc_pc_0c_m + 6fc_pc_m^2 + 6c_0}{f^2}\right) - 2\left(\frac{-2fc_pc_0^2 - 4f\lambda c_p + fc_0^2c_m + 2f\lambda c_m}{f^2}\right), \tag{C.38}$$

$$\frac{d^2c_p}{ds^2} = -2\left(\frac{7c_p + 2c_0 - fc_pc_0^2 + 3fc_pc_m^2 - 2f\lambda c_p - f\Delta_p + 8c_m}{f^2}\right), - 2\left(\frac{-10c_m - 8c_p}{f^2}\right) \tag{C.39}$$

$$\frac{d^2f}{ds^2} = -8c_mc_p. \tag{C.40}$$

Bibliography

[1] Project on Emerging Nanotechnologies, http://www.nanotechproject.org/, Woodrow Wilson International Center for Scholars and the Pew Charitable Trusts.

[2] B. Aggarwal. Signalling pathways of the TNF superfamily: A double-edged sword. *Nature Review: Immunology*, 3:745–756, 2003.

[3] B. B. Aggarwal. Tumour necrosis factors receptor associated signalling molecules and their role in activation of apoptosis and JNK and NF-κB. *Ann. Rheum. Dis.*, 59:i6–i16, 2000.

[4] M. Bagnoli, S. Canevari, and D. Mezzanzanica. Cellular FLICE-inhibitory protein (c-FLIP) signalling: A key regulator of receptor-mediated apoptosis in physiologic context and in cancer. *Int. J. Bio. and Cell Bio.*, 42:210–213, 2010.

[5] Baichwal and Baeuerle. Apoptosis: Activate NF-κB or die? *Current Biology*, 7:R94–R96, 1997.

[6] M. Bitzer, G. von Gersdorff, and D. Liang. A mechanism of suppression of TGF-β/SMAD signaling by NF-κB/RelA. *Genes Dev.*, 14:187–197, 2000.

[7] T. Blake, V. Castranova, D. Schwegler-Berry, P. Baron, G. Deye, C. Li, and W. Jones. Effect of fiber length on glass microfiber cytotoxicity. *J. Tox. Env. H. A*, 54:243–259, 1998.

[8] G. Blyth and C. Pozrikidis. Solution space of axisymmetric capsules enclosed by elastic membranes and biological cells. *Eur. J. Mech. A*, 23:877–892, 2004.

[9] K. Donaldson & V. Stone & C. L. Tran & W. Kreyling & P. J. A. Borm. Nanotoxicology. *Occup. Environ. Med.*, 61:727–728, 2004.

[10] F. Brochard. Spreading of liquid drops on thin cylinders: the 'manchon/droplet' transition. *J. Chem. Phys.*, 84:4664–4672, 1986.

[11] E. Burello and A. Worth. A theoretical framework of predicting the oxidative stress potential of oxide nanoparticles. *Nanotoxicology*, in press:in press, 2011.

[12] B.J. Carroll. The accurate measurement of contact angle and phase contact area and drop volume and and laplace excess pressure in drop-on-fiber systems. *J. Coll. and Int. Sci.*, 57:488–495, 1976.

[13] B.J. Carroll. Equilibrium conformations of liquid drops on thin cylinders under forces of capillarity. A theory for the roll-up process. *Langmuir*, 2:248–250, 1986.

[14] J.A. Champion and S. Mitragotri. Role of target geometry in phagocytosis. *PNAS*, 103:4930–4934, 2006.

[15] J.A. Champion and S. Mitragotri. Shape induced inhibition of phagocytosis of polymer particles. *Phar. Res.*, 26:244–249, 2008.

[16] Chin, Shu, Shan Shi, Yao, Kehrl, and Cheng. TANK potentiated Tumour Necrosis Factor Receptor-associated factor-mediated c-Jun N-terminal Kinase/ Stress-Activated Protein Kinase activation through the Germinal center kinase pathway. *Mol. Cell. Bio.*, 27:8152–8163, 2007.

[17] S. W. Chiu, M. Clark, V. Balaji, and S. Subramaniam. Incorporation of surface tension into molecular dynamics simulation of an interface: A fluid phase lipid bilayer membrane. *Biophys. J.*, 69:1230–1245, 1995.

[18] K.H. Cho, S.-Y. Shin, W. Kolch, and O. Wolkenhauer. Experimental design in systems biology and based on parameter sensitivity analysis using a monte carlo method: a case study for the TNF-mediated NF-κB signal transduction pathway. *Simulation*, 79:726–739, 2003.

[19] M. L. Circu and T. Y. Aw. Reactive oxygen species and cellular redox systems and and apoptosis. *Free Radical Biology and Medicine*, 48:749–762, 2010.

[20] P.-G. de Gennes, F. Brochard-Wyart, and D. Quere. *Capillarity and wetting phenomena: Pearls and bubbles and drops and waves.* Springer, 2004.

[21] P.G. de Gennes and J. Prost. *The Physics of Liquid Crystals.* OUP, 1993.

[22] Pierre-Gilles de Gennes. *Scaling concepts in polymer physics.* Cornell University Press, 1979.

[23] W. Declercq, T.V. Berghe, and P. Vandenabeele. RIP kinases at the cross-roads of cell death and survival. *Cell*, 138:229–232, 2009.

[24] M. Deserno and T. Bickel. Wrapping of a spherical colloid by a fluid membrane. *Europhys. Lett.*, 62:767–773, 2003.

[25] H.J. Deuling and W. Helfrich. The curvature elasticity of fluid membranes: A catalogue of vesicle shapes. *J. Physique*, 37:1335–1345, 1976.

[26] L. Ding, J. Stilwell, T Zhang, O. Elboudwarej, H. Jiang, J.P. Selegue, P.A. Cooke, J.W. Gray, and F.F. Chen. Molecular characterisation of the cytotoxic mechanism of multiwall carbon nanotubes and nano-onions on human skin fibroblast. *Nano Letters*, 5:2448–2464, 2005.

[27] H.G. Döbereiner, E. Evans, M. Kraus, U. Seifert, and M. Wortis. Mapping vesicle shapes into the phase diagram: A comparison of experiment and theory. *Phys. Rev. E*, 55:4458–4474, 1997.

[28] K. Donaldson, R. Aitken, L. Tran, V. Stone, R. Duffin, G. Forrest, and A. Alexander. Carbon nanotubes: A review of their properties in relation to pulmonary toxicology and workplace safety. *Toxicological Sciences*, 92:5–22, 2006.

[29] K. Donaldson, R.C. Brown, and G.M. Brown. Respirable industrial fibres: Mechanisms of pathogenicity. *Thorax*, 48:390–395, 1993.

[30] K. Donaldson and C. Poland. New insights into nanotubes. *Nature Nanotechnology*, 4:708–710, 2009.

[31] M. Dörger, S. Münzing, A.-M. Allmeling, K. Messmer, and F. Krombach. Differential responses of rat alveolar and peritoneal macrophages to man-made vitreous fibers in vitro. *Env. Res. Sec. A*, 85:207–214, 2001.

[32] W. Dreyer and F. Duderstadt. On the Becker-Döring theory of nucleation of liquid droplets in solids. *J. Stat. Phys.*, 123:55–87, 2006.

[33] E. Eisenriegler. Polymers interacting with spherical and rodlike particles. *Phys. Rev. E*, 52:1134–1152, 1996.

[34] E.A. Evans and R. Skalak. Mechanics and thermodynamics of biomembranes. *CRC*, 3:181–330, 1979.

[35] S. Fiedler and A. Violi. Simulation of nanoparticle permeation through a lipid membrane. *Biophys. J.*, 99:144–152, 2010.

[36] F.C. Frank. I. liquid crystals: On the theory of liquid crystals. *Discuss. Faraday Soc.*, 25:19–28, 1958.

[37] P. Frank and Y. Marcel. Apolipoprotein A-1: structure-function relationships. *J. Lipid Res.*, 41:853–872, 2000.

[38] S. K. Friedlander. *Smoke and dust and haze: Fundamentals of aerosol dynamics*. OUP, 2nd edition, 2000.

[39] Y. Gu and D. Li. A model for a liquid drop spreading on a solid surface. *Colloids and Surfaces*, 142:243–256, 1998.

[40] S.M. Hankin, C.L. Tran, B. Ross, K. Donaldson, V. Stone, and Q. Chaudhry. Cell pen: A study to identify the physico-chemical factors controlling the capacity of nanoparticles to penetrate cells. Research Consulting Services, August 2008.

[41] Diana Longo & Jeff Hasty. Dynamics of single-cell gene expression. *Mol. Sys. Bio.*, 2(64):1–10, 2006.

[42] T. Hayakawa, A. Matsuzawa, T. Noguchi, K. Takeda, and H. Ichijo. The ASK1-MAP kinase pathways om immune and stress responses. *Mic. Inf.*, 8:1098–1107, 2008.

[43] Heinrich, Neel, and Rapoport. Mathematical models of protein kinase signal transduction. *Mol. Cell*, 9:957–970, 2002.

[44] W. Helfrich. Elastic properties of lipid bilayers: Theory and possible experiments. *Z. Naturforsch*, 28:693–703, 1973.

[45] M. Herant, V. Heinrich, and M. Dembo. Mechanics of neutrophil phagocytosis: Experiments and quantitative models. *J. Cell. Sci.*, 119:1903–1913, 2006.

[46] J. Israelivichi. *Intermolecular and Surface Forces.* Academic Press, 1992.

[47] H. Jian-Guo and O.-Y. Zhong-Can. Shape equations of the axisymmetric vesicles. *Phys. Rev. E*, 47:461–467, 1992.

[48] Karin and Ben-Neriah. Phosphorylation meets ubiquitination: The control of NF-κB activity. *Ann. Rev. Imm.*, 18:621–663, 2000.

[49] J. Kas and E. Sackmann. Shape transitions and shape stability of giant phospholipid vesicles in pure water induced by area-to-volume changes. *Biophys. J.*, 60:825–844, 1991.

[50] J. Klein and V. Hořejší. *Immunology.* Blackwell Science, 1997.

[51] L. Kobzik, S. Huang, J. Paulauskis, and J. Godleski. Particle opsonization and lung macrophage cytokine response. *J. Imm.*, 151:2753–2759, 1993.

[52] I. Kusner and S. Srebnik. Conformational behavior of semi-flexible polymers confined to a cylindrical surface. *Chem. Phys. Lett.*, 430:84–88, 2006.

[53] Chang L., H. Kamata, G. Solinas, J.-L. Luo, S. Maeda, K. Venuprasad, Y.-C. Liu, and M. Karin. The E3 ubiquitin ligase Itch couples JNK activation to TNFα-induced cell death by inducing c-FLIP$_l$ turnover. *Cell*, 124:601–613, 2006.

[54] A. Laadhari, C. Misbah, and P. Saramito. On the equilibrium equation for a generalised biological membrane energy by using a shape optimisation approach. *Physica D: Nonlinear Phen.*, 239:1597–1572, 2011.

[55] S. J. Klaine & Pedro J. J. Alvarez & Graeme E. Batley & Teresa F. Fernandes & Richard D. Handy & Delina Y. Lyon & Shally Mahendra & Michael J. McLaughlin & Jamie R. Lead. Nanomaterials in the environment: Behaviour, face, biolavailability, and effects. *Env. Tox. Chem.*, 27(9):1825–1851, 2008.

[56] A. Leask and D.J. Abraham. TGF-β signaling and the fibrotic response. *FASEB J.*, 18:816–827, 2004.

[57] J. P. Ling. Elastic properties of carbon nanotubes and nanoropes. *Phys. Rev. Lett.*, 79:1297–1300, 1997.

[58] Liu and Lin. Role of JNK activation in apoptosis: A double-edged sword. *Cell Res.*, 15:36–42, 2005.

[59] I. Lynch, T. Cedervall, M. Lundqvist, C. Cabaleiro-Lago, S. Linse, and K. Dawson. The nanoparticle-protein complex as a biological entity; a complex fluids and surface science challenge for the 21st century. *Adv. Coll. Int. Sci.*, 134-135:167–174, 2007.

[60] L. Ma, J. Wagner, J.J. Rice, W. Hu, A.J. Levine, and G.A. Stolovitzky. A plausible model for the digital response to DNA damage. *PNAS*, 102:14266, 2005.

[61] J. Mahanty and B.W. Ninham. *Dispersion Forces*. AP, 1976.

[62] S.K. Manna, S. Sarkar, J. Barr, K. Wise, E.V. Barrera, O. Jejelowo amd A. Rice-Ficht, and G. Ramesh. Single-walled carbon nanotube induces and activates Transciption Factor-κ B in human keratinocytes. *Nano Letters*, 5:1671–2464, 2005.

[63] A. D. Maynard. Safe handling of nanotechnology. *Nature*, 444:267–269, 2006.

[64] G. McHale, N.A. Kab, M.I. Newton, and S.M. Rowan. Wetting of a high-energy fiber surface. *Jour. Coll. Int. Sci.*, 186:453–461, 1997.

[65] G. McHale, M.I. Newton, and B.J. Carroll. The shape and stability of small liquid drops on fibers. *Oil and Gas Science and Technology*, 56:47–54, 2001.

[66] H.T. McMahon and J.L. Gallop. Membrane curvature and mechanisms of dynamic cell membrane remodelling. *Nature*, 438:590–596, 2005.

[67] R.R. Mercer, J. Scabilloni, L. Wang, E. Kisin, and A.R. Murray. Alteration of deposition pattern and pulmonary response as a result of improved dispersion of aspirated single-walled carbon nanotubes in a mouse cell. *Am. J. Physiol. Lung Cell Mol. Physiol.*, 294:87–97, 2008.

[68] S.T. Milner. Polymer brushes. *Science*, 251:905–914, 1991.

[69] A. Mogilner. Mathematics of cell motility: Have we got its number? *J. Math. Biol.*, 58:105–134, 2009.

[70] A. Moligner and G. Oster. Cell motility driven by actin polymerization. *Biophys. J.*, 71:3030–3045, 1996.

[71] H. Mollmann. *Introduction to the theory of thin shells.* Wiley, 1981.

[72] H. Naito and M. Okuda. New solutions to the helfrich variation problem for the shapes of lipid bilayer vesicles: Beyond Delaunay's surfaces. *Phys. Rev. Lett.*, 74:4345–4348, 1995.

[73] A. Nakajima, S. Komazawa-Sakon, M. Takekawa, T. Sasazuki, W.-C., Yeh, H. Yagita, K. Okumura, and H. Nakano. An anti-apoptotic protein and c-FLIP$_l$ directly binds to MKK7 and inhibits the JNK pathway. *EMBO*, 25:5549–5559, 2006.

[74] H. Nakano, A. Nakajima, S. Sakon-Komazawa, J.-H. Piao, X. Xue, and K. Okumura. Reactive oxygen species mediate crosstalk beteen NF-κB and JNK. *Cell Death and Differentiation*, 13:730–737, 2006.

[75] W. Nazaroff and G. Cass. Mathematical modelling of indoor aerosol dynamics. *Env. Sci. Tech.*, 23:157–166, 1989.

[76] A. Nel, L. Mädler. D. Velegol, T. Xia, E. Hoek, P. Somasundaran, F. Klaessig, V. Castranova, and M. Thompson. Understanding biophysicochemical interactions at the nano-bio interface. *Nature Materials*, 8:543–557, 2009.

[77] A. Nel, T. Xia, L. Mädler, and N. Li. Toxic potential of materials at a the nanolevel. *Science*, 311:622–627, 2006.

[78] H. Dika Nguea, B. Rihn, D. Mahon, J.-L. Bernard, A. de Reydellet, and A. le Faou. Effects of various man-made mineral fibers on cell apoptosis and viability. *Arch. Toxicol.*, 79:487–492, 2005.

[79] D. Ni, H. Shi, and Y. Yin. Theoretical analysis of adhering lipid vesicles with free edges. *Coll. and Surf. B*, 46:162–168, 2005.

[80] G. Oberdörster, A. Oberdörster, and J. Oberdörster. Nanotoxicology: An emerging discipline evolving from studies of ultrafine particles. *Environment Health Perspectives*, 113:823–839, 2005.

[81] B. O'Neill. *Elementary differential geometry.* Academic Press, 2nd edition, 1997.

[82] L. Onsager. The effects of shape on the interaction of colloidal particles. *Acad. Sci.*, 51:627–659, 1949.

[83] J. Oprea. *Differential geometry and its applications.* Pearson Prentice Hall, 2nd edition, 2004.

[84] Papa, Bubici, Zazzeroni, and Franzoso. NF-κB meets ROS: An 'iron-ic' encounter. *Cell Death and Diff.*, 12:1259–1262, 2005.

[85] Papa, Bubici, Zazzeroni, Pham, Kuntzen, Knabb, Dean, and Franzoso. The NF-κB-mediated control of the JNK cascade in the antogonism of programmed cell death in health and disease. *Cell Death and Diff.*, 13:712–729, 2006.

[86] P.A. Pincus, C.J. Sandroff, and T.A. Witten. Polymer adsorption in colloidal particles. *J. Physique*, 45:725–729, 1984.

[87] C. Poland, R. Duffin, I. Kinloch, A. Maynard, W. Wallace, A. Seaton, V. Stone, S. Brown, W. MacNee, and K. Donaldon. Carbon nanotubes introduced into the abdominal cavity of mice show asbestos-like pathogenicity in a pilot study. *Nature Nanotechnology*, 3:423–428, 2008.

[88] C. Pozrikidis. *Modeling and simulation of capsules and biological cells.* Chapman and Hall/CRC, 2003.

[89] Rangamani and Sirovich. Survival and apoptotic pathways initiated by TNF-α: Modeling and predictions. *Biotech. and Bioeng.*, 97:1216–1229, 2007.

[90] Sanford M. Roberts and Jerome S. Shipman. *Two-point boundary value problems: shooting methods.* American Elsevier Pub. Co., 1972.

[91] George V. Buxton & Clive L. Greenstock & W. Philip Helman & Alberta B. Ross. Critical review of rate constants for reactions of hydrated electrons, hydrogen atoms and hydroxyl radicals (oh/o$_-$) in aqueous solution. *Atomic Energy*, 17(2):513, 1986.

[92] J.P. Ryman-Rasmussen, M. Cesta, A. Brody, J. Shipley-Phillips, J. Everitt, E. Tewksbury, O. Moss, B. Wong, D. Dodds, M. Andersen, and J. Bonner. Inhaled carbon nanotubes reach the subpleural tissue in mice. *Nature Nanotechnology*, 4:747–751, 2009.

[93] E. Sackmann. Membrane bending energy concept of vesicle-and-cell-shapes and shape-transitions. *FEBS Letters*, 246:3–16, 1994.

[94] Andrea Saltelli. *Sensitivity analysis in practice: A guide to assessing scientific models.* John Wiley and Sons, 2004.

[95] C. Salvador-Morales, E. Flahaut, E. Sim, J. Sloan, M. Green, and R. Sim. Complement activation and protein absorption by carbon nanotubes. *Mol. Imm.*, 43:193–201, 2006.

[96] Salveses and Duckett. Iap proteins: Blocking the road to death's door. *Nature Rev.: Mol. Cell Bio.*, 3:401–410, 2002.

[97] A. Sanchez-Capelo. Dual role for TGF-β1 in apoptosis. *Cytokine Growth Factor Reviews*, 16:15–34, 2005.

[98] U. Seifert. Configurations of fluid membranes and vesicles. *Adv. Phys.*, 46:13–137, 1997.

[99] U. Seifert, K. Berndl, and R. Lipowsky. Shape transformations of vesicles: Phase diagrams for spontaneous-curvature and bilayer-coupling models. *Phys. Revi. A*, 44:1182–1202, 1991.

[100] M. Seipenbusch, A. Binder, and G. Kasper. Temporal evolution of nanoparticle aerosols in workplace exposure. *Ann. Occup. Hyg.*, 52:707–716, 2008.

[101] M. Seipenbusch, P. Toneva, W. Peukert, and A. Weber. Impact fragmentation of metal nanoparticle agglomerates. *Part. Sci. Syst. Character.*, 24:193–200, 2007.

[102] M. Selman, T. King, and A. Pardo. Idiopathic pulmonary fibrosis: Prevailing and evolving hypotheses about its pathogenesis and implications for therapy. *Ann. Intern. Med.*, 134:136–151, 2001.

[103] Sethi, Seok Ahn, Xia, Kurie, and Aggarwal. Targeted deletion of MKK4 gene potentiates TNF-induced apoptosis through the down-regulation of NF-κB activation and NF-κB-regulated antiapoptotic gene products. *J. Immun.*, 179:1926–1933, 2007.

[104] K. Shibata, Y. Kudo, M. Tsunoda, M. Hosokawa, Y. Sakai, M. Kotani, and Y. Aizawa. Magnetometric evaluation of the effects of man-made mineral fibers on the function of macrophages using macrophage cell line RAW 264.7. *Ind. Hea.*, 45:426–436, 2007.

[105] H. Shinji, M. Watanabe, Y. Kudo, M. Niitsuya, M. Tsunoda, T. Satoh, Y. Sakai, M. Kotani, and Y. Aizawa. The cytotoxicity of microglass fibers on alveolar macrophages of Fischer 344 rats evaluated by cell magnetometry and cytochemistry and morphology. *Env. Hea. Prev. Med.*, 10:111–119, 2005.

[106] A. A. Shvedova, V. Castranova, E. Kisin, D. Schwegler-Berry andA. Murray, V. Gandelsman, A. Maynard, and P. Baron. Exposure to carbon nanotube material: Assessment of nanotube cytotoxicity using human keratinocyte cells. *Journal Tox. and Env. Health A*, 66:1909–1926, 2005.

[107] A.A. Shvedova, E.R. Kisin, R. Mercer, A. Murray, and V. Johnson. Unusual inflammatory and fibrogenic pulmonary reponses to single-walled carbon nanotubes in mice. *Am. J. Physiol. Lung. Cell. Mol. Physiol.*, 289:698–708, 2005.

[108] A.A. Shvedova, E.R. Kisin, D. Porter, P. Schulte, V.E. Kagan, B. Fadeel, and V. Castranova. Mechanisms of pulmonary toxicity and medical applications of carbon nanotubes: Two faces of Janus? *Parm. Thera.*, 121:192–204, 2009.

[109] Singh. *Oxidative Stress and Disease and Cancer.* Imperial College Press, 2006.

[110] K.I. Skau and E.M. Blokhuis. Polymer adsoption on curved surfaces: Finite chain length corrections. *Macromolecules*, 36:4637–4645, 2003.

[111] W. Song, P. Tang, H. Zhang, Y. Yang, and A.-C. Shi. New numerical implementation of self-consistent field theory for semiflexible polymers. *Macromolecules*, 42:6300–6309, 2009.

[112] V. Stone, K. Donaldson, and G. Oberdörster. Toxicology of nanoparticles: A historical perspective. *Nanotoxicology*, 1:2–25, 2007.

[113] B. Suki and J.H.T. Bates. Extracellular matrix mechanics in lung parenchymal diseases. *Respiratory Physiology & Neurobiology*, 163:33–43, 2008.

[114] B. Suki, S. Ito, D. Stamenovic, K.R. Lutchen, and E.P. Ingenito. Biomechanics of the lung parenchyma: Critical roles of collagen and mechanical forces. *J. Appl. Physiol.*, 98:1892–1899, 2005.

[115] V. Thannickal and J. Horowitz. Evolving concepts of apoptosis in idiopathic pulmonary fibrosis. *Proc. Am. Thorac. Soc.*, 3:350–356, 2006.

[116] M. Thome and J. Tschopp. Regulation of lymphocyte proliferation and death by FLIP. *Nature Rev. Immu.*, 1:50–58, 2001.

[117] F. Tian, D. Cui, H. Schwarz, G.G. Estrada, and H. Kobayashi. Cytotoxicity of single-wall carbon nanotubes on human fibroblasts. *Toxicology in Vitro*, 20:1202–1212, 2006.

[118] M. Toshima, Y. Ohtani, and O. Ohtani. Three-dimensional architecture of elastin and collagen fiber networks in the human and rat lung. *Arch. Histol. Cytol.*, 67:31–40, 2004.

[119] Z.C. Tu and Z.C. Ou-Yang. Lipid membranes with free edges. *Phys. Rev. E*, 68:061915, 2003.

[120] Kagen V.E., Rao K.M.K, Kisin E.R., Young S.-H., Meighan T., Murray A.R., Tyurina Y.Y., Castranova V., and Shvedova A.A. Pulmonary effects of single-walled carbon nanotubes: Inflammatory response and oxidative stress/signaling and recognition by macrophages. *Nanotechnology-Toxicological Issues and Environmental Safety*, 2007:65–75, 2007.

[121] Ventura, Cogswell, Flavell, Baldwin, and Davis. JNK potentiates TNF-simulated necrosis by increasing the production of cytotoxic reactive oxygen species. *Genes and Dev.*, 18:2905–2915, 2004.

[122] F. Verrecchia and A. Mauviel. TGF-β and TNF-α: Antagonistic cytokines controlling type I collagen gene expression. *Cellular Signalling*, 16:873–880, 2004.

[123] L. Verstrepen, T. Bekaert, T.-L. Chau, J. Tavernier, A. Chariot, and R. Beyaert. TLR-4 and IL-1R and TNF-R signaling to NF-κ B: Variations on a common theme. *Cell. Mol. Life Sci. and*, 65:2964–2978, 2008.

[124] M. Visvanathan, B. Pfeifer, C. Baumgartner, B. Tilg, and G.H. Lushington. Integrative approach for combining TNF-α-NFκb mathematical model to a protein interaction connectivity map. *LNCS*, 5542:63–74, 2009.

[125] J.A.D. Wattis. An introduction to mathematical models of coagulation-fragmentation processes: A discrete deterministic mean-field approach. *Physica D*, 222:1–20, 2006.

[126] W. Wei, A. Sethuraman, C. Jin, N.A. Monteiro-Riviere, and R.J. Narayan. Biological properties of carbon nanotubes. *Journal of Nanoscience and Nanotechnology*, 7:1–14, 2007.

[127] P. Wick, P. Manser, L.K. Limbach, U. Dettlaff-Weglikowska, F. Krumeich, S. Roth, W.J. Stark, and A. Bruinink. The degree and kind of agglomeration affect carbon nanotube cytotoxicity. *Tox. Lett.*, 168:121–131, 2007.

[128] X. Yan and Y. Chen. Regulation of TGF-β signaling by Smad7. *Acta Biochim Sin*, 41:263–272, 2009.

[129] J. Ye, X. Shi, W. Jones, Y. Rojanasakul, N. Cheng, D. Schwegler-Berry, P. Baron, G. Deye, C. Li, and V. Castranova. Critical role of glass fiber length in TNF-α production and transcription factor activation in macrophages. *Am. J. Physiol. Lung Cell Mol. Physiol.*, 276:426–434, 1999.

[130] O.-Y. Zhong-Can and W. Helfrich. Instability and deformation of a spherical vesicle by pressure. *Phys. Rev. Lett.*, 59:2486–2488, 1987.

[131] O.-Y. Zhong-Can and W. Helfrich. Bending energy of vesicle membranes: General expressions for the first and second and third variation of the shape energy and applications to spheres and cylinders. *Phys. Rev. A*, 39:5280–5288, 1989.